A NUMERICAL INVESTIGATION OF THE PLENUM CHAMBER AERODYNAMIC BEHAVIOUR OF MECHANICAL DRAUGHT AIR-COOLED HEAT EXCHANGERS

by

C.J. Meyer

Dissertation presented for the degree of Doctor of Philosophy (Mechanical Engineering) at the University of Stellenbosch.

PROMOTER: Prof. D.G. Kröger

Department of Mechanical Engineering

University of Stellenbosch

South Africa

November 2000

DECLARATION

I, the undersigned, hereby declare that the work contained in this dissertation is my own original work and that I have not previously in its entirety or in part submitted it at any other university for a degree.

SUMMARY

The primary purpose of this dissertation is to further the understanding of the influence of plenum chamber aerodynamic behaviour on mechanical draught air-cooled heat exchanger (ACHE) performance. The investigation, which included both forced and induced draught ACHEs, was conducted through the use of a commercially available computational fluid dynamics (CFD) code. A numerical axial flow fan and heat exchanger model that simulates the effect of the axial flow fan and heat exchanger bundle respectively on the flow field within the ACHE was developed and included in the CFD-code through user-programming. Where appropriate the numerical investigation was augmented with experimental data. The plenum chamber aerodynamic behaviour is characterised and included in the draught equations associated with forced and induced draught ACHEs through the introduction of dimensionless plenum chamber recovery and plenum chamber loss coefficient respectively. The influence of changes made to a range of mechanical draught ACHEs on plenum chamber aerodynamic behaviour was investigated. These changes include:

- Operating conditions of the axial flow fan.
- The height of the plenum chamber in the fan axial direction.
- The heat exchanger bundle isothermal flow resistance.
- The fan to heat exchanger area ratio.
- The axial position of the fan in the fan casing.

From the results of the numerical investigation a set of design guidelines are set for both forced and induced draught ACHEs. The design guidelines include recommended values for the dimensionless plenum chamber recovery and plenum chamber loss coefficient to be used in the respective draught equations enabling a more accurate prediction of the operating point of a proposed mechanical draught ACHE.

KEYWORDS: air-cooled heat exchanger
numerical investigation
plenum chamber
aerodynamic behaviour

OPSOMMING

Die primêre doel van hierdie proefskrif is om die kennis aangaande die invloed van plenum ruimte lugdinamiese gedrag op die werking van meganiese-trek lugverkoelde warmteruilers (LVWRs) te verbreed. Die ondersoek wat geforseerde- asook geïnduseerdetrek LVWRs ingesluit het is uitgevoer deur gebruik te maak van 'n kommersiële verkrygbare berekeningsvloeimeganika-pakket. 'n Numeriese aksiaalwaaier- en warmteruilermodel wat die invloed van respektiewelik die aksiaalwaaier en die warmteruiler op die vloeiveld in die LVWR simuleer is ontwikkel en in die berekeningsvloeimeganika-pakket geïnkorporeer d.m.v gebruikers-roetines. Waar van toepassing is die numeriese ondersoek aangevul met eksperimentele data. Die plenumruimte lugdinamiese gedrag word gekarakteriseer en ingesluit in die onderskeie trekvergelykings vir geforseerde- en geïduseerde-trek LVWRs deur die daarstelling van 'n dimensielose plenumruimteherwinnings- en plenumruimte-verlieskoëffisient. Die invloed van veranderinge wat aangebring is aan 'n reeks meganiese-trek LVWRs op die plenumruimte lugdinamiese gedrag is ondersoek. Hierdie veranderinge sluit die volgende in:

- Die werking van die aksiaalwaaier.
- Die hoogte van die plenumruimte in die aksiale rigting van die waaier.
- Die isotermiese lugweerstand van die warmteruiler.
- Die waaier-tot-warmteruiler area-verhouding.
- Die aksiale posisie van die aksiaalwaaier in die waaierring.

'n Stel ontwerpsriglyne vir beide geforseerde- en geïnduseerde-trek LVWRs word geformuleer gebaseer op die resultate van die numeriese ondersoek. Die ontwerpsriglyne sluit aanbevole waardes vir die dimensielose plenumruimte-herwinnings- en plenumruimte-verlieskoeffisient in wat op hulle beurt aangewend kan word om 'n meer akkurate aanduiding van die werkspunt van 'n beplande LVWR te bereken deur gebruik te maak van die toepaslike trekvergelyking.

SLEUTELWOORDE: lugverkoelde warmteruiler
numeriese ondersoek
plenumruimte, lugdinamiese gedrag

DEDICATION

To my father, Johannes Cornelius Meyer (1941 - 2000)

ACKNOWLEDGEMENTS

I would like to express my sincere gratitude towards the following individuals and institutions for contributing towards this study

- My Lord and Saviour, Jesus Christ without whom all is without purpose.
- Prof. D.G. Kröger for his assistance and guidance that reached further than the work represented here.
- My wife for her patience, encouragement and love.
- My family and friends for their help and support.
- Those who also helped: artisans, secretaries, cleaning staff, etc.
- The FRD, Harry Crossley Foundation, The Ernst and Ethel Eriksen Trust, the University of Stellenbosch and Prof. D.G. Kröger for financial support.

CONTENTS

NOMENCLATURE

Symbols

A	Area, m^2
a	Gradient, Ns/m^5 or constant, s^2/m^6
b	Constant, m^3/s
C	Constant
C_d	Airfoil drag coefficient
C_l	Airfoil lift coefficient
C_ε	Turbulence model constants
C_μ	Turbulence model constant
c	Chord, m or constant
D	Symbol used in control volume discretization process or drag force, N
d	Diameter, m or constant
e	Constant
F	Symbol used in control volume discretization process
f	Function
g	Gravitational acceleration, m/s^2 or constant
H	Height, m
h	Constant
i	Enthalpy, kJ/kg or constant
i'	Fluctuating component of enthalpy, kJ/kg
j	Constant
K	Dimensionless isothermal pressure loss or gain coefficient
k	Turbulent kinetic energy, m^2/s^2
L	Length, m or lift force, N
M	Normalization factor
m	Mass flow rate, kg/s
max	Maximum
min	Minimum
N	Rotational speed, rpm or number

N'	Rotational speed at reference conditions, rpm
P	Rate of work input, Nm/s or central point
Pe	Pectlet number
P_R	Power consumption of axial flow fan, Nm/s
P_R'	Power consumption of axial flow fan at reference conditions, Nm/s
r	Residual or radius, m
p	Pressure, N/m^2
Q	Rate of heat input, Nm/s or fan blade element tangential force, N
R	Gas constant, J/kgK
Re	Reynolds number
Ry	Characteristic flow parameter, m^{-1}
S	Source term,
s	Momentum source, kg/m^2s
T	Torque, Nm or fan blade element thrust, N or temperature, K
t	Time, s or thickness, m
u	Internal energy, J/kg or Cartesian velocity components(tensor notation), m/s or velocity in x-direction, m/s
u'	Fluctuating Cartesian velocity components, m/s
V	Volume flow rate, m^3/s
V'	Volume flow rate at reference conditions, m^3/s
v	Velocity normal to a cross-section in the flow, m/s or velocity in y-direction, m/s
W	Width, m
w	Velocity in z-direction, m/s
x	Cartesian direction
z	Elevation above ground level, m

Greek Symbols

α	Angle of attack, ° or constant
α_e	Kinetic energy coefficient
β	Angle, ° or constant
Δ	Difference

δ	Differential
δ_{ij}	Kronecker delta
ε	Rate of dissipation of turbulent kinetic energy, m^2/s^3
ϕ	Dependent variable
γ	Fan blade stagger angle, °
η	Efficiency, %
η'	Efficiency at reference conditions, %
μ	Molecular dynamic viscosity, kg/ms
π	3.14159265
θ	Air incidence angle, ° or angle, °
Γ	Coefficient of diffusion
ρ	Density, kg/m^3
ρ'	Reference density, kg/m^3
σ	Solidity ratio
σ_c	Jet contraction ratio
σ_{21}	Solidity ratio of plate fins
σ_h	Turbulent Prandtl number
σ_k	Turbulence model constant
σ_ε	Turbulence model constant
τ	Stress, N/m^2
Ω	Rotational speed of fan blade cross sectional profile, rad/s
ω	Rotational speed of fluid, rad/s
ξ	Friction coefficient or ξ-direction

Subscripts

1, 2, ...	Reference plane or cross section
a	Air
amb	Ambient
bell	Bellmouth
c	Contraction
cons	Conservative

d	Dynamic
diss	Dissipation
dj	Jetting
drift	Drift
E	Eastern point
e	Midpoint between central and eastern point or exit
eff	Effective
F	Fan
Fb	Fan blade
FC	Fan casing
FH	Fan hub
Fr	Fan rotor
f	Friction
HE	Heat exchanger
i	i-index or inlet
inc	Increase
isen	Isentropic
j	j-index
k	k-index
m	Mean or number of adjacent cells
n	n^{th} number
nom	Nominal
o	Outlet
P	Plenum or central point
R	Relative
rec	Recovery
root	Root
s	Static
sett	Settling chamber
source	Source
sys	System
sF	Fan static conditions
t	Total or turbulent

te	Trailing edge
tF	Fan total conditions
turn	Turning
venturi	Venturi
W	Western point
w	Midpoint between western and central point
zero	Zero
θ	Oblique flow conditions
ξ	Component in ξ-direction

CHAPTER 1 - Introduction

An air-cooled heat exchanger (ACHE) is a device that facilitates the cooling of a hot process fluid through the use of ambient air. More often than not the physical appearance of an ACHE takes the shape of rows of finned tubes arranged between headers to form a heat exchanger bundle. As ambient air passes through the heat exchanger bundle and over the extended surfaces of the finned tubes, the hot process fluid flowing through the interior of finned tubes is cooled.

The widespread use of air-cooled heat exchangers, or dry-cooling as the process is often referred to, facilitates the large degree of diversity found with regard to ACHE geometry and size. ACHEs are used in automotive engine cooling systems, household and industrial-sized air-conditioning systems as well as in the chemical and process industries, to name but a few areas of application. Air-cooled steam condensers have also been successfully employed in power plants located in regions where water for cooling purposes is either unavailable or prohibitively expensive. The world's largest direct air-cooled power plant, Matimba, is located near Ellisras in the Republic of South Africa [84VO1, 87KN1, 90KN1, 91KN1, 93GO1] where the arid conditions render any other form of cooling impractical.

Kröger [94KR1] suggests that dwindling supplies of cooling water and a lack of adequate plant sites coupled with increased water costs, environmental considerations and proliferating legislation will result in the increased use of ambient air for industrial and other cooling purposes in the foreseeable future.

Although a large number of different ACHE configurations are in use, two broad categories, based on the method used to create a draught through the heat exchanger bundles, can be identified: natural draught ACHEs, where the buoyancy effects associated with the air heated by the heat exchanger bundles are used to induce airflow through the ACHE, and mechanical draught ACHEs, where the air flow is the result of the action of some form of mechanical device, such as an axial flow fan, for example.

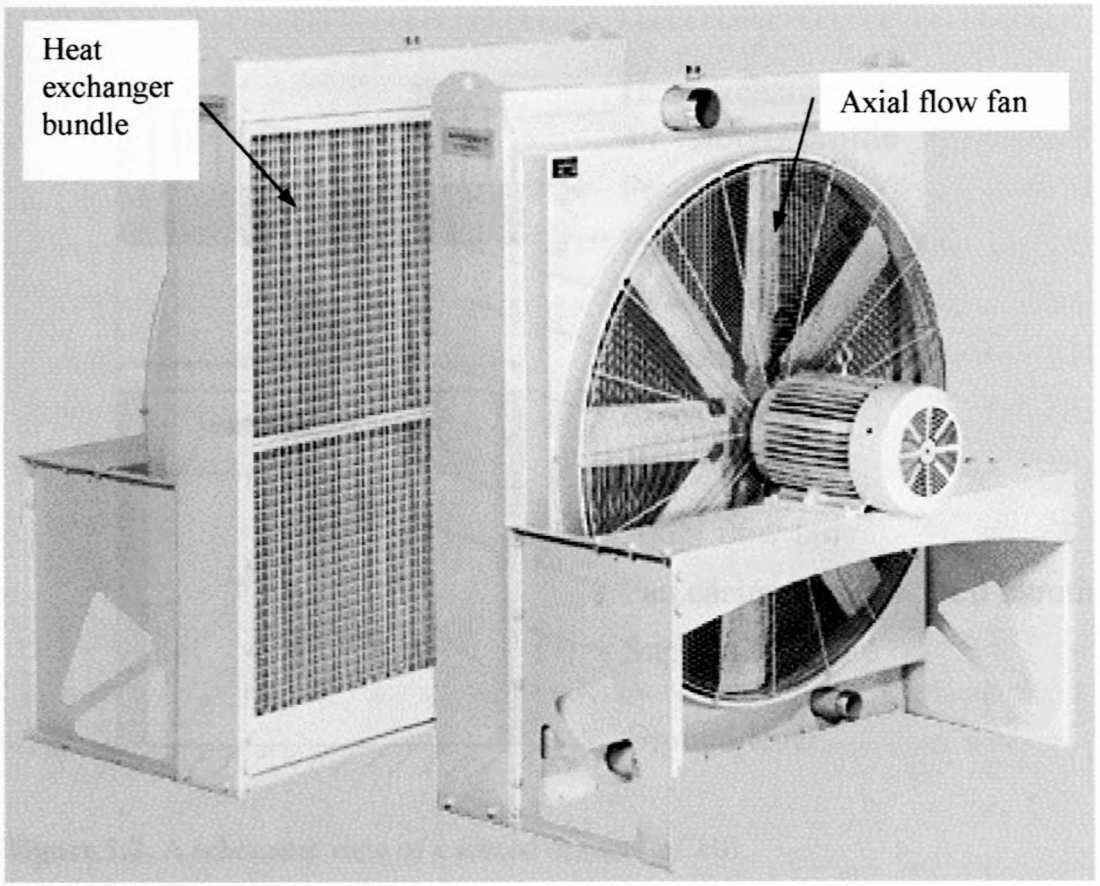

Figure 1.1. Examples of mechanical draught ACHE utilised in industry.

Figure 1.1 displays two mechanical draught ACHEs utilised in industry. The axial flow fan used to force ambient air through the heat exchanger bundles can clearly be seen on the ACHE in the foreground of figure 1.1, whilst the ACHE in the background affords a better view of the heat exchanger bundle.

Two categories of mechanical draught ACHEs can be distinguished, namely forced and induced draught ACHEs. Figures 1.2 and 1.3 are schematic representations of a forced and induced draught ACHE respectively and indicate that the two configurations differ in that ambient air entering the ACHEs passes through the axial flow fan and exits through the heat exchanger bundle in the forced draught configuration, with the reverse being true for the induced draught configuration.

The primary components of both forced and induced draught ACHEs are displayed in figures 1.2 and 1.3 respectively.

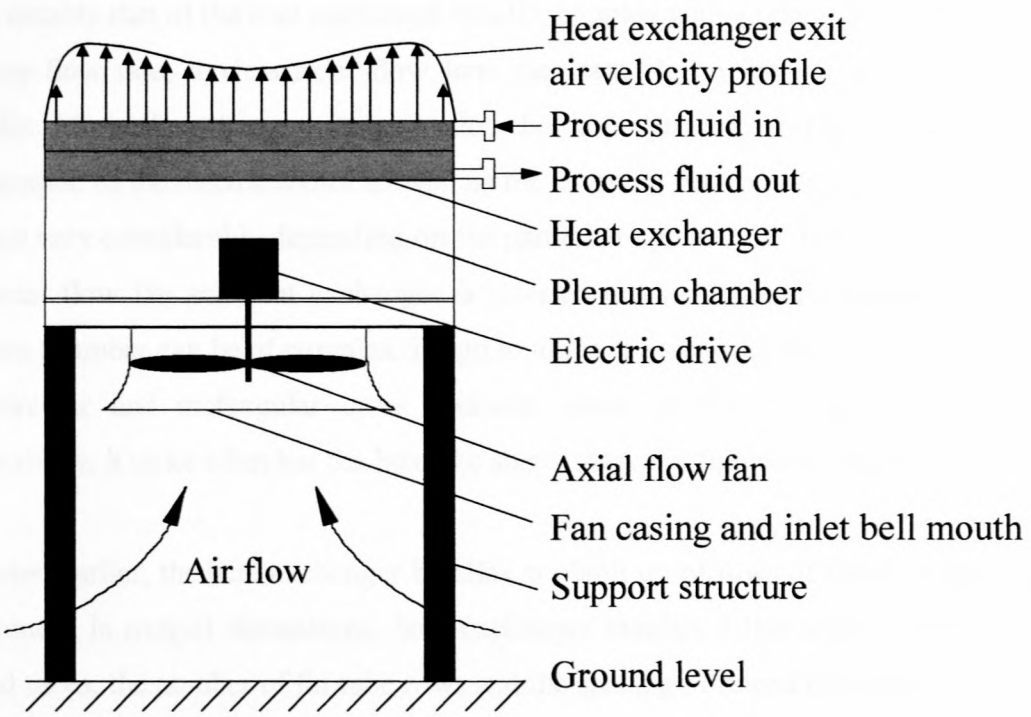

Figure 1.2. A schematic view of a forced draught ACHE.

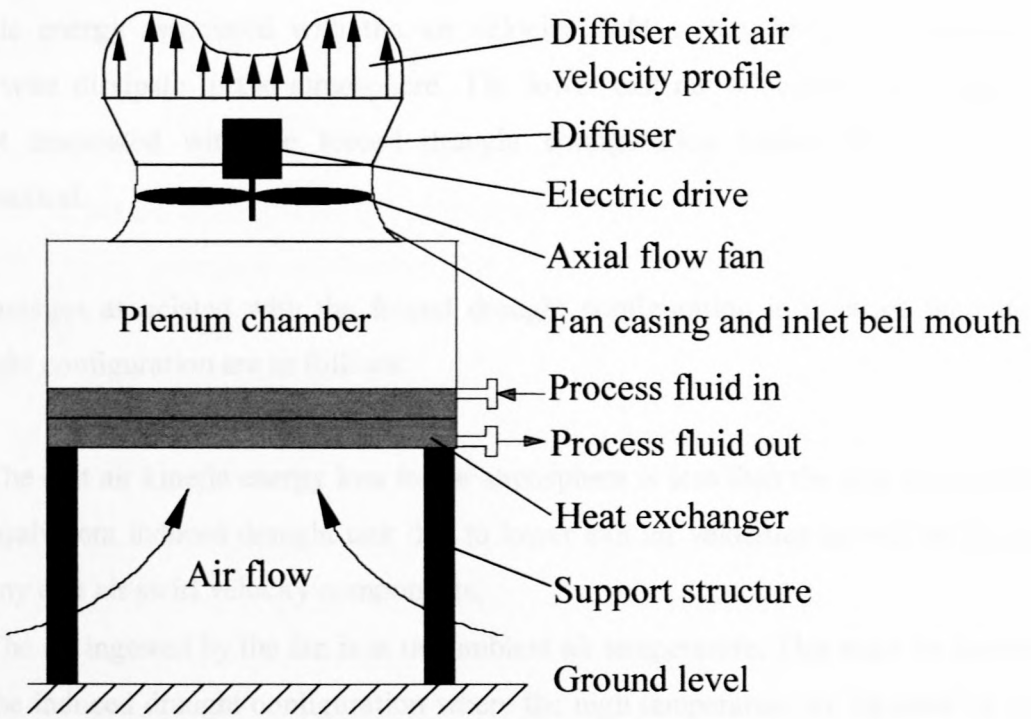

Figure 1.3. A schematic view of an induced draught ACHE.

The relatively low pressure rise requirement across the resistance devices in a typical ACHE, most notably that of the heat exchanger bundle, coupled with a relatively high operating point volume flow rate, renders axial flow fans the ideal choice for use in mechanical draught ACHEs. More often than not the axial flow fan is powered by an electric motor. In practice the location of the electric motor as well as the coupling between the latter and the axial flow fan can vary considerably depending on the particular application. The cavity formed between the axial flow fan and heat exchanger is referred to as the plenum chamber. Although the plenum chamber can be of complex design to aid in the smooth transition of air flow between the circular and rectangular cross sectional areas of the fan and the heat exchanger respectively, it quite often has the box-like shape shown in figures 1.2 and 1.3.

As noted earlier, the heat exchanger bundles are built up of rows of finned tubes. Apart from differences in overall dimensions, heat exchanger bundles differ with regard to the type of finned tubes, the number of fin tube rows and the spacing of finned tubes used.

Due to the high exit air velocities associated with the induced draught configuration, a diffuser is often installed at the fan exit (see figure 1.3) in an attempt to recover some of the kinetic energy associated with the air velocity field at the fan exit plane which would otherwise dissipate in the atmosphere. The lower exit air velocities at the heat exchanger outlet associated with the forced draught configuration render the use of a diffuser impractical.

Advantages associated with the forced draught configuration in contrast with the induced draught configuration are as follows:

- The exit air kinetic energy loss to the atmosphere is less than the loss associated with the equivalent induced draught unit due to lower exit air velocities as well as the absence of any exit air swirl velocity components.
- The air ingested by the fan is at the ambient air temperature. This must be contrasted with the induced draught configuration where the high temperature air ingested by the fan not only necessitates the use of expensive high temperature resistant fan blades and motor drives, but also requires a higher fan power consumption and/or a larger fan diameter to induce the required air mass flow rate.

- Due to the closer proximity of the fan blades and motor drives to the ground in the forced draught configuration in contrast with the induced draught configuration, maintenance to these components is less demanding.
- With the fan blades and motor drive located below the heat exchanger, construction costs are less than for the induced draught configuration where heavier construction is required to support these components above the heat exchanger.

The forced draught configuration also suffers from the following disadvantages:

- The distorted air velocity field at the fan exit results in flow maldistribution through the heat exchanger that could adversely affect the heat transfer characteristics of the heat exchanger.
- The associated flow distortions in the plenum chamber are believed to result in an increased flow resistance through the heat exchanger.
- The low heat exchanger bundle exit velocity results in hot plume recirculation.

The incidence of use of forced draught ACHEs in industry seems to indicate that the advantages of this particular configuration outweigh the disadvantages [95DU1].

A literature survey reveals that there seems to exist an imbalance between the relatively small number of papers dealing with the aerodynamic performance characteristics of ACHEs and the far larger contingent of those dealing with other aspects, such as the performance characteristics of the various heat exchanger finned tubes, for example. Nowhere else is this imbalance better illustrated than in the absence of any references to the flow losses associated with the fan system in a popular test code for ACHE performance [91AS1].

The small number of papers dealing with the aerodynamic performance of ACHEs might easily create the impression that the aerodynamic behaviour of an ACHE has little or no influence on the overall performance of the system. Kröger [94KR1], however, points to the failure of some operational air-cooled condensers to achieve the specified performance requirements and goes on to illustrate that this failure results from the use of inadequate design procedures, which in turn reflects on a poor understanding of the aerodynamic behaviour of the air-cooled condensers. Although the large-scale application of ACHEs in,

for example, the aforementioned 6 × 650 MW Matimba power plant, where close to 5500 MW of heat is rejected to the atmosphere by the dry-cooled condenser unit where 288 axial flow fans are operated simultaneously [84VO1, 87KN1, 90KN1, 91KN1, 93GO1], might be viewed as the exception rather than the rule. It does however serve to illustrate the fact that the failure of an ACHE to achieve specified performance requirements due to bad aerodynamic design could prove to be very costly in terms of not only operational costs but also capital expenditure.

It is furthermore an acknowledged fact that the performance characteristics of mechanical draught ACHEs can be affected by the system or interference effect [96ME1]. The system effect has been the subject of a number of experimental investigations [90BO1, 90CO1, 84DE1, 84RO1, 83OC1, 84DA1, 91VE1]. It can best be described as the aerodynamic interaction between different components within the ACHE that often adversely affects the performance characteristics of either one or both of the interacting components and as a result also the performance characteristics of the ACHE in question. The central location of the plenum chamber between the axial flow fan and heat exchanger bundle in a typical mechanical draught ACHE suggests that the aerodynamic interaction between plenum chamber and axial flow fan as well as plenum chamber and heat exchanger bundle could significantly influence the aerodynamic behaviour of the plenum chamber and therefore the performance characteristics of mechanical draught ACHEs.

The need for a better understanding of the influence of the plenum chamber aerodynamic behaviour on ACHE performance characteristics as well as for a means by which the plenum chamber aerodynamic behaviour can find expression within the currently accepted mechanical draught ACHE design methodologies, is apparent and forms the subject of this investigation.

In an effort to overcome the near prohibitive nature of a purely experimental approach to the investigation, extensive use is made of a commercially available computational fluid dynamics (CFD) code to investigate the performance characteristics of a range of mechanical draught ACHEs numerically. Where necessary, the results of the numerical investigation are augmented with data obtained through experiments.

Inclusion of the plenum chamber aerodynamic behaviour into the mechanical draught ACHE design process requires modification of the draught equation used to determine the operating or duty point of the ACHE under consideration. This is addressed in Chapter 2 of this dissertation. A critical evaluation of the methods and principles used to formulate the draught equation associated with both forced and induced draught ACHEs is followed by the introduction of a dimensionless plenum chamber recovery coefficient and a plenum chamber loss coefficient for the inclusion of the plenum chamber aerodynamic behaviour into the respective draught equations.

The sensitivity of the operating point volume flow rate of forced and induced draught ACHEs to changes in the value of the respective dimensionless coefficients formulated in Chapter 2 as well as changes in the value of the other variables that form part of the respective draught equations, is expounded in Chapter 3.

In Chapter 4 a brief overview is given of the commercially available CFD-code as well as the numerical strategies employed to resolve the internal flow field of the range of mechanical draught ACHEs under investigation. Development of the numerical models that enable the CFD-code to include the effect of the axial flow fan and heat exchanger on the ACHE flow field is also discussed in detail.

Chapters 5 - 9 and Chapters 10 - 14 give a detailed account of the numerical investigation conducted on a range of different forced and induced draught ACHEs respectively. The dimensionless recovery and plenum loss coefficients are related to the geometrical as well as other variable values used to characterise the different ACHEs investigated.

In Chapter 15 a final summery is given of the most important conclusions drawn from the results of the numerical and experimental investigations. Recommendations pertaining to important areas for future research are also made.

CHAPTER 2 - Quantifying the plenum chamber aerodynamic behaviour of mechanical draught ACHEs

One of the main objectives of the design procedure associated with mechanical draught ACHEs is to determine the operating or duty point of the proposed ACHE. The accuracy with which the operating point volume flow rate can be determined, depends on the extent to which the design procedure includes the various flow phenomena associated with the ACHE. Popular texts on the subject [83WA1, 78DA1] usually refer to the procedure employed to determine the operating point as a matching of the fan and resistance device performance characteristics. More often than not this statement is followed by a brief discussion of the relevant fan and resistance devices characteristic advocated for use in the matching procedure. The matching of fan and heat exchanger performance characteristics finds mathematical expression as a draught equation where the terms in the equation are a function of the operating point volume flow rate alone.

Before an attempt can be made at including the plenum chamber aerodynamic behaviour into the mechanical draught ACHE design process, a thorough understanding of the method and principles used to determine the operating point volume flow rate of a proposed ACHE is required. The first part of this chapter is therefore devoted to a critical evaluation of the formulation of the draught equation associated with forced and induced draught ACHEs respectively. The discussion includes an overview of the fan and heat exchanger bundle performance characteristics used in the design process and shows how these performance characteristics are embodied in the respective draught equations. The chapter is concluded with the formulation of a method to include the plenum chamber aerodynamic behaviour into the draught equation associated with forced and induced draught ACHEs.

2.1. Energy equation

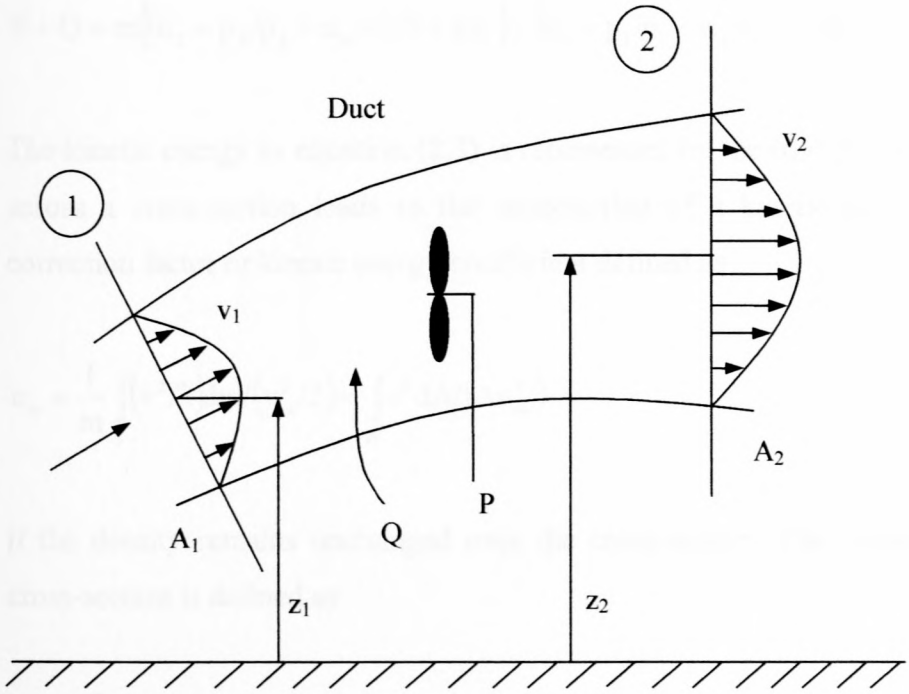

Figure 2.1. Control volume.

The first law of thermodynamics states that for steady flow the sum of the external work done on and the thermal energy transferred from or to a system equals the change in the energy of the system. Application of the first law of thermodynamics to the control volume shown in figure 2.1 yields the following expression [98KR1]

$$P + Q = m\left[\left(i_2 + \alpha_{e2} v_2^2/2 + g z_2\right) - \left(i_1 + \alpha_{e1} v_1^2/2 + g z_1\right)\right] \qquad (2.1)$$

where P and Q represent the rate of work and the rate of heat input into the fluid respectively and m the mass flow rate.

The enthalpy of a fluid is defined as

$$i = u + p/\rho \qquad (2.2)$$

where u is the fluid internal energy.

Substitution of equation (2.2) into equation (2.1) yields

$$P + Q = m\left[\left(u_2 + p_2/\rho_2 + \alpha_{e2}v_2^2/2 + gz_2\right) - \left(u_1 + p_1/\rho_1 + \alpha_{e1}v_1^2/2 + gz_1\right)\right] \tag{2.3}$$

The kinetic energy in equation (2.3) is represented by the $\alpha_e v^2/2$ – term. Velocity variations across a cross-section leads to the introduction of a kinetic energy velocity distribution correction factor or kinetic energy coefficient defined as

$$\alpha_e = \frac{1}{m}\int_A \left(v^2/2\right)dm/\left(v_m^2/2\right) = \int_A v^3 dA/\left(Av_m^3\right) \tag{2.4}$$

if the density remains unchanged over the cross-section. The mean velocity, v_m, over the cross-section is defined as

$$v_m = \int_A vdA/A \tag{2.5}$$

Kröger [98KR1] shows that, for a perfect gas under isentropic flow conditions, equation (2.3) reduces to

$$P_{isen}/V = \left(p_2 + \alpha_{e2}\rho_2 v_2^2/2 + \rho_2 gz_2\right) - \left(p_1 + \alpha_{e1}\rho_1 v_1^2/2 + \rho_1 gz_1\right) \tag{2.6}$$

where V is the volume flow rate through the control volume.

The terms in parenthesis are often referred to as the total pressure associated with a cross-section of the flow field

$$p_t = \left(p + \alpha_e \rho v^2/2 + \rho gz\right) \tag{2.7}$$

It is worth noting that equation (2.7) is an expression for the mechanical energy per unit volume associated with the flow through the particular cross-sectional area of the control volume under consideration.

2.2. Mechanical energy per unit volume and the draught equation

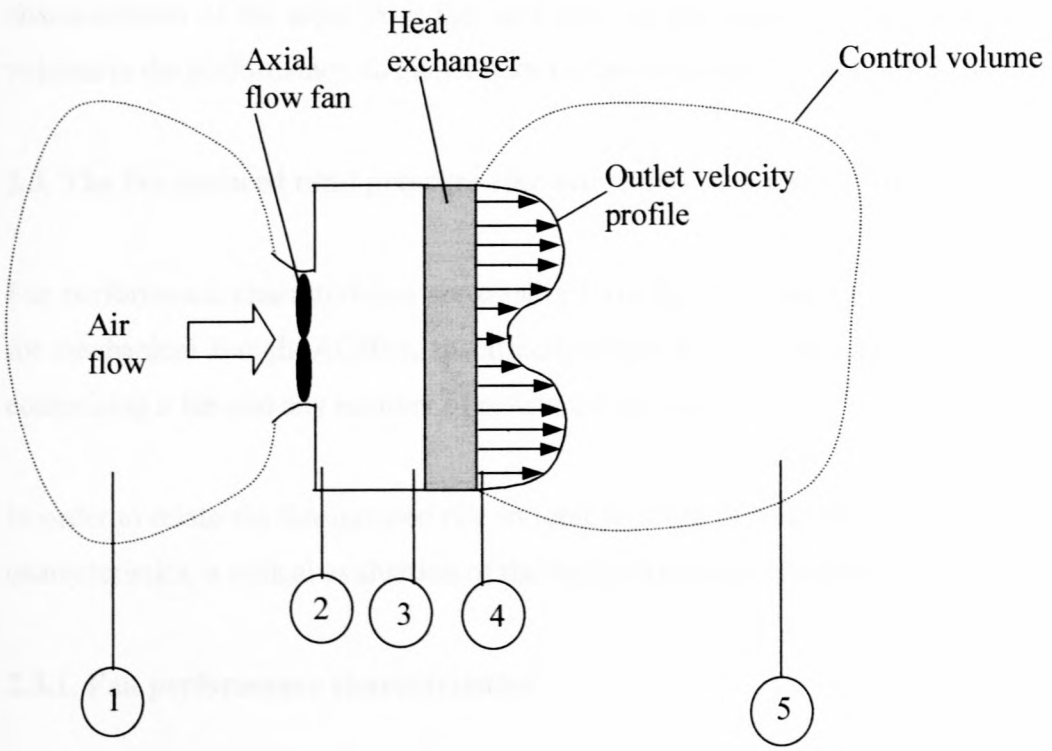

Figure 2.2. Control volume based on a forced draught ACHE.

Figure 2.2 is a schematic representation of a forced draught ACHE where sections 1 to 5 indicate the positions of specific cross-sectional areas of interest through the control volume, which is shown partially in dotted lines. Isothermal flow through the ACHE is assumed, whilst cross-sections 1 and 5 are assumed to be located at a distance sufficiently large to ensure negligible velocity values. At the operating point of the ACHE the total pressure at cross-section 1 equals that at cross-section 5. The total pressure is a maximum at cross-section 2 at the fan exit. It follows that the fan induced total pressure rise between cross-sections 1 and 2 must equal the reduction in total pressure between cross-sections 2 and 5. In other words, the fan-induced increase in the mechanical energy per unit volume equals the total dissipation of mechanical energy per unit volume in the fan system

$$\Delta p_{t\,Inc} = \Delta p_{t\,Diss} \tag{2.8}$$

In order to determine the fan system operating point through the application of equation (2.8), it is necessary to equate the increase in mechanical energy per unit volume to the performance characteristics of the axial flow fan, and also the dissipation of mechanical energy per unit volume to the performance characteristics of the resistance devices.

2.3. The fan-induced total pressure rise associated with a fan system

Fan performance characteristics are usually formulated for fan systems in general rather than for mechanical draught ACHEs, specifically where a fan system can be described as a system comprising a fan and any number of resistance devices.

In order to relate the fan-induced rise in total pressure of a fan system to the fan performance characteristics, a critical evaluation of the fan performance characteristics is necessary.

2.3.1. Fan performance characteristics

The performance characteristics of an axial flow fan are usually determined experimentally in a code fan test facility as prescribed by, for example by the British Standards Organisation in BS 848 [80BS1]. Although not the only test standard available for axial flow fans, Bolton [90BO1] remarks that BS 848 [80BS1] will in all probability become the industry standard. As a result the current discussion will be limited to this particular standard.

One of the aims of the 1980 revision of BS 848 [80BS1] was to relate the fan performance characteristics specifically to the duct connections applied to the fan [84DE1]. The fan specifier is then left the task to select a fan whose accompanying duct work most closely resembles that of the fan system in which the fan is to be used in.

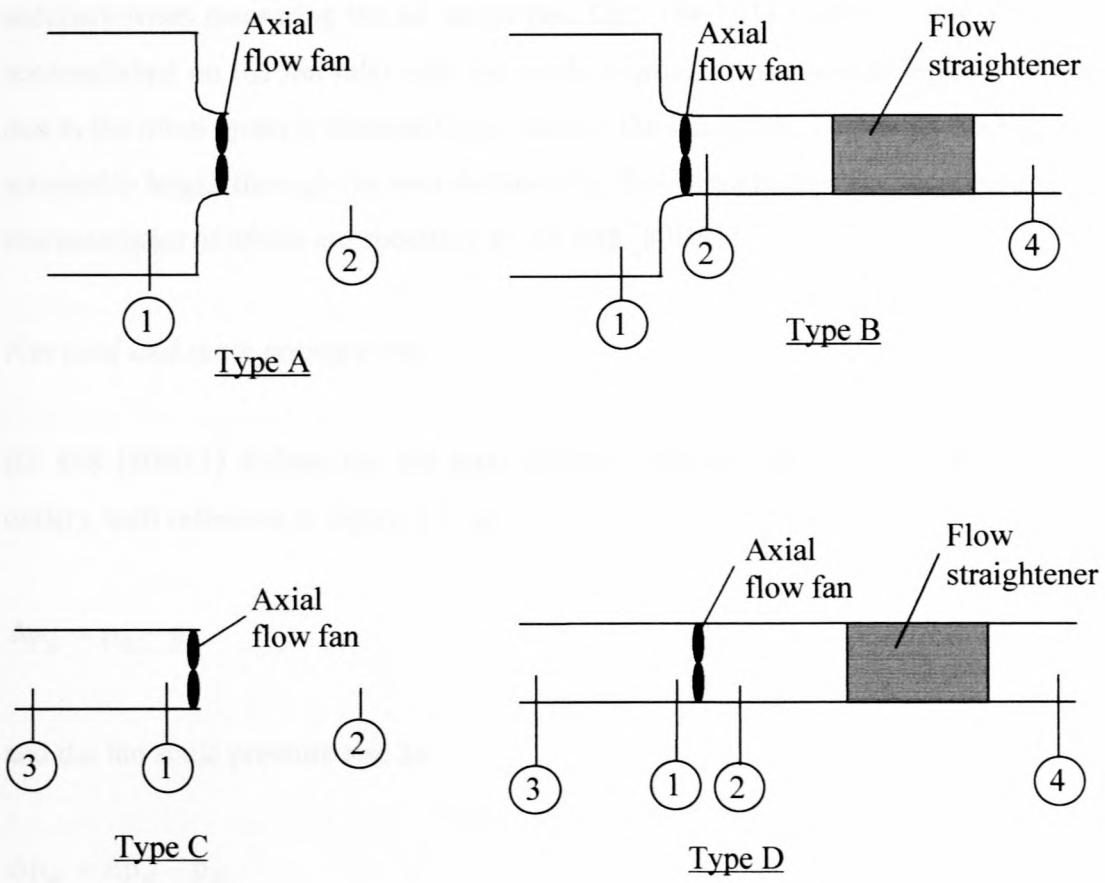

Figure 2.3. The four installation types specified in BS 848 [80BS1].

The four standard fan installation types provided for in BS 848 [80BS1] are

1. Type A: free inlet, free outlet.
2. Type B: free inlet, ducted outlet.
3. Type C: ducted inlet, free outlet.
4. Type D: ducted inlet, ducted outlet.

Figure 2.3 is a schematic representation of the four installation types. Free inlet or outlet refers to air leaving or entering the fan directly from or to the free atmosphere. For the type A test a division wall between fan inlet and outlet supports the pressure differential between fan inlet and outlet. Ducted inlet or outlet indicates a straight length of ducting on the fan inlet or outlet side with the same cross-sectional area as the fan.

The ducting used for type B, C and D tests should ideally be of sufficient length to ensure fully developed flow at the plane of measurement in order to facilitate a high degree of

accuracy when measuring the air properties. Daly [84DA1] notes that this is relatively easily accomplished on the fan inlet side but could require an impractical length of outlet ducting due to the often severely distorted flow field at the fan outlet. The outlet ducting is kept to an acceptable length through the introduction of a flow straightener, the location and geometrical characteristics of which are specified by BS 848 [80BS1].

Fan total and static pressure rise

BS 848 [80BS1] defines the fan total pressure rise for type B and D installations (ducted outlet), with reference to figure 2.3, as

$$\Delta p_{tF} = p_{t2} - p_{t1} \tag{2.9}$$

and the fan static pressure rise as

$$\Delta p_{sF} = \Delta p_{tF} - p_{dF} \tag{2.10}$$

where p_{dF} is the fan dynamic pressure defined as

$$p_{dF} = 0.5\rho \cdot v_{sett}^2 \tag{2.11}$$

and v_{sett} is the average velocity based on the settling chamber area.

It should be noted that all references in BS 848 [80BS1] to the total pressure at a cross-section in the flow field assume a kinetic energy coefficient of unity, $\alpha_e = 1$. It should also be noted that the kinetic energy per unit volume term, $0.5\rho v^2$, is referred to as the dynamic pressure.

For type A and C installations (free outlet) the fan static pressure rise is defined as

$$\Delta p_{sF} = p_{s2} - p_{t1} \tag{2.12}$$

and the fan total pressure rise as

$$\Delta p_{tF} = \Delta p_{sF} + p_{dF} \tag{2.13}$$

Due to the presence of duct work the total pressure at section 2 for type B and D installations and the total pressure at section 1 for type C and D installations cannot be measured directly.

For type B and D installations the total pressure at section 2 is determined according to

$$p_{t2} = p_{t4} + p_{d4}(1 + \zeta_{24}) \tag{2.14}$$

where p_{d4} is the dynamic pressure at section 4, and ζ_{24} is a friction coefficient that accounts for the frictional losses in the duct section between sections 2 and 4.

According to BS 848 [80BS1], ζ_{24} is expressed as

$$\xi_{24} = 0.015 + 1.26 \cdot (\mathrm{Re})^{-0.3} + 0.95 \cdot (\mathrm{Re})^{-0.12} \tag{2.15}$$

where Re is the Reynolds number at section 4.

It should be noted that, although ζ_{24} accounts for the frictional losses associated with the duct section at the fan outlet as well as the flow straightener, it is valid only for fully developed pipe flow.

For types C and D installations the total pressure at section 1 is determined according to

$$p_{t1} = p_{t3} - \zeta_{31} p_{d1} \tag{2.16}$$

where ζ_{31} is a friction coefficient that accounts for the frictional losses in the duct section between sections 3 and 1.

According to BS 848 [80BS1] ζ_{31} is expressed as

$$\xi_{31} = 0.015 + 1.26 \cdot (\mathrm{Re})^{-0.3} \tag{2.17}$$

where Re is the Reynolds number at section 1.

ζ_{31} is also based on fully developed pipe flow.

Fan power consumption

The fan power consumption is determined according to

$$P_R = \frac{2\pi NT}{60} \tag{2.18}$$

where N is the fan rotational speed and T the input torque to the fan shaft.

Fan total and static efficiency

Fan total efficiency is defined as

$$\eta_{tF} = \frac{\Delta p_{tF} V}{P_R} \tag{2.19}$$

and fan static efficiency as

$$\eta_{sF} = \frac{\Delta p_{sF} V}{P_R} \tag{2.20}$$

2.3.2. Representing the fan-induced total pressure rise in a fan system

Representation of the fan-induced total pressure rise (left-hand side of equation (2.8)) of a fan system is influenced by the geometrical characteristics of the fan system under consideration. For example, in a fan system where the axial flow fan experiences steady, uniform inlet flow conditions and exits directly into the free atmosphere, the static pressure rise as defined for a type C installation will represent not only the increase in mechanical energy per unit volume, but also the loss of kinetic energy per unit volume to the free atmosphere. If, however, a 90° bend is installed in close proximity of the fan inlet and the fan outlet is furnished with a diffuser, the choice of installation type (A, B, C or D) and fan pressure rise characteristic (static or total) becomes less obvious.

In truth, any set of fan performance characteristics determined under conditions that differ from the conditions encountered by the axial flow fan within the fan system, will be, to some degree, an inaccurate representation of the actual fan performance. It is, of course unrealistic to expect a single fan test code to yield fan performance characteristics applicable to all possible fan system arrangements. According to Deeprose and Smith [84DE1], BS 848 [80BS1] (which is a revision of the 1963 fan test code) relates the fan performance characteristics of a given fan to the duct components applied to the fan. This would then enable the designer to select a fan on the basis of fan performance characteristics applicable to a test installation that more closely resembles the conditions encountered by the fan within the fan system.

Although the inclusion of the four installation types in BS 848 [80BS1] does seemingly offer more flexibility with regard to fan selection, it must be remembered that the usefulness of these four installation types is dependent on the way in which the defined fan pressure rise characteristics can be related to the mechanical energy per unit volume interactions within a particular fan system.

The fact that the fan total and static pressure rise definitions, save for the fan static pressure rise definition for type A and C installations as defined in BS 848 [80BS1], assume a kinetic energy coefficient, α_e, of unity when referring to the total pressure at the fan exit all but negates the possibility of an accurate formulation of the relationship between the fan pressure

rise characteristics and the mechanical energy per unit volume interactions within the standard test installation. The fact that this relationship cannot be accurately determined for even the standard installation does not bode well for any attempt to establish the relationship between the standard fan pressure rise characteristics and the mechanical energy per unit volume interactions of an arbitrary fan system.

Daly [84DA1] concedes that the kinetic energy coefficient can be as high as 3 at the fan exit, but maintains that BS 848 [80BS1] provides conventional values of power output so that conventional efficiencies can be calculated. According to Daly [84DA1], the calculated efficiencies, especially the fan total efficiency, should be regarded as an index of quality rather than as a reference to the efficiency of the fan within the fan system. When consideration is given to the fact that the α_e-value at the fan exit varies with volume flow rate, it is debatable whether the fan total efficiency, as defined by BS 848 [80BS1] for the different installation types, is truly an index of quality, since it does not in any sense accurately reflect the kinetic energy content of the air stream exiting from the axial flow fan.

The addition of a flow straightener in the outlet ducting associated with type B and D installations adds further ambiguity with regard to the interpretation of the fan pressure rise characteristics. Equation (2.14) indicates the way in which the flow conditions at the exit of the flow straightener are employed in conjunction with empirical data based on fully developed pipe flow to determine the total pressure at the fan outlet. The latter is used in the formulation of both the fan total and static pressure rise for type B and D installations, as is evident from equations (2.9) and (2.10). To assume that empirical data, based on fully developed pipe flow, can accurately predict the flow losses associated with the complex interaction between the swirling flow issuing from an axial flow fan and the radial vanes of the flow straightener, is rather naive. It should be noted that, according to Daly [84DA1], the addition of a flow straightener to the exit ducting of type B and D installations was motivated not by its potential to yield a more accurate representation of the fan pressure rise characteristics, but rather by an attempt to ensure less complex velocity and pressure field distributions at the plane of measurement in order to facilitate ease of measurement of these variables. As such the fan total and static pressure rise definitions employed by BS 848 [80BS1] for type B and D installations are contaminated by the addition of a flow straightener and the accompanying assumptions. As a result, an accurate relationship between the fan

pressure rise characteristics and the mechanical energy per unit volume interactions within installation types B and D becomes just about impossible.

Bolton [90BO1] determined the performance characteristics of a mixed flow fan in all four standard types of fan installations. Based on the results of the investigation, Bolton [90BO1] concludes that, provided the inlet flow conditions are steady and uniform, the performance characteristics determined under free and ducted inlet conditions are the same. These results confirm observations reported by Daly [84DA1].

It is clear that the choice of the fan performance characteristics used in determining the operating point of a fan system is not necessarily obvious and also that the different installation types introduced in BS 848 [80BS1] do not necessarily make for a better or easier choice. It is important to remember that the fan performance characteristics are related to the increase in the air mechanical energy per unit volume of the fan system. The choice of a fan performance characteristic based on the resemblance between the duct work of the test installation used to determine the fan performance characteristics and the duct work of the actual fan system, can therefore be misleading.

2.4. Resistance device isothermal performance characteristics

The resistance device isothermal performance characteristics and in particular the heat exchanger total pressure loss characteristics of the types commonly used in ACHE can be expressed in the form of a dimensionless isothermal loss coefficient, defined, with reference to figure 2.4, as

$$K = \frac{\left(p_1/\rho_1 + \alpha_{e1} v_1^2/2\right) - \left(p_2/\rho_2 + \alpha_{e2} v_2^2/2\right)}{v^2/2} \qquad (2.21)$$

where v is based on conditions at either section 1 or section 2.

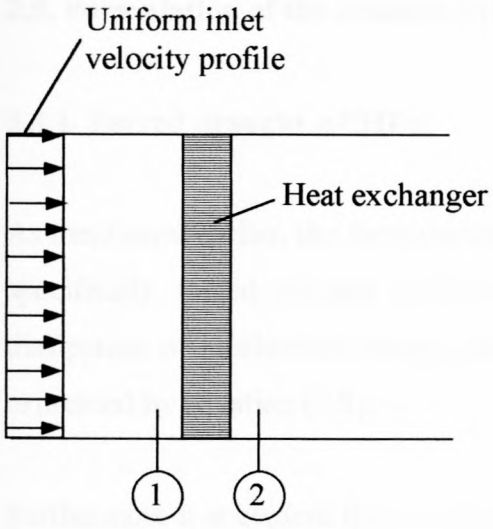

Figure 2.4. Schematic representation of the set-up used to determine the heat exchanger dimensionless pressure loss coefficient.

For incompressible isothermal flow equation (2.21) reduces to

$$K = (p_{t1} - p_{t2})/(\rho v^2/2) \qquad (2.22)$$

The total pressure loss characteristics of a heat exchanger are usually determined under the ideal flow conditions shown in figure 2.4 and include a steady, uniform inlet flow field with a free exit to the atmosphere.

These ideal flow conditions are however not necessarily representative of the flow conditions experienced within a fan system due to the often severely distorted fan-induced velocity fields. The distorted plenum chamber flow field in the case of a forced draught ACHE can have a marked effect on the total pressure loss experienced by the heat exchanger within the fan system, as indicated by the results of the experimental investigation in Appendix A of this dissertation.

2.5. Formulation of the draught equation of mechanical draught ACHEs

2.5.1. Forced draught ACHEs

As mentioned earlier, the formulation of the draught equation associated with mechanical and specifically forced draught ACHEs is based on the balance between the creation and dissipation of mechanical energy per unit volume of the air flowing through the ACHE as expressed by equation (2.8).

Furthermore it is evident that the fan static pressure rise characteristics for type A and type C installations, determined according to the specifications of BS 848 [80BS1], are the only fan pressure rise characteristics in which no attempt at either altering or expressing the kinetic energy content of the velocity field at the fan exit plane. The use of the fan static pressure rise for a type A installation to present the increase in mechanical energy per unit volume of the air flowing through a forced draught ACHE is advocated by Daly [78DA1] and Wallis [83WA1]. The kinetic energy per unit volume content of the velocity field at the fan exit plane is thus entirely omitted from the ensuing draught equation which is the same as assuming that all the kinetic energy present at the fan exit plane is dissipated within the ACHE plenum chamber. Should this prove to be a less than accurate assumption, the ensuing draught equation would yield a conservative estimate of the operating point volume flow rate.

In most cases, however, a portion of the kinetic energy per unit volume of the velocity field at the fan exit plane is converted into static pressure in the plenum chamber which promotes the flow of air through the forced draught ACHE. The converted pressure is said to be recovered within the ACHE plenum chamber. The portion of kinetic energy per unit volume that is recovered within the plenum chamber together with the fan static pressure rise as defined for a type A installation, thus represents the increase in mechanical energy per unit volume associated with the air stream through the forced draught ACHE.

The draught equation for the forced draught ACHE shown in figure 2.2 can now be formulated as follows

$$\Delta p_{sF} + K_{rec}\rho v_{FC}^2/2 = K_{HE}\rho v_{HE}^2/2 + \alpha_{eHE}\rho v_{HE}^2/2 \qquad (2.23)$$

where K_{rec} is the dimensionless recovery coefficient based on the average axial velocity through the fan ring and K_{HE} is the isothermal dimensionless heat exchanger pressure loss coefficient.

The term containing K_{rec} in equation (2.23) represents the portion of kinetic energy per unit volume present at the fan exit plane that is recovered within the plenum chamber. K_{rec} is therefore a quantitative measure of the plenum chamber aerodynamic behaviour. The term containing K_{HE} accounts for the dissipation of mechanical energy per unit volume as a result of the air flowing through the heat exchanger bundle, and the $\alpha_{eHE}\rho v_{FC}^2/2$ term accounts for the kinetic energy per unit volume present at the heat exchanger outlet plane dissipated within the atmosphere between cross-sections 4 and 5 in figure 2.2.

Figure 2.5 contrasts the use of equation (2.23) to determine the operating point volume flow rate with the method proposed by popular texts related to mechanical draught ACHEs, such as those of Wallis [83WA1] and Daly [78DA1]. It should be noted that both Wallis [83WA1] and Daly [78DA1] assume that $\alpha_{eHE} = 1$.

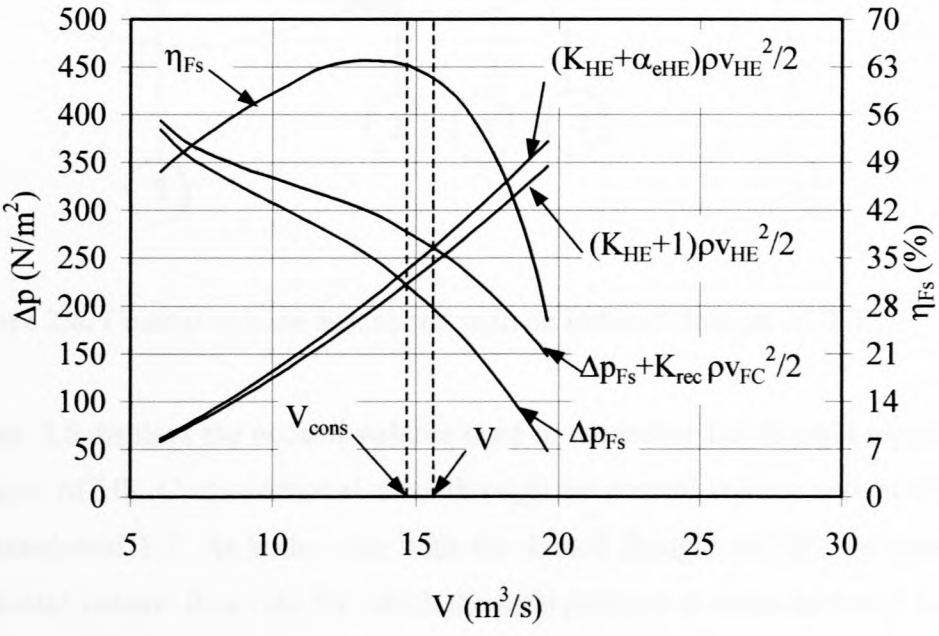

Figure 2.5. Determining the operating point volume flow rate of a forced draught ACHE.

In reality the K_{rec}-value associated with a particular forced draught ACHE would also include the effect of the non-uniform velocity distribution in the ACHE plenum chamber on the ideal total pressure loss characteristics of the heat exchanger. Calculations performed by Kröger [94KR1] however indicate that these effects are relatively small in forced draught ACHEs where A-frame type heat exchangers are used. With the assumption that this will also hold true for other heat exchanger configurations, it can be concluded that the predominant effect that determines the K_{rec}-value associated with a particular forced draught ACHE, is indeed the proportion of the kinetic energy per unit volume recovered within the plenum chamber.

2.5.2. Induced draught ACHEs

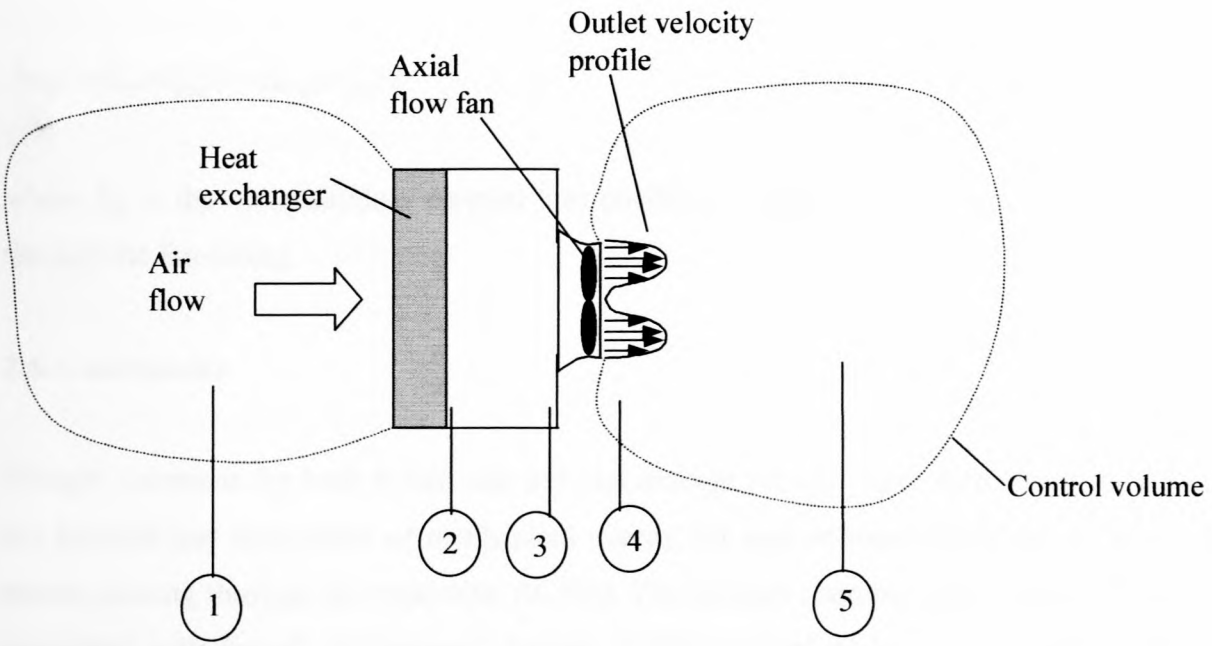

Figure 2.6. Control volume associated with an induced draught ACHE.

Figure 2.6 displays the control volume used to determine the draught equation for an induced draught ACHE. Cross-sectional areas through the control volume shown withinin dotted lines are numbered 1-5. As is the case with the forced draught ACHE, the operating point is the particular volume flow rate for which the total pressure at cross-section 1 equals that at cross-section 5.

From figure 2.6 it is clear that all the kinetic energy per unit volume present at the fan exit plane is dissipated in the atmosphere. The combined effect on the mechanical energy per unit

volume associated with the air flowing through the ACHE of the axial flow fan and the kinetic energy per unit volume dissipated in the atmosphere can thus be expressed by the fan static pressure rise for a type A installation.

The plenum chamber in figure 2.6 accelerates the air flowing from the heat exchanger exit into the axial flow fan and thus acts as a nozzle. The flow through a nozzle is generally associated with frictional losses and, as a result, a dissipation of mechanical energy per unit volume.

The draught equation for the induced draught ACHE shown in figure 2.6 can thus be formulated as

$$\Delta p_{sF} = K_P \rho v_{FC}^2/2 + K_{HE} \rho v_{HE}^2/2 \qquad (2.24)$$

where K_P is the dimensionless plenum loss coefficient based on the average axial velocity through the fan casing.

2.6. Conclusions

Draught equations for both forced and induced draught ACHEs were formulated in terms of the increase and dissipation of mechanical energy per unit volume associated with the air-stream moving through the respective ACHEs. The plenum chamber aerodynamic behaviour associated with forced and induced draught ACHEs is included in the respective draught equations through the introduction of a dimensionless recovery coefficient, K_{rec}, for forced and a dimensionless plenum chamber loss coefficient, K_P, for induced draught ACHEs.

CHAPTER 3 - The sensitivity of mechanical draught ACHE performance characteristics to plenum chamber aerodynamic behaviour

The draught equations formulated for forced and induced draught ACHEs and presented in Chapter 2 include a dimensionless recovery coefficient, K_{rec}, and a dimensionless plenum chamber loss coefficient, K_P, respectively. The respective dimensionless coefficients are said to account for the plenum chamber aerodynamic behaviour associated with ACHEs of the particular type involved. Prior to further numerical investigation it is advantageous to gain a better understanding of the effect that a change in the dimensionless coefficient-values of a particular mechanical draught ACHE will have on the operation of the ACHE, as it will enable the researcher to determine whether the observed changes in operation are less or more significant than those associated with other mechanical draught ACHE configurations.

In this chapter the sensitivity of the performance characteristics of a range of forced and induced draught ACHEs to a change in their associated K_{rec}- and K_P-values are investigated.

3.1. Forced draught ACHEs

3.1.1. Analysis

The draught equation for a forced draught ACHE is presented in Chapter 2 and given as

$$\Delta p_{sF} + K_{rec}\rho v_{FC}^2/2 = K_{HE}\rho v_{HE}^2/2 + \alpha_{eHE}\rho v_{HE}^2/2 \qquad (2.23)$$

The fan static pressure rise characteristics associated with most axial flow fans display a distinct non-linear relationship with the volume flow rate. It is, however, inadvisable to operate an axial flow fan close to the point of stall, as this might lead to instabilities, according to Kröger [98KR1]. At volume flow rates in excess of those associated with the region of stall the non-linear relationship between the fan static pressure rise and volume flow rate is seen to be less severe for most axial flow fans and can, as a result, be approximated as a linear function of volume flow rate, so that

$$\Delta p_{sF} = aV + b \tag{3.1}$$

where V is the operating point volume flow rate, a the gradient of the static pressure rise characteristic and b the fan static pressure rise at a volume flow rate of zero.

The experimental investigation of Meyer and Kröger [98ME1] showed that for the particular range of forced draught ACHEs investigated, the kinetic energy coefficient at the heat exchanger outlet, α_{eHE}, exhibits a value close to unity. As a result the current analysis assumes $\alpha_{eHE} = 1$.

The investigation of Meyer and Kröger [98ME1] also indicated that at a sufficiently high volume flow rate the heat exchanger dimensionless pressure loss coefficient, K_{HE}, becomes invariant with a change in the volume flow rate. In the current analysis it is assumed that the calculated volume flow rate is sufficiently high so that K_{HE} = constant..

Inclusion these assumptions as well as the substitution of equation (3.1) into equation (2.23) yields the following form of the draught equation

$$aV + b + K_{rec}\rho\left(\frac{V}{A_{FC}}\right)^2/2 = (K_{HE}+1)\rho\left(\frac{V}{A_{HE}}\right)^2/2 \tag{3.2}$$

where A_{FC} and A_{HE} are the fan casing and heat exchanger frontal areas respectively.

Upon rearrangement find

$$\left[K_{rec}/A_{FC}^2 - (K_{HE}+1)/A_{HE}^2\right]\cdot V^2 + 2a/\rho \cdot V + 2b/\rho = 0 \tag{3.3}$$

Equation (3.3) reduces to the problem of finding the roots of a second order polynomial, which can be determined from the following expression

$$V = \frac{-a/\rho \pm \sqrt{(a/\rho)^2 - \frac{2b}{\rho}\left[K_{rec}/A_{FC}^2 - (K_{HE}+1)/A_{HE}^2\right]}}{\left[K_{rec}/A_{FC}^2 - (K_{HE}+1)/A_{HE}^2\right]} \tag{3.4}$$

Closer scrutiny of equation (3.4) reveals that there is only one positive root, given by

$$V = \frac{-a/\rho - \sqrt{(a/\rho)^2 - \frac{2b}{\rho}\left[K_{rec}/A_{FC}^2 - (K_{HE}+1)/A_{HE}^2\right]}}{\left[K_{rec}/A_{FC}^2 - (K_{HE}+1)/A_{HE}^2\right]} \tag{3.5}$$

Equation (3.5) can be differentiated with respect to K_{rec} to yield the following expression

$$\frac{dV}{dK_{rec}} = -\frac{V^2/2}{V\left[K_{rec} - (A_{FC}/A_{HE})^2(K_{HE}+1)\right] + aA_{FC}^2/\rho} \tag{3.6}$$

Meyer and Kröger [98ME1] expressed the ACHE operating point volume flow rates determined during their experimental investigation as a percentage of the conservative volume flow rate, V_{cons}. With the fan pressure rise characteristic, the heat exchanger dimensionless total pressure loss coefficient and the kinetic energy coefficient at the heat exchanger exit known for a particular ACHE, V_{cons} can be determined from equation (3.5) by setting $K_{rec} = 0$. It follows that

$$V_{cons} = \frac{-a/\rho - \sqrt{(a/\rho)^2 + \frac{2b}{\rho}(K_{HE}+1)/A_{HE}^2}}{-(K_{HE}+1)/A_{HE}^2} \tag{3.7}$$

With V_{cons} known, it is also possible to calculate $d(V/V_{cons})/dK_{rec}$ as follows

$$\frac{d(V/V_{cons})}{dK_{rec}} = \frac{dV}{dK_{rec}} \times \frac{1}{V_{cons}} \tag{3.8}$$

3.1.2. Discussion

From the previous analysis it is now possible to plot V/V_{cons} and $d(V/V_{cons})/dK_{rec}$ for different forced draught ACHEs as a function of K_{rec}. The V/V_{cons}-values provide a means with which to compare the performance characteristics of different forced draught ACHEs directly whilst $d(V/V_{cons})/dK_{rec}$ is an indication of the sensitivity of the operating point volume flow rate to a change in K_{rec}.

The investigation of Meyer and Kröger [98ME1] yielded K_{rec}-values in the range 0 - 1.5 for the different forced draught ACHEs tested. K_{rec}-values in the range 0 - 1.5 are consequently used in the current analysis.

The different forced draught ACHEs under consideration are characterised by the combination of values chosen for K_{HE}, A_{FC}, A_{FC}/A_{HE}, a and b.

In order to provide a point of departure, the fan static pressure rise characteristics of the B-fan described in Appendix D and set at a blade root stagger angle, $\gamma = 63.5°$ are utilised. Figure 3.1 displays the result of a linear fit through the data points.

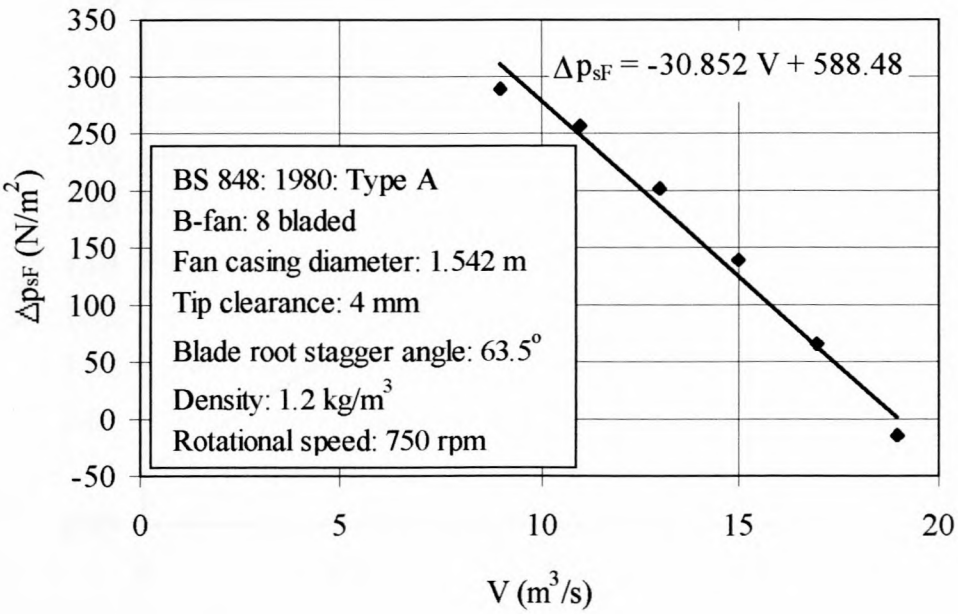

Figure 3.1. Fan static pressure rise for the B-fan for a blade root stagger angle of 63.5°.

Figures 3.2 and 3.3 display V/V_{cons} and $d(V/V_{cons})/dK_{rec}$ respectively as functions of K_{rec} for a forced draught ACHE where $K_{HE} = 20$, $A_{FC} = 1.867\ m^2$, $A_{FC}/A_{HE} = 0.517$, $a = -23.714\ Ns/m^5$ and $b = 455.134\ N/m^2$.

Figure 3.2 indicates that the operating point volume flow rate expressed as a fraction of the conservative operating point volume flow rate increases in a near linear fashion with an increase in K_{rec}. Figure 3.2 also reveals that at the maximum K_{rec}-value a volume flow rate increase of 8% above the estimate given results when using the conservative approach. In other words, should the ACHE under consideration suffer some change that has as a net result a decrease in the K_{rec}-value from the maximum value of 1.5 to a value of 0, the associated percentage decrease in the volume flow rate would be in the order of 8%.

The near linear relationship that exists between V/V_{cons} and K_{rec} is also reflected by figure 3.3 that displays the gradient of the function shown in figure 3.2 over the range of K_{rec}-values considered. As mentioned earlier, $d(V/V_{cons})/dK_{rec}$ is an indication of the sensitivity of the volume flow rate to a change in K_{rec}. It is clear from figure 3.3 that there is very little change in the sensitivity of the ACHE operating point volume flow rate over the K_{rec}-value range.

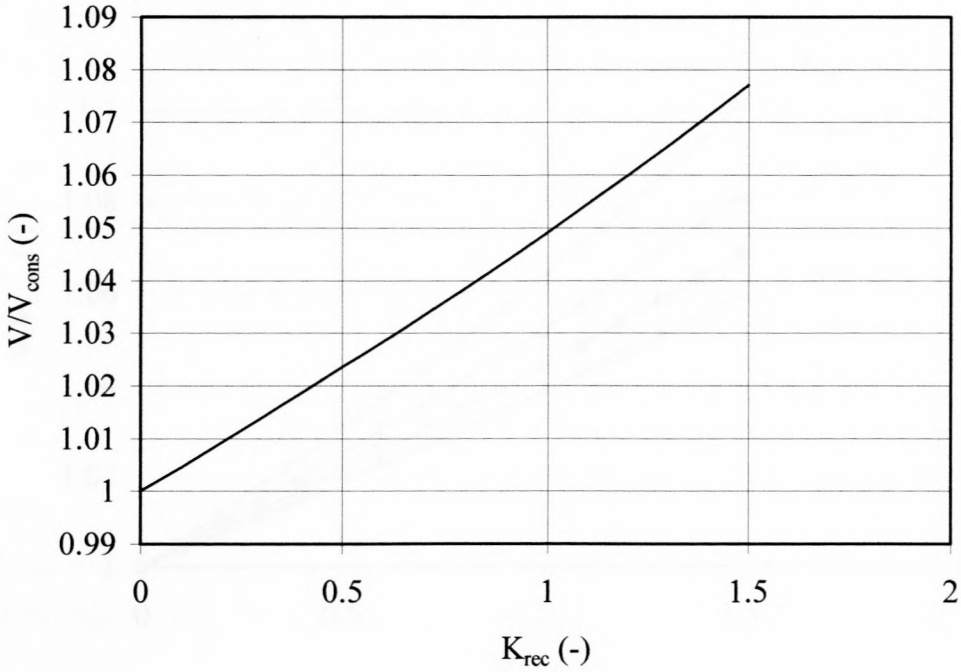

Figure 3.2. V/V_{cons} vs. K_{rec} for an ACHE where $K_{HE} = 20$, $A_{FC} = 1.867\ m^2$, $A_{FC}/A_{HE} = 0.517$, $a = -23.714\ Ns/m^5$ and $b = 455.134\ N/m^2$.

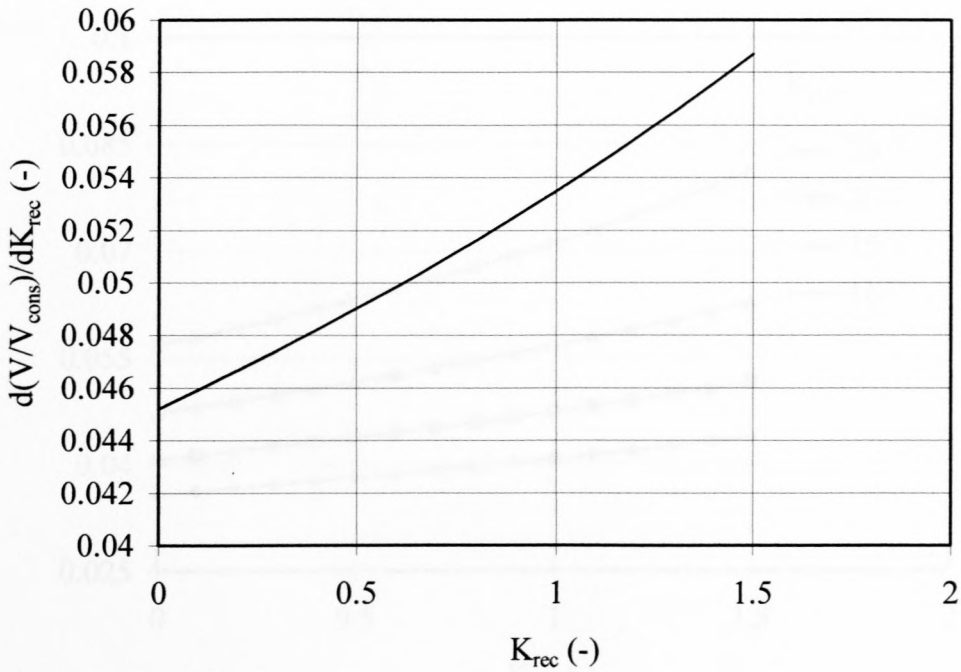

Figure 3.3. $d(V/V_{cons})/dK_{rec}$ vs. K_{rec} for an ACHE where $K_{HE} = 20$, $A_{FC} = 1.867\ m^2$, $A_{FC}/A_{HE} = 0.517$, $a = -23.714\ Ns/m^5$ and $b = 455.134\ N/m^2$.

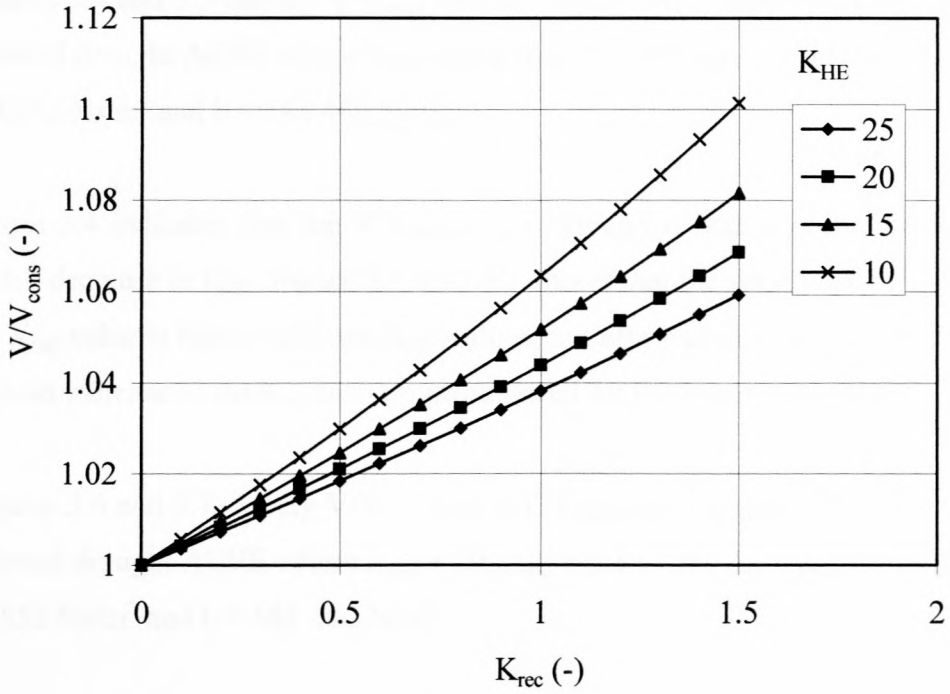

Figure 3.4. V/V_{cons} vs. K_{rec} for an ACHE where K_{HE} varies from 10 - 25, A_{FC} = 1.867 m^2, A_{FC}/A_{HE} = 0.517, a = -30.852 Ns/m^5 and b = 588.480 N/m^2.

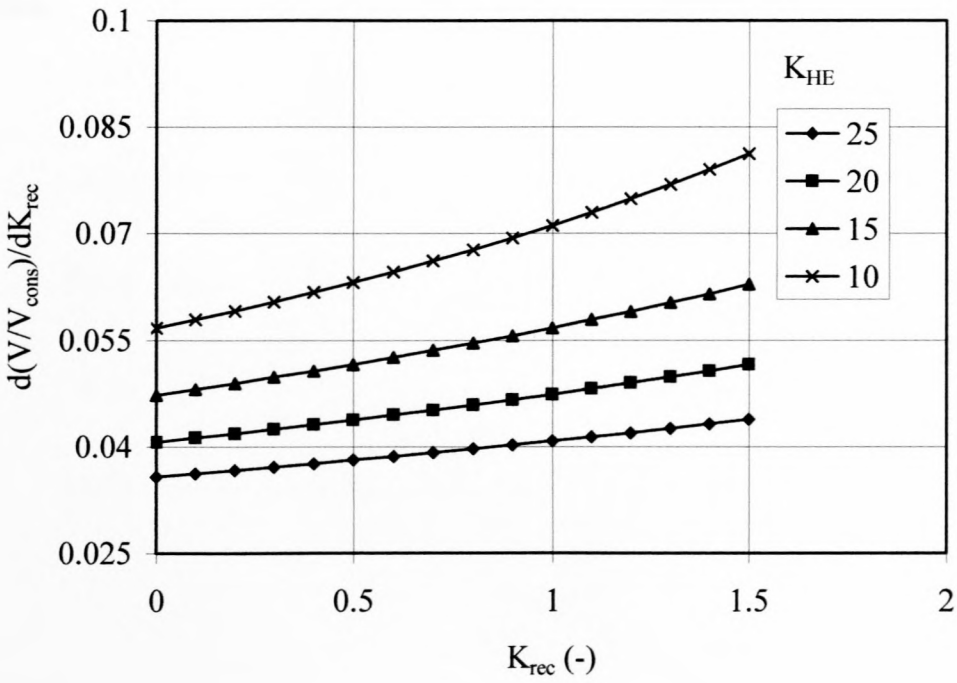

Figure 3.5. $d(V/V_{cons})/dK_{rec}$ vs. K_{rec} for an ACHE where K_{HE} varies from 10 - 25, A_{FC} = 1.867 m^2, A_{FC}/A_{HE} = 0.517, a = -30.852 Ns/m^5 and b = 588.480 N/m^2.

Figures 3.4 and 3.5 display V/V_{cons} and $d(V/V_{cons})/dK_{rec}$ respectively as a function of K_{rec} for a forced draught ACHE where K_{HE} varies from 10 - 25, $A_{FC} = 1.867\ m^2$, $A_{FC}/A_{HE} = 0.517$, a = $-30.852\ Ns/m^5$ and b = $588.480\ N/m^2$.

Figure 3.4 indicates that the V/V_{cons}-value associated with a particular K_{rec}-value increases with a decrease in K_{HE}. Figure 3.5 not only shows that the sensitivity of V/V_{cons} to a change in the K_{rec}-value is higher at lower K_{HE}-values, but also that the increase in sensitivity associated with an increase in the K_{rec} is more pronounced for the lower K_{HE}-values.

Figures 3.6 and 3.7 display V/V_{cons} and $d(V/V_{cons})/dK_{rec}$ respectively as a function of K_{rec} for a forced draught ACHE where $K_{HE} = 20$, $A_{FC} = 1.867\ m^2$, A_{FC}/A_{HE} varies from 0.4 - 0.6, a = $-30.852\ Ns/m^5$ and b = $588.480\ N/m^2$.

Figure 3.6 indicates that the V/V_{cons}-value associated with a particular K_{rec}-value increases with a decrease in A_{FC}/A_{HE}. Figure 3.5 not only shows that the sensitivity of V/V_{cons} to a change in the K_{rec}-value value is higher at lower A_{FC}/A_{HE}-values, but also that the increase in sensitivity associated with an increase in the K_{rec} is more pronounced for the lower A_{FC}/A_{HE}-values.

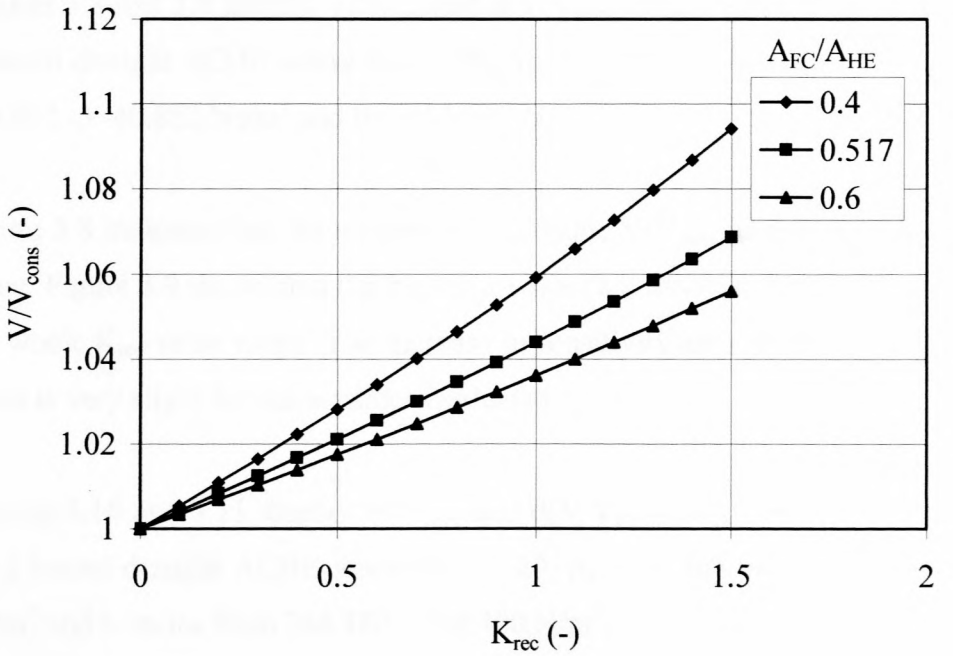

Figure 3.6. V/V_{cons} vs. K_{rec} for an ACHE where K_{HE} = 20, A_{FC} = 1.867 m^2, A_{FC}/A_{HE} varies from 0.4 - 0.6, a = -30.852 Ns/m^5 and b = 588.480 N/m^2.

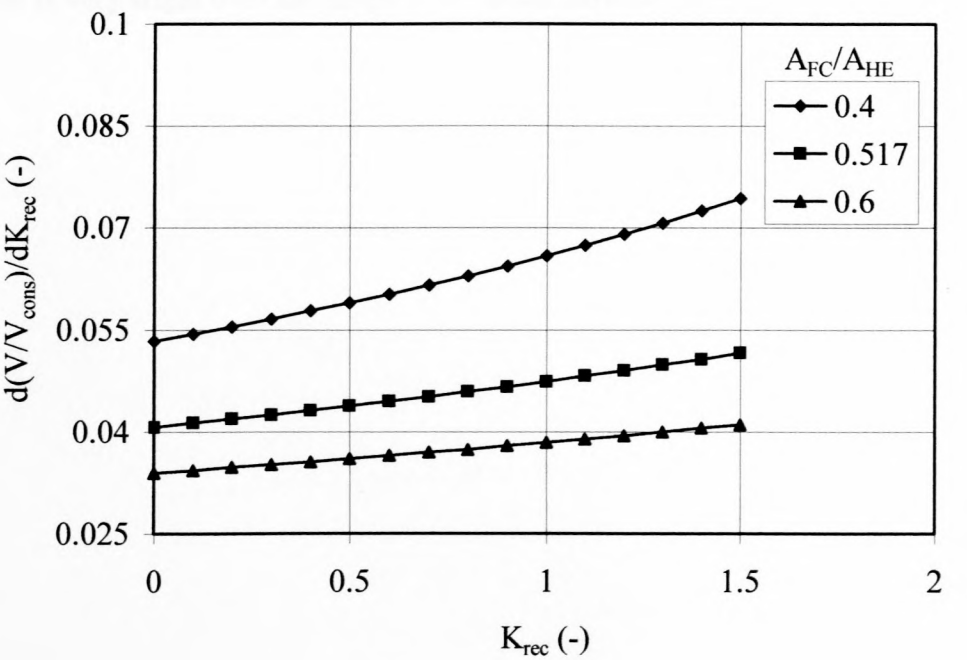

Figure 3.7. $d(V/V_{cons})/dK_{rec}$ vs. K_{rec} for an ACHE where K_{HE} = 20, A_{FC} = 1.867 m^2, A_{FC}/A_{HE} varies from 0.4 - 0.6, a = -30.852 Ns/m^5 and b = 588.480 N/m^2.

Figures 3.8 and 3.9 display V/V_{cons} and $d(V/V_{cons})/dK_{rec}$ respectively as a function of K_{rec} for a forced draught ACHE where $K_{HE} = 20$, $A_{FC} = 1.867\ m^2$, $A_{FC}/A_{HE} = 0.517$, a varies from -20.852 to -40.852 Ns/m^5 and $b = 455.134\ N/m^2$.

Figure 3.8 indicates that for a constant K_{rec}-value V/V_{cons} increases with an increase in the a-value. Figure 3.9 shows that the higher a-values are associated with increased sensitivity over the whole K_{rec}-value range. The increase in sensitivity associated with an increase in the K_{rec}-value is very slight for the a-values evaluated.

Figures 3.10 and 3.11 display V/V_{cons} and $d(V/V_{cons})/dK_{rec}$ respectively as a function of K_{rec} for a forced draught ACHE where $K_{HE} = 20$, $A_{FC} = 1.867\ m^2$, $A_{FC}/A_{HE} = 0.517$, $a = -30.852$ Ns/m^5 and b varies from 388.480 - 788.480 N/m^2.

Figure 3.10 shows that V/V_{cons} increases with an increase in the b-value for a constant K_{rec}-value. Figure 3.11 indicates that the higher b-values are associated with increased sensitivity over the whole K_{rec}-range. The increase in sensitivity associated with an increase in the K_{rec}-value is very slight over the range of b-values considered.

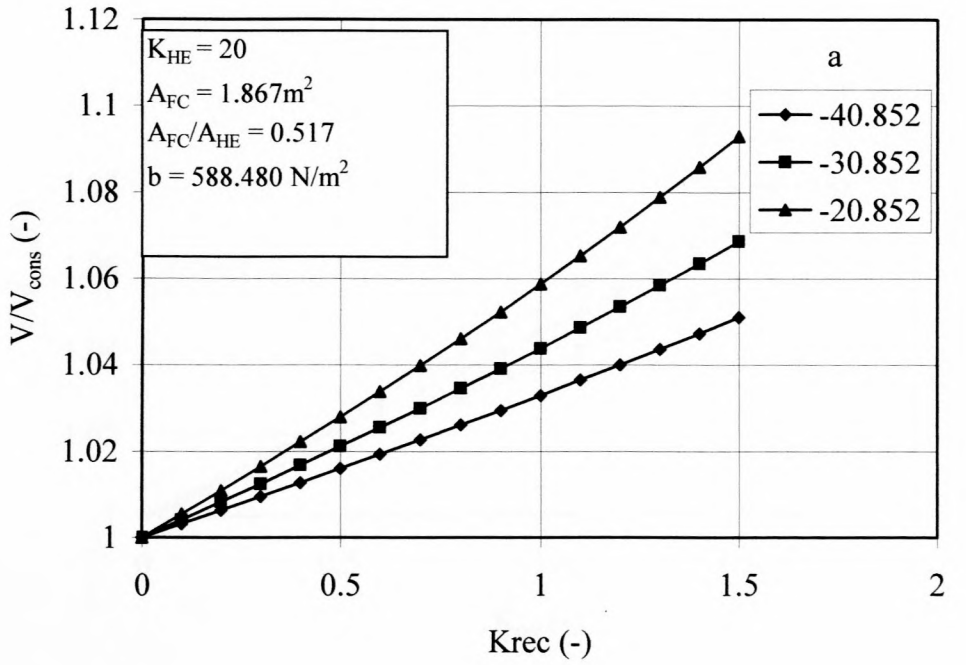

Figure 3.8. V/V_{cons} vs. K_{rec} for an ACHE where $K_{HE} = 20$, $A_{FC} = 1.867\ m^2$, $A_{FC}/A_{HE} = 0.517$, a varies from -20.852 to -40.852 Ns/m^5 and $b = 588.480\ N/m^2$.

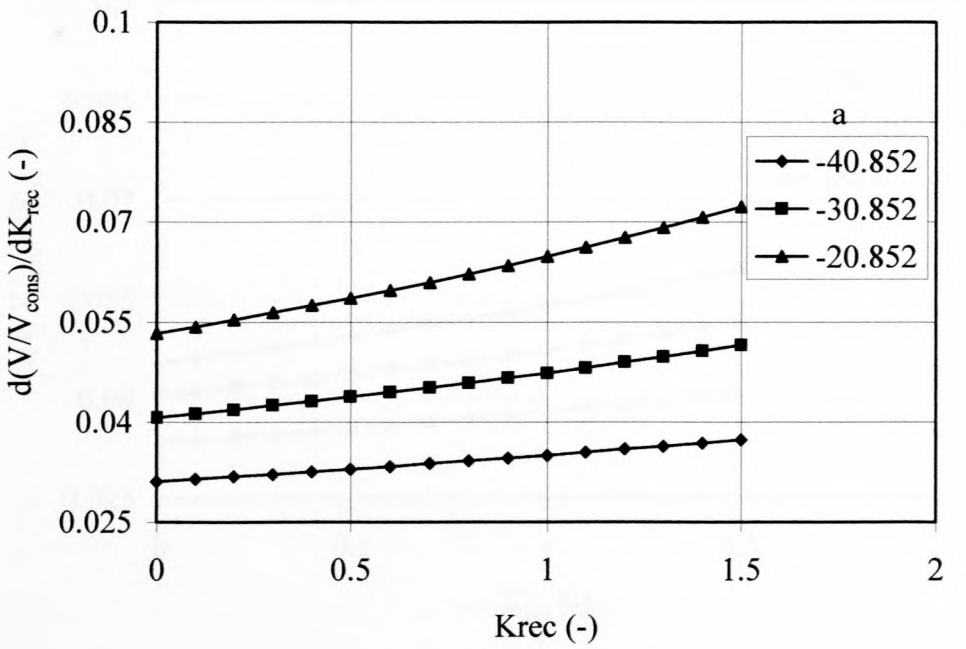

Figure 3.9. $d(V/V_{cons})/dK_{rec}$ vs. K_{rec} for an ACHE where $K_{HE} = 20$, $A_{FC} = 1.867\ m^2$, $A_{FC}/A_{HE} = 0.517$, a varies from -20.852 to -40.852 Ns/m^5 and $b = 588.480\ N/m^2$.

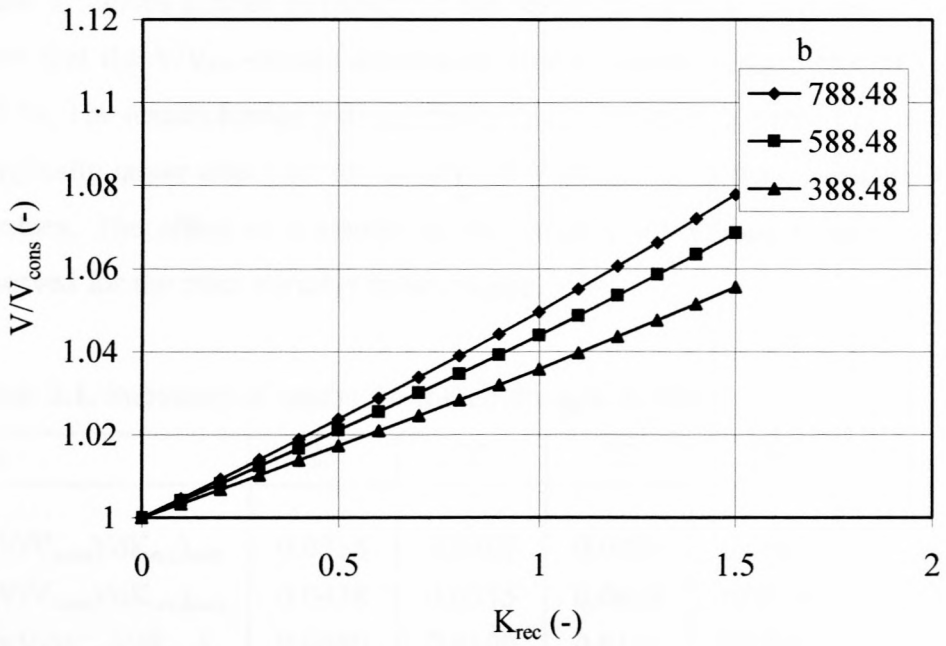

Figure 3.10. V/V_{cons} vs. K_{rec} for an ACHE where K_{HE} = 20, A_{FC} = 1.867 m^2, A_{FC}/A_{HE} = 0.517, a = -30.852 Ns/m^5 and b varies from = 388.480 N/m^2 - 788.480 N/m^2.

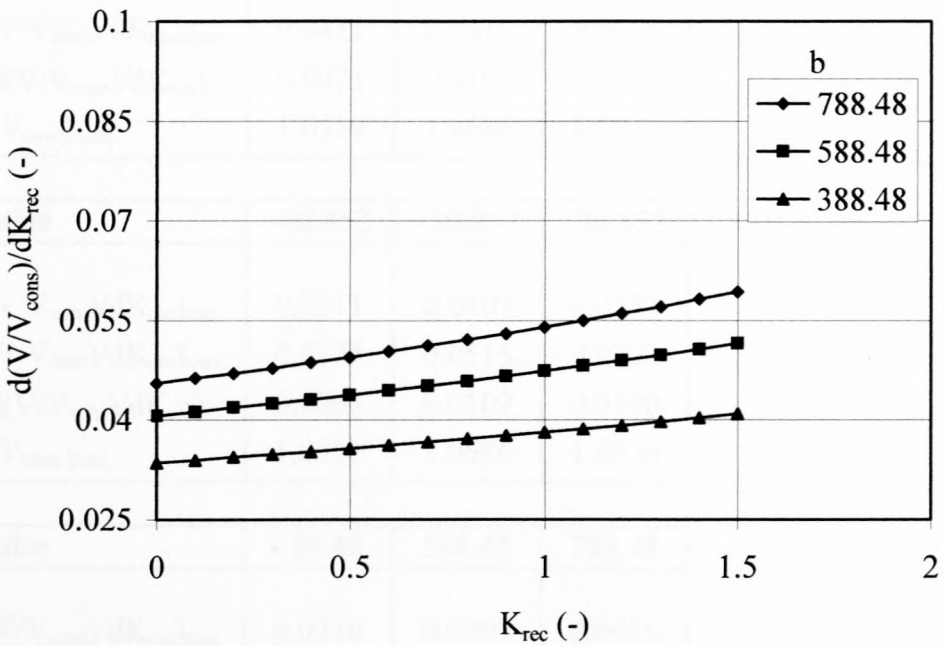

Figure 3.11. $d(V/V_{cons})/dK_{rec}$ vs. K_{rec} for an ACHE where K_{HE} = 20, A_{FC} = 1.867 m^2, A_{FC}/A_{HE} = 0.517, a = -30.852 Ns/m^5 and b varies from = 388.480 N/m^2 - 788.480 N/m^2.

Table 3.1 gives a brief summary of the results displayed in figures 3.4 - 3.11. The results show that the V/V_{cons}-values associated with a maximum K_{rec}-value of 1.5 range from 105 - 112 %. The results further indicate that a change in the K_{HE}-value of a particular ACHE has a marginally larger effect on the associated V/V_{cons}-values than a change in the A_{HE}/A_{FC}- and a-values. The effect of a change in the b-value on V/V_{cons} is seen to be less than those observed for the other variable value ranges.

Table 3.1. Summary of results for forced draught ACHEs.

K_{HE}	25	20	15	10
$(d(V/V_{cons})/dK_{rec})_{min}$	0.0358	0.0407	0.0473	0.0567
$(d(V/V_{cons})/dK_{rec})_{max}$	0.0438	0.0515	0.0628	0.0812
$\Delta(d(V/V_{cons})/dK_{rec})$	0.0080	0.0109	0.0156	0.0245
$(V/V_{cons})_{max}$	1.0593	1.0686	1.0816	1.1014
A_{FC}/A_{HE}	0.6	0.517	0.4	
$(d(V/V_{cons})/dK_{rec})_{min}$	0.0339	0.0407	0.0533	
$(d(V/V_{cons})/dK_{rec})_{max}$	0.0411	0.0516	0.0744	
$\Delta(d(V/V_{cons})/dK_{rec})$	0.0071	0.0109	0.0210	
$(V/V_{cons})_{max}$	1.0559	1.0686	1.0942	
a-value	-40.852	-30.852	-20.852	
$(d(V/V_{cons})/dK_{rec})_{min}$	0.0311	0.0407	0.0533	
$(d(V/V_{cons})/dK_{rec})_{max}$	0.0374	0.0515	0.0723	
$\Delta(d(V/V_{cons})/dK_{rec})$	0.0063	0.0109	0.0190	
$(V/V_{cons})_{max}$	1.0511	1.0686	1.0930	
b-value	388.48	588.48	788.48	
$(d(V/V_{cons})/dK_{rec})_{min}$	0.0336	0.0407	0.0456	
$(d(V/V_{cons})/dK_{rec})_{max}$	0.0409	0.0515	0.0593	
$\Delta(d(V/V_{cons})/dK_{rec})$	0.0073	0.0109	0.0138	
$(V/V_{cons})_{max}$	1.0555	1.0686	1.0779	

From table 3.1 it is also observed that for the variable-value ranges considered, the $d(V/V_{cons})/dK_{rec}$-values range from 0.031 - 0.081. The minimum and maximum values for $d(V/V_{cons})/dK_{rec}$ are associated with the minimum and maximum K_{rec}-values, as noted earlier and, according, to table 3.1 the difference between $(d(V/V_{cons})/dK_{rec})_{max}$ and $(d(V/V_{cons})/dK_{rec})_{min}$ ranges from 0.006 - 0.025. The last result underlines the near linear relationship that exists between V/V_{cons} and K_{rec}.

3.2. Induced draught ACHEs

3.2.1. Analysis

The draught equation for a induced draught ACHE is presented in Chapter 2 and given as

$$\Delta p_{sF} = K_{HE}\rho v_{HE}^2/2 + K_P\rho v_{FC}^2/2 \qquad (2.24)$$

The previous assumptions are applied to yield the following expression for the operating point volume flow rate

$$V = \frac{a/\rho + \sqrt{(a/\rho)^2 + \frac{2b}{\rho}\left[K_P/A_{FC}^2 + K_{HE}/A_{HE}^2\right]}}{\left[K_P/A_{FC}^2 + K_{HE}/A_{HE}^2\right]} \qquad (3.9)$$

The conservative operating point volume flow rate is obtained by setting $K_P = 0$ in equation (3.9). It follows that

$$V_{cons} = \frac{a/\rho + \sqrt{(a/\rho)^2 + \frac{2b}{\rho}K_{HE}/A_{HE}^2}}{K_{HE}/A_{HE}^2} \qquad (3.10)$$

Differentiation of equation (3.9) with respect to K_P yields

$$\frac{dV}{dK_P} = \frac{V^2/2}{-V\left[K_P + (A_{FC}/A_{HE})^2 K_{HE}\right] + aA_{FC}^2/\rho} \qquad (3.11)$$

$d(V/V_{cons})/dK_P$ is given as

$$\frac{d(V/V_{cons})}{dK_P} = \frac{dV}{dK_P} \times \frac{1}{V_{cons}} \tag{3.12}$$

3.2.2. Discussion

Currently no experimental data exists that provides K_P-values associated with a particular range of induced draught ACHEs. A negative K_P-value indicates that the plenum chamber acts as a source of mechanical energy per unit volume which is of course unrealistic. It is however possible that the plenum chamber aerodynamic behaviour could influence the velocity field at the fan inlet in such a way as to improve the performance characteristics of the axial flow fan which could then result in a negative K_P-value. As a result an arbitrary K_P-value range of -1.0 to 1.0 is chosen for the current analysis.

Figures 3.12 and 3.13 display V/V_{cons} and the absolute value of $d(V/V_{cons})/dK_P$ as a function of K_P respectively for an induced draught ACHE where $K_{HE} = 20$, $A_{FC} = 1.867\ m^2$, $A_{FC}/A_{HE} = 0.517$, $a = -23.714\ Ns/m^5$ and $b = 455.134\ N/m^2$. Note that a change in the sensitivity of V/V_{cons} to a change in K_P is not associated with the sign of the $d(V/V_{cons})/dK_P$-value and in order to avoid confusion the absolute value of $d(V/V_{cons})/dK_P$ is plotted.

Figure 3.12 displays the near linear reduction in V/V_{con} for an increase in K_P over the range of K_P-values considered. This result is confirmed by the data displayed in figure 3.13 which indicates that the sensitivity of the ACHE to a change in K_P does not change dramatically over the range of K_P-values.

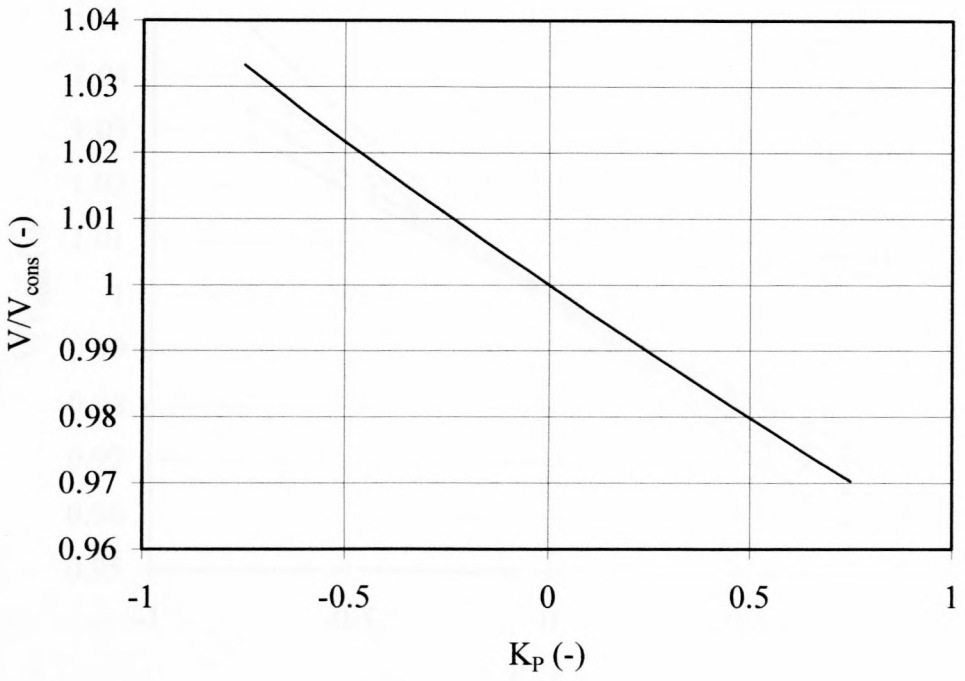

Figure 3.12. V/V_{cons} vs. K_P for an ACHE where $K_{HE} = 20$, $A_{FC} = 1.867\ m^2$, $A_{FC}/A_{HE} = 0.517$, $a = -23.714\ Ns/m^5$ and $b = 455.134\ N/m^2$.

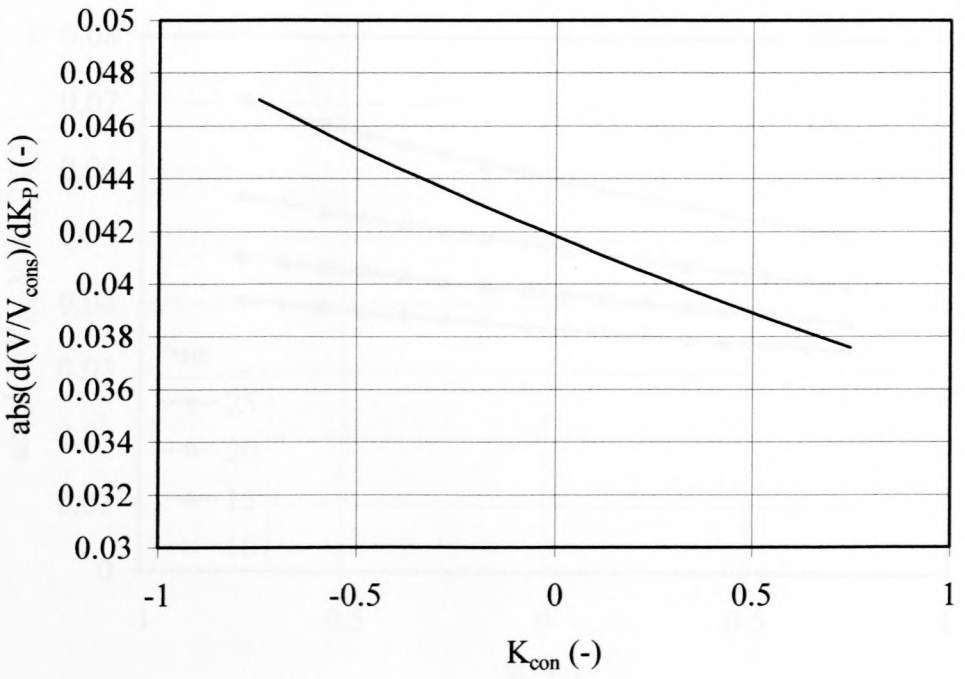

Figure 3.13. $abs(d(V/V_{cons})/dK_P)$ vs. K_P for an ACHE where $K_{HE} = 20$, $A_{FC} = 1.867\ m^2$, $A_{FC}/A_{HE} = 0.517$, $a = -23.714\ Ns/m^5$ and $b = 455.134\ N/m^2$.

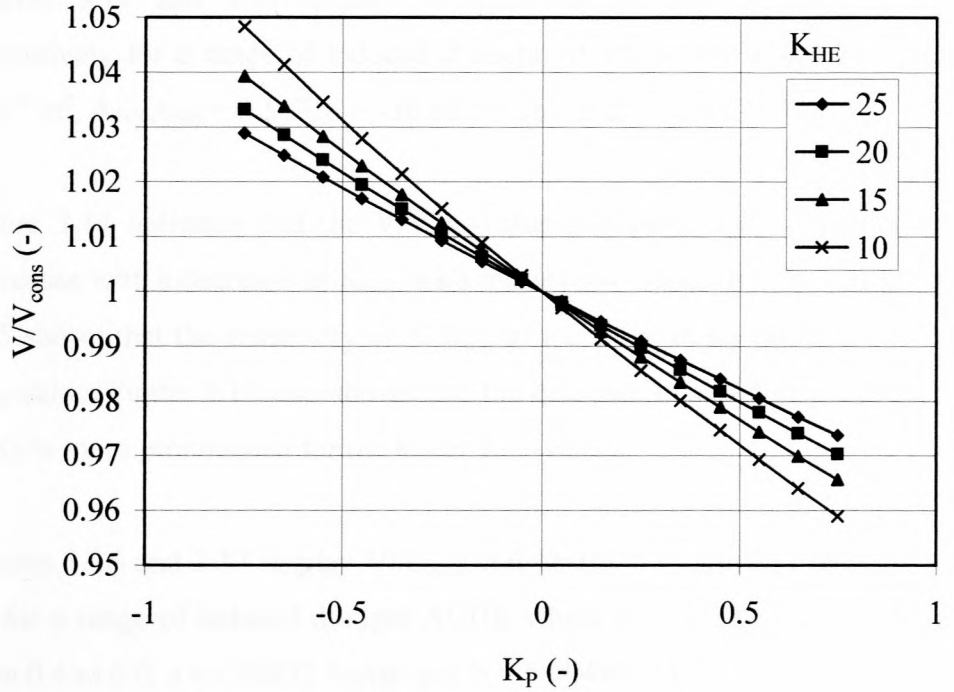

Figure 3.14. V/V_{cons} vs. K_P for an ACHE where K_{HE} varies from 10 - 25, A_{FC} = 1.867 m^2, A_{FC}/A_{HE} = 0.517, a = -30.852 Ns/m^5 and b = 588.480 N/m^2.

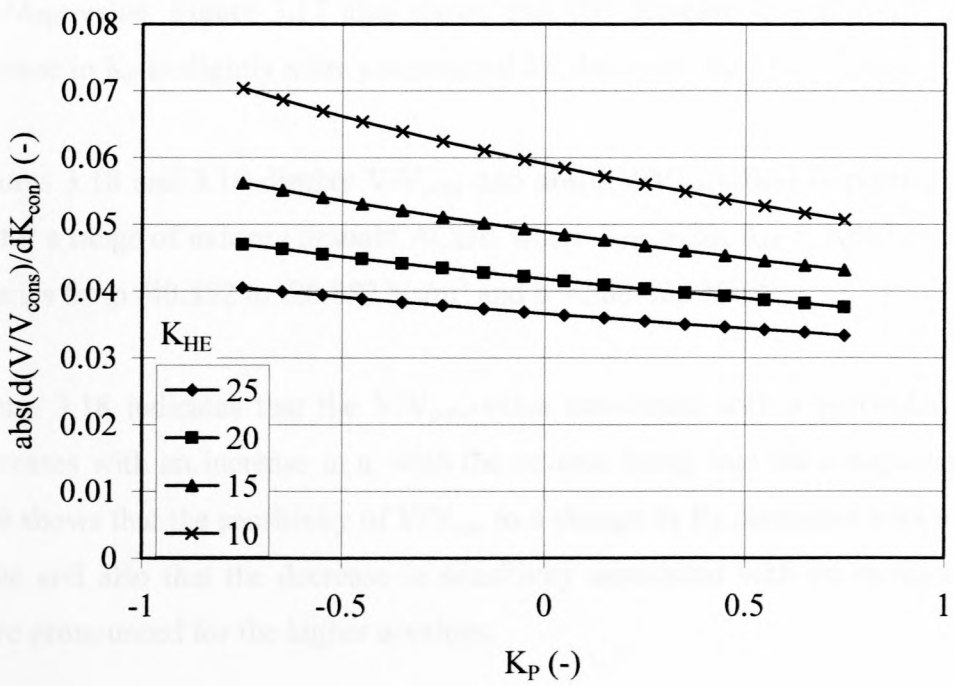

Figure 3.15. $d(V/V_{cons})/dK_P$ vs. K_P for an ACHE where K_{HE} varies from 10 - 25, A_{FC} = 1.867 m^2, A_{FC}/A_{HE} = 0.517, a = -30.852 Ns/m^5 and b = 588.480 N/m^2.

Figures 3.14 and 3.15 display V/V_{cons} and $abs(d(V/V_{cons})/dK_P)$ as a function of K_P respectively for a range of induced draught ACHE where K_{HE} varies from 10 to 25, A_{FC} = 1.867 m^2, A_{FC}/A_{HE} = 0.517, a = -30.852 Ns/m^5 and b = 588.480 N/m^2.

Figure 3.14 indicates that the V/V_{cons}-value associated with a particular positive K_P-value decreases with a decrease in K_{HE}, with the reverse being true for a negative K_P-value. Figure 3.15 shows that the sensitivity of V/V_{con} to a change in K_P decreases with an increase in the K_{HE}-value. Figure 3.15 also shows that the decrease in sensitivity associated with an increase in K_P is more pronounced for the lower K_{HE}-values.

Figures 3.16 and 3.17 display V/V_{cons} and $abs(d(V/V_{cons})/dK_P)$ respectively as a function of K_P for a range of induced draught ACHE where K_{HE} = 20, A_{FC} = 1.867 m^2, A_{FC}/A_{HE} varies from 0.4 to 0.6, a = -30.852 Ns/m^5 and b = 588.480 N/m^2.

Figure 3.16 indicates that the V/V_{cons}-value associated with a particular positive K_P-value decreases with a decrease in K_{HE}, with the reverse being true for a negative K_P-value. Figure 3.17 shows that the sensitivity of V/V_{con} to a change in K_P decreases with an increase in the A_{FC}/A_{HE}-value. Figure 3.17 also shows that the decrease in sensitivity associated with an increase in K_P is slightly more pronounced for the lower A_{FC}/A_{HE}-values.

Figures 3.18 and 3.19 display V/V_{cons} and $abs(d(V/V_{cons})/dK_P)$ respectively as a function of K_P for a range of induced draught ACHE where K_{HE} = 20, A_{FC} = 1.867 m^2, A_{FC}/A_{HE} = 0.517, a varies from -40.852 to -20.852 Ns/m^5 and b = 588.480 N/m^2.

Figure 3.18 indicates that the V/V_{cons}-value associated with a particular positive K_P-value decreases with an increase in a, with the reverse being true for a negative K_P-value. Figure 3.19 shows that the sensitivity of V/V_{con} to a change in K_P decreases with a decrease in the a-value and also that the decrease in sensitivity associated with an increase in K_P is slightly more pronounced for the higher a-values.

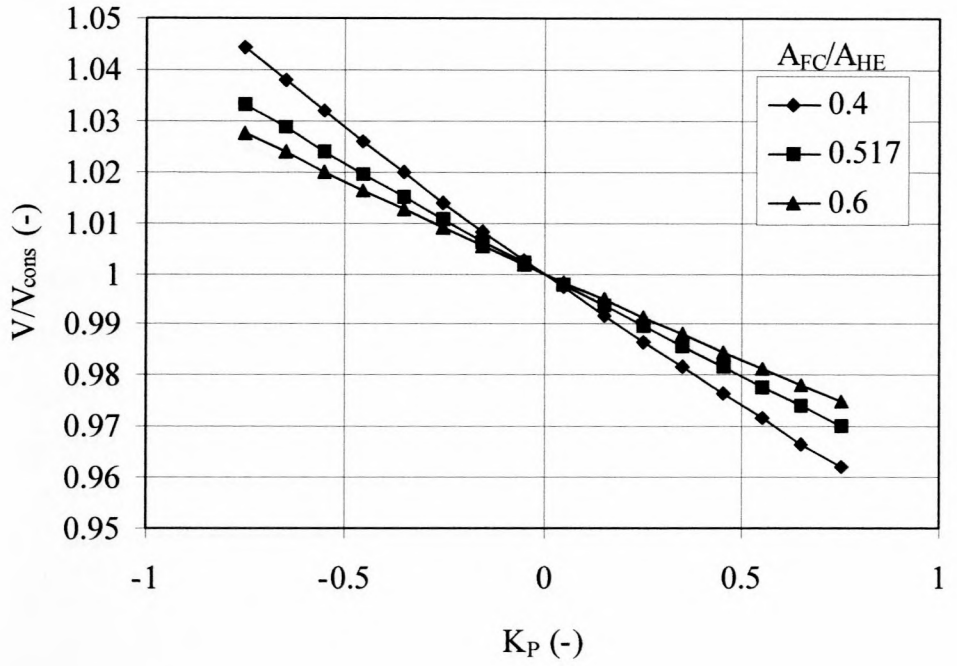

Figure 3.16. V/V_{cons} vs. K_P for an ACHE where K_{HE} = 20, A_{FC} = 1.867 m^2, A_{FC}/A_{HE} varies from 0.4 - 0.6, a = -30.852 Ns/m^5 and b = 588.480 N/m^2.

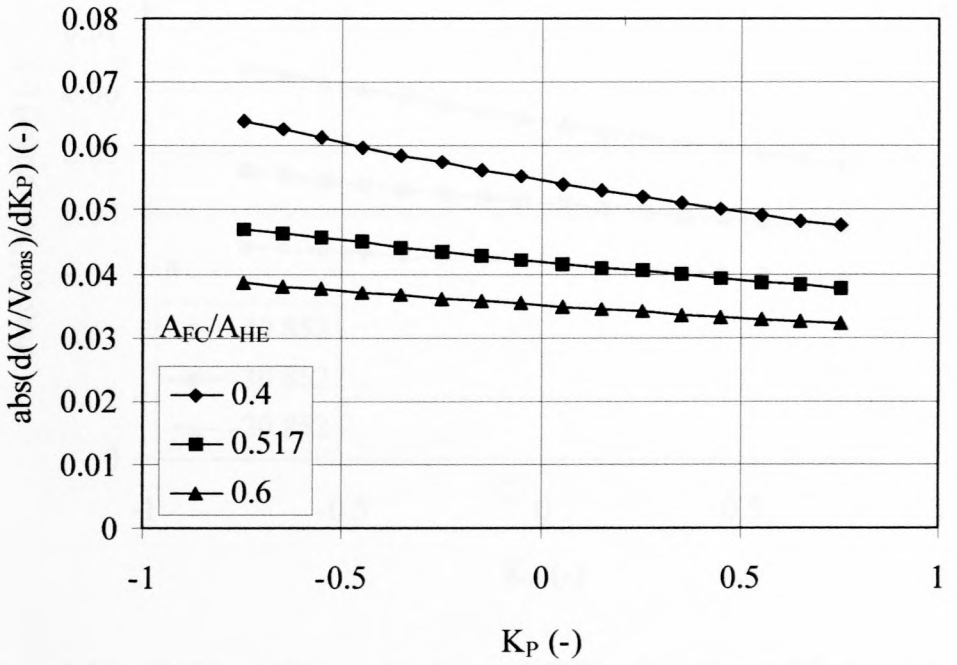

Figure 3.17. abs($d(V/V_{cons})/dK_P$) vs. K_P for an ACHE where K_{HE} = 20, A_{FC} = 1.867 m^2, A_{FC}/A_{HE} varies from 0.4 - 0.6, a = -30.852 Ns/m^5 and b = 588.480 N/m^2.

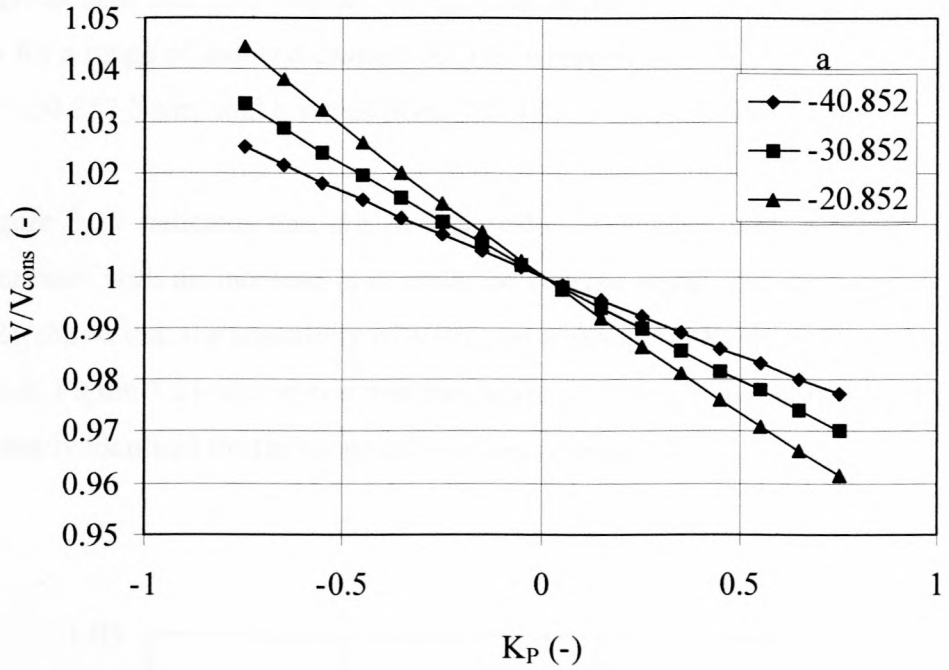

Figure 3.18. V/V_{cons} vs. K_P for an ACHE where $K_{HE} = 20$, $A_{FC} = 1.867\ m^2$, $A_{FC}/A_{HE} = 0.517$, a varies from -20.852 to -40.852 Ns/m^5 and $b = 588.480\ N/m^2$.

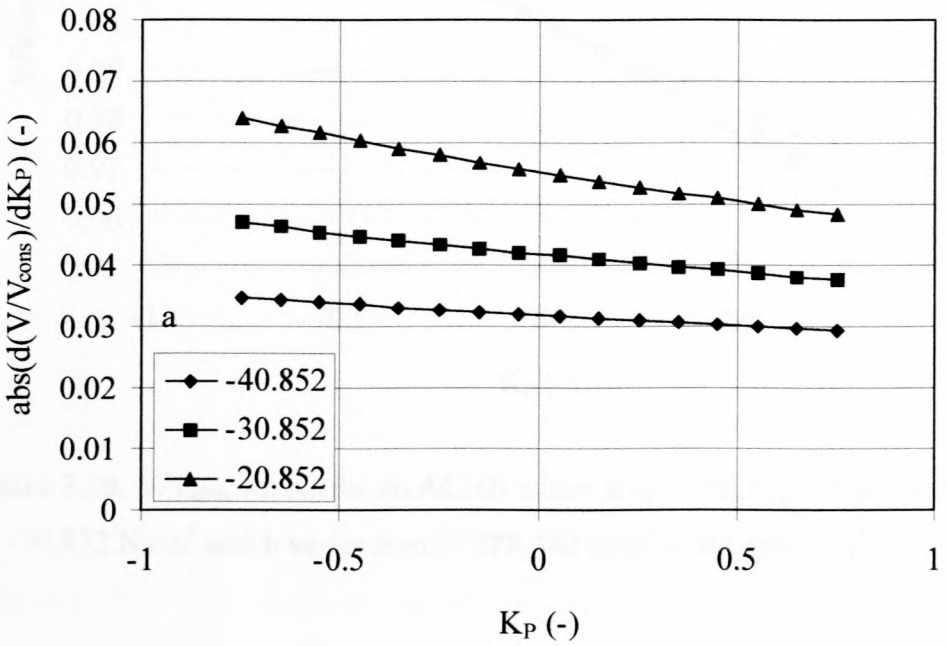

Figure 3.19. $d(V/V_{cons})/dK_P$ vs. K_P for an ACHE where $K_{HE} = 20$, $A_{FC} = 1.867\ m^2$, $A_{FC}/A_{HE} = 0.517$, a varies from -20.852 to -40.852 Ns/m^5 and $b = 588.480\ N/m^2$.

Figures 3.20 and 3.21 display V/V_{cons} and $abs(d(V/V_{cons})/dK_P)$ respectively as a function of K_P for a range of induced draught ACHE where $K_{HE} = 20$, $A_{FC} = 1.867\ m^2$, $A_{FC}/A_{HE} = 0.517$, $a = -30.852\ Ns/m^5$ and b varies from 388.480 to 788.480 N/m^2.

Figure 3.20 indicates that the V/V_{cons}-value associated with a particular positive K_P-value decreases with an increase in b, with the reverse being true for a negative K_P-value. Figure 3.21 shows that the sensitivity of V/V_{con} to a change in K_P decreases with a decrease in the b-value. Figure 3.21 also shows that the decrease in sensitivity associated with an increase in K_P is nearly identical for the range of b-values considered.

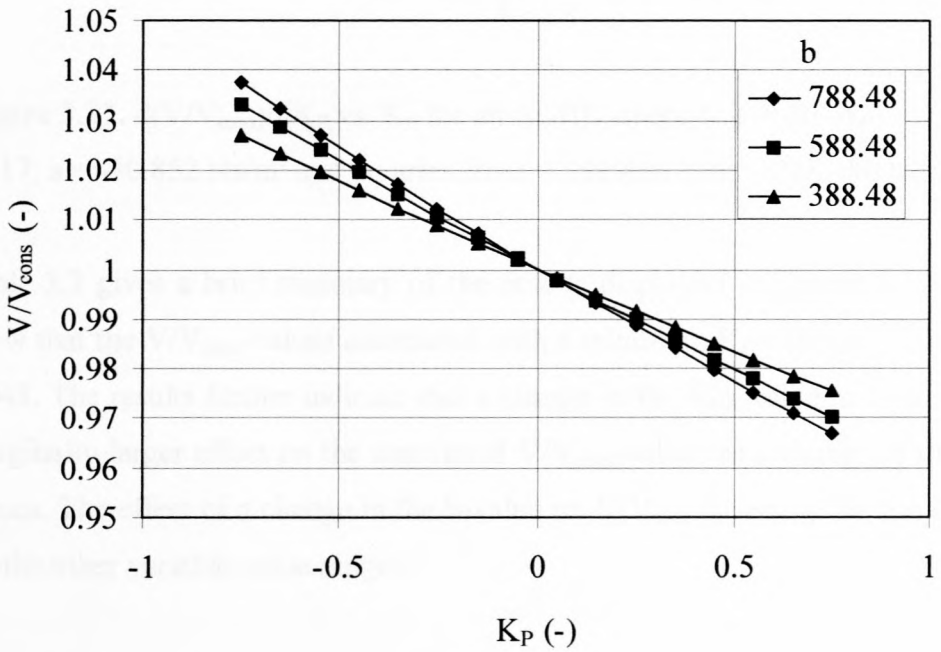

Figure 3.20. V/V_{cons} vs. K_P for an ACHE where $K_{HE} = 20$, $A_{FC} = 1.867\ m^2$, $A_{FC}/A_{HE} = 0.517$, $a = -30.852\ Ns/m^5$ and b varies from = 388.480 N/m^2 - 788.480 N/m^2.

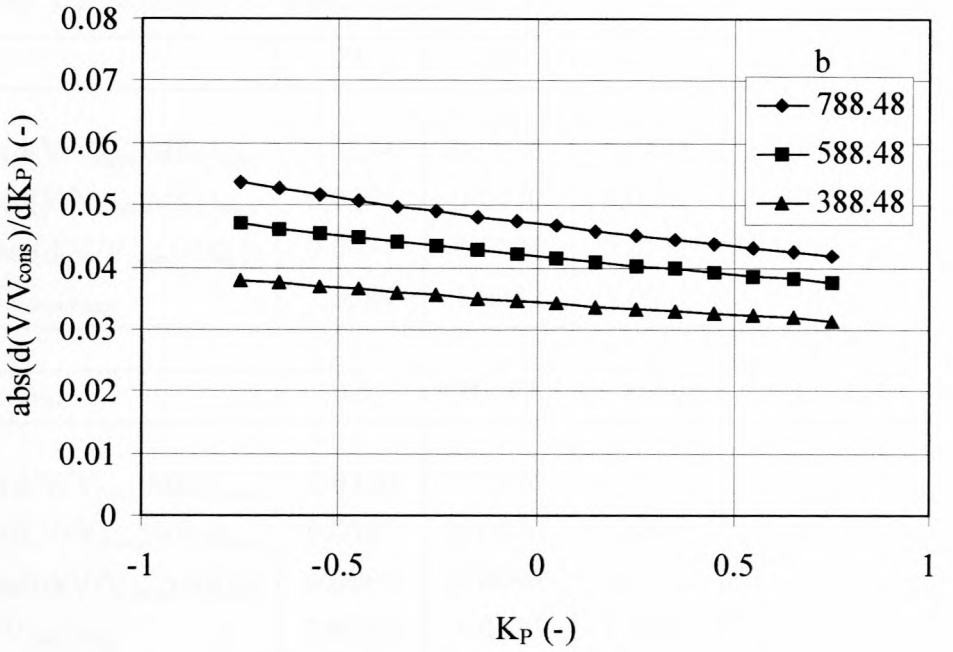

Figure 3.21. $d(V/V_{cons})/dK_P$ vs. K_P for an ACHE where $K_{HE} = 20$, $A_{FC} = 1.867\ m^2$, $A_{FC}/A_{HE} = 0.517$, $a = -30.852\ Ns/m^5$ and b varies from = 388.480 N/m^2 - 788.480 N/m^2.

Table 3.2 gives a brief summary of the results displayed in figures 3.12 - 3.21. The results show that the V/V_{cons}-values associated with a minimum K_P-value of -1.0 range from 1.025 - 1.048. The results further indicate that a change in the K_{HE}-value of a particular ACHE has a marginally larger effect on the associated V/V_{cons}-values as a change in the A_{HE}/A_{FC}- and a-values. The effect of a change in the b-value on V/V_{cons} is seen to be less than those observed for the other variable value ranges.

From table 3.2 it is also observed that for the variable-value ranges considered the $abs(d(V/V_{cons})/dK_P)$-values range from 0.0292 to 0.0704. According to table 3.2 the difference between $(d(V/V_{cons})/dK_P)_{max}$ and $(d(V/V_{cons})/dK_P)_{min}$ range from 0.0056 - 0.0197. The last result underlines the near linear relationship that exists between V/V_{cons} and K_P.

Table 3.2. Summary of results for induced draught ACHEs.

K_{HE}	25	20	15	10
$abs(d(V/V_{cons})/dK_P)_{min}$	0.0334	0.0376	0.0431	0.0507
$abs(d(V/V_{cons})/dK_P)_{max}$	0.0405	0.0470	0.0562	0.0704
$\Delta abs((d(V/V_{cons})/dK_P))$	0.0071	0.0094	0.0131	0.0197
$(V/V_{cons})_{max}$	1.0289	1.0332	1.0393	1.0483
A_{FC}/A_{HE}	0.6	0.517	0.4	
$abs(d(V/V_{cons})/dK_P)_{min}$	0.0320	0.0376	0.0474	
$abs(d(V/V_{cons})/dK_P)_{max}$	0.0385	0.0470	0.0640	
$\Delta abs((d(V/V_{cons})/dK_P))$	0.0065	0.0094	0.0166	
$(V/V_{cons})_{max}$	1.0275	1.0333	1.0443	
a-value	-40.852	-30.852	-20.852	
$abs(d(V/V_{cons})/dK_P)_{min}$	0.0292	0.0376	0.0483	
$abs(d(V/V_{cons})/dK_P)_{max}$	0.0348	0.0470	0.0641	
$\Delta abs((d(V/V_{cons})/dK_P))$	0.0056	0.0094	0.0158	
$(V/V_{cons})_{max}$	1.0250	1.0332	1.0446	
b-value	388.48	588.48	788.48	
$abs(d(V/V_{cons})/dK_P)_{min}$	0.0314	0.0376	0.0418	
$abs(d(V/V_{cons})/dK_P)_{max}$	0.0379	0.0470	0.0535	
$\Delta abs((d(V/V_{cons})/dK_P))$	0.0065	0.0094	0.0117	
$(V/V_{cons})_{max}$	1.0271	1.0332	1.0376	

3.3. Conclusions

One of the most important conclusions that can be made from the results of the preceding analysis is that the K_{rec}-value associated with a particular forced draught ACHE cannot necessarily be used as a comparative measure between differing ACHE configurations. This statement is based on the fact that for a constant K_{rec}-value the V/V_{cons}-value is a function, to a varying degree of all the remaining variables considered in the analysis. The preceding argument is also true of the K_P-value associated with induced draught ACHEs.

The results further indicate that the sensitivity of V/V_{cons} to a change in K_{rec} for forced draught ACHEs and K_P for induced draught ACHEs does not change dramatically for a particular ACHE over the respective range of K_{rec}- and K_P-values considered. The sensitivity of V/V_{cons} at a constant K_{rec}-value is seen to increase for a decrease in K_{HE} and A_{PC}/A_{HE} and an increase in the a- and b-values. This trend is also observed for induced draught ACHEs displaying a constant K_P-value.

For both the forced and induced draught ACHE configurations the effect of variable value changes within the range considered for the K_{HE}-, A_{FC}/A_{HE}- and a-values have a similar effect in magnitude on V/V_{cons} as well as the sensitivity of the latter to a change in K_{rec} or K_P, whilst a change in the b-value has a lesser effect.

CHAPTER 4 - An overview of the CFD-code and associated numerical models

The commercially available CFD-code, Flo^{++}, is used to investigate numerically the aerodynamic characteristics of not only a range of ACHEs, but also some of the individual components comprising the ACHEs.

Flo^{++} makes use of a finite volume formulation to discretisise a set of partial differential equations over a specific computational domain through the use of a previously defined computational grid with appropriately defined boundary conditions. A solution of the resulting set of non-linear equations is obtained in the form of flow field variable values at points within the computational domain.

In order to resolve the detailed internal flow field associated with an ACHE numerically, the complex geometrical features of the axial flow fan and the heat exchanger need to be reflected by the computational grid. Also required would be an appropriate numerical strategy to deal with the rotational motion of the fan blades. This task can only be accomplished at a prohibitively expensive computational cost and, as a result, an alternative method to include the influence of the axial flow fan and heat exchanger on the ACHE internal flow field is sought.

The developers of the CFD-code allow the user to expand the capabilities of the basic CFD-code in a controlled manner through the alteration of certain programme units referred to as user-subroutines. A number of these user-subroutines are re-programmed to include computationally more cost-effective fan and heat exchanger models into the CFD-code. A further advantage gained by the use of the fan and heat exchanger models is a marked reduction in the degree of complexity associated with the construction of the computational grid.

The objective of this chapter is to present a brief overview of the governing equations and strategies employed by the CFD-code to resolve the internal flow fields associated with the

ACHEs under investigation and also to disclose the manner in which the fan and heat exchanger models are formulated and incorporated into the CFD-code. In addition the construction and important features of the computational grids used during the course of the investigation is discussed.

4.1. Conservation equations

The following Reynolds-averaged conservation equations for steady, incompressible and viscous fluid flows are solved by the CFD code. For the sake of brevity the equations are presented in Cartesian tensor notation [72FR1].

Conservation of mass

Mass conservation is expressed by

$$\frac{\partial}{\partial x_j}\left(u_j\right)=0 \tag{4.1}$$

where u_j is the fluid velocity tensor.

Conservation of momentum

The Navier-Stokes equations for the conservation of momentum is given as

$$\rho u_i+\frac{\partial}{\partial x_j}\left(\rho u_j u_i-\tau_{ij}\right)=-\frac{\partial}{\partial x_j}(p)+s_i \tag{4.2}$$

where ρ is the fluid density, τ_{ij} the stress tensor, s_i the momentum source tensor and p the static pressure.

The stress tensor, τ_{ij}, consists of the following terms

$$\tau_{ij} = \mu\left(\frac{\partial}{\partial x_j}(u_i) + \frac{\partial}{\partial x_i}(u_j)\right) - \frac{2}{3}\mu\frac{\partial}{\partial x_k}(u_k)\delta_{ij} - \overline{\rho u'_i u'_j} \tag{4.3}$$

where μ is the molecular dynamic fluid viscosity and δ_{ij} the Kronecker delta which is unity when i=j and zero otherwise. The turbulent Reynolds stresses are represented by the last term on the right-hand side of equation (4.3) and contains the fluctuating part of the velocity tensor, u'_i.

4.2. Fluid turbulence model

The k-ε turbulence model of Launder and Spalding [74LA1] is used to model the effects of turbulence on the fluid flow field. The additional turbulent stresses and heat flux terms are expressed, respectively as

$$-\overline{\rho u'_i u'_j} = \mu_t\left(\frac{\partial}{\partial x_j}(u_i) + \frac{\partial}{\partial x_i}(u_j)\right) - \frac{2}{3}\left(\mu_t\frac{\partial}{\partial x_k}(u_k) + \rho k\right)\delta_{ij} \tag{4.4}$$

and

$$\overline{\rho u'_j i'} = -\frac{\mu_t}{\sigma_h}\frac{\partial}{\partial x_j}(i) \tag{4.5}$$

where μ_t is the fluid turbulent dynamic viscosity, σ_h the turbulent Prandtl number and k the turbulent kinetic energy defined as

$$k = \frac{\overline{u'_i u'_i}}{2} \tag{4.6}$$

The turbulent viscosity is linked to the turbulent kinetic energy and the dissipation rate of turbulent kinetic energy, ε, via

$$\mu_t = C_\mu \frac{\rho k^2}{\varepsilon} \tag{4.7}$$

where C_μ is a model constant.

The conservation equation for the turbulent kinetic energy is given as

$$\left(\rho u_j k - \frac{\mu_{eff}}{\sigma_k}\frac{\partial}{\partial x_j}(k)\right) = \mu_t\left(\left(\frac{\partial}{\partial x_j}(u_i)+\frac{\partial}{\partial x_i}(u_j)\right)\frac{\partial}{\partial x_j}(u_i) - \frac{g_i}{\sigma_h \rho}\frac{\partial}{\partial x_i}(\rho)\right) - \rho\varepsilon - \frac{2}{3}\left(\mu_t\frac{\partial}{\partial x_i}(u_i)+\rho k\right)\frac{\partial}{\partial x_i}(u_i) \tag{4.8}$$

where $\mu_{eff} = \mu+\mu_t$ and σ_k is a model constant.

The dissipation rate of turbulent kinetic energy conservation equation is given as

$$\left(\rho u_j \varepsilon - \frac{\mu_{eff}}{\sigma_\varepsilon}\frac{\partial}{\partial x_j}(\varepsilon)\right) = C_{\varepsilon 1}\frac{\varepsilon}{k}\left(\mu_t\left(\left(\frac{\partial}{\partial x_j}(u_i)+\frac{\partial}{\partial x_i}(u_j)\right)\frac{\partial}{\partial x_j}(u_i) - C_{\varepsilon 3}\frac{g_i}{\sigma_h \rho}\frac{\partial}{\partial x_j}(\rho)\right) - \frac{2}{3}\left(\mu_t\frac{\partial}{\partial x_i}(u_i)+\rho k\right)\frac{\partial}{\partial x_i}(u_i)\right) - C_{\varepsilon 2}\rho\frac{\varepsilon^2}{k} - C_{\varepsilon 4}\rho\varepsilon\frac{\partial}{\partial x_i}(u_i) \tag{4.9}$$

where σ_ε, $C_{\varepsilon 1}$, $C_{\varepsilon 2}$, $C_{\varepsilon 3}$ and $C_{\varepsilon 4}$ are empirical coefficients.

The empirical constants associated with the k-ε turbulence model are taken from references [74LA1, 79RO1 and 83EL1] and are listed in table 4.1.

Table 4.1. Values assigned to k-ε turbulence model coefficients.

C_μ	σ_k	σ_ε	$C_{\varepsilon 1}$	$C_{\varepsilon 2}$	$C_{\varepsilon 3}$	$C_{\varepsilon 4}$
0.09	1.00	1.22	1.44	1.92	1.44	-0.33

4.3. Control volume formulation and discretization practices

4.3.1. Control volume formulation

According to Patankar [80PA1], the partial differential equations of the previous section conform to a general conservation principle and, by denoting the dependent variable by ϕ, a general differential equation can be formulated as follows

$$\frac{\partial}{\partial t}(\rho \varphi)+\frac{\partial}{\partial x_j}(\rho u_j \varphi)=\frac{\partial}{\partial x_j}\left(\Gamma \frac{\partial \varphi}{\partial x_j}\right)+S \qquad (4.10)$$

where Γ denotes the coefficient of diffusion and S a source term.

Taking into account that equation (4.10) must be solved without violating continuity as expressed by equation (4.1), it follows that equation (4.10) can be written as

$$\rho \frac{\partial}{\partial t}(\varphi)+\rho u_j \frac{\partial}{\partial x_j}(\varphi)=\frac{\partial}{\partial x_j}\left(\Gamma \frac{\partial \varphi}{\partial x_j}\right)+S \qquad (4.11)$$

where the terms, from left to right, are the unsteady, convection, diffusion and source term.

Although the discretisation of equation (4.11) for the node points defined within and on the boundaries of the calculation domain can be accomplished in a number of ways, the use of the Control Volume (CV) formulation has gained popularity in the field of computational fluid dynamics.

In the CV formulation all nodal points in the calculation domain are surrounded by non-overlapping control volumes. The governing differential equation, in this case the general differential equation (4.11) is integrated over every individual control volume yielding expressions consisting of terms that include values of the independent variable as well as values of the independent variable gradients at the control volume faces. The independent variable values and the independent variable gradient values at the control volume faces are in turn

expressed in terms of the independent variable values at the surrounding node points through the use of various interpolation schemes. The result is a set of equations that express the independent variable values at every node point as a function of the surrounding node point independent variable values in a manner consistent with the governing differential equation.

Patankar [80PA1] illustrates the discretisation process described above by considering steady one-dimensional convection and diffusion in the absence of source terms

$$\frac{d}{dx}(\rho u \varphi) = \frac{d}{dx}\left(\Gamma \frac{d\varphi}{dx}\right) \tag{4.12}$$

The discretisation is carried out for the control volume shown in figure 4.1.

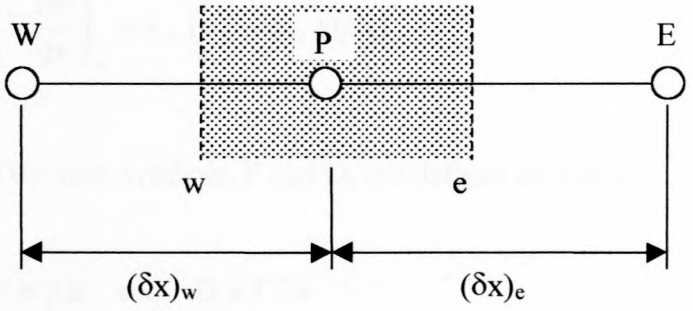

Figure 4.1. Control volume around point P.

It should be noted that although Flo^{++} utilises an unstructured grid formulation, the principles embodied by figure 4.1 and the ensuing discussion are applicable.

Integration of equation (4.12) over the control volume yields the following expression

$$(\rho u \varphi)_e - (\rho u \varphi)_w = \left(\Gamma \frac{d\varphi}{dx}\right)_e - \left(\Gamma \frac{d\varphi}{dx}\right)_w \tag{4.13}$$

where e and w denote the eastern and western control volume faces respectively.

Assuming a piece-wise linear profile through points W, P and E where $(\delta x)_w = (\delta x)_e$, the following expressions for the independent variable values and independent variable gradient values at the control volume faces result

$$\varphi_e = (\varphi_E + \varphi_P)/2$$
$$\varphi_w = (\varphi_P + \varphi_W)/2 \qquad (4.14)$$

and

$$\left(\Gamma \frac{d\varphi}{dx}\right)_e = \Gamma_e (\varphi_E - \varphi_P)/(\delta x)_e$$
$$\left(\Gamma \frac{d\varphi}{dx}\right)_w = \Gamma_w (\varphi_P - \varphi_W)/(\delta x)_w \qquad (4.15)$$

Two new symbols, F and D, are defined as follows

$$F \equiv \rho u \quad \text{and} \quad D \equiv \Gamma/\delta x \qquad (4.16)$$

Substituting equations (4.14) and (4.15) into equation (4.13) and using the definitions expressed in equation (4.16) the following discretisised form of equation (4.12) results

$$a_P \varphi_P = a_E \varphi_E + a_W \varphi_W \qquad (4.17)$$

where

$$a_E = D_e - F_e/2$$
$$a_W = D_w + F_w/2 \qquad (4.18)$$
$$a_P = D_e + F_e/2 + D_w - F_w/2 = a_E + a_W + (F_e - F_w)$$

4.3.2. Discretisation practices

In the discretisation of equation (4.12) use was made of a linear interpolation scheme between nodes to determine the independent variable values and the independent variable gradient values at the control volume faces. This interpolation scheme is referred to as a central difference scheme (CDS) and is said to be of second order accuracy. The CDS can be formulated using a truncated Taylor series where only the first three terms are considered and as a result is said to be of second order accuracy.

In practice the choice of a discretisation scheme is a compromise between accuracy, boundedness, numerical stability and required computer processing time. The boundedness of a discretisation scheme refers to the ability of the scheme to yield interpolated values of the independent variable between node points that are physically realistic. In the case of equation (4.12) boundedness of the discretisation scheme implies that control volume face values of ϕ must fall within the maximum and minimum limit set by the immediate up- and downstream nodal values of ϕ. Numerical stability refers to the ease with which a converged solution of the discretized equations is obtained.

First order discretisation schemes, like the upwind difference scheme UDS (also referred to as the donor-cell method), are unconditionally stable, bounded and require the least computer processing power. These schemes are however numerically diffuse, i.e. the error introduced by these schemes have as a net effect an increase in the coefficient of diffusion. This phenomenon is often referred to as false or numerical diffusion.

Higher order schemes, on the other hand, are more accurate, but also more complex and, as a result, require more computer processing power. A further disadvantage is that higher order discretisation schemes suffer from unboundedness that could lead to numerical instabilities in especially convection-dominated flows. These numerical instabilities result in oscillations in the independent variable field in regions associated with steep variable gradients and, in extreme cases, even to numerical divergence.

The response to the difficulties associated with the numerical modelling of convection-dominated flows has varied from the defence of existing discretisation schemes to the formulation of involved techniques to maintain the accuracy of high order schemes whilst avoiding unboundedness and numerical instabilities.

In defence of the UDS Patankar [80PA1] notes that the order of accuracy of a discretisation scheme is only meaningful if the variation of the independent variable between nodes conforms to the variation implied by the truncated Taylor series on which the order of accuracy is based. Although this statement might be valid in some instances, there exists an overwhelming body of evidence against the use of the UDS, mainly as a result of its diffuse characteristics in instances where the flow field streamlines are not aligned along a principal axis of the calculation domain and also in regions associated with steep variable gradients [78LE1, 80LE1, 81HA1, 82SM1, 82PO1, 90ZU1, 93TA1 and 96FE1]. In an effort to decrease the error associated with the streamline-to-grid skewness, Raithby [76RA1] introduced the skew up-wind scheme (SUDS) where first order up-winding is used along streamlines in the flow field. Although yielding more accurate solutions than the UDS in some cases [80LE1, 82SM1, 85HU1] the SUDS also introduces false diffusion in regions associated with steep variable gradients [82SM1], as predicted by Leonard [78LE1]. Leonard [78LE1] further comments on the usefulness of the UDS by showing that impractical fine grids are necessary to diminish the influence of false diffusion on solutions obtained by using the UDS.

The CDS is a discretisation scheme of second order accuracy as noted earlier, but suffers from unboundedness and numerical instability at high grid Peclet numbers [80PA1, 96FE1]. The latter is defined as

$$Pe \equiv \frac{\rho u L}{\Gamma} \tag{4.19}$$

where the grid spacing is characterised by L.

Largely based on results obtained from the solution of one-dimensional problems in the absence of source terms, Ferziger and Perić [96FE1] express confidence in the satisfactory performance of the CDS for grid Peclet numbers smaller than 2. Leonard [78LE1], however, is

of the opinion that the criteria used to guarantee the numerical boundedness and stability of the CDS in one-dimensional problems cannot be generalised to two- and three-dimensions.

In response to his criticism of the up-wind and central difference schemes Leonard [78LE1] proposes the QUICK (**Q**uadratic **U**pstream **I**nterpolation for **C**onvective **K**inematics) scheme where a second-degree polynomial is fitted through the central node (point P in figure 4.1) and the two nodes directly upstream of the central node. According to Leonard [78LE1], the QUICK scheme yields results of comparable accuracy to the CDS whilst utilising a coarser grid.

This statement of Leonard [78LE1] should however be seen in the light of the fact that no discretisation scheme, regardless of its degree of complexity, can accurately include the effect of physical flow phenomena that are geometrically smaller than the grid spacing employed. Use of the QUICK scheme on a coarser grid will therefore not necessarily yield results comparable to those obtained with a CDS on a refined grid.

Based on the advantages listed by Leonard [78LE1], the QUICK scheme is the discretization scheme of choice in the numerical analysis that form part of this investigation. Stability problems are remedied through grid refinement and in extreme cases through the combination or blending of the QUICK scheme with an UDS. The latter is accomplished through the introduction of a blending factor that specifies the degree of blending. Blending of the QUICK scheme with an UDS is restricted to the discretisation of the conservation equations for turbulent kinetic energy and the rate of dissipation of turbulent kinetic energy.

4.4. Convergence criteria

As with most other CFD-codes the set of equations resulting from the discretisation of the non-linear partial differential equations that govern fluid flow is solved in an iterative manner by Flo^{++}. By implication the solution obtained after any number of iterations will not completely satisfy the set equations, but will either converge or diverge from the correct solution. As a result it is not only important to decide when the solution is converging or diverging, but in the case of the former also whether the solution is at an acceptable level of

accuracy. It is therefore necessary to define convergence criteria. A necessary but not sufficient convergence criterion is the calculation of normalised residual values.

Equation (4.17) can be rewritten as follows for an unstructured 3-dimensional control volume

$$a_P \varphi_P = \sum_m a_m \varphi_m \tag{4.20}$$

where a_m denotes the diffuse and convective contributions of the adjacent cell volumes and ϕ_m denotes the dependent variable values at the centre of the adjacent cell volumes.

For any given iteration in the solution process a residual, r_ϕ can be calculated for every cell volume in the computational domain. The residual, based on equation (4.20), is given as

$$r_\varphi = a_P \varphi_P - \sum_m a_m \varphi_m \tag{4.21}$$

The normalised absolute residual sum for all the control volumes of the computational domain, R_ϕ, is determined according to

$$R_\varphi = \frac{\sum |r_\varphi|}{M_\varphi} \tag{4.22}$$

where M_ϕ is a normalisation factor.

Table 4.2 displays the normalisation factors used in Flo^{++} for the different dependent variables. In table 4.2 m_i is the mass flow rate associated with a particular inlet boundary, L a characteristic length of the flow domain and v_{nom} a mean inlet velocity. Note that the summation signs in table 4.2 apply to the inlet boundaries of the flow domain alone.

Table 4.2. Normalisation factors.

Equation	Variable, ϕ	Normalisation factor, M_ϕ
Continuity	p	$M_p = \sum_{in} m_i$
Momentum	u, v, w	$M_{u,v,w} = \sum_{in} m_i \left(u_i^2 + v_i^2 + w_i^2\right)^{0.5}$
Turbulence Energy	k	$M_k = \sum_{in} m_i \left(u_i^2 + v_i^2 + w_i^2\right)$
Turbulence Dissipation	ε	$M_\varepsilon = M_k / \left(L/v_{nom}\right)$

The monotonic decrease of the residual values displayed in table 4.2 to values in the order of 10^{-3} combined with insignificant changes in the variable values in critical areas of the flow domain with further iteration, is usually considered an adequate means with which to confirm convergence of the solution.

4.5. Axial flow fan model

Although quite a number of commercially available CFD-codes include special features to accommodate rotating blades, there is a penalty to be paid in terms of computer processing power, computational grid complexity and the time required to obtain a solution. The need for a model that accurately simulates the effect of a particular axial flow fan on the air flow field in the vicinity of the axial flow fan blades without imposing the constraints mentioned earlier, is apparent.

In their numerical analysis of the flow field in chemical agitators, Pericleous and Patel [86PE2] used an actuator disc model to simulate the effect of various forms of agitator blades on the flow field. Of particular interest is their use of the lift and drag characteristics of the agitator blade cross-sectional profiles at different radial stations to calculate the actuator disc forces. The actuator disc forces were expressed as sources/sinks of momentum in the Navier-Stokes equations which were solved using a control volume formulation to yield the chemical agitator flow field. Good agreement is reported between the numerical results and experimental measurements.

A similar actuator disc model that utilises blade element lift and drag characteristics in order to determine the actuator disc forces was developed by Thiart and Von Backström [93TH1] and successfully used to determine the flow field in the vicinity of an axial flow fan subject to distorted inlet flow conditions.

Löstedt [95LO1] simulated the effect of an aircraft propeller on the air flow field around an aircraft using an actuator disc model where the actuator disc forces were determined with a combined momentum-blade element theory. Results compared favourably with experimental data.

Pelletier et al. [86PE1, 88SC1, 91PE1] used actuator disc theory to predict the air flow field in the vicinity of a propeller in free stream. The flow field calculations were performed by solving the Navier-Stokes equations, using a finite element formulation. The calculated actuator disc forces were included in the numerical scheme as momentum sources/sinks. The numerically predicted air flow field compared favourably with experimental data.

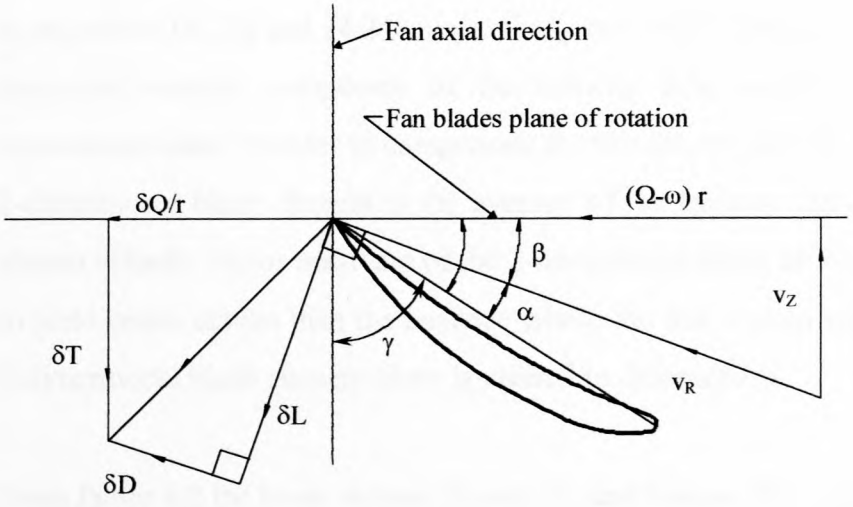

Figure 4.2. Blade element.

In the current investigation the axial flow fan is modelled as an actuator disc. According to Von Mises [45VO1], the force exerted on the fluid stream at any location within the actuator disc is a function of the fluid velocity vector relative to the fan blade, v_R, as well as the lift and drag characteristics of the fan blade cross-sectional profile. Figure 4.2 shows the relative

velocity vector, v_R, as well as the resulting lift, δL, and drag force, δD, on a blade element at a fan blade radius r.

The lift and drag force are determined according to

$$\delta L = \frac{1}{2}\rho|v_R|^2 C_l \cdot c_{Fb} \cdot \delta r \tag{4.23}$$

$$\delta D = \frac{1}{2}\rho|v_R|^2 C_d \cdot c_{Fb} \cdot \delta r \tag{4.24}$$

where C_l and C_d are the coefficients of lift and drag respectively, c_{Fb}, the fan blade chord length and δr the blade element radial thickness. It should be noted that the relative velocity vector, v_R, is the average of the fan blade leading edge and trailing edge velocity vectors.

The velocity field encountered by the 2-dimensional blade elements of the axial flow fan model differs considerably from the uniform velocity field for which the lift and drag coefficients used in equations (4.23) and (4.24) respectively are valid. The most notable difference being the tangential velocity component of the velocity field on the 2-dimensional blade element downstream side. In order to compensate for this discrepancy the relative velocity vector at the 2-dimensional blade element is the average of the trailing edge velocity vector and the free-stream velocity vector upstream of the 2-dimensional blade element. This arrangement is found to yield better results than the instance where the free stream velocity vector upstream of the 2-dimensional blade element alone is utilised to determine v_R.

From figure 4.2 the blade element thrust, δT, and torque, δQ, is given as

$$\delta T = \delta L \cdot \cos\beta - \delta D \cdot \sin\beta \tag{4.25}$$

$$\delta Q = (\delta L \cdot \sin\beta + \delta D \cdot \cos\beta) \cdot r \tag{4.26}$$

where β is the angle between the relative velocity vector, v_R, and the fan blade plane of rotation.

The blade forces are expressed as momentum sources/sinks in equation (4.2) and the blade element thrust and torque need therefore be expressed as force per unit volume. It follows that

$$\frac{\delta T}{\delta V} = \frac{n_{Fb} \cdot \delta T}{2\pi r \cdot \delta r \cdot t_{Fr}} = \frac{\sigma \cdot \delta T}{c_{Fb} \cdot \delta r \cdot t_{Fr}} \tag{4.27}$$

$$\frac{\delta Q}{\delta V} = \frac{n_{Fb} \cdot \delta T}{2\pi r \cdot \delta r \cdot t_{Fr}} = \frac{\sigma \cdot \delta Q}{c_{Fb} \cdot \delta r \cdot t_{Fr}} \tag{4.28}$$

where $\sigma = c_{Fb}n_{Fb}/2\pi r$ is the solidity ratio of the fan, t_{Fr} the average fan rotor thickness in the fan axial direction and n_{Fb} the fan blade rotational speed.

Substitution of equations (4.23) to (4.26) into equations (4.27) and (4.28) yields

$$\frac{\delta T}{\delta V} = \frac{1}{2}\rho \overline{v_R}^2 \frac{\sigma}{t_{Fr}}\left(C_l \cdot \cos\beta - C_d \cdot \sin\beta\right) \tag{4.29}$$

$$\frac{\delta Q}{\delta V} = \frac{1}{2}\rho \overline{v_R}^2 \cdot r \cdot \frac{\sigma}{t_{Fr}}\left(C_l \cdot \sin\beta + C_d \cdot \cos\beta\right) \tag{4.30}$$

It only remains to calculate the coefficient of lift and drag to resolve equations (4.29) and (4.30). Within a specified range of Mach numbers the lift and drag characteristics of a profile section is a function of the Reynolds number and angle of attack, α, alone. With the angle between the fan blade chord and the plane of rotation of the fan blades, referred to as the stagger angle, γ, known at a particular radial station, the angle of attack can be calculated according to

$$\alpha = \gamma - \beta \tag{4.31}$$

The fan model is used to simulate numerically the operation of an axial flow fan of which the detailed geometric characteristics are known. Details pertaining to the investigation are contained in Appendix C. From the investigation it is concluded that the fan model yields results of an acceptable level of accuracy provided that the air flow direction across the fan blades does not deviate dramatically from the fan blade tangential direction and that volume flow rate regimes associated with flow separation across the fan blades are avoided.

4.6. Heat exchanger model

The heat exchanger not only effects a pressure drop in the air flow field, but also directs the flow in a direction parallel to the fins of the heat exchanger finned tubes. These two effects can be adequately simulated through the use of orthotropic porous cells in the volume occupied by the heat exchanger.

The flow is directed in the direction of the heat exchanger finned tube fins by specifying a maximum resistance in the directions orthogonal to the finned tube fins direction. The porosity in the finned tube fins-direction is in turn related to the average air velocity through the heat exchanger as well as the angle of incidence of the incoming flow with respect to the heat exchanger.

According to Van Aarde and Kröger [93VA1], the pressure drop across a heat exchanger inclined at an angle to the incoming, uniform air flow field shown in figure 4.3 can be expressed as the sum of the following dimensionless pressure loss coefficients

$$K_\theta = \frac{\Delta p_t}{1/2\rho v_{HE}^2} = K_{i\theta} + K_f + K_e + K_{dj} + K_o \qquad (4.32)$$

where Δp_t is the total pressure drop across the heat exchanger, v_{HE} the average air velocity through the heat exchanger, K_θ the dimensionless total pressure loss coefficient, $K_{i\theta}$ the inlet loss coefficient, K_f the frictional loss coefficient, K_e the exit loss coefficient, K_{dj} the jetting loss coefficient and K_o the outlet kinetic energy loss coefficient. The heat exchanger model has to simulate the inlet, frictional and exit losses adequately.

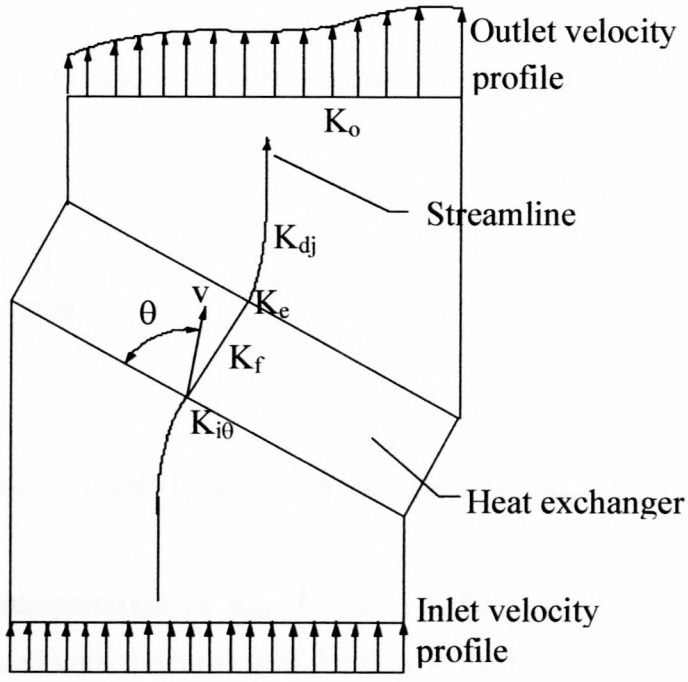

Figure 4.3. Heat exchanger model.

Mohandes [84MO1] found that for finned tubes with a finite fin thickness the inlet loss coefficient is given by

$$K_{i\theta} = \left(K_c^{0.5} + \frac{1}{\sin\theta} - 1 \right)^2 \tag{4.33}$$

where K_c is the inlet contraction loss coefficient, which is a function of the finned tube geometry and θ, the angle defined in figure 4.3.

Substitution of equation (4.33) into (4.32) and setting θ = 90°, finds the following expression after rearrangement

$$K_f + K_e = K_{HE} - K_c \tag{4.34}$$

where K_{HE} is the dimensionless total pressure loss coefficient of the heat exchanger under normal flow conditions.

Substitution of equations (4.33) and (4.34) into equation (4.32) yields the following expression for K_θ

$$K_\theta = \left(\frac{1}{\sin\theta} - 1\right)\left[2K_c^{0.5} + \left(\frac{1}{\sin\theta} - 1\right)\right] + K_{HE} + K_{dj} + K_o \qquad (4.35)$$
$$= K_{turn} + K_{he} + K_{dj} + K_o$$

where $K_{turn} = (1/\sin\theta\text{-}1)[2K_c^2+(1/\sin\theta\text{-}1)]$ is the dimensionless turning loss coefficient.

Note that the physical interpretation of K_{turn} becomes difficult since this coefficient would include the losses associated with the turning of the flow in the fin tube fin-direction as well as any changes in the K_c-value due to the oblique flow into the heat exchanger. Closer scrutiny of the experimental investigation of heat exchanger inlet flow losses contained in Appendix A reveals that the $(K_\theta - K_{\theta=90^\circ})$-value calculated for the different heat exchanger bundles tested is equivalent to K_{turn}.

From equation (4.35) it follows that the proposed heat exchanger model must account for the first two terms on the right-hand side of equation (4.35). Flo^{++} models the pressure drop characteristics of a porous medium with the following expression

$$-K u_\xi = \frac{\partial p}{\partial \xi} \qquad (4.36)$$

where ξ is, in this instance, interpreted as a direction parallel to the heat exchanger finned tube fins. The permeability in the ξ - direction, K, is expressed as a linear function of the average velocity in the ξ - direction, u_ξ, so that

$$K = \alpha\left|u_\xi\right| + \beta \qquad (4.37)$$

where the values of α and β are specified by the user.

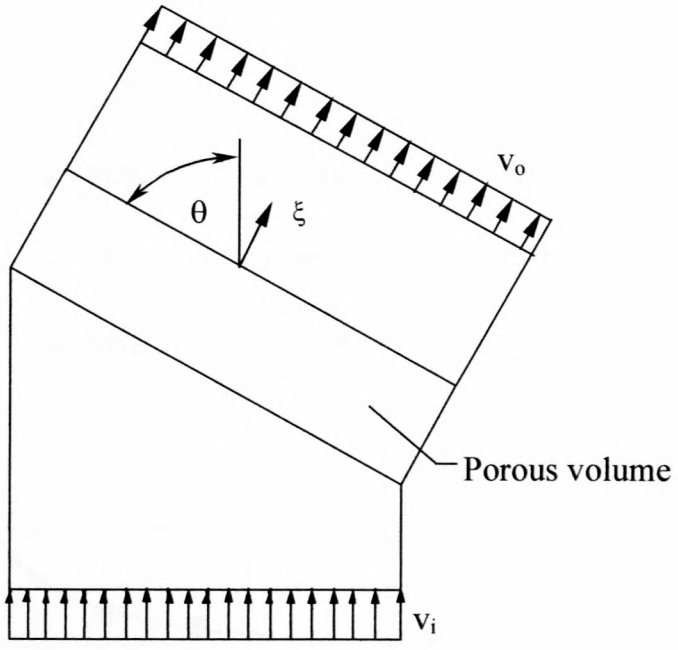

Figure 4.4. Analytical model of porous cell volume.

Figure 4.4 is an analytical model for the flow through a porous cell volume of the type used in Flo^{++}. A uniform inlet and outlet velocity profile is assumed. If the permeability, K, of the porous cell volume should assume a zero value, it follows from equation (4.36) that the pressure at the porous cell volume inlet face and outlet face should be equal in magnitude. K_{turn} can now be calculated for the porous cell volume, noting that the outlet velocity, v_o is related to the inlet velocity as follows

$$v_i = v_o/\sin(\theta) \tag{4.38}$$

K_{turn} is given as

$$K_{turn} = (p_{ti} - p_{to})/(0.5\rho.\,{}^{2}_{o}) = (v_i^2 - v_{oi}^2)/v_o^2 = 1/\tan^2(\theta) \tag{4.39}$$

Figure 4.5 contrasts $K_{turn}=(K_{\theta}- K_{\theta=90^{\circ}})$ for all the different heat exchanger bundles tested in the experimental investigation contained in Appendix A with K_{turn} determined according to equation (4.39).

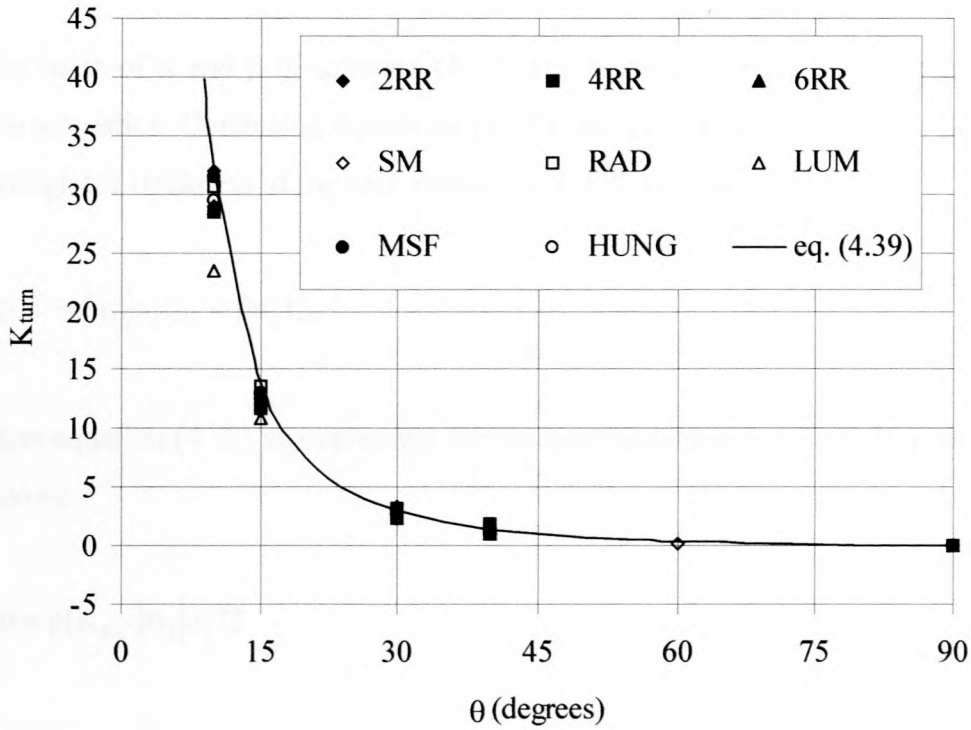

Figure 4.5. K_{turn} as a function of θ.

From figure 4.5 it is clear that K_{turn} determined according to equation (4.39) closely resembles the K_{turn}-values determined from the experimental investigation.

From the above it follows that no additional terms need to be included in the heat exchanger model to include the turning losses associated with the different heat exchanger bundles. The heat exchanger model needs only account for the normal pressure loss through the heat exchanger.

The K_{HE} - value of a heat exchanger is determined experimentally and is usually displayed in the following form

$$K_{HE} = a \cdot Ry^{b} \qquad (4.40)$$

where a and b are constants and Ry is the characteristic flow parameter defined as

$$Ry = (\rho v_{HE})/\mu \tag{4.41}$$

The value of α and β in equation (4.37) are dependent on the heat exchanger pressure drop characteristics. Combining equations (4.36) and (4.37) and assuming a linear pressure drop through the thickness of the heat exchanger, it follows that

$$\Delta p = -\alpha|u_\xi|u_\xi t_{HE} - \beta u_\xi t_{HE} \tag{4.42}$$

From equation (4.32) an expression for the heat exchanger pressure drop can be formulated as follows

$$\Delta p = \rho(K_{HE})|u_\xi|u_\xi/2 \tag{4.43}$$

Comparison of equations (4.42) and (4.43) yields the following expressions for α and β

$$\alpha = (K_{HE})\rho/(2t_{he})$$
$$\beta = 0 \tag{4.44}$$

From equation (4.37) it can be seen that for β=0 K$\rightarrow$0 as $|u_\xi| \rightarrow 0$, which leads to a potentially unstable situation. A value for β is therefore chosen that is sufficiently large to avoid this condition and yet small enough to ensure an accurate pressure drop prediction across the heat exchanger.

In the directions normal to the ξ-direction, large values are specified for α and β, effectively forcing the flow in the desired direction.

4.7. Computational grids

The construction of the computational grids used during the course of the numerical investigation was a compromise between the maximum number of computational cells that could be supported by the computational platform (approximately 500 000 cells), the stability of the solution process and the level of detail required with regard to the resolved flow field.

From the discussion in section 4.3.2 it is clear that the discretisation scheme used will, too a large degree, dictate the grid spacing used and, ultimately, also the number of computational cells comprising the grid. As mentioned earlier, the QUICK discretisation scheme of Leonard [78LE1] was employed for the duration of the numerical investigation. The high-order accuracy of this discretisation scheme necessitated a considerable amount of grid refinement in areas associated with high variable value gradients.

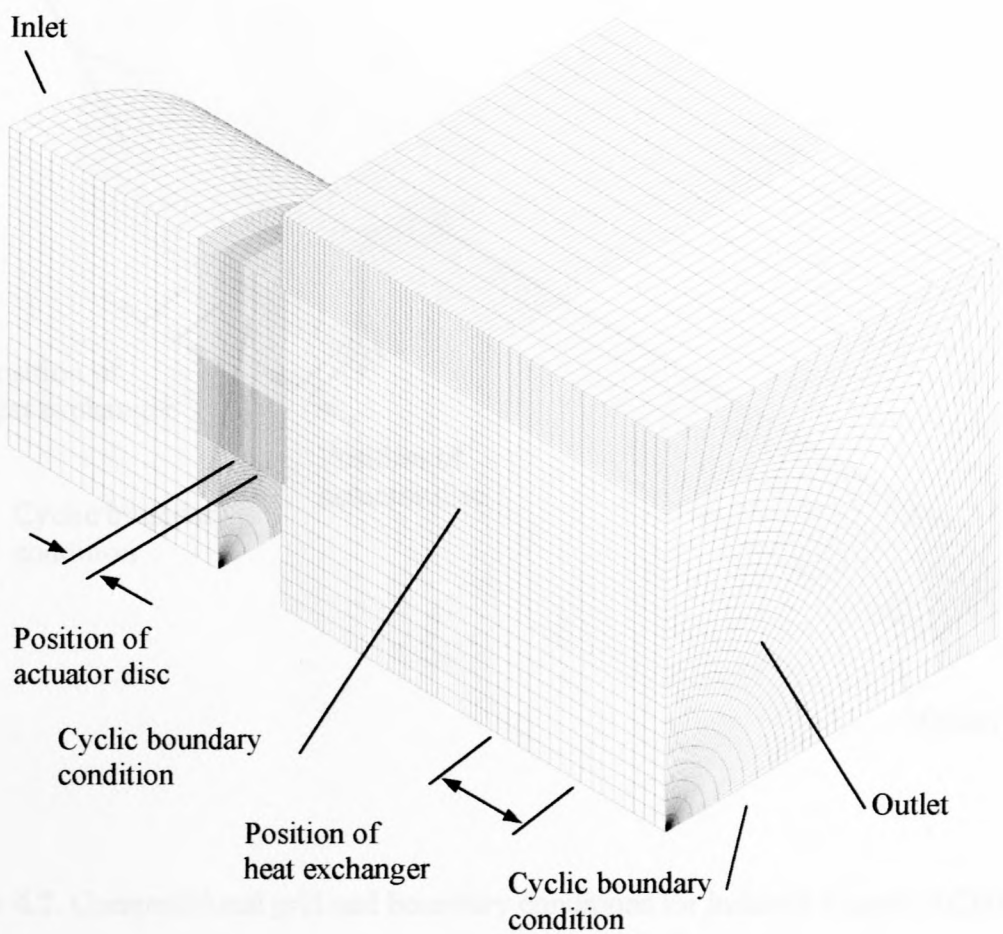

Figure 4.6. Computational grid and boundary conditions for forced draught ACHEs.

The computational grids used during the course of the numerical investigation were constructed in such a way as to ensure a stable solution process until the convergence criteria stated in section 4.4 was met. In most instances further grid refinement had no observable influence on the numerical results.

Figures 4.6 and 4.7 display examples of the computational grids used to numerically investigate forced and induced draught ACHEs respectively. In both instances it was only necessary to model a quarter segment of the geometry due to the axisymmetric nature of the numerical problem.

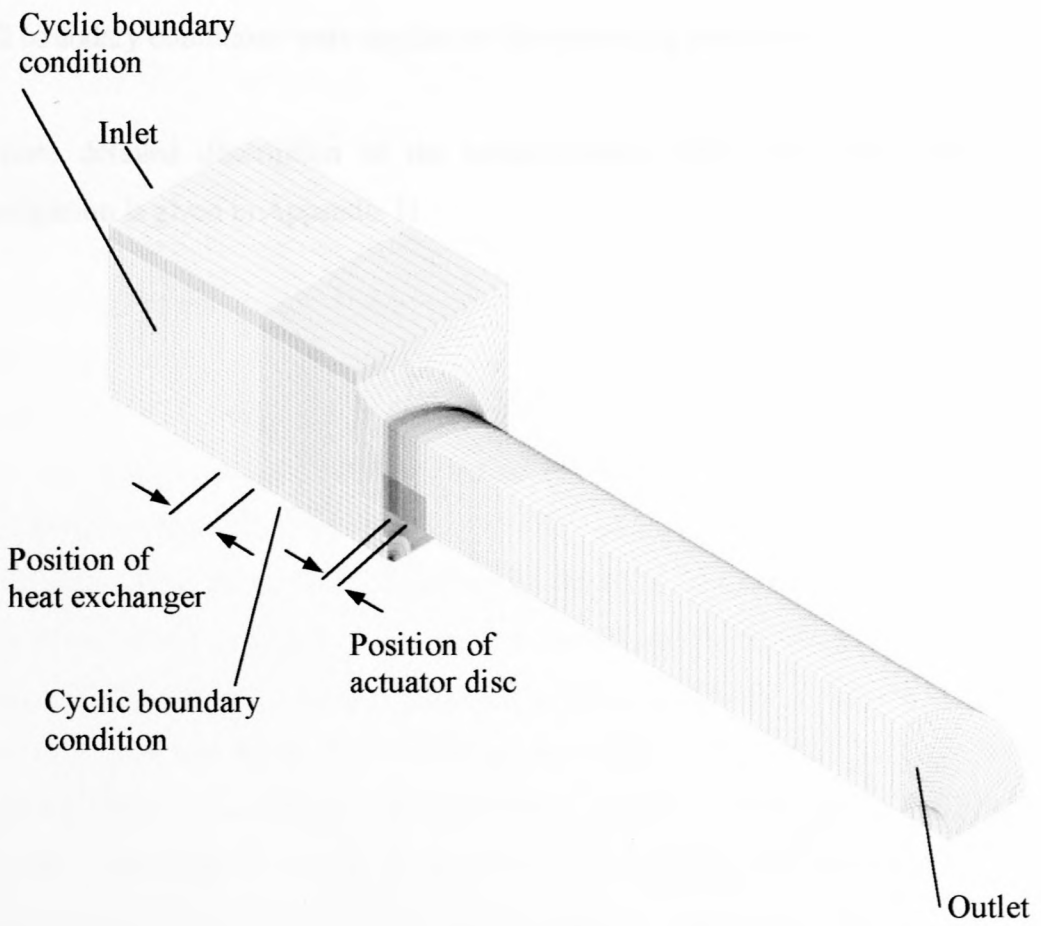

Figure 4.7. Computational grid and boundary conditions for induced draught ACHEs.

At the inlet boundary a constant and uniform velocity field as well as constant values for the turbulent kinetic energy, k, and rate of dissipation of turbulent kinetic energy, ε, was specified. All variable gradient values at the outlet boundary were assumed to be constant. The axisymmetric nature of the flow field was enforced through the application of cyclic boundaries to the grid faces designated in figures 4.6 and 4.7.

Cyclic boundaries are pairs of geometrically identical boundary faces where the flow is repeated. The latter implies that scalar values, like temperature and pressure for example, are identical at the corresponding points of a cyclic boundary pair and that the Cartesian velocity components are also identical, apart from being rotated to ensure the same orientation relative to each of the boundary faces comprising the cyclic boundary pair.

Wall boundary conditions were applied to the remaining boundaries.

A more detailed description of the computational grids used during the course of the investigation is given in Appendix H.

CHAPTER 5 - The influence of axial flow fan operation on the plenum chamber aerodynamic behaviour associated with forced draught ACHEs

In Chapter 2 of this text much is made of the fact that the performance characteristics of a particular fan as determined in a code fan test facility do not necessarily reflect the performance of the same fan within a fan system such as an ACHE, for example. Daly [84DA1] readily admits that standard fan test codes, and in particular BS 848 [80BS1], do not necessarily provide a comprehensive description of axial flow fan performance. This is largely due to the inability of these test codes to include the effect of the highly three-dimensional nature of the velocity field at the fan exit.

The fact that the air at the fan outlet exits directly into the ACHE plenum chamber gives reason to believe that the plenum chamber flow field and consequently also the ACHE performance characteristics are directly affected by the characteristics of the velocity field at the fan outlet. It is further reasonable to assume that the characteristics of the velocity field at the fan exit is determined by the type of the axial flow fan used as well as its operating conditions.

The air-flow patterns within ACHE plenum chambers have been previously investigated by a number of authors [72LA1, 75TU1, 87BE1, 95DU1]. Lambert et al. [72LA1], Turner [75TU1] and Duvenhage [95DU1] all report the flow patterns within forced draught ACHEs to be characterised by a core of low velocity air above the fan hub extending into the plenum chamber surrounded by a conically shaped column of rotating air expanding into the plenum chamber before reattaching to the plenum chamber walls prior to flowing through the heat exchanger bundle. Similar flow patterns were observed by Berryman and Russel [87BE1], although the column of rotating air was seen to be more cylindrical than conical in shape with no reattachment to the plenum chamber walls. In comparing their results with those of Lambert et al. [72LA1], Berryman and Russel [87BE1] attribute the formation of a cylindrical as opposed to a conical column of rotating air in the plenum chamber to the differences in the axial flow fans used. Lambert et al. [72LA1] used a narrow chord axial flow fan whereas

Berryman and Russel [87BE1] used a broad chord fan. The latter is believed to generate smaller radial flow components than the narrower chord variants.

Meyer [96ME1] experimentally investigated a range of forced draught ACHEs in which different axial flow fans were utilised. The results of the experimental investigation [96ME1] indicate that some of the axial flow fans tested are more sensitive to changes made to the ACHE geometry than others. Meyer [96ME1] also showed that the K_{rec}-values associated with geometrically identical ACHEs utilising different axial flow fans vary dramatically.

It is clear that differences in the plenum chamber flow field and consequently in ACHE performance can be directly attributed to the operation of the axial flow fan. In this chapter the plenum chamber flow field characteristics observed during the course of the numerical investigation are compared with those observed by previous investigators [72LA1, 75TU1, 87BE1, 95DU1]. The influence of different axial flow fan configurations on the plenum chamber flow field and consequently the performance characteristics of a range of forced draught ACHEs are also investigated.

5.1. Characterisation of forced draught ACHEs

In order to differentiate between the different ACHEs investigated, it becomes necessary to formulate a criterion by which ACHEs can be characterised. An obvious choice for such a criterion is the geometrical features of the ACHEs investigated. It would however become increasingly difficult to use geometrical features alone in the characterisation of the axial flow fan as well as the heat exchanger bundle employed in a specific ACHE, as these components are geometrically complex (different cross-sectional blade profiles are utilised, blade twist as a function of radial position varies for different fans, a wide range of different finned tubes are used in heat exchanger bundles, etc.). As a result a combination of the geometrical features of an ACHE as well as the actual performance characteristics of the axial flow fans and heat exchanger bundles utilised in the ACHE are used to characterise these components and consequently the particular ACHE in question.

Forced draught ACHE geometrical characteristics

Figure 5.1 is a schematic representation of a forced draught ACHE displaying the relevant geometrical characteristics. This includes the fan casing diameter, d_{FC}, the heat exchanger bundle height, H_{HE} and breadth, B_{HE}, the plenum chamber height, H_{PC} and the position of the axial flow fan within the fan ring denoted by the length between the fan blade tip trailing edge and the surface defining the plenum chamber inlet, L_{te}.

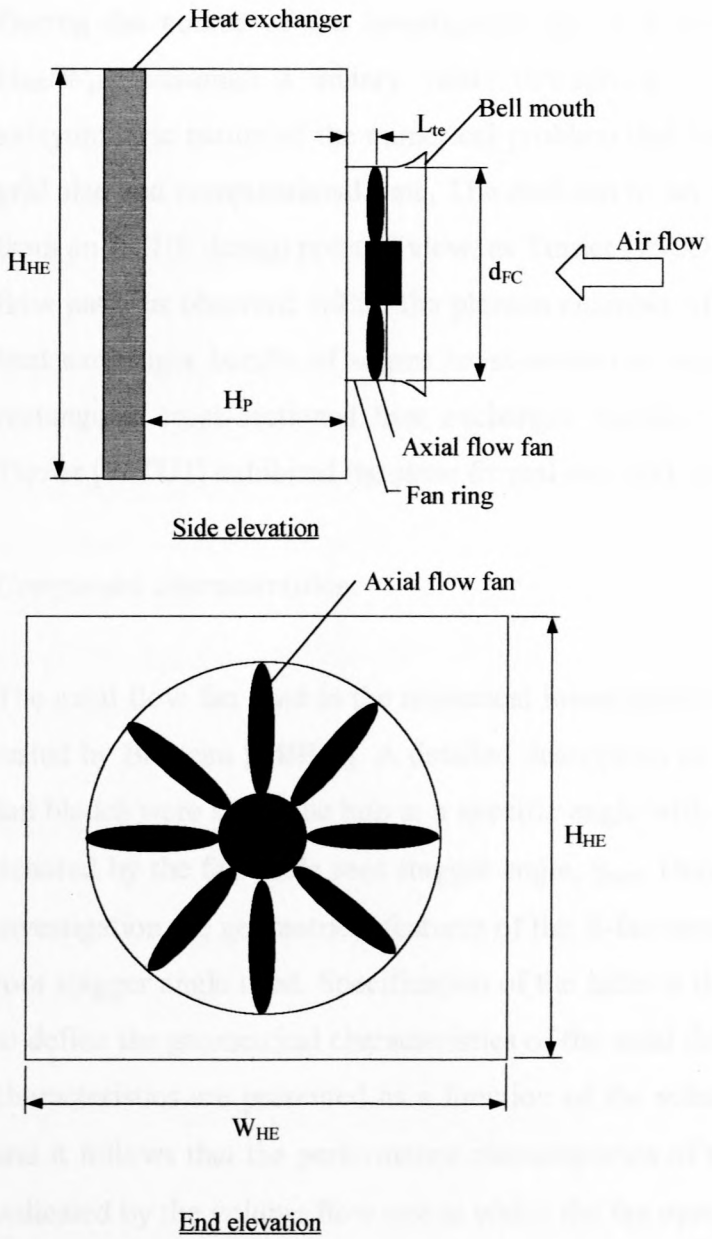

Figure 5.1. Geometrical characteristics of a typical forced draught ACHEs.

The following dimensionless groups are defined utilising these geometrical characteristics:

- the plenum chamber height is expressed as a fraction of the fan casing diameter, H_P/d_{FC}
- the fan casing to heat exchanger frontal area ratio, A_{FC}/A_{HE}
- the position of the axial flow fan within the fan ring is expressed as a fraction of the fan casing diameter, L_{te}/d_{FC}
- the heat exchanger bundle height to width ratio, H_{HE}/W_{HE}.

During the course of the investigation the heat exchanger bundle height to width ratio, H_{HE}/W_{HE}, assumed a unitary value throughout. This was done to exploit the ensuing axisymmetric nature of the numerical problem that lead to significant reductions in terms of grid size and computational time. The decision to set $H_{HE}/W_{HE}=1$ is not totally without merit from an ACHE design point of view, as Turner [75TU1] reports a marked improvement in the flow patterns observed within the plenum chamber of a forced draught ACHE that utilised a heat exchanger bundle of square cross-section as opposed to an ACHE that made use of a rectangular cross-sectioned heat exchanger bundle. The heat exchanger bundles tested by Turner [75TU1] exhibited the same frontal area and air-flow resistance.

Component characteristics

The axial flow fan used in the numerical investigation is the eight-bladed B-fan designed and tested by Bruneau [94BR1]. A detailed description of the B-fan is given in Appendix C. The fan blades were set in the hub at a specific angle with respect to the fan axis. This position is denoted by the fan blade root stagger angle, γ_{root}. During the course of the current numerical investigation the geometrical features of the B-fan remained unchanged save for the fan blade root stagger angle used. Specification of the latter is therefore an adequate means with which to define the geometrical characteristics of the axial flow fan. The axial flow fan performance characteristics are presented as a function of the volume flow rate as shown in Appendix C and it follows that the performance characteristics of the B-fan for a particular γ_{root}-value are indicated by the volume flow rate at which the fan operates.

As noted in Chapter 2, the heat exchanger bundle pressure drop characteristics are expressed in dimensionless form through the introduction of a dimensionless total pressure loss

coefficient, K_{HE}. Furthermore, in Chapter 4 it is stated that it is customary to express K_{HE} as a function of the characteristic flow parameter, Ry, defined as

$$Ry = (\rho v_{HE})/\mu \tag{4.41}$$

where ρ is the fluid density, v_{HE} the average velocity through the heat exchanger bundle and μ the fluid molecular viscosity.

In Chapter 4 it is also stated that, for a particular heat exchanger bundle, K_{HE} is given as

$$K_{HE} = a \cdot Ry^{b} \tag{4.40}$$

where a and b are constants.

From the above it follows that for a particular heat exchanger bundle K_{HE} can be calculated according to equation (4.40) provided that constants a and b in equation (4.40) as well as the operating point volume flow rate is known. The heat exchanger bundle used in an ACHE can as a result be uniquely characterised through specification of the K_{HE}-value as well as the operating point volume flow rate. Note that it is not necessary to specify the heat exchanger bundle dimensions as these are included in the ACHE geometrical characteristics discussed previously.

5.2. Analysis

The draught equation formulated for the forced draught ACHE shown in figure 2.2 of Chapter 2 is given as

$$\Delta p_{sF} + K_{rec}\rho v_{FC}^2/2 = K_{HE}\rho v_{HE}^2/2 + \alpha_{eHE}\rho v_{HE}^2/2 \tag{2.23}$$

It should however be remembered that neither the K_{rec}-value nor the operating point volume flow rate that satisfies equation (2.23) is known prior to performing an analysis of the flow field through the ACHE. As mentioned in the preceding section, a constant volume flow rate was specified at the inlet boundary of the computational grid of the specific ACHE under

consideration. Since the operating point volume flow rate of the particular forced draught ACHE is unknown, it is very likely that the specified volume flow rate differs from the operating point volume flow rate of the ACHE with the result that equation (2.23) will not be satisfied when using the specified volume flow rate.

The above situation can however be remedied through the introduction of an additional mechanical energy per unit volume term in equation (2.23), so that

$$\Delta p_{sF} + (K_{source} + K_{rec})\rho v_{FC}^2/2 = (K_{HE} + \alpha_{eHE})\rho v_{HE}^2/2 \qquad (5.3)$$

where K_{source} is a dimensionless total pressure source coefficient based on the average velocity through the fan casing.

The physical interpretation of the addition of the term containing K_{source} to equation (2.23) is that a flow device is introduced to the forced draught ACHE that acts as a source of mechanical energy per unit volume as shown schematically in figure 5.2. A positive value for K_{source} is associated with an increase in mechanical energy per unit volume and vice versa.

It should be noted from figure 5.2 that the device that acts as an additional source of mechanical energy per unit volume is located on the fan upstream side and does not alter the velocity field at the fan inlet. Figure 5.2 further indicates that the numerical analysis was confined to the geometry between sections 2 and 4.

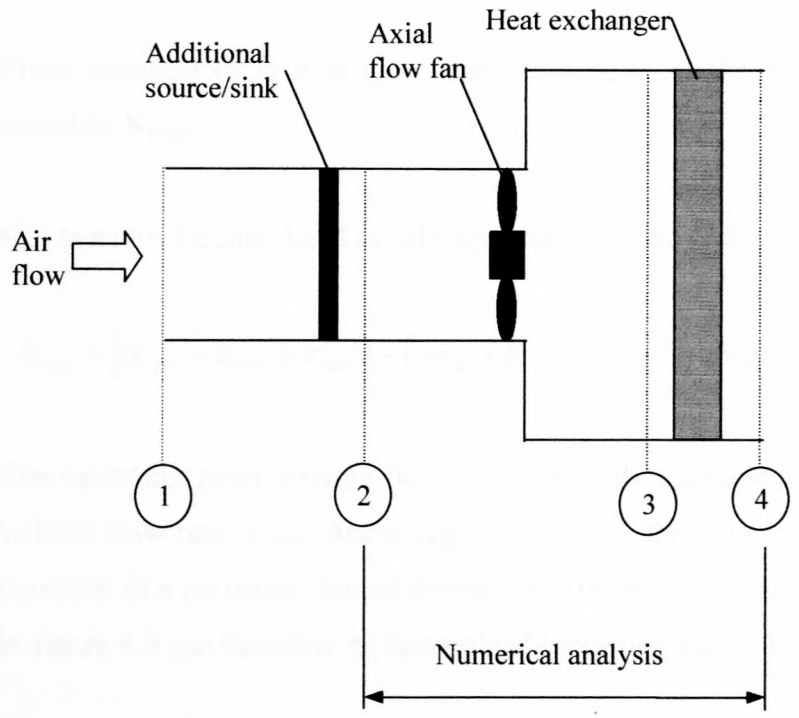

Figure 5.2. Schematic representation of a forced draught ACHE with an additional source/sink of mechanical energy.

A necessary condition to ensure that the specified volume flow rate satisfies equation (5.3) is that the total pressure at section 1 equals the static pressure at section 4 in figure 5.2 so that

$$p_{s1} + \rho v_{FC}^2/2 = p_{s4} \tag{5.4}$$

Upon rearrangement find the following expression for the static pressure at section 1

$$p_{s1} = p_{s4} - \rho v_{FC}^2/2 \tag{5.5}$$

K_{source} is defined as

$$K_{source} = (p_{t2} - p_{t1})/(\rho v_{FC}^2/2) = (p_{s2} - p_{s1})/(\rho v_{FC}^2/2) \tag{5.6}$$

Substitution of equation (5.5) into (5.6) yields the following expression for K_{source}:

$$K_{source} = 1 + (p_{s2} - p_{s4})/(\rho v_{FC}^2/2) \tag{5.7}$$

From equation (5.7) it is clear that the results of the numerical analysis is sufficient to calculate K_{source}.

K_{rec} can now be calculated as follows from equation (5.3)

$$K_{rec} = \left[\left(K_{HE} + \alpha_{eHE}\right)\rho v_{HE}^2/2 - \left(\Delta p_{sF} + K_{source}\rho v_{FC}^2/2\right)\right]/\left(\rho v_{HE}^2/2\right) \tag{5.8}$$

The operating point volume flow rate is usually expressed as a fraction of the conservative volume flow rate, V_{cons}. According to Chapter 2 the latter can be calculated from the draught equation of a particular forced draught ACHE by setting $K_{rec} = 0$. V_{cons} for the ACHE shown in figure 5.3 can therefore be determined by setting $K_{rec} = 0$ in equation (5.3) so that

$$\Delta p_{sF} + K_{source}\rho v_{FC}^2/2 = \left(K_{HE} + \alpha_{eHE}\right)\rho v_{HE}^2/2 \tag{5.9}$$

In Chapter 2 the kinetic energy coefficient, α_e, associated with any cross-section in a flow field, is given as

$$\alpha_e = \frac{1}{m}\int_A \left(v^2/2\right)dm/\left(v_m^2/2\right) = \int_A v^3 dA/\left(Av_m^3\right) \tag{2.4}$$

From the results of the numerical analysis it is possible to calculate the kinetic energy coefficient at the heat exchanger outlet based on the following form of equation (2.4)

$$\alpha_{eHE} = \sum_{i=1}^{N} v_i^3 A_i/\left(V^3/A_{HE}^2\right) \tag{5.10}$$

where N is the number of cell faces associated with the cross-section at the heat exchanger outlet, v_i is the average velocity across the relevant cell faces in the fan axial direction at the heat exchanger outlet and A_i is the cross-sectional area of the cell faces.

5.3. Numerical investigation

Table 5.1. The range of forced draught ACHEs numerically investigated.

No. (-)	γ_{root} (deg)	d_{FC} (m)	L_{te}/d_{FC} (-)	H_{HE} (m)	H_{HE}/W_{HE} (-)	K_{HE} (-)	H_P/d_{FC} (-)	A_{FC}/A_{HE} (-)	V (m^3/s)	K_{source} (-)
1	63.5	1.542	0.0389	1.9	1	24.45	0.4	0.517	10.99	-6.277
2	63.5	1.542	0.0389	1.9	1	24.50	0.4	0.517	11.99	-3.275
3	63.5	1.542	0.0389	1.9	1	24.49	0.4	0.517	12.49	-2.023
4	63.5	1.542	0.0389	1.9	1	24.49	0.4	0.517	12.99	-0.917
5	63.5	1.542	0.0389	1.9	1	24.48	0.4	0.517	13.99	0.984
6	63.5	1.542	0.0389	1.9	1	24.48	0.4	0.517	14.99	2.470
7	63.5	1.542	0.0389	1.9	1	24.47	0.4	0.517	15.99	3.635
8	61	1.542	0.0389	1.9	1	24.48	0.4	0.517	10.99	-8.032
9	61	1.542	0.0389	1.9	1	24.46	0.4	0.517	12.78	-3.269
10	61	1.542	0.0389	1.9	1	24.45	0.4	0.517	14.99	0.648
11	61	1.542	0.0389	1.9	1	24.44	0.4	0.517	16.99	3.050
12	61	1.542	0.0389	1.9	1	24.43	0.4	0.517	18.99	4.730
13	60	1.542	0.0389	1.9	1	24.45	0.4	0.517	10.99	-8.394
14	60	1.542	0.0389	1.9	1	24.50	0.4	0.517	11.99	-5.548
15	60	1.542	0.0389	1.9	1	24.49	0.4	0.517	12.99	-3.287
16	60	1.542	0.0389	1.9	1	24.48	0.4	0.517	13.99	-1.453
17	60	1.542	0.0389	1.9	1	24.48	0.4	0.517	14.99	0.090
18	60	1.542	0.0389	1.9	1	24.47	0.4	0.517	15.99	1.394
19	59	1.542	0.0389	1.9	1	24.50	0.4	0.517	11.99	-5.891
20	59	1.542	0.0389	1.9	1	24.49	0.4	0.517	12.99	-3.658
21	59	1.542	0.0389	1.9	1	24.48	0.4	0.517	13.99	-1.851
22	59	1.542	0.0389	1.9	1	24.48	0.4	0.517	14.99	-0.364
23	59	1.542	0.0389	1.9	1	24.47	0.4	0.517	15.99	0.929
24	58	1.542	0.0389	1.9	1	24.50	0.4	0.517	11.99	-6.191
25	58	1.542	0.0389	1.9	1	24.49	0.4	0.517	12.99	-3.957
26	58	1.542	0.0389	1.9	1	24.48	0.4	0.517	13.99	-2.171
27	58	1.542	0.0389	1.9	1	24.48	0.4	0.517	14.99	-0.683
28	58	1.542	0.0389	1.9	1	24.47	0.4	0.517	16.04	0.605

As mentioned earlier, the performance of an axial flow fan can be affected through a change in either the volume flow rate and/or a change of the blade setting indicated by the γ_{root}-value. The influence of the axial flow fan on ACHE performance can therefore be isolated by keeping the geometrical characteristics of the range of ACHEs tested as well as the associated heat exchanger bundle K_{HE}-values constant whilst treating the operating point volume flow

rate and the γ_{root}-value as variable. Table 5.1 lists the ACHEs that were numerically investigated.

5.5. Discussion of results

The velocity field within the plenum chamber of an ACHE is displayed through the use of 2-dimensional surfaces that intersect the plenum chamber as indicated in figure 5.3. Figure 5.3 is a schematic representation of the ACHE and displays the location and orientation of the 2-dimensional surfaces. The one side of the 2-dimensional surfaces is seen to remain on the ACHE centre line whilst the orientation of the surface is determined by the value θ in figure 5.3.

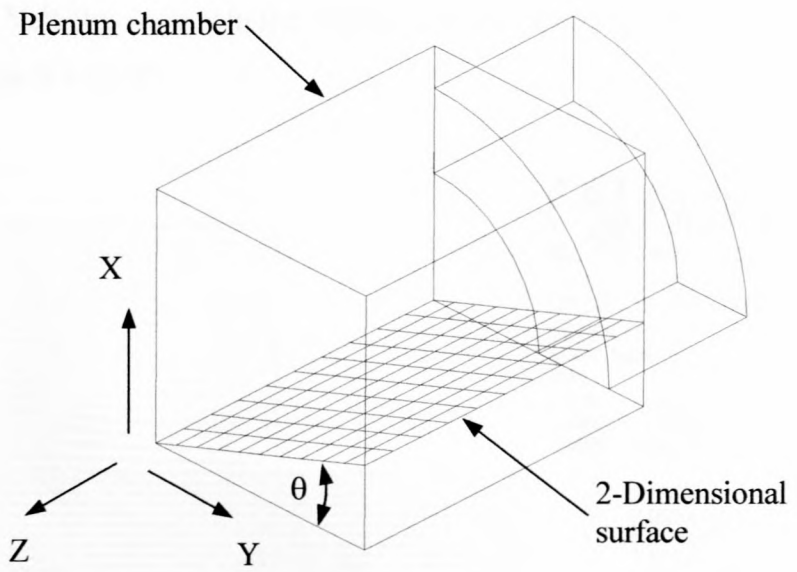

Figure 5.3. Location and orientation of a plenum chamber intersecting 2-dimensional surface.

Figures 5.4 - 5.6 display the velocity vectors associated with three plenum chambers intersecting 2-dimensional surfaces where θ = 22.5°, 45° and 67.5° respectively. In figures 5.4 - 5.6 a region of low velocity air extending into the plenum chamber can be observed in the region above the fan hub confirming the results of previous researchers [72LA1, 75TU1, 87BE1, 95DU1].

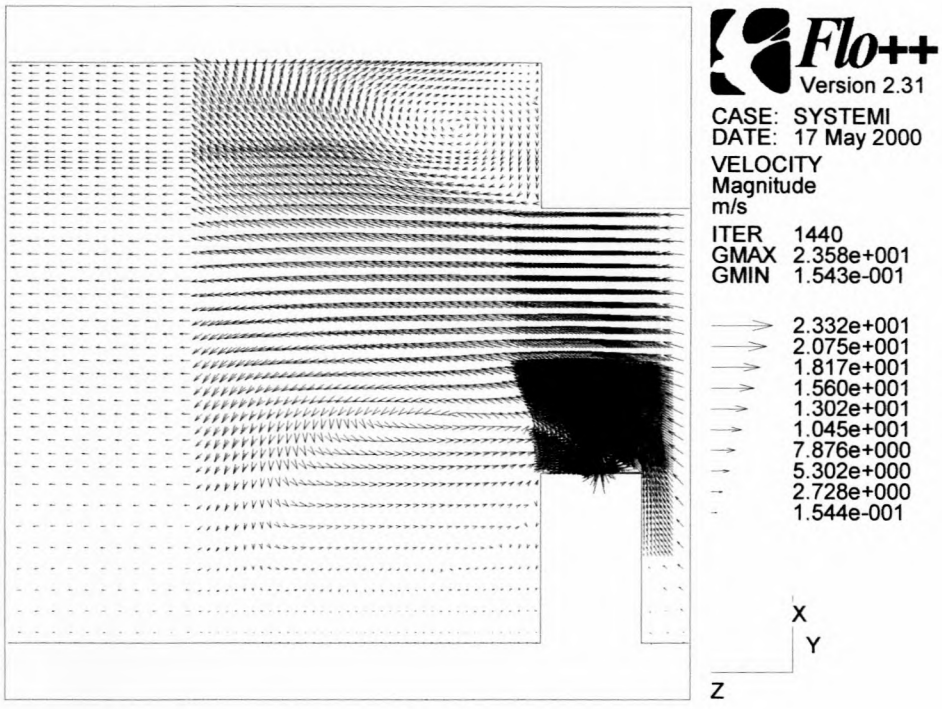

Figure 5.4. Velocity vectors in the plenum chamber of ACHE no. 9 on a 2-dimensional surface where $\theta = 22.5°$.

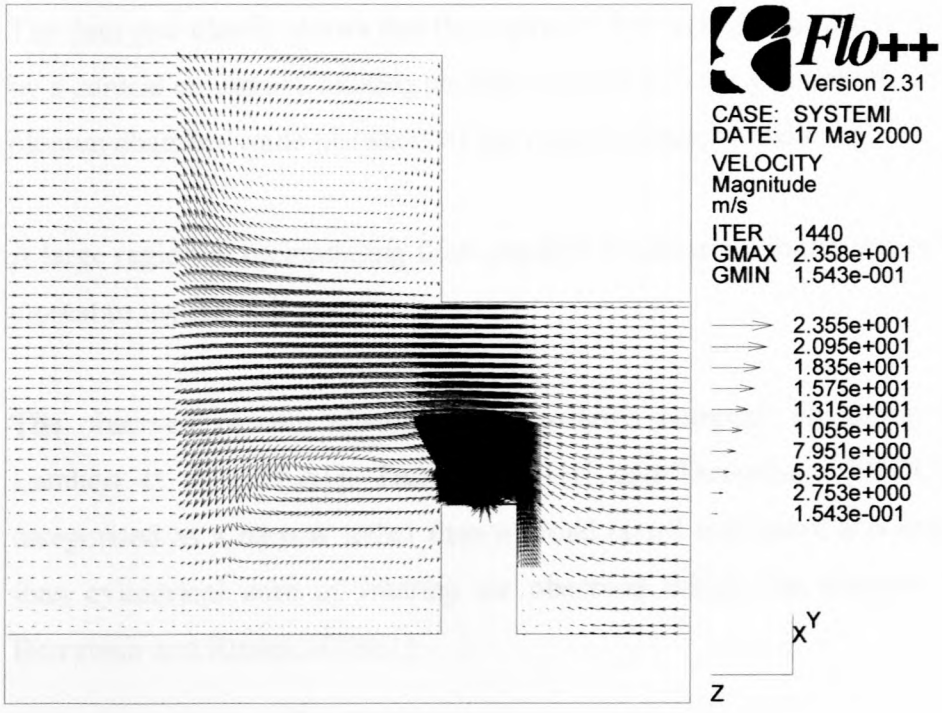

Figure 5.5. Velocity vectors in the plenum chamber of ACHE no. 9 on a 2-dimensional surface where $\theta = 45°$.

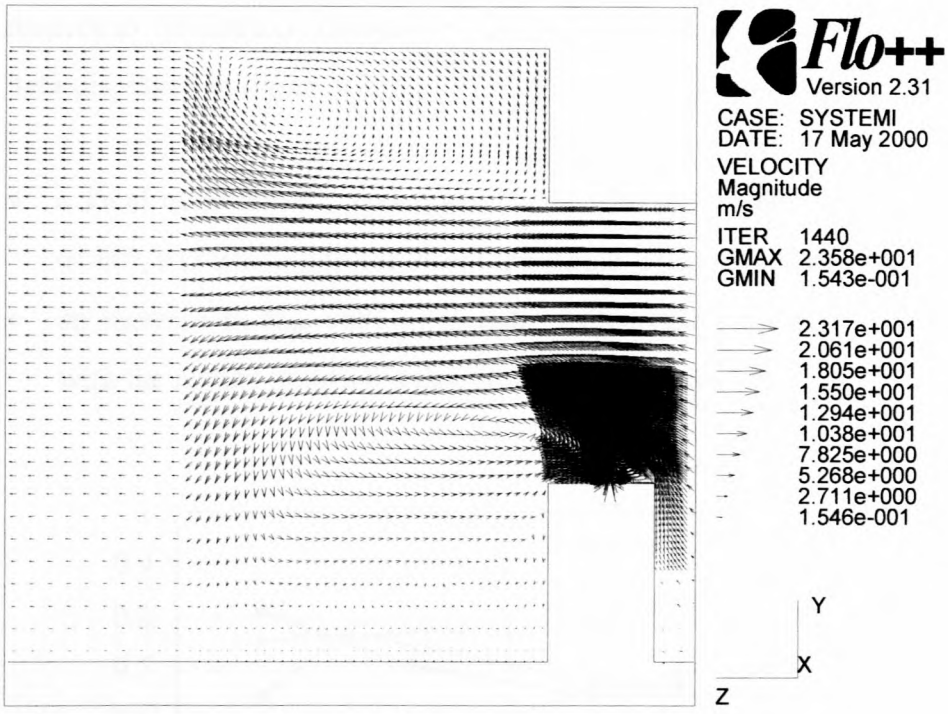

Figure 5.6. Velocity vectors in the plenum chamber of ACHE no. 9 on a 2-dimensional surface where $\theta = 67.5°$.

The data also clearly shows that the region of low velocity air above the fan hub is surrounded by a conical column of rotating air that expands into the plenum chamber and reattaches to the plenum chamber walls just short of the heat exchanger bundle.

A large region of recirculating flow can also be observed in the corner of the plenum chamber closest to the fan exit plane.

The observed plenum chamber flow patterns compare favourably to those observed by Lambert et al. [72LA1], Turner [75TU1] and Duvenhage [95DU1]. The B-fan can be categorised as a narrow rather than a broad chord fan which accounts for the conical rather than cylindrical core of rotating air observed within the plenum chamber, according to Berryman and Russel [87BE1].

Figure 5.7 displays K_{rec} as a function of the operating point volume flow rate, V for the ACHEs tested. The data of figure 5.7 clearly indicates that K_{rec} is a function of both the operating point volume flow rate as well as the position of the axial flow fan blade with

respect to the fan axis denoted by the γ_{root}-value. Two distinct trends can be observed in the data displayed in figure 5.7:

- a local minimum K_{rec}-value associated with the results of ACHEs that utilise γ_{root}-values of 60°, 61° and to a lesser extent the results of ACHEs that utilise a γ_{root}-value of 63.5°
- an increase in K_{rec} with an increase in the operating point volume flow rate associated with the results of ACHEs that utilise γ_{root}-values of 58° and 59°.

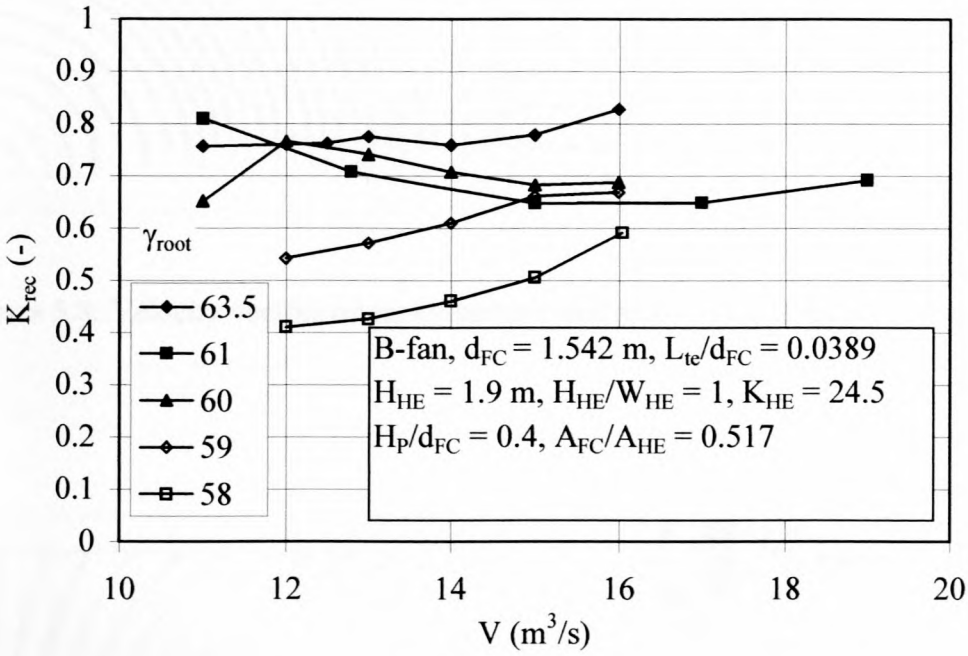

Figure 5.7. The plenum chamber pressure recovery as a function of the operating point volume flow rate.

The trends in the K_{rec}-value data of figure 5.7 are associated with different flow patterns within the plenum chambers of the range of ACHEs investigated. Figures 5.8 and 5.9 display two distinctly different flow patterns associated with xy-surfaces located midway in the plenum chamber of ACHEs no. 1 and 7 respectively. Both ACHEs utilise a γ-value of 63.5° and differ only in their respective operating point volume flow rates where ACHE no. 1 is associated with a low and ACHE no. 7 with a high operating point volume flow rate, as indicated in table 5.1.

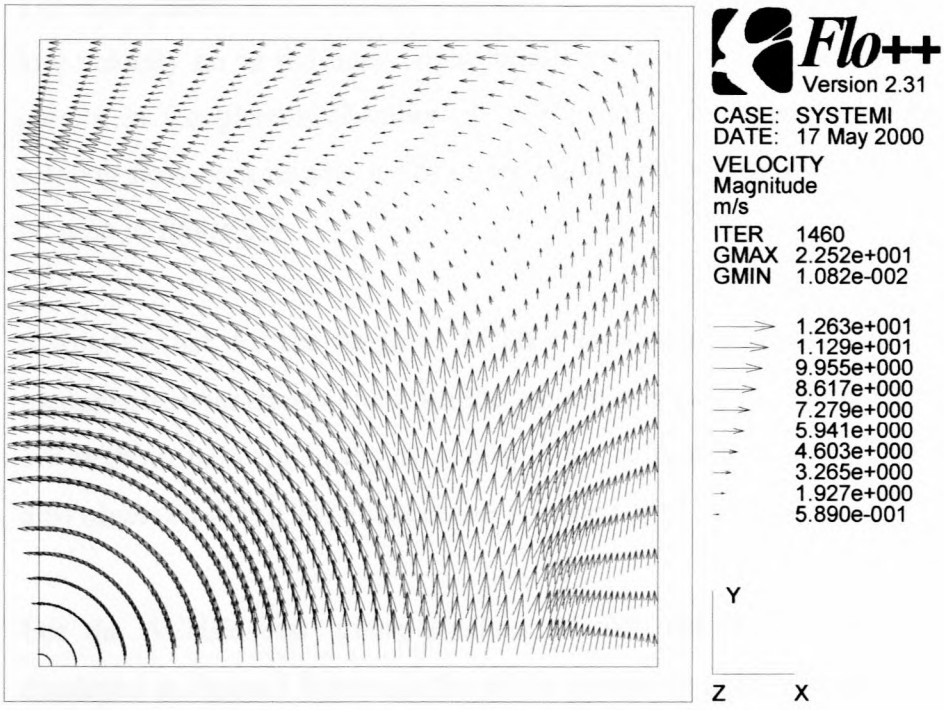

Figure 5.8. Velocity vectors on an xy-surface midway in the plenum chamber of ACHE no.1.

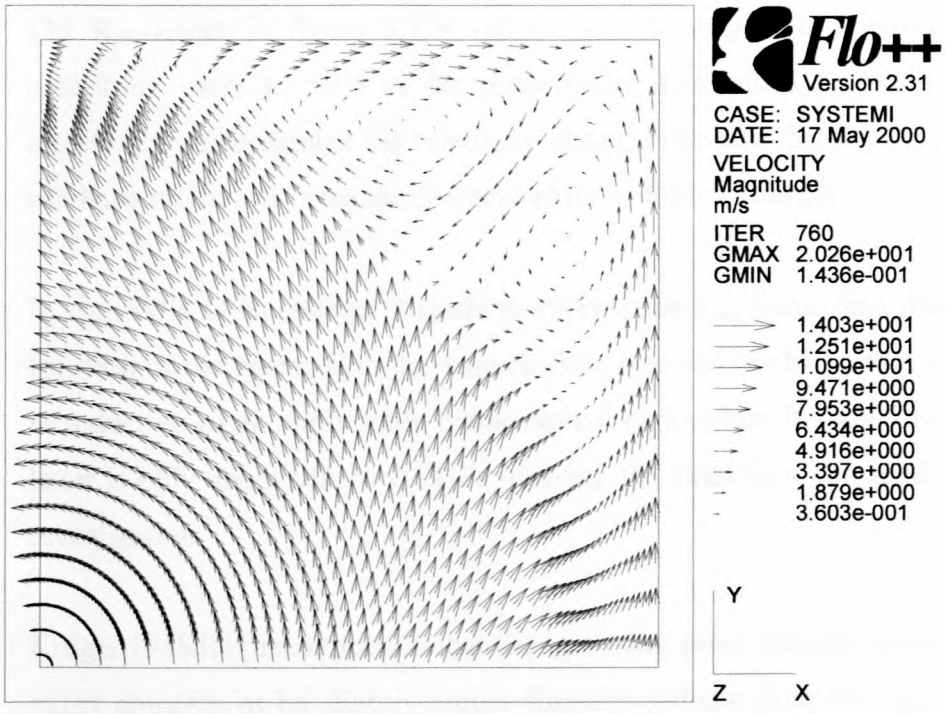

Figure 5.9. Velocity vectors on an xy-surface midway in the plenum chamber of ACHE no.7.

The flow pattern in the plenum chamber of ACHE no. 1 is characterised by a single region of low velocity air in the upper right-hand corner of the 2-dimensional surface whilst the flow pattern in the plenum chamber of ACHE no. 7 is characterised by two adjacent counter-rotating flow regions also in the upper right-hand corner of the 2-dimensional surface, as can be seen in figure 5.9.

It follows that, for the range of ACHEs associated with a γ-value of 63.5°, the flow in the plenum chamber transitions from the pattern observed in figure 5.9 to that displayed in figure 5.9 with an increase in the operating point volume flow rate. This transitional behaviour is also observed for ACHEs that utilise γ-values of 61° and 60°.

For the ACHEs that utilise γ-values of 58° and 59° the plenum chamber flow pattern displayed in figure 5.8 prevails for all the operating point volume flow rates investigated.

The numerical results indicate that the transition from the plenum chamber flow patterns associated with γ-values of 58° and 59° to those associated with γ-values of 60°, 61° and 63.5° occur abruptly in the narrow γ-value range of 59° - 60°.

The K_{rec}-values in figure 5.7 is further seen to vary from approximately 0.4 - 0.8, which constitutes close to 50% of the numerically determined K_{rec}-value range. The last result effectively demonstrates the relatively strong influence that the type of axial flow fan used can have on the performance characteristics of forced draught ACHEs.

In Appendix G an attempt is made to express the K_{rec}-value data displayed in figure 5.7 as a function of the operating point volume flow rate and the blade root stagger angle through the introduction of an appropriate mathematical expression. It should however be noted that the latter is only applicable to ACHEs utilising the axial flow fan used in the current numerical investigation.

Kröger [94KR1] recommends that the operating point volume flow rate of an ACHE should either coincide or be slightly higher than the volume flow rate associated with the point of maximum fan static efficiency. This is done not only to ensure that the axial flow fan operates at the highest possible efficiency, but also to ensure that should the ACHE operating point

volume flow rate decrease due to for example detrimental wind effects an increase in the fan static efficiency will result. This is in line with statements made by Daly [84DA1].

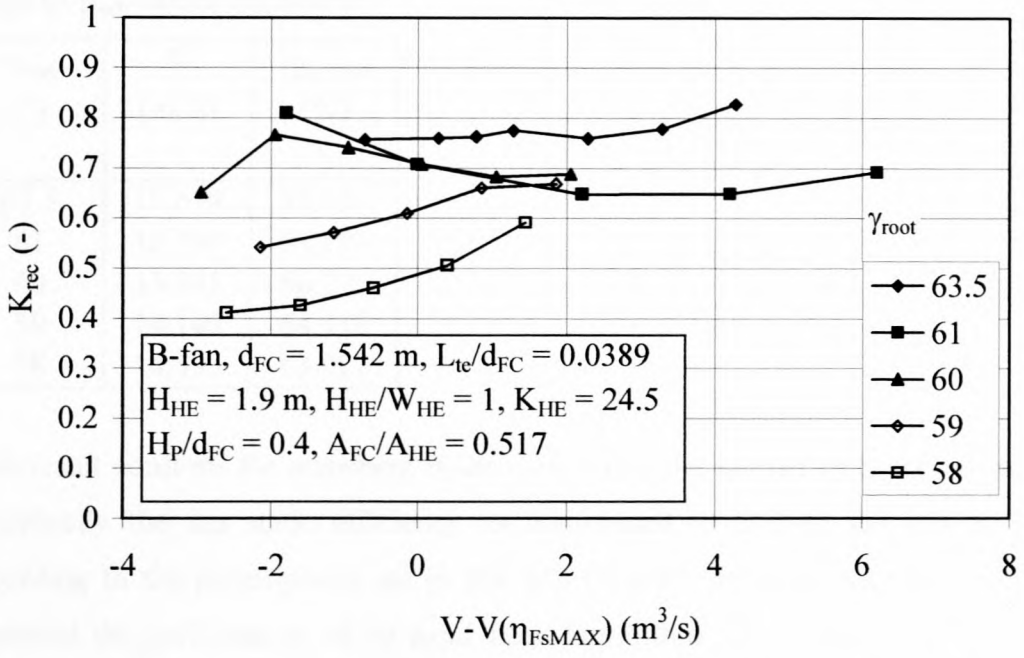

Figure 5.10. The plenum chamber total pressure recovery as a function of the point of maximum fan static efficiency.

Figure 5.10 displays the K_{rec}-value data of figure 5.7 plotted against modified operating point volume flow rate values. The modified operating point volume flow rate values are determined by subtracting the volume flow rate associated with the point of maximum fan static efficiency of the particular fan in use from the operating point volume flow rate of the ACHE under consideration. Table 5.2 lists the maximum fan static efficiency as well as the volume flow rate at maximum fan static efficiency for the range of blade root stagger angles considered.

The point of maximum fan static efficiency is therefore indicated by $(V\text{-}V(\eta_{FsMAX})) = 0$ in figure 5.10 for the range of γ_{root}-values tested.

Figure 5.10 indicates that the point of maximum fan static efficiency does not coincide with the maximum K_{rec}-value for any of the ACHEs associated with a specific γ_{root}-value. For three of the five blade settings tested the K_{rec}-value is seen to increase rather than decrease for operating point volume flow rates slightly higher than those associated with the point of maximum fan static efficiency.

Table 5.2. Maximum fan static efficiency values and the associated volume flow rates for the range of γ_{root}-values considered.

γ_{root} (°)	V (m^3/s)	η_{FsMAX} (%)
63.5	10.679	72.631
61	12.790	67.193
60	13.941	66.221
59	14.140	64.918
58	14.595	63.983

This result confirms the statement made earlier that the fan performance characteristics, and specifically the fan static efficiency as determined in a code fan test facility designed according to the prescriptions set in BS 848 [80BS1] for type A tests, do not necessarily represent the performance of an axial flow fan within a fan system, in this case a forced draught ACHE.

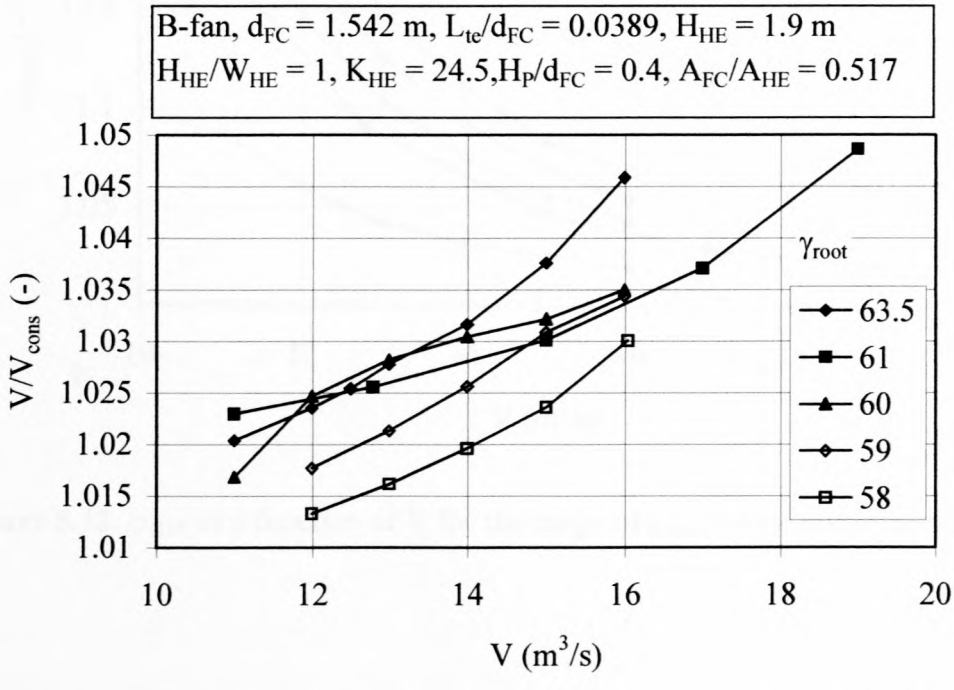

Figure 5.11. V/V_{cons} plotted as a function of the operating point volume flow rate.

Figure 5.11 shows V/V_{cons} as a function of the operating point volume flow rate, V, for the ACHEs investigated. Figure 5.11 indicates that V/V_{cons} increases with an increase in V. In the

analysis of forced draught ACHE performance characteristics of Chapter 3, figure 3.4 shows that for a constant value of K_{rec} V/V_{cons} increases with a decrease in K_{HE}. Table 5.1 indicates that for the respective range of ACHEs associated with the same γ_{root}-value K_{source} increases with an increase in the operating point volume flow rate. From equation (5.3) it follows that an increase in K_{source} is analogous to a decrease in K_{HE}. The latter is seen to account for the increase in V/V_{cons} associated with an increase in V observed in figure 5.11.

Figures 5.12 and 5.13 display α_{eHE} as a function of V and the kinetic energy coefficient at the fan exit, α_{eF}, respectively for the range of γ_{root}-values investigated. Figure 5.12 indicates that α_{eHE} decreases exponentially for an increase in the operating point volume flow rate.

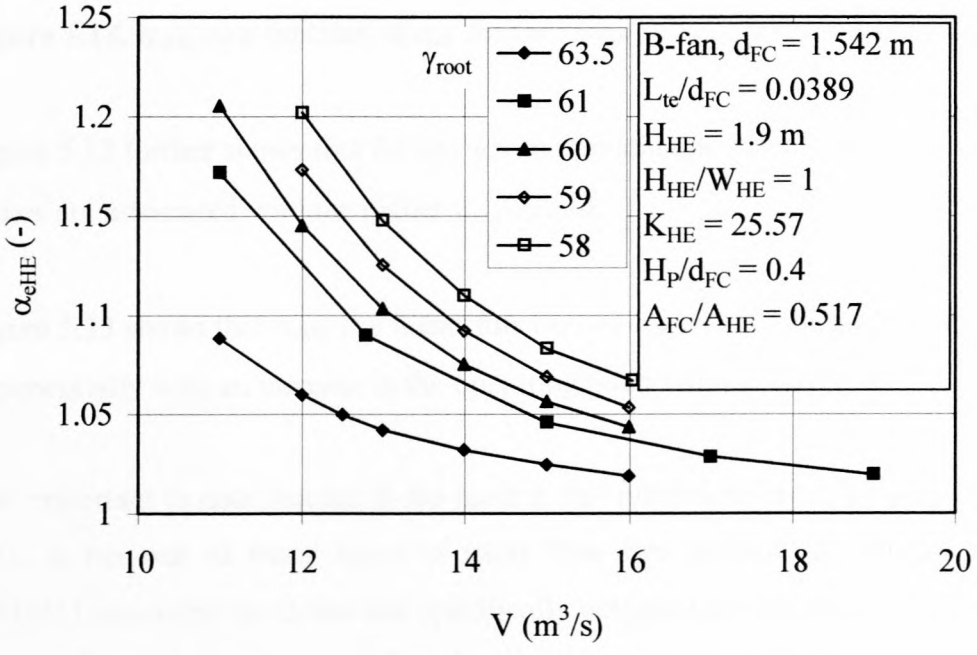

Figure 5.12. α_{eHE} as a function of V for the range of γ_{root}-values investigated.

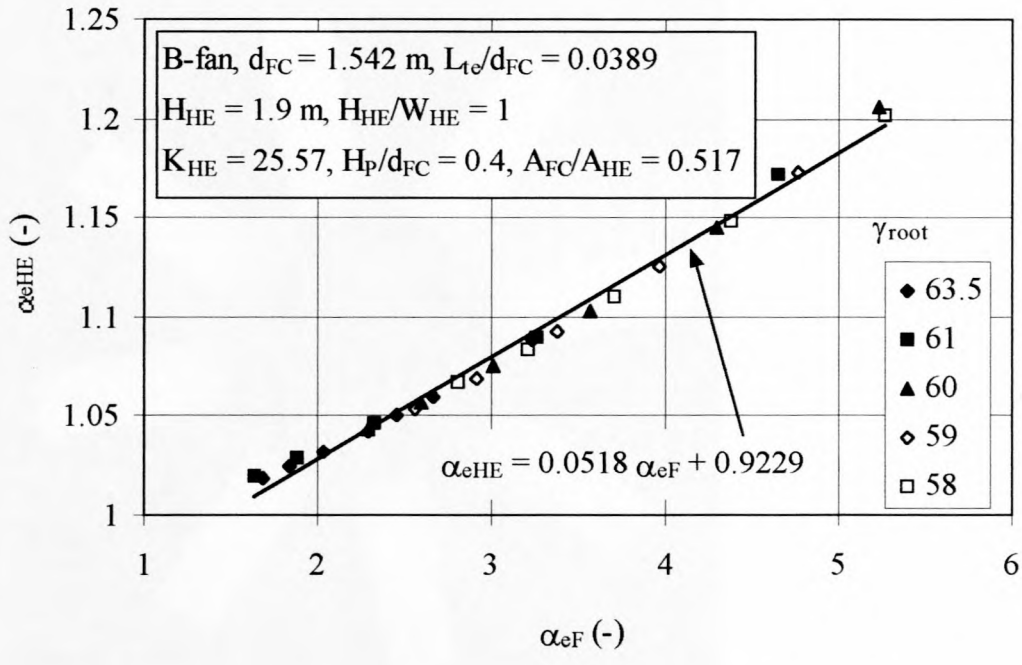

Figure 5.13. α_{eHE} as a function of α_{eF} for the range of γ_{root}-values investigated.

Figure 5.12 further shows that for any given operating point volume flow rate the lower α_{eHE}-values are associated with the higher γ_{root}-values.

Figure 5.13 shows that α_{eHE} is a linear function of α_{eF} which indicates that α_{eHE} also decreases exponentially with an increase in the operating point volume flow rate.

It is important to note that the B-fan used in this numerical investigation and shown in figure 5.14, is but one of many types of axial flow fans utilised in industry. In fact, Bruneau [94BR1] states that the B-fan was specifically designed for use in ACHEs. The latter does not necessarily apply to other axial flow fans used in industrial ACHEs.

One of the axial flow fans investigated by Meyer and Kröger [98ME1], the S-fan shown in figure 5.15 differs substantially from the B-fan. The S-fan exhibits a relatively narrow average chord length with the chord length and blade twist increasing very slightly in the region close to the fan hub. The B-fan on the other hand exhibits a larger average chord length with a marked increase in both chord length and blade twist as the fan hub is neared in the radial direction. The B-fan hub diameter is also seen to be substantially larger than that of the S-fan.

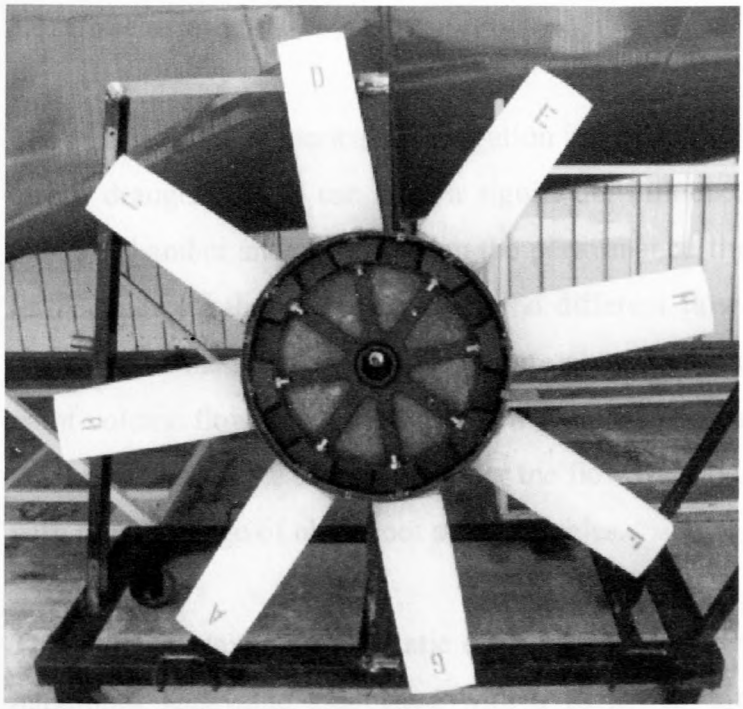

Figure 5.14. Photographic image of the B-fan.

The fact that the results of this numerical investigation indicate that the plenum chamber aerodynamic behaviour is sensitive to changes to the single axial flow fan used in this investigation, strongly suggests that the results are not necessarily applicable to mechanical draught ACHEs utilising an entirely different axial flow fan, such as the S-fan for example.

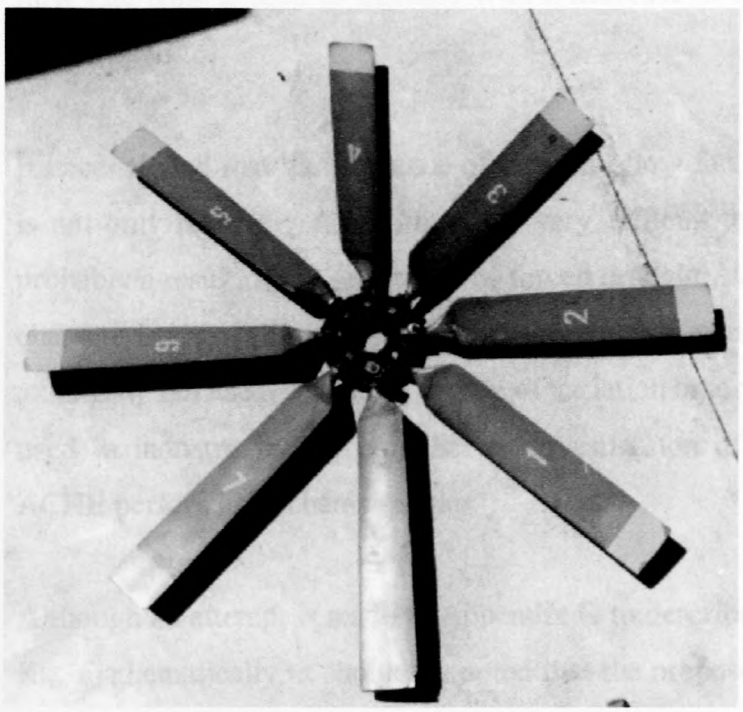

Figure 5.15. Photographic image of the S-fan [98ME1].

5.5. Conclusions

The results of the numerical investigation indicates that the axial flow fan used in a particular forced draught ACHE can have a significant influence on the flow field within the ACHE plenum chamber and as a result on the performance characteristics of the ACHE. The results further indicate that transitions between different flow patterns observed within the plenum chambers of the ACHEs investigated are associated with not only a change in the operating point volume flow rate, but also with a change in the fan blade root stagger employed by the axial flow fan. In the case of the latter the flow transitions are seen to occur suddenly within a very narrow range of blade root stagger angles.

The point of maximum fan static efficiency is also seen to not necessarily coincide with the maximum K_{rec}-value associated with a particular forced draught ACHE. K_{rec} is seen to increase with an increase in operating point volume flow rates in excess of the volume flow rate associated with the point of maximum fan static efficiency for the ACHEs investigated.

The kinetic energy coefficient at the heat exchanger bundle outlet, α_{eHE}, is a linear function of the kinetic energy coefficient at the fan outlet, α_{eF}. α_{eHE} is seen to decrease exponentially with an increase in the operating point volume flow rate. At a constant operating point volume flow rate α_{eHE} is seen to increase with a decrease in the γ_{root}-value for the range of ACHEs investigated.

It is concluded that the influence of the axial flow fan on ACHE performance characteristics is not only relatively strong, but also very difficult to predict. This state of affairs is most probably a result of the sensitivity of forced draught ACHE performance characteristics to the characteristics of the velocity field at the fan exit, which is in turn a function of the type of axial flow fan used. The large degree of variation associated with the different axial flow fans used in industry further complicates investigation of the influence of axial flow fans on ACHE performance characteristics.

Although an attempt is made in Appendix G to describe the influence of the axial flow fan on K_{rec} mathematically, it should be noted that the proposed correlation is applicable to the axial

flow fan used in this investigation alone. The more conservative K_{rec}-value of 0.3, as proposed by Meyer [98ME1], is recommended for design purposes.

CHAPTER 6 - The influence of plenum chamber height on the plenum chamber aerodynamic behaviour associated with forced draught ACHEs

The influence of forced draught ACHE plenum chamber height on the performance characteristics of ACHEs has been observed and experimentally investigated by a number of authors [60RU1, 73RO1, 88RU1, 95SA1, 96ME1]. Authoritative ACHE design texts, like that of the American Petroleum Institute [92AP1], the Air-cooled Heat Exchanger Manufacturers Association [86AI1] and the Heat Exchanger Design Handbook [83PA1], recognise the influence of plenum chamber height on forced draught ACHE performance characteristics and prescribe minimum allowable plenum chamber heights for design purposes.

Rubin [60RU1] notes that most forced draught ACHEs used in industry exhibit a plenum chamber height of half the fan diameter, but adds that the majority of ACHE manufacturers prefer a plenum chamber height equal to the fan diameter. Rose et al. [73RO1] prescribes a plenum chamber height of half a fan diameter. Neither Rubin [60RU1] nor Rose et al. [73RO1] makes reference to any experimental data on which their respective recommendations are based.

Russel and Berryman [88RU1] compare the results of three separate experimental investigations of the effect of plenum chamber height on ACHE performance characteristics carried out by the Heat Transfer and Fluid Flow Service (HTFS). Increased plenum chamber flow losses are reported for plenum chamber height to fan diameter ratios lower than 0.5. A plenum chamber height to fan diameter ratio of 0.4 is consequently recommended for design purposes.

Based on experimental results, Salta [95SA1] recommends a minimum plenum chamber height to fan diameter ratio in the range of 0.25 - 0.35.

Meyer [96ME1] experimentally investigated the isothermal performance characteristics of a range of forced draught ACHEs utilising different combinations of axial flow fans and heat

exchanger bundles often encountered in industry. Meyer [96ME1] notes the existence of a definite critical plenum chamber height below which ACHE performance deteriorates dramatically. It is further reported that the critical plenum chamber height is indifferent to the type of axial flow fan or heat exchanger bundle used, as well as to changes in the fan to heat exchanger bundle area ratios utilised. The critical plenum chamber height is however seen to increase for heat exchanger bundles with lower K_{HE}-values. Meyer [96ME1] recommends a minimum plenum chamber height to fan diameter ratio of 0.3 in the K_{HE}-value range of 15 to 25 for design purposes.

In this chapter the influence of plenum chamber height on the plenum chamber aerodynamic behaviour associated with forced draught ACHEs is investigated numerically. The investigation includes a comparison of the numerical results with the available experimental data. The influence of the heat exchanger dimensionless total pressure loss coefficient, K_{HE}, on the minimum plenum chamber height to fan diameter ratio is also investigated.

6.1. Numerical procedure

In order to isolate the influence of H_P/d_{FC} on ACHE performance, all of the variable values used to define a particular ACHE uniquely, as demonstrated in Chapter 5, were kept constant whilst H_P/d_{FC} was treated as variable. Table 6.1 lists the range of forced draught ACHEs numerically investigated. From table 6.1 it is possible to distinguish three groups of ACHEs:

- ACHEs nos. 1 - 6 where $\gamma_{root} = 63.5°$, $K_{HE} \approx 20.8$ and $V \approx 13.96$
- ACHEs nos. 7 - 11 where $\gamma_{root} = 63.5°$, $K_{HE} \approx 6.91$ and $V \approx 16.82$
- ACHEs nos. 12 - 19 where $\gamma_{root} = 61°$, $K_{HE} = 22.81$ and $V = 14.83$

The analysis described in Chapter 5 was employed to determine K_{source}, K_{rec}, α_{eHE} and V/V_{cons} from the numerical data for the ACHEs investigated.

Table 6.1. Range of ACHEs numerically investigated.

No. (-)	γ_{root} (°)	d_{FC} (m)	L_{te}/d_{FC} (-)	H_{HE} (m)	H_{HE}/W_{HE} (-)	K_{HE} (-)	H_P/d_{FC} (-)	A_{FC}/A_{HE} (-)	V (m^3/s)	K_{source} (-)
1	63.5	1.542	0.0389	1.9	1	20.80	0.25	0.517	13.83	0.000
2	63.5	1.542	0.0389	1.9	1	20.80	0.3	0.517	13.92	0.000
3	63.5	1.542	0.0389	1.9	1	20.80	0.35	0.517	13.97	0.000
4	63.5	1.542	0.0389	1.9	1	20.80	0.4	0.517	14.00	0.000
5	63.5	1.542	0.0389	1.9	1	20.80	0.45	0.517	14.01	0.000
6	63.5	1.542	0.0389	1.9	1	20.80	0.5	0.517	14.02	0.000
7	63.5	1.542	0.0389	1.9	1	6.91	0.5	0.517	17.01	0.000
8	63.5	1.542	0.0389	1.9	1	6.91	0.4	0.517	16.98	0.000
9	63.5	1.542	0.0389	1.9	1	6.91	0.3	0.517	16.86	0.000
10	63.5	1.542	0.0389	1.9	1	6.91	0.25	0.517	16.72	0.000
11	63.5	1.542	0.0389	1.9	1	6.91	0.2	0.517	16.55	0.000
12	61	1.542	0.0389	1.9	1	22.81	0.15	0.517	14.83	0.947
13	61	1.542	0.0389	1.9	1	22.81	0.2	0.517	14.83	0.485
14	61	1.542	0.0389	1.9	1	22.81	0.25	0.517	14.83	0.199
15	61	1.542	0.0389	1.9	1	22.81	0.3	0.517	14.83	0.117
16	61	1.542	0.0389	1.9	1	22.81	0.35	0.517	14.83	0.031
17	61	1.542	0.0389	1.9	1	22.81	0.4	0.517	14.83	0.000
18	61	1.542	0.0389	1.9	1	22.81	0.45	0.517	14.83	-0.052
19	61	1.542	0.0389	1.9	1	22.81	0.5	0.517	14.83	-0.058

6.2. Discussion of results

The axial flow fan model used in the current numerical investigation is based on the B-fan designed by Bruneau [94BR1] and was also used in the experimental investigation of Meyer [96ME1]. Appendix E indicates that the numerically determined performance characteristics of the B-fan compares favourably with those obtained experimentally by Bruneau [94BR1] and Stinnes [99ST1].

A unique opportunity therefore exists to compare numerically and experimentally determined forced draught ACHE performance characteristics where use is made of the same axial flow fan, effectively eliminating the influence of the axial flow fan on the results which were seen to have the potential of dominating forced draught ACHE performance characteristics. It is however important to establish first whether the performance characteristics determined

experimentally by Meyer [96ME1] for the B-fan compare favourably to those of Bruneau [94BR1] and Stinnes [99ST1].

In Appendix C a description of two methods used to define the position of the fan blades with respect to the fan axis is given. The first method involves measurement of the fan blade root stagger angle, γ_{root}, as shown in figure C.3 in Appendix C, whilst the second method used by Meyer [96ME1] and illustrated in figure C.4, involves measurement of the fan blade tip angle.

Figures 6.1 - 6.3 contrast the fan static pressure rise, fan power consumption and fan static efficiency determined numerically for $\gamma_{root} = 63.5°$ with the experimental data of Meyer [96ME1] determined for a blade tip angle of 7°. It should be noted that the two blade settings were not necessarily physically identical. Figure 6.1 indicates that the fan static pressure rise characteristics of the two data sets are near identical. Figures 6.2 and 6.3 however display a discrepancy between the experimental and numerical data sets for the fan power consumption and fan static efficiency respectively.

The results displayed in figures 6.1 - 6.3 indicate that either the experimental or the numerical data suffers from some form of inaccuracy. As mentioned previously, the numerical investigation contained in Appendix E clearly demonstrated the ability of the axial flow fan model developed in Chapter 4 to simulate accurately the operation of the B-fan over a range of blade root stagger angles.

Closer inspection of the B-fan revealed that the fan blades have sustained extensive damage to their trailing edges, especially in areas close to the blade tips. The condition of the fan blade tip trailing edges had an obvious negative influence on the ability to measure the fan blade tip angle accurately, as defined in Appendix C and also used by Meyer [96ME1]. Further damage in the form of warping due to exposure to the sun could also have been sustained by the fan blades. It is therefore assumed that the discrepancy observed between the numerically determined fan performance characteristics and those experimentally determined by Meyer [96ME1] is due to extensive damage sustained by the fan blades.

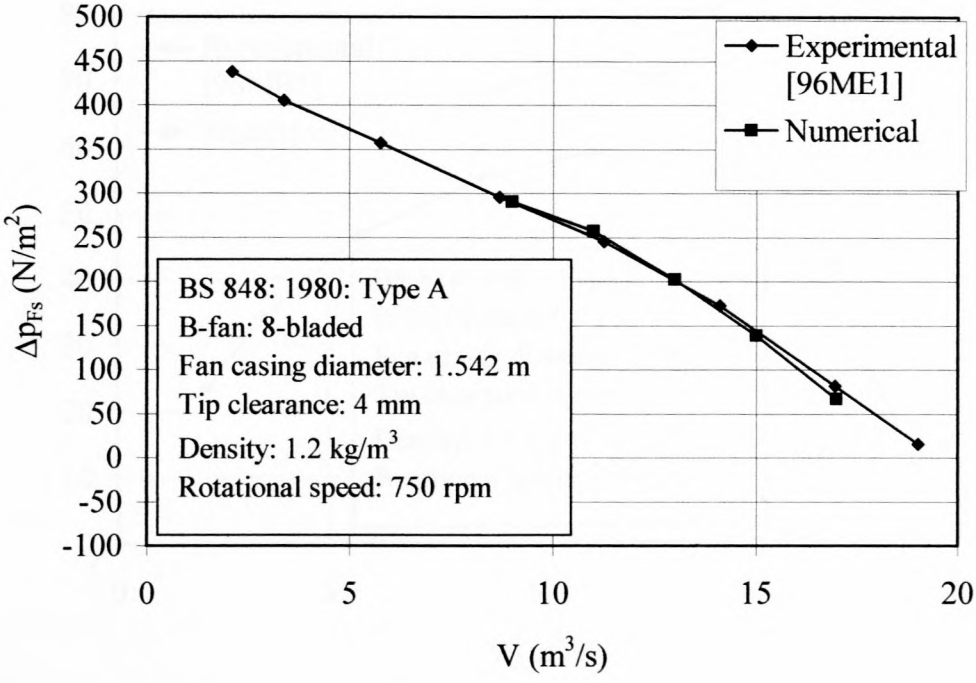

Figure 6.1. Contrasting the numerically determined fan static pressure rise characteristics with those experimentally determined by Meyer [96ME1].

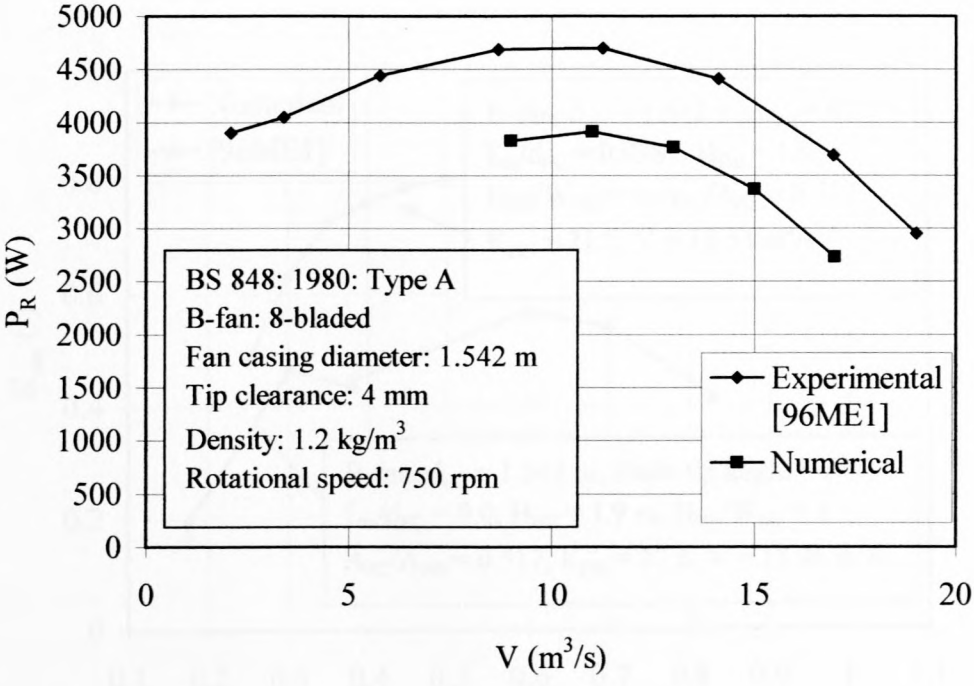

Figure 6.2. Contrasting the numerically determined fan power consumption characteristics with those experimentally determined by Meyer [96ME1]..

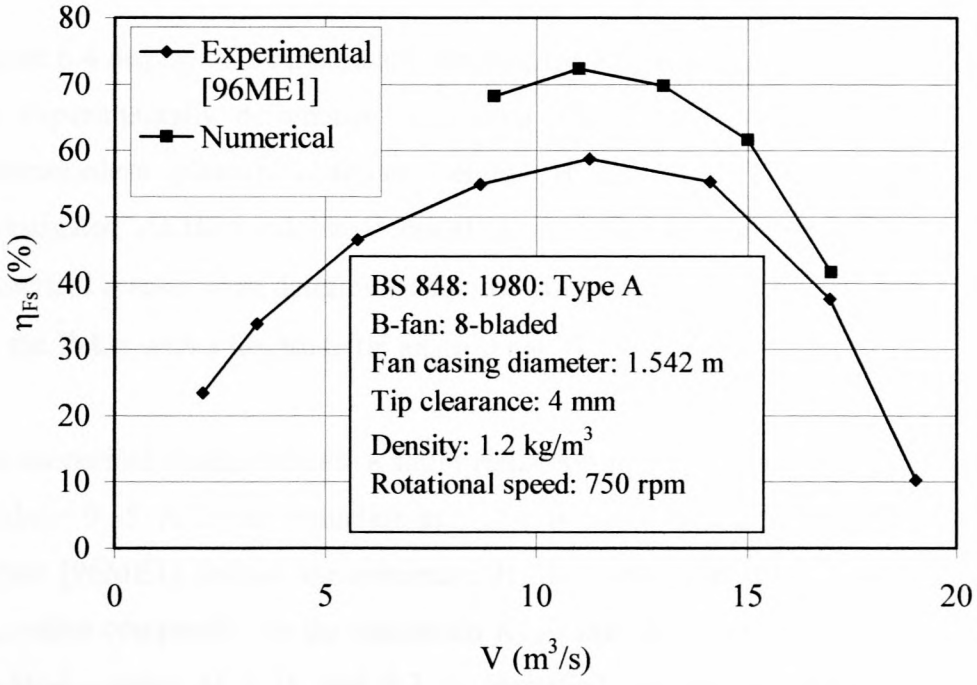

Figure 6.3. Contrasting the numerically determined fan static efficiency characteristics with those experimentally determined by Meyer [96ME1]..

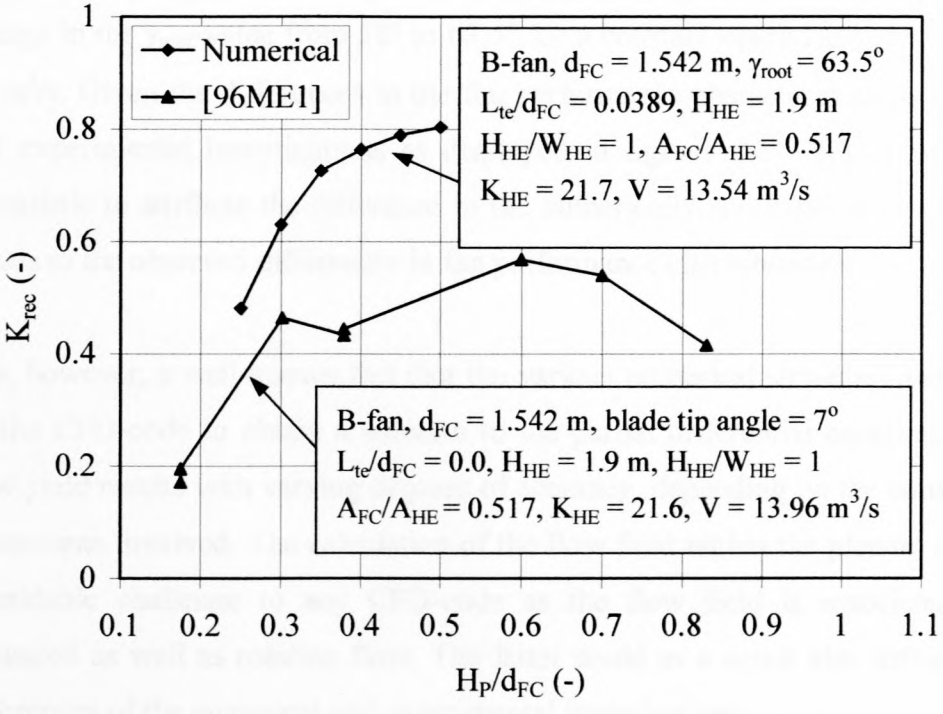

Figure 6.4. Contrasting the numerically determined plenum chamber pressure recovery as a function of H_P/d_{FC} with the experimental results of Meyer [96ME1].

Figure 6.4 displays the numerically determined K_{rec}-value data for ACHE nos. 1 - 6 as well as the experimentally determined K_{rec}-value data of Meyer [96ME1] as a function of the dimensionless plenum chamber height, H_P/d_{FC}. The numerically and experimentally investigated ACHEs exhibit identical A_{FC}/A_{HE}-values and near identical K_{HE}-values. The numerical results were determined for the B-fan with $\gamma_{root} = 63.5°$ and the experimental data for the B-fan with a fan blade tip angle set at 7°.

The numerical results indicate a slight reduction in K_{rec} for decreasing H_P/d_{FC}-values down to $H_P/d_{FC} = 0.35$. A further reduction in H_P/d_{FC} is characterised by an increased reduction in K_{rec}. Meyer [96ME1] defines the minimum H_P/d_{FC}-value that still allows ACHE operation at a K_{rec}-value comparable to the maximum K_{rec}-value as the critical H_P/d_{FC}-value, $(H_P/d_{FC})_{crit}$. A $(H_P/d_{FC})_{crit}$-value of 0.35 and 0.3 is identified for the numerical and experimental data respectively.

Figure 6.4 also indicates that the numerically determined K_{rec}-values are significantly higher than their experimentally determined counterparts. The results of the numerical investigation of Chapter 5 displayed in figure 5.8 show that a K_{rec}-value increase of 0.4 results through a change in the γ_{root}-value from 58° to 63.5° for a constant operating point volume flow rate of 12 m^3/s. Given the differences in the fan performance characteristics used for the numerical and experimental investigations as displayed in figures 6.1 - 6.3, it would not be totally unrealistic to attribute the difference in the numerically and experimentally determined K_{rec}-values to the observed differences in fan performance characteristics.

It is, however, a well-known fact that the various numerical strategies and models employed by the CFD-code to obtain a solution to the partial differential equations that govern fluid flow yield results with varying degrees of accuracy, depending on the complexity of the flow phenomena involved. The calculation of the flow field within the plenum chamber presents a formidable challenge to any CFD-code as the flow field is associated with regions of separated as well as rotating flow. The latter could as a result also influence the K_{rec}-value differences of the numerical and experimental investigations.

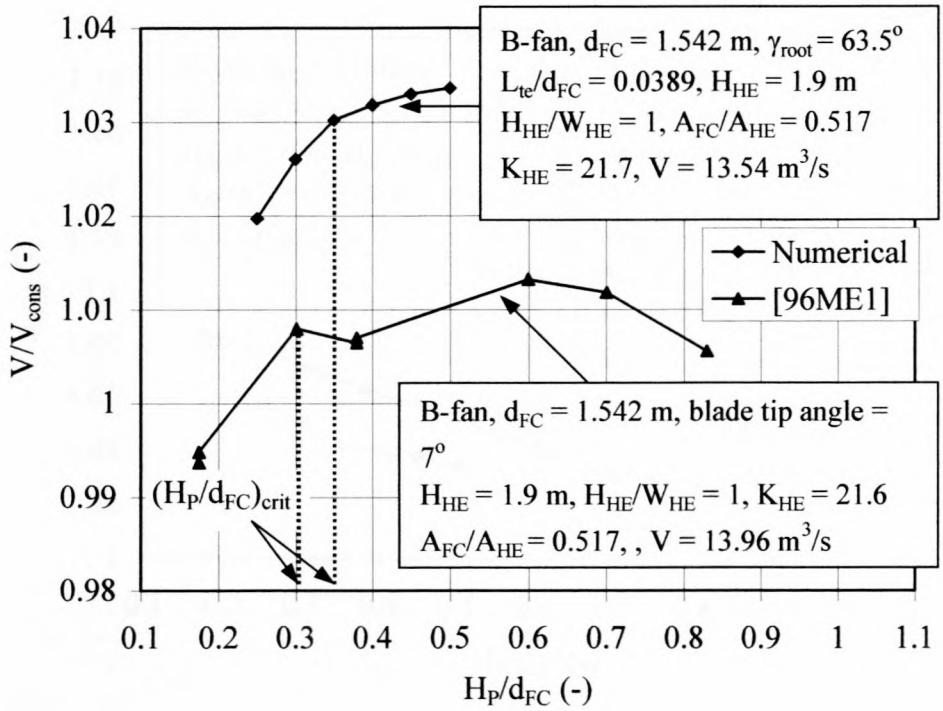

Figure 6.5. Contrasting V/V_{cons} as a function of H_P/d_{FC} determined from the numerical investigation with the experimental data of Meyer [98ME1].

Figure 6.5 displays V/V_{cons} as a function of H_P/d_{FC} for the numerical as well as the experimental results. The V/V_{cons}-value data follows the same trend observed in the K_{rec}-data of figure 6.4. It is important to note from figure 6.5 that the difference between the experimentally determined and the numerically determined maximum V/V_{cons}-value is close to 0.02 as this difference indicates that the numerically determined maximum operating point volume flow rate overestimates its experimental counterpart by approximately 2 %.

Figure 6.6 contrasts the numerically determined α_{eHE}-values with the experimental data of Meyer [96ME1]. Both the experimental as well as the numerical results show that a decrease in H_P/d_{FC} is accompanied by an increase in α_{eHE}.

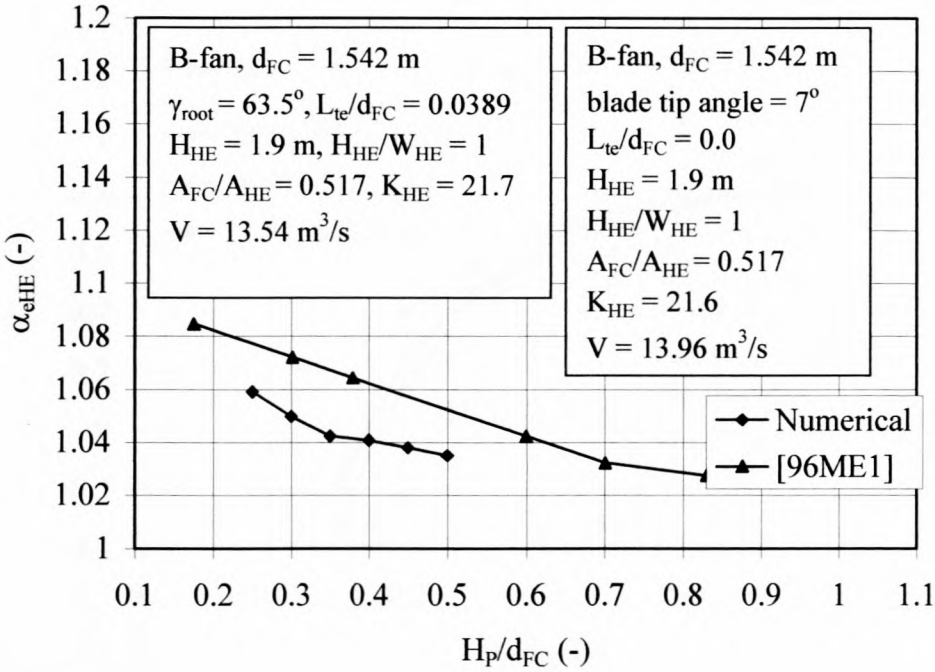

Figure 6.6. Contrasting the numerically determined α_{eHE} as a function of H_P/d_{FC} with the experimental results of Meyer [96ME1].

The experimentally determined α_{eHE}-values are higher than the numerically determined values over the whole H_P/d_{FC}-range investigated. In the previous chapter it was shown that the kinetic energy coefficient at the heat exchanger exit plane is a linear function of the kinetic energy coefficient at the fan exit plane, α_{eF}. The fact that the fan performance characteristics of the axial flow fan used by Meyer [96ME1] exhibits lower fan static efficiencies than the axial flow fan used in the numerical investigation, whilst the fan static pressure rise for both fans are near identical is a strong indication that the kinetic energy coefficients at the fan exit plane of the fan used by Meyer [96ME1] are higher than those for the fan used in the numerical investigation. The latter would then account for the higher experimentally determined α_{eHE}-values.

The K_{rec}-, V/V_{cons}-, and α_{eHE}-values for the ACHEs listed in table 6.1 are plotted as a function of H_P/d_{FC} in figures 6.7 - 6.9 respectively.

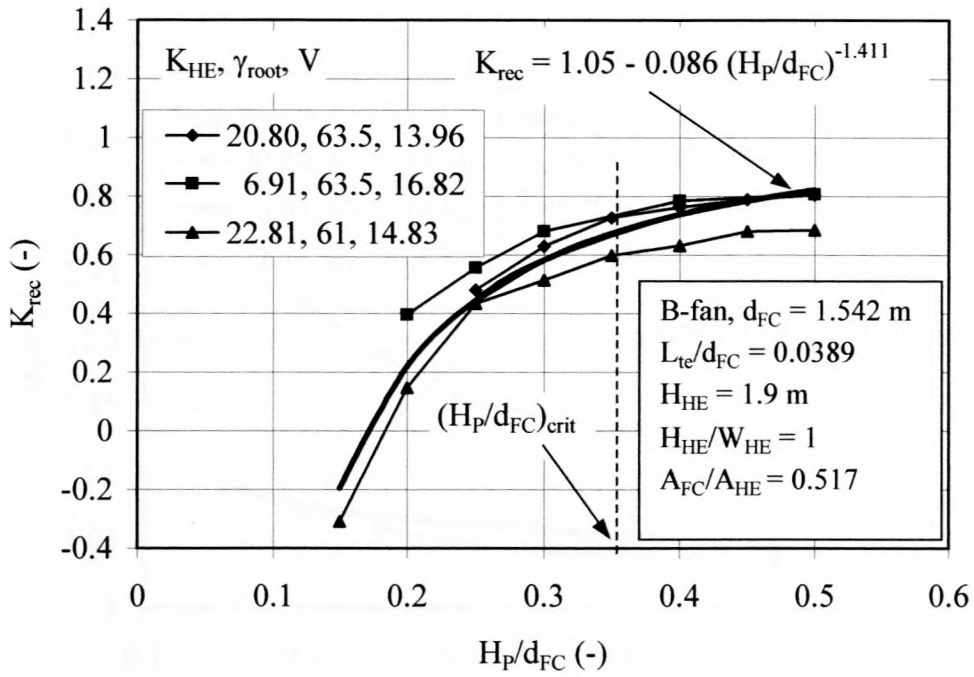

Figure 6.7. K_{rec} as a function of H_P/d_{FC} for the three different combinations of K_{HE}-, γ_{root}- and V-value investigated.

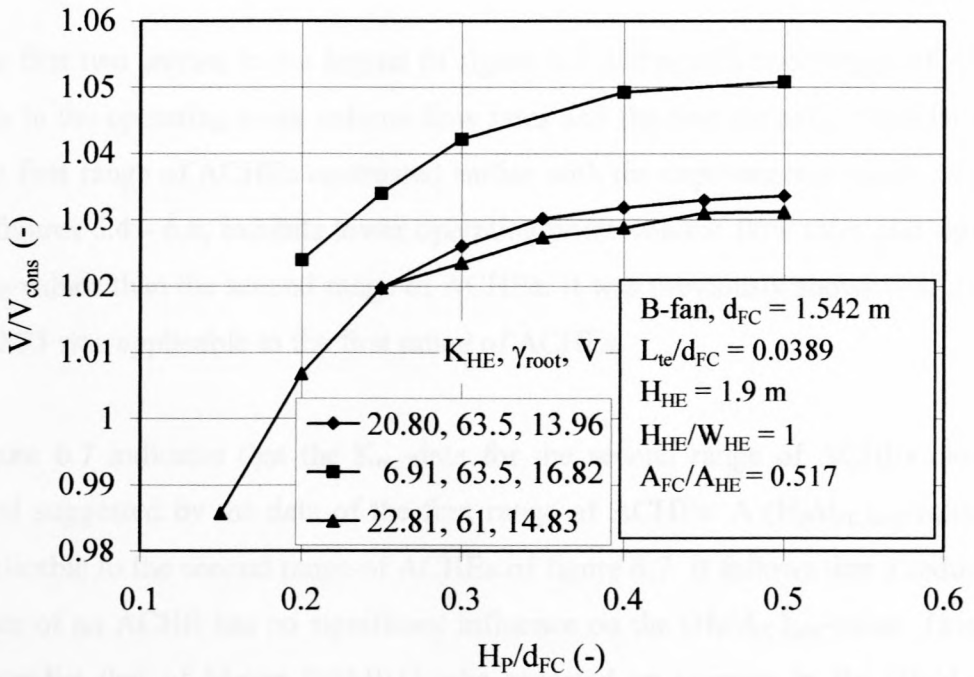

Figure 6.8. V/V_{cons} as a function of H_P/d_{FC} for the three different combinations of K_{HE}-, γ_{root}- and V-value investigated.

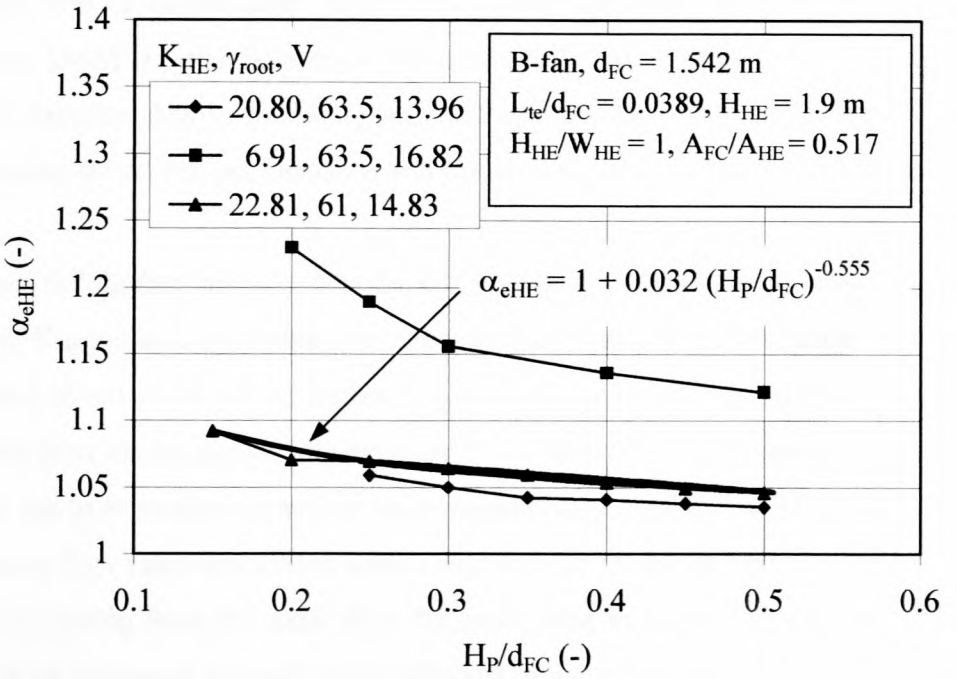

Figure 6.9. α_{eHE} as a function of H_P/d_{FC} for the three different combinations of K_{HE}-, γ_{root}- and V-value investigated.

The first two entries in the legend of figure 6.7 distinguish two ranges of ACHEs that differ only in the operating point volume flow rates and the heat exchanger bundle resistances used. The first range of ACHEs contrasted earlier with the experimental results of Meyer [96ME1] in figures 6.4 - 6.6, exhibits lower operating point volume flow rates and significantly higher K_{HE}-values than the second range of ACHEs. It was previously shown that a $(H_P/d_{FC})_{crit}$-value of 0.35 was applicable to the first range of ACHEs.

Figure 6.7 indicates that the K_{rec}-data for the second range of ACHEs closely follows the trend suggested by the data of the first range of ACHEs. A $(H_P/d_{FC})_{crit}$-value of 0.35 is also applicable to the second range of ACHEs of figure 6.7. It follows that a reduction in the K_{HE}-value of an ACHE has no significant influence on the $(H_P/d_{FC})_{crit}$-value. This result seems to contradict that of Meyer [96ME1] who reported an increase in the $(H_P/d_{FC})_{crit}$-value for a decrease in the K_{HE}-value of the heat exchanger bundle used. Closer inspection of the heat exchanger bundle employed by Meyer [96ME1] showed that a single row of finned tubes was used in the construction of the heat exchanger bundle. Heat exchanger bundles used for industrial purposes make use of multiple rows of finned tubes with the result that the air is

forced to flow through the heat exchanger in the fan axial direction. In the instance where a single row of finned tubes is used as is the case with the heat exchanger bundle used by Meyer [96ME1], the flow does not necessarily flow through the heat exchanger in the fan axial direction. Meyer [96ME1] demonstrated that such an arrangement can have a significant influence on ACHE performance and presumably also on the $(H_P/d_{FC})_{crit}$-value.

Figure 6.7 further indicates that the K_{rec}-values associated with the ACHEs making use of the lower K_{HE}-values, are lower over most of the H_P/d_{FC}-range investigated. The latter is thought to be a direct result of the higher K_{HE}-values associated with the first range of ACHEs, as a higher heat exchanger bundle resistance will force the high velocity air exiting from the axial flow fan to expand more within the plenum chamber of the ACHE. The lower operating point volume flow rates associated with a higher heat exchanger bundle resistance will also allow the air exiting from the axial flow fan more time to expand within the plenum chamber. The result of increased expansion or diffusion of air within the ACHE plenum chamber is that a greater proportion of the kinetic energy at the fan exit is recovered in the plenum chamber. The latter is associated with higher K_{rec}-values.

Figure 6.7 displays the mathematical expression of the regression fitted through the K_{rec}-data. It should be noted that the function displayed in figure 6.7 is applicable only to the ACHEs listed in table 6.1. What is however important is that the function indicates the form of the expression that relates K_{rec} to H_P/d_{FC}.

The V/V_{cons}-values of the first two ranges of ACHEs shown in figure 6.8 show that, although the range of ACHEs associated with the lower K_{HE}-values exhibits lower K_{rec}-values than the first, it yields higher V/V_{cons}-values. The analysis performed in Chapter 2 showed that the V/V_{cons}-value of a forced draught ACHE is a function of not only the K_{rec}-value, but also of the heat exchanger bundle flow resistance. The analysis of Chapter 2 further showed that for a constant K_{rec}-value a reduction in K_{HE} is accompanied by an increase in V/V_{cons} for a range of forced draught ACHEs that differ only in the respective K_{HE}-values employed.

Figure 6.9 indicates that the α_{eHE}-values associated with the range of ACHEs with lower K_{HE}-values are higher than those of the first range of ACHEs with higher K_{HE}-values. A higher heat exchanger bundle resistance will result in lower α_{eHE}-values, as the flow through the heat

exchanger bundle is more uniform. Figure 6.9 also indicates that the α_{eHE}-values for all three ranges of heat exchangers tested increase with a decrease in H_P/d_{FC} as the flow within the ACHE plenum has less time and space to diffuse before entering the heat exchanger bundle. For the ACHEs with higher K_{HE}-values the increase associated with a decrease in H_{PC}/d_{FC} is less pronounced than for the ACHEs with lower K_{HE}-values.

The third entry in the legend of figure 6.6 refers to a range of forced draught ACHEs that are close to identical to the range of ACHEs referred to in the first entry of the legend. The first and third range of ACHEs differ only in the γ_{root}-value employed by the axial flow fans utilised. The first range of ACHEs makes use of a γ_{root}-value of 63.5° and the third range of a γ_{root}-value of 61°. Figures 6.6 - 6.9 indicate that the K_{rec}-, V/V_{cons}- and α_{eHE}-data of the third range of ACHEs are near identical to the results observed for the first range of ACHEs. It follows that a change in the γ_{root}-value of the axial flow fan employed in the range of forced draught ACHEs investigated had an insignificant effect on ACHE performance.

The previous result must however be seen in context of the results of the numerical investigation of Chapter 5. The results displayed in Chapter 5 very clearly indicate that the γ_{root}-value employed by the axial flow fan used in an ACHE does have an influence on the magnitude of the associated K_{rec}-value. It follows that the fact that the magnitude of the K_{rec}-, V/V_{cons}- and α_{eHE}-values of the first and third range of ACHEs investigated is near identical, is the result of a fortunate choice of variables. What is however significant, is the fact that the results of the numerical investigations clearly indicates that a change in the axial flow fan γ_{root}-value has no effect on the observed $(H_P/d_{FC})_{crit}$-values associated with the first and third range of ACHEs tested.

Figure 6.9 also displays the mathematical expression of a regression fitted through the α_{eHE}-value data of the range of ACHEs associated with the second and third entry in the legend of figure 6.9. Again it should be noted that the expression displayed in figure 6.9 is not generally applicable to all ACHEs, but serves to demonstrate the form of the mathematical expression used to express α_{eHE} as a function of H_P/d_{FC}.

6.3. Conclusions

The results of the numerical investigation indicate that a reduction in the plenum chamber height is associated with a reduction in the K_{rec}-value. Lower plenum chamber heights are associated with an increased reduction in the K_{rec}-values.

The results further indicate that a reduction of the plenum chamber height leads to an increase in α_{eHE}, and that this increase is more pronounced for ACHEs that make use of lower K_{HE}-values. The latter is also associated with higher α_{eHE}-values over the range of H_P/d_{FC}-values investigated.

The critical H_P/d_{FC}-value, $(H_P/d_{FC})_{crit}$, is defined as the minimum H_P/d_{FC}-value that yields a K_{rec}-value comparable to that achieved at higher H_P/d_{FC}-values. The results of the numerical investigation indicate that the $(H_P/d_{FC})_{crit}$-values associated with the forced draught ACHEs investigated are unaffected by a reduction of the K_{HE}-value as well as a change in the γ_{root}-value employed by the axial flow fan

The results of the numerical investigation compare favourably with the experimental results of Meyer [96ME1], although there is some indication that the numerically determined K_{rec}-values of the ACHEs investigated are slightly elevated. There also exists a discrepancy between the numerical results and the experimental data of Meyer [96ME1] concerning the influence of a reduction in K_{HE} on the $(H_P/d_{FC})_{crit}$-value. The lowest K_{HE}-value numerically investigated was approximately 7.15, whilst the experimental investigation of Meyer [96ME1] made use of a minimum K_{HE}-value of 7.3. Both these K_{HE}-values fall well outside the range of K_{HE}-values most often used in industry. It is very likely that the experimental results of Meyer [96ME1] are contaminated by cross-flow effects through the heat exchanger bundle due to the latter consisting of a single row of finned tubes alone.

A $(H_P/d_{FC})_{crit}$-value of 0.35 is applicable to the numerically investigated forced draught ACHEs as opposed to a value of 0.3 for the ACHEs experimentally investigated by Meyer [96ME1].

Meyer [96ME1] also proposes a K_{rec}-value of 0.3 for the same K_{HE}-value range and, although the numerical investigation has yielded higher K_{rec}-values, the recommendation of Meyer [96ME1] is proposed as a conservative means by which to estimate forced draught ACHE performance.

The results of the numerical investigation confirm the recommendation by Meyer [96ME1] that a $(H_P/d_{FC})_{crit}$-value of 0.3 for a K_{HE}-value range of 15 - 25 should be used for design purposes. Meyer [96ME1] also proposes a K_{rec}-value of 0.3 for the same K_{HE}-value range and, although the numerical investigation has yielded higher K_{rec}-values the recommendation of Meyer [96ME1] is proposed as a conservative means by which to estimate forced draught ACHE performance.

CHAPTER 7 - The influence of fan to heat exchanger area ratio on the plenum chamber aerodynamic behaviour associated with forced draught ACHEs

Although a number of authors make reference to or even recommend A_{FC}/A_{HE}-values for design purposes, little of this information is based on comprehensive experimental investigation [60RU1, 73RO1, 75TU1, 79MO1].

Rubin [60RU1] comments on the fact that forced draught ACHEs utilised in industry exhibits fan diameters ranging from 60-100% of the heat exchanger bundle width. Rose et al. [73RO1] as well as Turner [75TU1] recommends a minimum fan to heat exchanger area ratio of 0.4, whilst Monroe [79MO1] advises a value of no less than 0.5.

Based on experimental results, Meyer [96ME1] concludes that the A_{FC}/A_{HE}-value has very little influence on the performance characteristics of forced draught ACHEs.

In this chapter the influence of A_{FC}/A_{HE}-values on the plenum chamber aerodynamic behaviour associated with a range of forced draught ACHEs is numerically investigated and the results compared to those of Meyer [96ME1]. Recommendations based on the numerical results are subsequently made for design purposes.

7.1. Numerical procedure

The influence of A_{FC}/A_{HE} on plenum chamber aerodynamic behaviour and consequently on the performance characteristics of forced draught ACHEs was determined by numerically investigating a range of ACHEs where all variable values used to characterise an ACHE uniquely, as demonstrated in Chapter 5, were kept constant, whilst treating A_{FC}/A_{HE} as a variable. Table 7.1 lists the range of forced draught ACHEs numerically investigated.

A K_{HE}-value of 21.43 was used as it falls within the range of K_{HE}-values most often used in industrial ACHEs. A H_P/d_{FC}-value of 0.4 was employed for all the ACHEs investigated. The latter was based on the results of Chapter 6 that indicate that the $(H_P/d_{FC})_{crit}$-value does not

exceed 0.35. A constant volume flow rate of 16.89 m^3/s was employed so as to yield relatively small absolute values for K_{source}. Previous investigations have indicated that numerical solutions become unstable for high absolute values of K_{source}.

The analysis described in Chapter 5 was employed to determine K_{source}, K_{rec}, α_{eHE} and V/V_{cons} from the numerical data for the range of ACHEs investigated.

Table 7.1. Range of ACHEs numerically investigated.

No. (-)	γ_{root} (°)	d_{FC} (m)	L_{te}/d_{FC} (-)	H_{HE} (m)	H_{HE}/W_{HE} (-)	K_{HE} (-)	H_P/d_{FC} (-)	A_{FC}/A_{HE} (-)	V (m^3/s)	K_{source} (-)
1	61	1.542	0.0389	1.76	1	21.42	0.4	0.603	16.89	4.166
2	61	1.542	0.0389	1.843	1	21.42	0.4	0.550	16.89	2.876
3	61	1.542	0.0389	1.9	1	21.43	0.4	0.517	16.89	2.150
4	61	1.542	0.0389	2.03	1	21.43	0.4	0.453	16.89	0.893
5	61	1.542	0.0389	2.16	1	21.43	0.4	0.400	16.87	0.000

7.2. Discussion of results

Figures 7.1 - 7.3 display the K_{rec}-, V/V_{cons}- and α_{eHE}-value data of the ACHEs investigated as a function of A_{FC}/A_{HE} respectively.

Figure 7.1 indicates that K_{rec} increases in a near linear fashion with an increase in A_{FC}/A_{HE} as indicated by the regression fitted through the numerical data.

Elevated K_{rec}-values are synonymous with increased recovery of the kinetic energy present at the fan exit within the ACHE plenum chamber. The fact that the cross-sectional area of the ACHE plenum chamber is larger than that of the fan casing creates the impression that the kinetic energy recovery mechanisms at work within the ACHE plenum chamber are the same as those governing the function of a diffuser. Should this be true, an increase in K_{rec} is expected with a reduction in A_{FC}/A_{HE}.

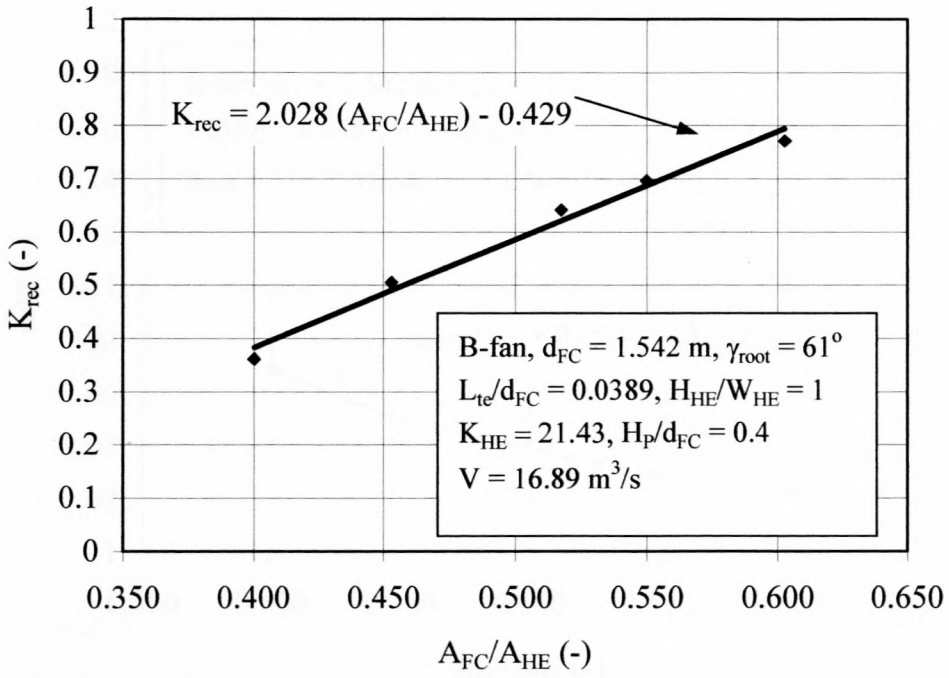

Figure 7.1. Plenum chamber pressure recovery as a function of the fan to heat exchanger area ratio.

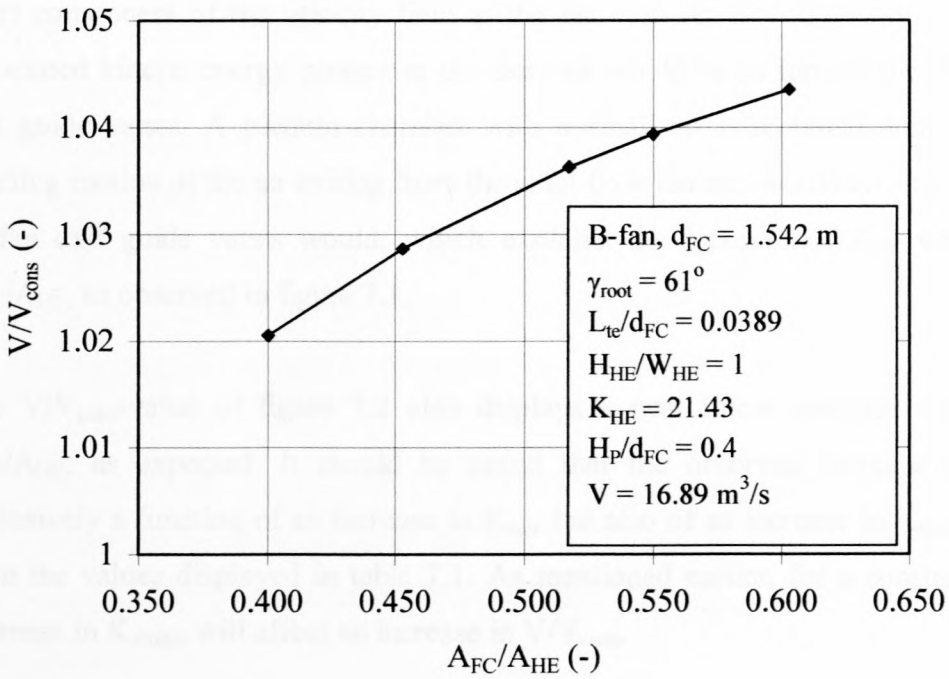

Figure 7.2. V/V_{cons} plotted as a function of the fan to heat exchanger area ratio.

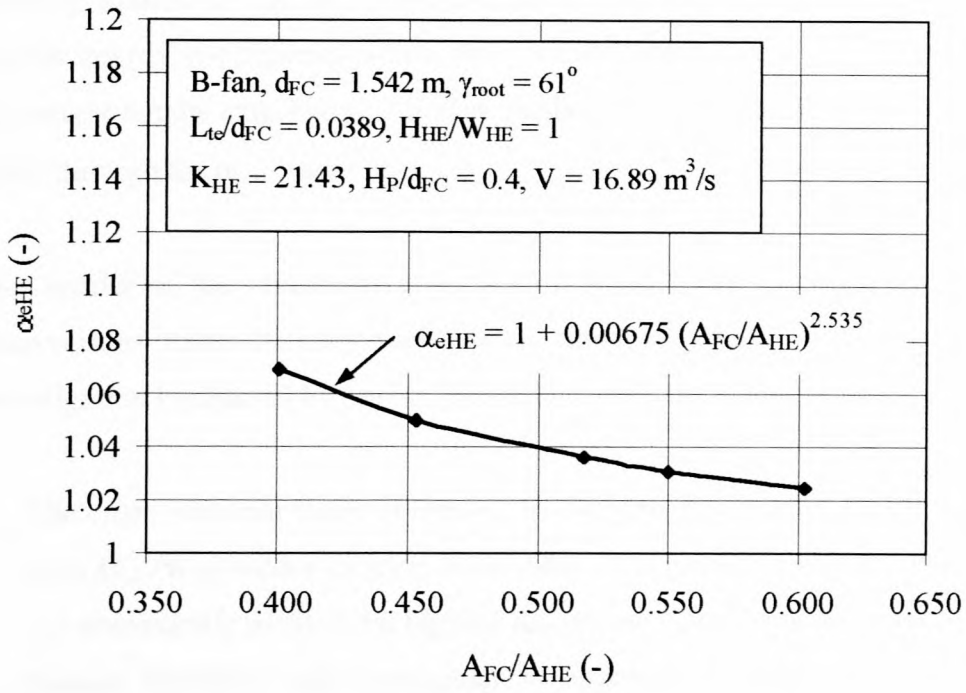

Figure 7.3. α_{eHE} plotted as a function of the fan to heat exchanger area ratio.

Figure 7.1 however indicates quite the opposite to be true. It is important to remember that a large proportion of the kinetic energy present at the fan exit is represented by the fan induced swirl component of the velocity field at the fan exit. An effective way to recover the swirl associated kinetic energy present at the fan exit would be to furnish the axial flow fan with exit guide vanes. A plenum chamber with a small cross-sectional area would impair the swirling motion of the air exiting from the axial flow fan and would act in much the same way as fan exit guide vanes would, which explains the increase of K_{rec} with an increase in A_{FC}/A_{HE}, as observed in figure 7.1.

The V/V_{cons}-value of figure 7.2 also displays a near linear increase with an increase in A_{FC}/A_{HE}, as expected. It should be noted that the observed increase in V/V_{cons} is not exclusively a function of an increase in K_{rec}, but also of an increase in K_{source}, as can be seen from the values displayed in table 7.1. As mentioned earlier, for a constant value of K_{rec} a decrease in K_{source} will affect an increase in V/V_{cons}.

The α_{eHE}-value data of figure 7.3 indicates that a slight increase in α_{eHE} is accompanied by a reduction of A_{FC}/A_{HE}. This is consistent with the explanation used earlier with respect to the K_{rec}-data of figure 7.1, as a smaller plenum chamber cross-sectional area would impair the

swirling motion of the air within the ACHE plenum chamber and would result in lower kinetic energy coefficients within the plenum chamber and consequently also at the heat exchanger bundle exit. Figure 7.3 also displays the mathematical expression of the regression fitted through the α_{eHE}-value data.

The results of the numerical investigation would seem to stand in stark contrast to the observations made by Meyer [96ME1]. However, closer inspection of the experimental investigation conducted by Meyer [96ME1] reveals the following:

- The cross-sectional shape of the ACHE plenums investigated by Meyer [96ME1] differed, with H_{HE}/W_{HE}-values ranging from 0.86 - 1. The ACHEs displaying H_{HE}/W_{HE}-values of 1.0 consistently yielded the highest K_{rec}-values. According to Turner [75TU1], the use of plenum chambers with rectangular as opposed to square cross-sectional profiles has a severe effect on the flow patterns observed within the ACHE plenum chamber and consequently ACHE performance. It could very well be that the influence of a plenum chamber with a rectangular shaped cross-sectional profile obscures the effect of a change in A_{FC}/A_{HE} on ACHE performance, especially when compared with the ACHEs where $H_{HE}/W_{HE} = 1$.
- Meyer [96ME1] used two axial flow fans operated at different rotational speeds and displaying different geometrical features as well as different fan casing diameters to evaluate the effect of a change in A_{FC}/A_{HE} on ACHE performance. Although the two axial flow fans form part of the same range of fans, the results displayed in Chapter 5 indicate that axial flow fan operation could have a marked effect on ACHE performance. It is very possible that the results reported by Meyer [96ME1] concerning the influence of a change in A_{FC}/A_{HE} on ACHE performance are contaminated by the influence of different axial flow fans.
- The results by Meyer [96ME1] indicate that the α_{eHE}-values determined for ACHEs that utilise the same axial flow fan are near identical irrespective of the A_{FC}/A_{HE}-value employed. The last result agrees with the results of the numerical investigation displayed in figure 7.3.

7.3. Conclusions

The results of the numerical investigation indicate that an increase in the fan to heat exchanger area ratio is associated with a linear increase in the K_{rec}-value for the range of ACHEs investigated. This is thought to be the result of the effect of the plenum chamber walls on the rotational component of the air flow exiting from the axial flow fan that acted in a manner similar to fan exit guide vanes. A slight increase in the α_{eHE}-value is observed with a reduction in A_{FC}/A_{HE}. A high A_{FC}/A_{HE}-value with a plenum chamber of square cross-sectional profile is recommended for design purposes.

CHAPTER 8 - The influence of heat exchanger bundle flow resistance on the plenum chamber aerodynamic behaviour associated with forced draught ACHEs

Few of the limited number of technical papers concerned with the operation and design of forced draught ACHEs make mention of the influence of heat exchanger bundle performance characteristics on the plenum chamber aerodynamic behaviour associated with forced draught ACHEs. Reference to the latter is usually reserved for comment on the thermal performance characteristics of the heat exchanger bundle which includes the adverse influence of non-uniform air-flow patterns through the heat exchanger bundle. Turner [75TU1] notes that the heat exchanger bundle resistance seems to have an insignificant influence on the plenum chamber flow field and presumable also on ACHE performance. The last statement is based on observations made of the flow field within a model forced draught ACHE where the heat exchanger bundle and axial flow fan were simulated through the use of an array of threaded rods and by forcing air through a set of swirl-inducing guide vanes respectively [75TU1].

A notable exception to the above mentioned state of affairs is the experimental investigation by Meyer and Kröger [98ME1], where it is shown that the heat exchanger bundle resistance not only influences the $(H_{PC}/d_{FC})_{crit}$-value, but also the system effect associated with forced draught ACHEs. Meyer and Kröger [98ME1] also place emphasis on the oblique flow characteristics of heat exchanger bundles and demonstrate the influence of the latter on the ACHE performance characteristics. The results of the numerical investigation of Chapter 6 have shown that the $(H_{PC}/d_{FC})_{crit}$-value of the range of forced draught ACHEs investigated are not influenced by the heat exchanger bundle flow resistance. The oblique flow characteristics of a range of heat exchanger bundles were experimentally investigated and the results are displayed in Appendix A.

In this chapter the influence of the heat exchanger bundle flow resistance on the plenum chamber aerodynamic behaviour associated with a range of forced draught ACHEs is investigated numerically. The results are compared with those obtained during the experimental investigation by Meyer and Kröger [98ME1].

8.1. Numerical procedure

The influence of heat exchanger bundle resistance on the plenum chamber aerodynamic behaviour associated with forced draught ACHEs was determined by numerically investigating a range of ACHEs where the variable values used to characterise a particular forced draught ACHE uniquely, as demonstrated in Chapter 5, were kept constant, whilst treating K_{HE} as variable. Table 8.1 lists the range of forced draught ACHEs numerically investigated.

An A_{FC}/A_{HE}-value of 0.517 was used, as it falls midway in the range of A_{FC}/A_{HE}-values typically used in industrial forced draught ACHEs. The operating point volume flow rate was chosen so as to ensure that no numerical instabilities would arise for the range of K_{HE}-values investigated. A H_P/d_{FC}-value of 0.4 was employed as this is higher than the $(H_P/d_{FC})_{crit}$-value of 0.35 indicated in Chapter 6.

The analysis, as described in Chapter 5, was employed to determine K_{source}, K_{rec}, α_{eHE} and V/V_{cons} from the numerical data for the range of ACHEs investigated.

Table 8.1. Range of ACHEs numerically investigated.

No. (-)	γ_{root} (°)	d_{FC} (m)	L_{te}/d_{FC} (-)	H_{HE} (m)	H_{HE}/W_{HE} (-)	K_{HE} (-)	H_P/d_{FC} (-)	A_{FC}/A_{HE} (-)	V (m^3/s)	K_{source} (-)
1	61	1.542	0.0389	1.9	1	7.26	0.4	0.517	15.99	-2.537
2	61	1.542	0.0389	1.9	1	9.65	0.4	0.517	15.99	-1.940
3	61	1.542	0.0389	1.9	1	17.05	0.4	0.517	15.99	0.000
4	61	1.542	0.0389	1.9	1	19.25	0.4	0.517	15.99	0.574
5	61	1.542	0.0389	1.9	1	23.93	0.4	0.517	15.99	1.825

8.2. Discussion of results

Figure 8.1 indicates a slight but linear increase in the K_{rec}-value with an increase in K_{HE}. As mentioned earlier, a higher heat exchanger bundle flow resistance will promote diffusion of the high velocity air exiting from the axial flow fan. The latter results in higher levels of kinetic energy recovery within the ACHE plenum chamber and hence in higher K_{rec}-values.

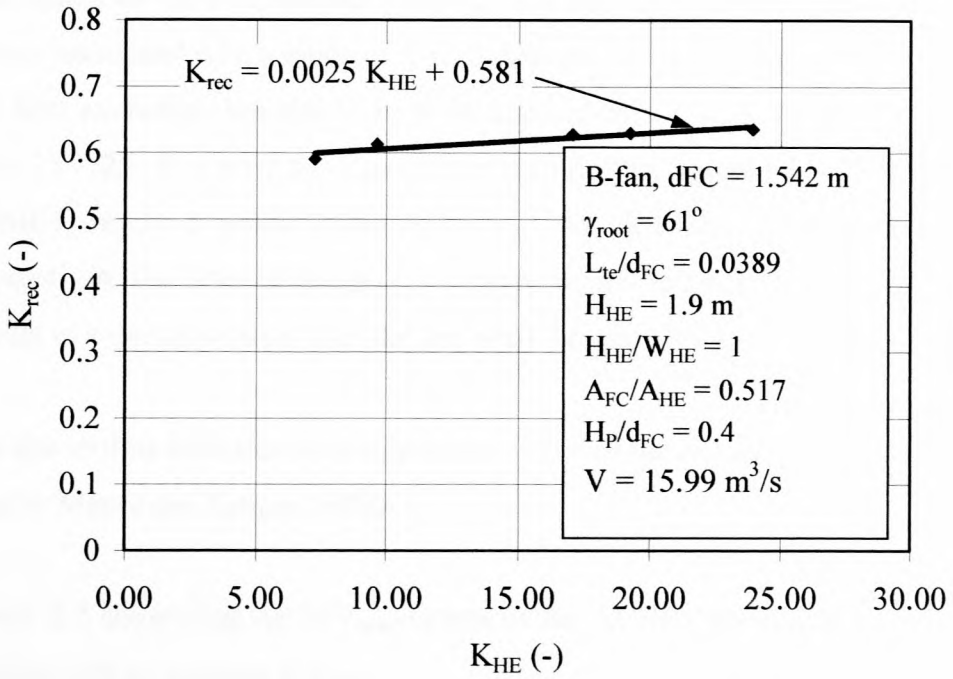

Figure 8.1. Plenum chamber pressure recovery as a function of the heat exchanger bundle isothermal flow resistance.

In the previous chapter, concerned with the influence of the A_{FC}/A_{HE}-value on ACHE performance, it was shown that one of the ways in which kinetic energy, and in particular the kinetic energy associated with the swirl component of the velocity field at the fan exit, is recovered within the ACHE plenum chamber is that the walls of the latter act in a manner similar to guide vanes installed at the fan outlet. It was also mentioned that this mechanism of kinetic energy recovery seems to dominate other possible mechanisms of kinetic energy recovery within the ACHE plenum chamber. The latter would include the recovery of kinetic energy through diffusion of the air exiting from the fan in a manner analogous to the mechanism at work in a diffuser which is subject to non-swirling inlet flow. The K_{rec}-value data of figure 8.1 bears some testimony to the truth of the last two statements, as the increased diffusion in the plenum chamber resulting from increased K_{HE}-values increases K_{rec} by approximately 0.05 over the K_{HE}-value range considered, whereas the increase associated with a change in the A_{FC}/A_{HE}-value is nearly eight times this value over the applicable range of A_{FC}/A_{HE}-values. Furthermore, K_{HE}-values smaller than 15 are not readily encountered in industry, which serves to emphasize further the relatively insignificant influence of K_{HE} on ACHE performance.

The results of the experimental investigation by Meyer and Kröger [98ME1] show the K_{rec}-values associated with a range of forced draught ACHEs using combinations of different fans and heat exchanger bundles to be little affected by a change in K_{HE} for a K_{HE}-value ranging from 15 - 25. It is only for K_{HE}-values significantly lower than 15 that Meyer and Kröger [98ME1] report dramatic increases in K_{rec}. As mentioned in Chapter 6 and expounded in Appendix A, the latter is thought to be the result of the air flowing through the heat exchanger bundle in a direction other than the fan axial direction.

The above thus indicates good agreement between the numerical results and the experimental data by Meyer and Kröger [98ME1].

Figure 8.2 shows that the V/V_{cons}-values of the ACHEs investigated also increase in a linear fashion with an increase in K_{HE}.

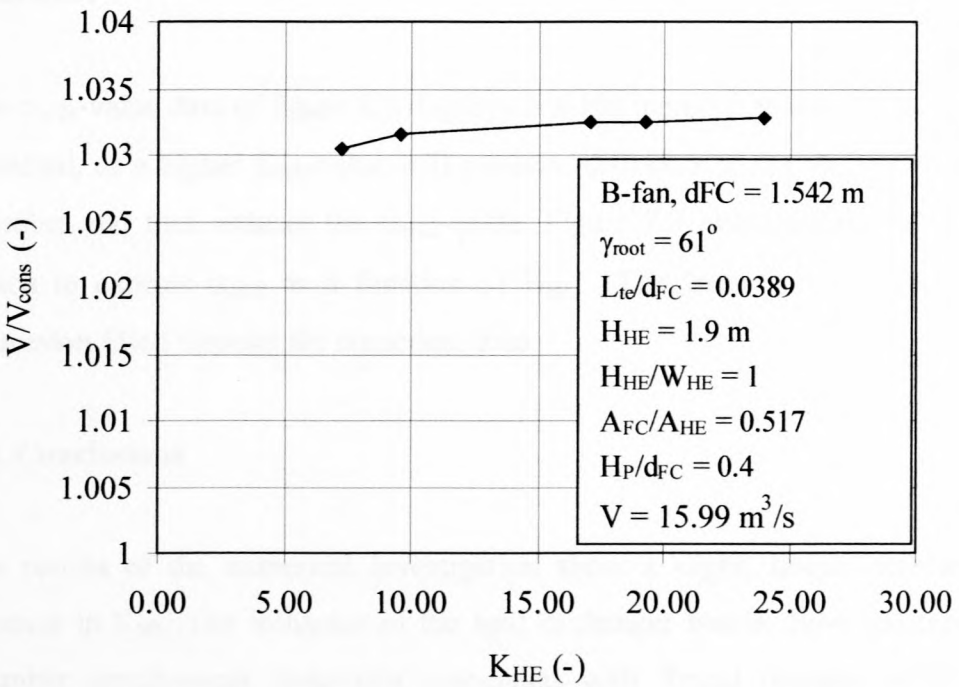

Figure 8.2. V/V_{cons} plotted as a function of the heat exchanger bundle isothermal flow resistance.

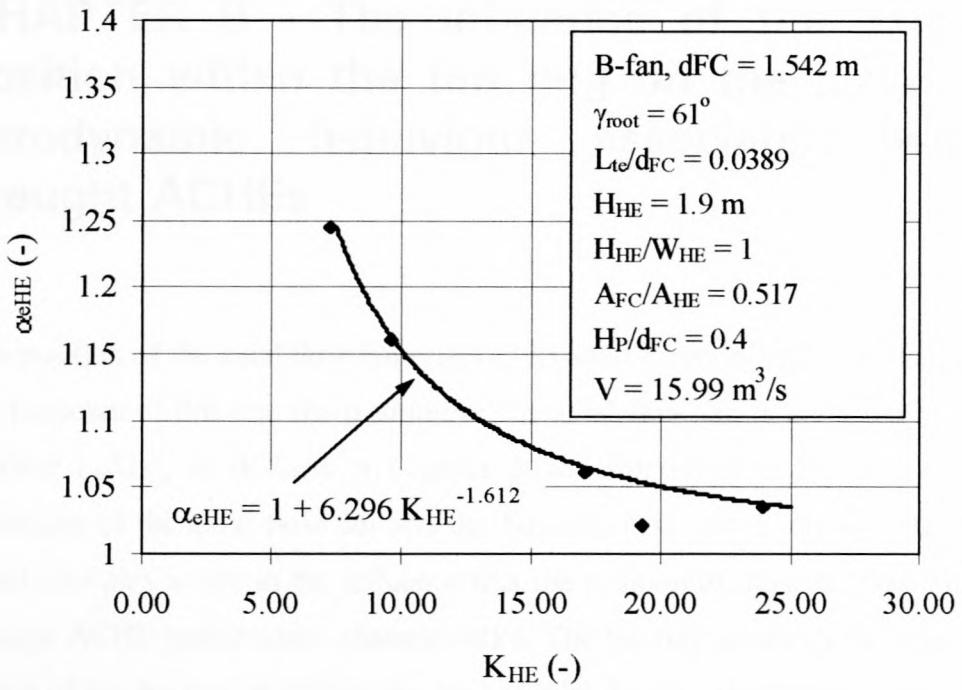

Figure 8.3. α_{eHE} plotted as a function of the heat exchanger bundle isothermal flow resistance.

The α_{eHE}-value data of figure 8.3 displays a slight increase at lower K_{HE}-values. This is to be expected, as a higher K_{HE}-value will promote diffusion of the air within the ACHE plenum chamber and thus reduces the α_{eHE}-value. Figure 8.3 also displays the function used with which to express α_{eHE} as a function of K_{HE}. The latter is indicated in figure 8.3 by a regression fitted through the numerical data.

8.3. Conclusions

The results of the numerical investigation show a slight, linear increase in K_{rec} with an increase in K_{HE}. The influence of the heat exchanger bundle flow resistance on the plenum chamber aerodynamic behaviour associated with forced draught ACHEs is seen to be relatively small when compared to the influence of a change in A_{FC}/A_{HE}. V/V_{cons} increases linearly with an increase in K_{HE}. A slight increase in α_{eHE} is observed at lower K_{HE}-values. The numerical results compare favourably with the experimental data by Meyer and Kröger [98ME1].

CHAPTER 9 - The influence of the axial flow fan position within the fan ring on the plenum chamber aerodynamic behaviour associated with forced draught ACHEs

The position of the axial flow fan refers to its axial location within the fan ring or shroud. For the purposes of this text the position of the axial flow fan is indicated by the dimensionless number L_{te}/d_{FC}, as defined in Chapter 5 and illustrated in figure 5.1. Due to the close proximity of the axial flow fan and the fan ring it is very likely that the fan ring geometry could also play a role in the influence that the position of the axial flow fan exerts on forced draught ACHE performance characteristics. The fan ring geometry includes the depth or axial length of the fan ring as well as the type of inlet fitted to the fan ring. The latter usually takes on the form of a bell mouth or a conical or cylindrical section. The influence of the axial flow fan position within the fan ring on forced draught ACHE performance characteristics as well as the effect of the fan ring geometry on the latter has either been commented on and/or experimentally investigated by a number of authors [60RU1, 74BA1, 75US1, 76TA1, 79MO1, 96ME1, 98KR1].

Rubin [60RU1] declares the depth of the fan ring to be a critical dimension. The latter is based on the experimental observation that an increase in the air volume flow rate of 5 - 15% accompanied by no observable increase in fan power consumption is affected through the doubling of the fan ring depth. Unfortunately no further detail pertaining to the type of fan or test installation used is given.

Baranski [74BA1] states that there exists an optimum position of the fan within the fan shroud with regard to the fan performance characteristics and advises that the fan penetration should be 0.5 - 0.66 of the projected fan width into the shroud, with the larger projection on the fan shroud inlet side. From the text it is not clear whether the last statement refers to either forced or induced draught ACHEs, or whether it includes both configurations. The latter is assumed. Baranski [74BA1] further warns that the optimum fan position, as determined in a standard fan test installation, does not necessarily coincide with the optimum position associated with the system within which the fan is employed.

The Engineering Design Handbook of the United States Army [75US1] recommends that a third of the projected width of the axial flow fan should penetrate into the fan shroud for forced draught ACHEs. It should be noted that the stringent space limitations associated with military vehicles necessitates the use of very short fan casings.

Based on experimental results, Taylor and Chu [76TA1] state that, although the type of fan shroud used (referring to the type of inlet attached to the fan ring) has an insignificant influence on ACHE performance, the position of the fan within the fan shroud is critical. The investigation by Taylor and Chu [76TA1] included the use of a bell mouth inlet as well as an inlet consisting of a cylindrical section of ducting. The investigation was also limited to induced draught ACHEs of the type used in military vehicles, with the result that the axial flow fans were furnished with very short fan casings.

In stark contrast to the observations by Taylor and Chu [76TA1], Monroe [79MO1] reports a loss in fan efficiency of up to 18% in the case where the inlet bell mouth is removed from the fan ring. It should be noted that the paper by Monroe [79MO1] deals primarily with cooling towers where the latter is generally associated with longer fan casings than encountered in ACHEs used for automotive engine cooling purposes.

Meyer [96ME1] experimentally investigated the performance characteristics of a range of forced draught ACHEs and axial flow fans and concluded that different positions of the axial flow fan within the particular fan ring utilised have no observable influence on either ACHE or axial flow fan performance. It should be noted that the ACHEs and axial flow fans investigated by Meyer [96ME1] made exclusive use of bell mouth type inlets at the fan ring.

The above listed seemingly conflicting statements are somewhat clarified by Kröger [98KR1], who notes that the location of the axial flow fan within the fan ring only becomes critical when very short fan rings are utilised. Kröger [98KR1] further states that the optimal fan ring geometry would include a sufficiently long fan ring furnished with a bell mouth type inlet. It should be noted that Kröger [98KR1] refers to the combination of the fan ring and fan ring inlet section as the fan casing. According to Kröger [98KR1], a sufficient length for the fan casing is at the very least 1/6 of the fan diameter.

What makes the issue of fan position in a forced draught ACHE fan ring seemingly complex, is that very few of the authors listed above care to state whether they are investigating fan position with regard to the fan ring inlet or fan ring outlet. Differentiation between the fan ring inlet and outlet is critical, as two very different flow phenomena are involved.

Figure 9.1 indicates that an axial flow fan installed in a fan ring fitted with a cylindrical or conical inlet section, as opposed to a bell mouth type inlet, will inevitably suffer from a distorted inlet velocity field. The latter is the result of flow separation that occurs at the sharp edges of these inlet sections, as indicated in figure 9.1. It follows that fan performance and consequently performance of the forced draught ACHE will be adversely affected should the axial flow fan be installed close enough to or even within these regions of separation.

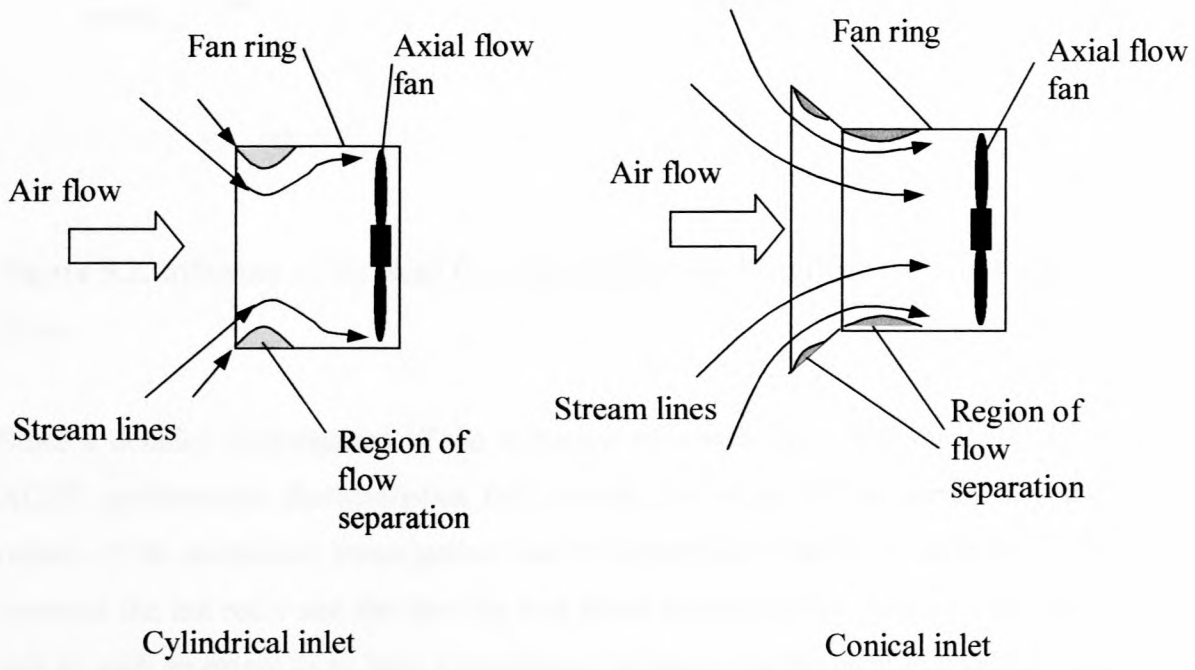

Figure 9.1. Flow separation associated with cylindrical and conical fan ring inlet sections.

Conditions at the fan ring outlet are somewhat different. It is a well-known fact that the rotational component of the velocity field at the fan outlet is influenced by both the geometrical characteristics of the axial flow fan as well as the operating conditions [83WA1]. The latter would include the volume flow rate as well as rotational speed of the fan. In axial flow fans, where the rotational component of the fan exit velocity field is sufficiently large,

the rotational motion of the air could facilitate the diffusion of the air within the forced draught ACHE plenum chamber due to the outward movement of the air. It now follows that should the section of the fan ring between the fan rotor exit plane and the fan ring exit plane be sufficently long, as illustrated in figure 9.2(b), the outward movement of the air due to its high rotational component might be inhibited, as opposed to the instance where the fan is mounted at the fan ring exit, as shown in figure 9.2(a).

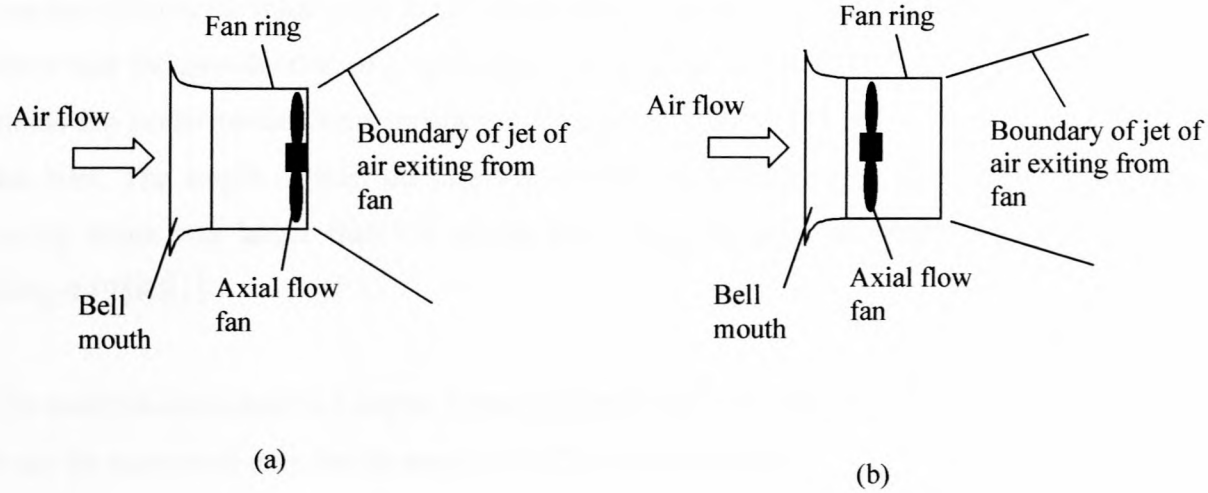

Figure 9.2. Influence of the axial flow fan position on the diffusion of air at the fan ring exit plane.

Since a detailed investigation of the influence of conditions at the fan inlet on the fan and ACHE performance characteristics falls outside the scope of the current investigation, the object of the numerical investigation was to determine whether a variation in the distance between the fan rotor and the fan ring exit plane influences the velocity field at the fan ring exit to such an extent as to have a significant influence on the plenum chamber velocity field and hence on forced draught ACHE performance characteristics.

9.1. Numerical procedure

The influence of the position of the axial flow fan within the fan ring on forced draught ACHEs performance was determined by treating all variable values used to characterise the range of ACHEs investigated as constant, whilst changing the value of L_{te}/d_{FC}. Table 9.1 lists the two forced draught ACHEs numerically investigated.

The particular K_{HE}- and A_{FC}/A_{HE}-values used were chosen so as to be representative of forced draught ACHEs used in industry, whilst the operating point volume flow rate was chosen in such a way as to ensure numerical stability of the solution process.

Note that the computational grid utilised for this investigation and shown in figure 5.2 made no use of a length of inlet ducting upstream of the axial flow fan. A uniform velocity field was specified at the inlet to the length of ducting. The experimental results of Stinnes [99ST1] show that the introduction of a sufficiently long length of inlet ducting to the axial flow fan yields fan performance characteristics comparable to those obtained using a bell mouth at the fan inlet. The length of inlet ducting was more than sufficiently long to ensure that the fan casing depth was larger than 1/6 of the fan casing diameter according to the proposal by Kröger [98KR1].

The analysis described in Chapter 5 was employed to determine K_{source}, K_{rec}, α_{eHE} and V/V_{cons} from the numerical data for the range of ACHEs investigated.

Table 9.1. Range of ACHE numerically investigated.

No. (-)	γ_{root} (°)	d_{FC} (m)	L_{te}/d_{FC} (-)	H_{HE} (m)	H_{HE}/W_{HE} (-)	K_{HE} (-)	H_P/d_{FC} (-)	A_{FC}/A_{HE} (-)	V (m^3/s)	K_{source} (-)
1	61	1.542	0.0700	1.9	1	13.57	0.4	0.517	16.84	0.00
2	61	1.542	0.0389	1.9	1	13.57	0.4	0.517	16.80	0.00

9.2. Discussion of results

Figures 9.3 - 9.5 display the K_{rec}-, V/V_{cons}- and α_{eHE}-values of the ACHEs investigated as a function of L_{te}/d_{FC}. The results confirm the experimental results by Meyer [96ME1] and shows ACHE performance to be unaffected by the position of the axial flow fan, provided that the fan inlet conditions are ideal. It should be noted that the latter is subject to the type of fan used as well as the fan operating conditions and, as a result, should not be generalized to include all types of axial flow fans.

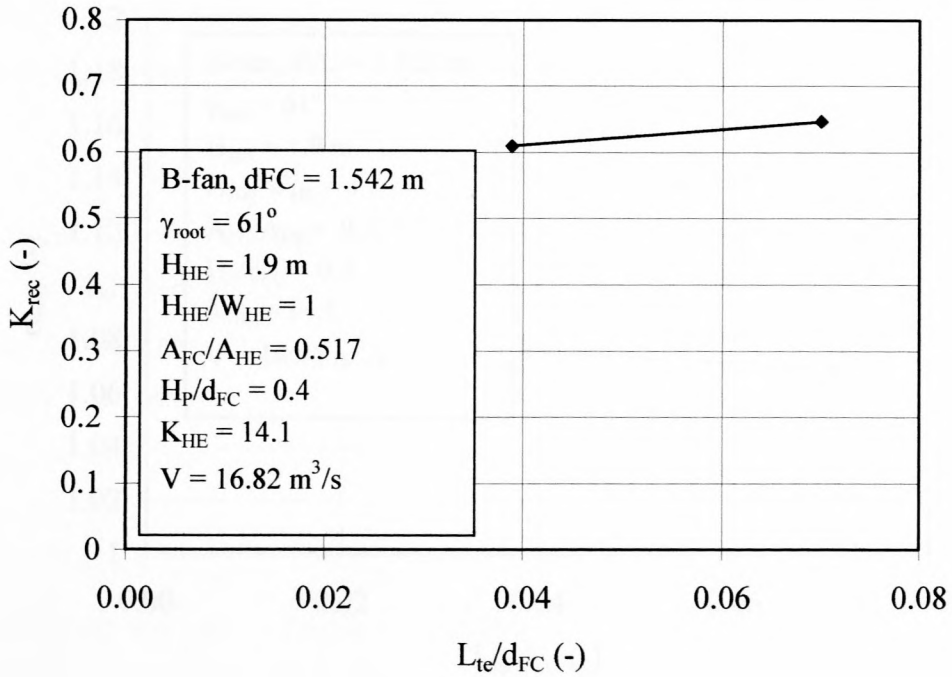

Figure 9.3. Plenum chamber pressure recovery as a function of the position of the axial flow fan within the fan ring.

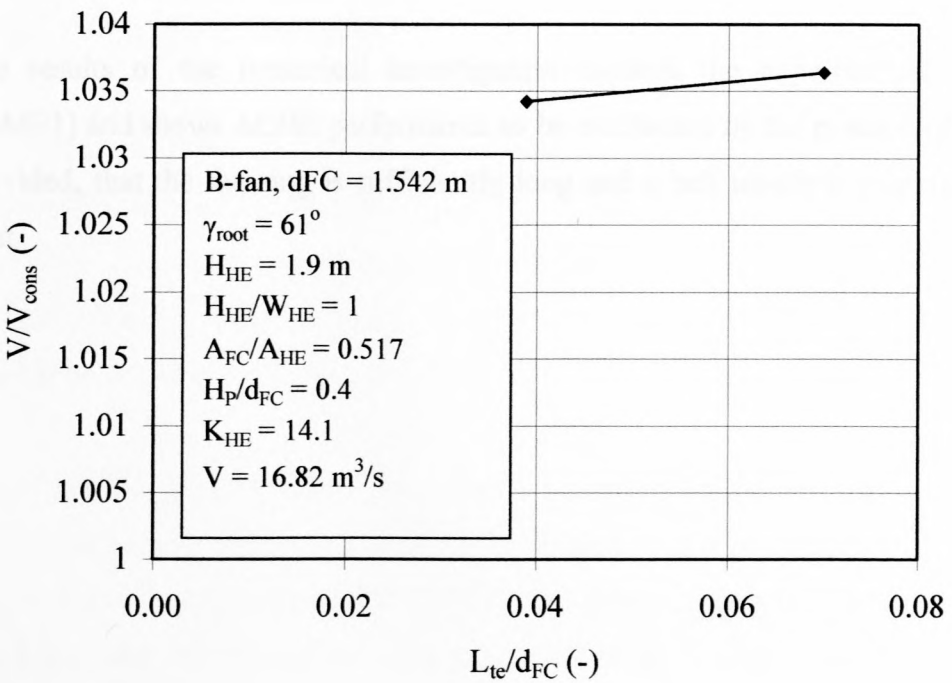

Figure 9.4. V/V_{cons} plotted as a function of the position of the axial flow fan within the fan ring.

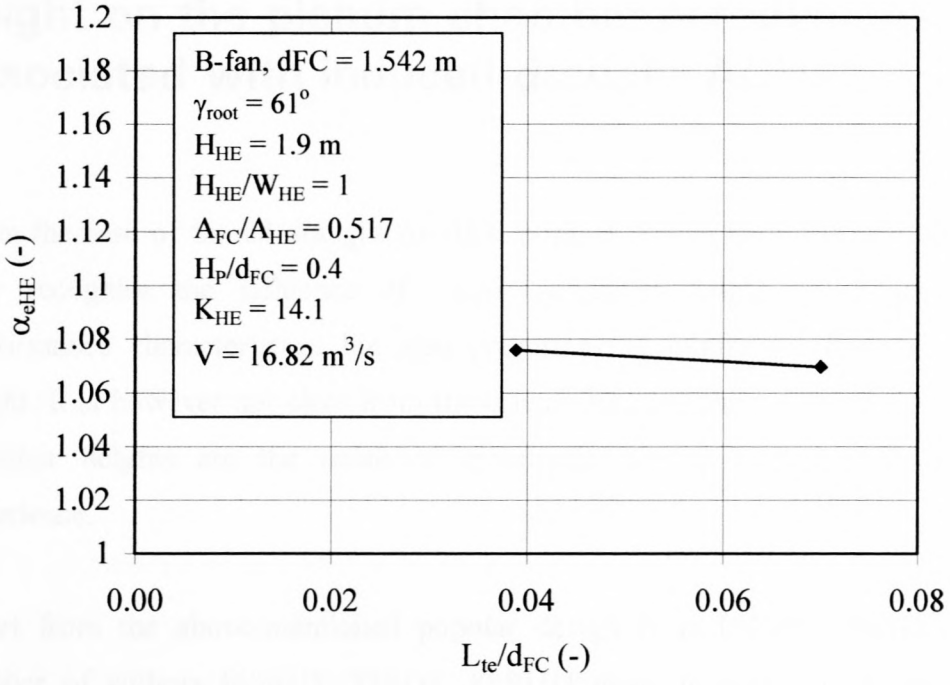

Figure 9.5. α_{eHE} plotted as a function of the position of the axial flow fan within the fan ring.

9.3. Conclusions

The results of the numerical investigation confirm the experimental results by Meyer [96ME1] and shows ACHE performance to be unaffected by the position of the axial flow fan provided, that the fan ring is sufficiently long and a bell mouth is employed at the fan ring inlet.

CHAPTER 10 - The influence of plenum chamber height on the plenum chamber aerodynamic behaviour associated with induced draught ACHEs

As in the case of forced draught ACHEs, popular design texts [92AP1, 86AI1, 83PA1] not only recognise the influence of plenum chamber height on induced draught ACHE performance characteristics, but also prescribe the minimum allowable plenum chamber height. It is however not clear from these texts whether the recommended minimum plenum chamber heights are the result of systematic experimental investigation or based on experience.

Apart from the above-mentioned popular design texts [92AP1, 86AI1, 83PA1], a small number of authors [60RU1, 73RO1, 88RU1] make mention of the influence of plenum chamber height on forced draught ACHE performance characteristics.

Rubin [60RU1] gives an overview of general design practices associated with air-cooled heat exchangers and states that the distance between the fan and heat exchanger bundle is usually not less than half a fan diameter.

The article by Rose et al. [73RO1] was written as a supplement to the 1968 American Petroleum Institute Standard 661 [68AP1]. A minimum distance between the plane of the axial flow fan and the heat exchanger bundle of at least a third of the fan diameter is recommended for design purposes. From the text it is not clear whether this recommendation is based on experimental data.

Russel and Berryman [88RU1] state that it is an established fact that a too shallow plenum chamber adversely influences the air volume flow rate delivered by an axial flow fan in an ACHE. Russel and Berryman [88RU1] furthermore compare three sets of experimental data and show that for two of the data sets a minimum plenum chamber depth of 0.35 fan diameters is applicable, as opposed to 0.25 fan diameters for the remaining data set. As a result a minimum plenum chamber depth of 0.3 fan diameters is recommended by Russel and Berryman [88RU1] for design purposes.

The primary objective of the numerical investigation associated with this chapter was to determine the influence of a variation in plenum chamber depth on the performance characteristics of an induced draught ACHE. The particular induced draught ACHE considered was constructed in a way as to not be a special case when compared to induced draught ACHEs used in industry. Due to the large degree of variation associated with the latter it would be near impossible to construct a single induced draught ACHE that could be considered representative of those used in industry. A further objective of the numerical investigation was to determine the influence of a change in the fan to heat exchanger area ratio on the minimum allowable plenum chamber height.

10.1. Characterisation of induced draught ACHEs

Since both induced and forced draught ACHEs make use of the same components, the ACHE geometrical characteristics as well as the axial flow fan and heat exchanger bundle isothermal performance characteristics used to characterise forced draught ACHEs in Chapter 5 were utilised to characterise the range of induced draught ACHEs investigated.

ACHE geometrical characteristics

Figure 10.1 is a schematic representation of an induced draught ACHE displaying the associated geometrical characteristics. The latter includes the fan casing diameter, d_{FC}, the heat exchanger bundle height, H_{HE}, and breadth, B_{HE}, the plenum chamber height, H_P, and the position of the axial flow fan within the fan ring denoted by the length between the fan blade tip trailing edge and the surface defining the plenum chamber inlet, L_{te}.

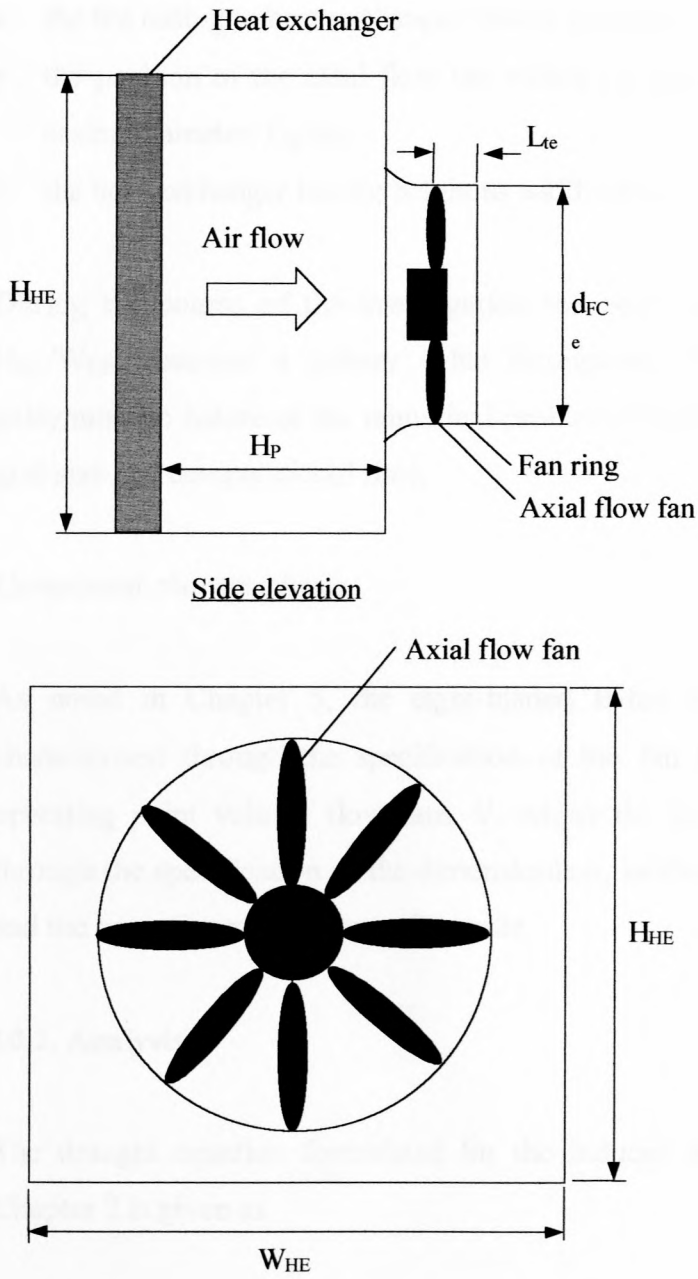

Figure 10.1. Geometrical characteristics of a typical induced draught ACHE.

The dimensionless groups associated with the geometrical characteristics of the range of forced draught ACHEs investigated is also utilised to express the geometrical characteristics of the range of induced draught ACHEs investigated. These dimensionless groups are:

- the plenum chamber height expressed as a fraction of the fan casing diameter, H_P/d_{FC}

- the fan casing to heat exchanger frontal area ratio, A_{FC}/A_{HE}
- the position of the axial flow fan within the fan ring expressed as a fraction of the fan casing diameter, L_{te}/d_{FC}
- the heat exchanger bundle height to width ratio, H_{HE}/W_{HE}.

During the course of the investigation the heat exchanger bundle height to width ratio, H_{HE}/W_{HE}, assumed a unitary value throughout. This was done to exploit the ensuing axisymmetric nature of the numerical problem that lead to significant reductions in terms of grid size and computational time.

Component characteristics

As noted in Chapter 5, the eight-bladed B-fan of Bruneau [94BR1] can be uniquely characterised through the specification of the fan blade root stagger angle, γ_{root} and the operating point volume flow rate, V, whilst the heat exchanger bundles are characterised through the specification of the dimensionless, isothermal total pressure loss coefficient, K_{HE} and the operating point volume flow rate.

10.2. Analysis

The draught equation formulated for the induced draught ACHE shown in figure 2.6 of Chapter 2 is given as

$$\Delta p_{sF} = K_{HE}\rho v_{HE}^2/2 + K_P\rho v_{FC}^2/2 \qquad (2.24)$$

It should however be remembered that neither the K_P-value nor the operating point volume flow rate that satisfies equation (2.24) is known prior to performing an analysis of the flow field through the ACHE. As mentioned in the preceding section, a constant volume flow rate was specified at the inlet boundary of the computational grid of the specific ACHE under consideration. Since the operating point volume flow rate of the particular induced draught ACHE was unknown, it was highly likely that the specified volume flow rate would differ from the operating point volume flow rate of the ACHE with the result that equation (2.24) would not be satisfied when using the specified volume flow rate.

The above situation can however be remedied, just as described in paragraph 5.2 for the forced draught configuration, through the introduction of an additional mechanical energy per unit volume term in equation (2.24), so that

$$\Delta p_{sF} + (K_{source} - K_P)\rho v_{FC}^2/2 = K_{HE}\rho v_{HE}^2/2 \qquad (10.1)$$

where K_{source} is a dimensionless total pressure source coefficient based on the average velocity through the fan casing.

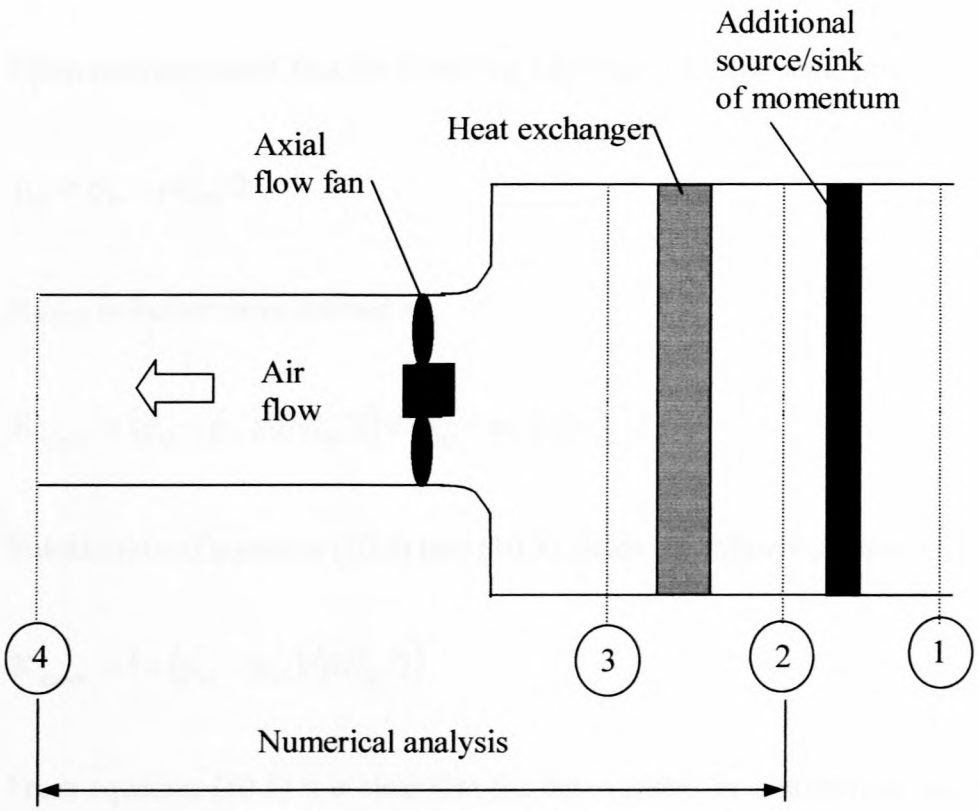

Figure 10.2. Schematic representation of an induced draught ACHE with an additional source/sink of mechanical energy located upstream of the heat exchanger bundle.

The physical interpretation of the addition of the term containing K_{source} to equation (2.24) is that a flow device is introduced to the induced draught ACHE that acts as a source of mechanical energy per unit volume, as shown schematically in figure 10.2. A positive value for K_{source} is associated with an increase in mechanical energy per unit volume, and vice versa.

It should be noted from figure 10.2 that the device that acts as an additional source of mechanical energy per unit volume is located on the heat exchanger bundle upstream side and do not alter the velocity field at the heat exchanger inlet. Figure 10.2 further indicates that the numerical analysis was confined to the geometry between sections 2 and 4.

A necessary condition to ensure that the specified volume flow rate satisfies equation (10.1) is that the total pressure at section 1 equal the static pressure at section 4 in figure 10.2, so that

$$p_{s1} + \rho v_{HE}^2/2 = p_{s4} \tag{10.2}$$

Upon rearrangement find the following expression for the static pressure at section 1

$$p_{s1} = p_{s4} - \rho v_{HE}^2/2 \tag{10.3}$$

K_{source} is furthermore defined as

$$K_{source} = (p_{t2} - p_{t1})/(\rho v_{HE}^2/2) = (p_{s2} - p_{s1})/(\rho v_{HE}^2/2) \tag{10.4}$$

Substitution of equation (10.3) into (10.4) yields the following expression for K_{source}

$$K_{source} = 1 + (p_{s2} - p_{s4})/(\rho v_{HE}^2/2) \tag{10.5}$$

From equation (10.5) it is clear that the data yielded by a numerical analysis of the section of the induced draught ACHE indicated in figure 10.2 is a sufficient means with which to calculate K_{source}.

With the value of K_{source} known, K_P can be calculated, utilising equation (10.1) as follows

$$K_P = \left[K_{HE}\rho v_{HE}^2/2 - (\Delta p_{sF} + K_{source}\rho v_{FC}^2/2)\right]/(\rho v_{HE}^2/2) \tag{10.6}$$

The operating point volume flow rate is usually expressed as a fraction of the conservative volume flow rate, V_{cons}. According to Chapter 2 the latter can be calculated from the draught equation of a particular induced draught ACHE by setting $K_P = 0$. V_{cons} for the ACHE shown in figure 10.2 can therefore be determined by setting $K_P = 0$ in equation (10.1) so that

$$\Delta p_{sF} + K_{source}\rho v_{HE}^2/2 = K_{HE}\rho v_{HE}^2/2 \qquad (10.7)$$

10.3. Numerical investigation

In order to isolate the effect of plenum chamber height on induced draught ACHE performance characteristics all variable values used to characterise an induced draught ACHE as listed previously remained constant whilst the plenum chamber height was treated as variable. Table 10.1 lists the range of induced draught ACHEs investigated.

Table 10.1. The range of induced draught ACHEs numerically investigated.

No. (-)	γ_{root} (°)	d_{FC} (m)	L_{te}/d_{FC} (-)	H_{HE} (m)	H_{HE}/W_{HE} (-)	K_{HE} (-)	H_P/d_{FC} (-)	A_{FC}/A_{HE} (-)	V (m^3/s)	K_{source} (-)
1	61	1.542	0.0389	2.5	1	18.95	0.1	0.299	13.01	-65.546
2	61	1.542	0.0389	2.5	1	18.95	0.2	0.299	13.00	-76.691
3	61	1.542	0.0389	2.5	1	18.95	0.25	0.299	13.00	-78.727
4	61	1.542	0.0389	2.5	1	18.95	0.3	0.299	13.00	-80.267
5	61	1.542	0.0389	2.5	1	18.95	0.4	0.299	13.00	-81.318
6	61	1.542	0.0389	2.5	1	18.95	0.5	0.299	13.01	-81.157
7	61	1.542	0.0389	1.9	1	18.86	0.1	0.517	13.00	-12.058
8	61	1.542	0.0389	1.9	1	18.96	0.2	0.517	13.00	-13.842
9	61	1.542	0.0389	1.9	1	18.87	0.25	0.517	13.00	-14.428
10	61	1.542	0.0389	1.9	1	19.05	0.3	0.517	13.00	-14.475
11	61	1.542	0.0389	1.9	1	18.95	0.35	0.517	13.00	-14.760
12	61	1.542	0.0389	1.9	1	19.09	0.4	0.517	13.00	-14.735
13	61	1.542	0.0389	1.84	1	18.99	0.1	0.552	13.00	-8.406
14	61	1.542	0.0389	1.84	1	18.90	0.2	0.552	13.00	-10.058
15	61	1.542	0.0389	1.84	1	18.89	0.3	0.552	13.00	-10.682
16	61	1.542	0.0389	1.84	1	18.90	0.4	0.552	13.00	-10.653

From table 10.1 it is possible to discern 3 distinct groups of induced draught ACHEs for which the plenum chamber height was treated variable. The 3 groups are distinguished by the

different A_{FC}/A_{HE}-values utilised, where the latter was affected through a change in the heat exchanger frontal area.

10.4. Discussion of results

Figures 10.3 and 10.4 display K_P and V/V_{cons} as a function of H_P/d_{FC} respectively for the range of induced draught ACHEs listed in table 10.1.

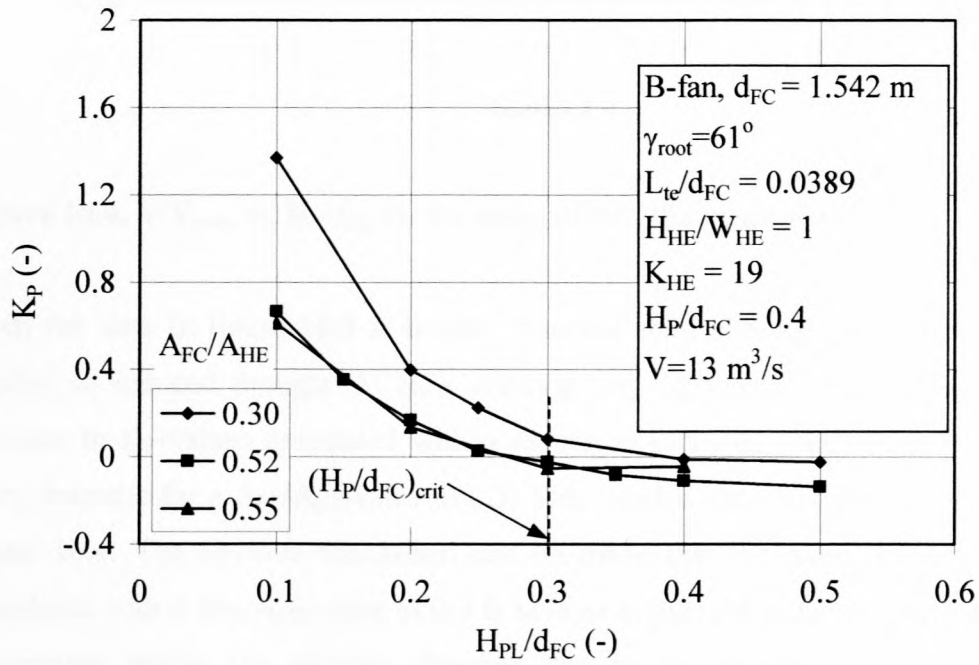

Figure 10.3. K_P vs. H_P/d_{FC} for the range of ACHEs investigated.

Figure 10.3 indicates that for all three of the different A_{FC}/A_{HE}-values evaluated, K_P remains virtually unchanged at a value close to zero for H_P/d_{FC}-values in excess of 0.3. A reduction in the H_P/d_{FC}-value to levels below 0.3 lead to an increase in the plenum chamber flow losses as indicated by the elevated K_P-values. A $(H_P/d_{FC})_{crit}$-value defined as the minimum H_P/d_{FC}-value that still allows for ACHE performance comparable to that associated with higher H_P/d_{FC}-values of 0.3 is consequently recommended for the induced draught ACHEs investigated. These trends are also reflected in the V/V_{cons}-data of figure 10.4. The above are in agreement with the results reported by Russel and Berryman [88RU1].

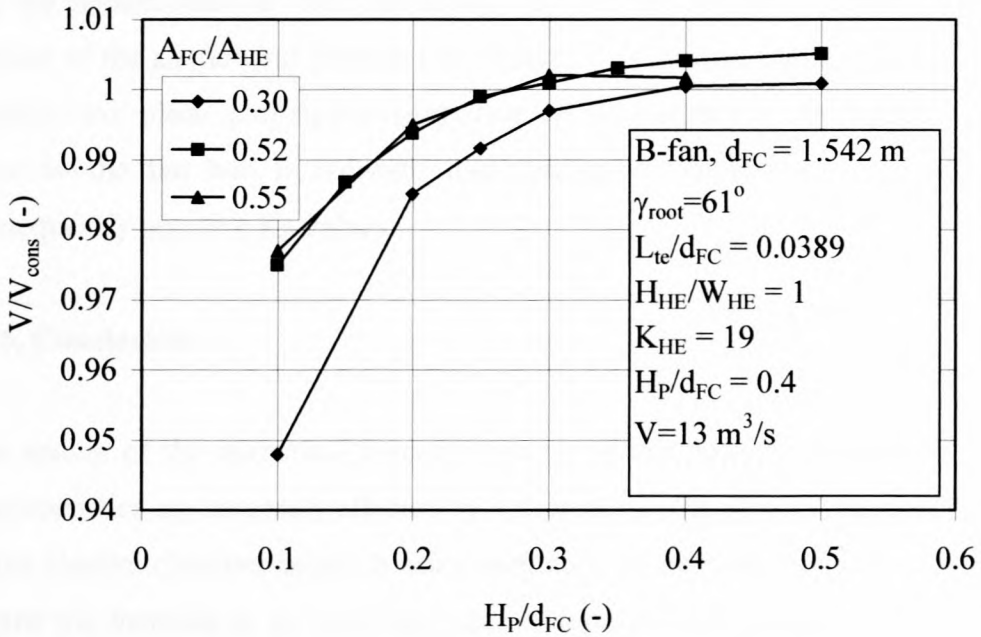

Figure 10.4. V/V_{cons} vs. H_P/d_{FC} for the range of ACHEs investigated.

From the data in figure 10.3 it is also observed that, although the same $(H_P/d_{FC})_{crit}$-value applies to induced draught ACHEs utilising any of the A_{FC}/A_{HE}-values considered, the increase in K_P-values associated with a reduction in H_P/d_{FC} below the $(H_P/d_{FC})_{crit}$-value is more dramatic for a A_{FC}/A_{HE}-value of 0.3. This trend is also suggested by the V/V_{cons}-data of figure 10.4. The obvious conclusion can be made that the more dramatic increase in K_P associated with a A_{FC}/A_{HE}-value of 0.3 is at least in part the result of increased dissipation of momentum within the plenum chamber due to the increase in the contraction effect experienced by the air flowing from the heat exchanger bundle exit to the fan inlet. A less obvious result of an increase in the A_{FC}/A_{HE}-value is that the inward radial velocity component will increase resulting in a more distorted fan inlet velocity field. The latter would adversely affect axial fan performance and would therefore yield elevated K_P-values. A distortion of the fan inlet velocity could also account for the fact that the K_P- data for A_{FC}/A_{HE}-values of 0.55 and 0.52 are near identical, seeing that the degree of distortion of the fan inlet velocity field and its consequent effect on fan performance are not necessarily linear functions of the A_{FC}/A_{HE}-value.

Figure 10.3 further indicates that for ACHEs with A_{FC}/A_{HE}-values of 0.52 and 0.55 and H_P/d_{FC}-values in excess of approximately 0.25, negative K_P-values result. The negative K_P-values result in V/V_{cons}-values larger than 1, as indicated in figure 10.4. As it is impossible

that the plenum chamber itself can in any way increase the mechanical energy per unit volume content of the air flowing through the plenum, it is thought that the flow field at the plenum chamber exit plane is of such a nature that the flow separation associated with the flow field close to the fan hub is reduced, thus leading to an increase in fan performance and consequently negative K_P-values.

10.5. Conclusions

The results of the numerical investigation show that induced draught ACHE performance characteristics are adversely affected by a decrease in the plenum chamber height. A decrease in the plenum chamber height is associated with an increase in K_P. At low plenum chamber depths the increase in K_P becomes more severe. An increase in plenum chamber depth in excess of that indicated by the $(H_P/d_{FC})_{crit}$-value has a negligible effect on induced draught ACHE performance characteristics. A $(H_P/d_{FC})_{crit}$-value of 0.3 is recommended for design purposes.

The results also indicate that, although a change in the A_{FC}/A_{HE}-value has an insignificant effect on the $(H_P/d_{FC})_{crit}$-value associated with the induced draught ACHEs investigated, it does however influence the way in which K_P increases for a reduction of the H_P/d_{FC}-value. A more severe increase in K_P is associated with lower A_{FC}/A_{HE}-values. The latter should however be of little importance from a design point of view, as it is recommended that plenum chamber depths should never be less than the value indicated by a $(H_P/d_{FC})_{crit}$-value of 0.3.

The results further indicate that for induced draught ACHEs with A_{FC}/A_{HE}-values of 0.52 and 0.55 and H_P/d_{FC}-values in excess of approximately 0.25 negative K_P-values result where the latter is thought to be the result of a decrease in the flow separation associated with the flow field around the fan hub and a consequent increase in fan performance. It should however be noted that this increase in fan performance is marginal.

CHAPTER 11 - The influence of fan to heat exchanger area ratio on the plenum chamber aerodynamic behaviour associated with induced draught ACHEs

As is the case with the plenum chamber depth of induced draught ACHEs, the influence of the fan to heat exchanger area ratio on the performance characteristics of induced draught ACHEs is acknowledged in ACHE design texts [92AP1, 86AI1, 83PA1]. Recommendations concerning the acceptable A_{FC}/A_{HE}-value range are often made, as is the case with the design code of the American Petroleum Institute that recommend that the fan area should cover at least 40% of the area of the heat exchanger bundle.

The popular design texts [92AP1, 86AI1, 83PA1] are augmented by a small group of authors [60RU1, 73RO1, 79MO1] who have published their experimental results and/or recommendations in open literature.

In a general overview of ACHE design practice, Rubin [60RU1] states that, although it is common practice that the heat exchanger bundle width and fan diameter coincide, induced draught ACHEs are in use where the fan diameter covers only 60 - 80% of the bundle width. It is assumed that Rubin [60RU1] refers to heat exchanger bundles displaying a square cross-sectional profile.

In a paper written as a supplement to the 1968 API Standard 661 [68AP1] Rose et al. [73RO1] state that the fan area should cover at least 30% of the heat exchanger bundle area. A value of 40% is recommended by Monroe [79MO1].

Although nearly every one of the above-mentioned papers contains some form of recommendation with regards to the fan to heat exchanger area ratio, very little is available in terms of experimental evidence to justify these recommendations. As a result the object of the numerical investigation associated with the current chapter was to evaluate a range of induced draught ACHEs that are identical but for the fan to heat exchanger area utilised in order to determine in what way and to what extent induced draught ACHE performance characteristics are influenced by the fan to heat exchanger area ratio. The range of fan to heat exchanger area

ratios considered were chosen in such a way as to be representative of that used in induced draught ACHEs found in industry.

11.1. Numerical procedure

The influence of A_{FC}/A_{HE} on the plenum chamber aerodynamic behaviour associated with induced draught ACHEs was determined by numerically investigating a range of ACHEs where all variable values used to characterise an ACHE uniquely, as demonstrated in Chapter 10, were kept constant whilst treating A_{FC}/A_{HE} as a variable. Table 11.1 lists the range of induced draught ACHEs numerically investigated.

Table 11.1. Range of ACHEs numerically investigated.

No. (-)	γ_{root} (°)	d_{FC} (m)	L_{te}/d_{FC} (-)	H_{HE} (m)	H_{HE}/W_{HE} (-)	K_{HE} (-)	H_P/d_{FC} (-)	A_{FC}/A_{HE} (-)	V (m^3/s)	K_{source} (-)
1	61	1.542	0.0389	2.5	1	19.10	0.4	0.299	13.00	-83.092
2	61	1.542	0.0389	2.3	1	19.10	0.4	0.353	13.00	-53.784
3	61	1.542	0.0389	2.161	1	19.10	0.4	0.400	13.00	-37.660
4	61	1.542	0.0389	2.1	1	19.09	0.4	0.423	13.00	-31.461
5	61	1.542	0.0389	1.983	1	19.09	0.4	0.475	13.00	-21.148
6	61	1.542	0.0389	1.93	1	19.10	0.4	0.501	13.00	-16.939
7	61	1.542	0.0389	1.9	1	19.09	0.4	0.517	13.00	-14.735
8	61	1.542	0.0389	1.84	1	19.09	0.4	0.552	13.00	-10.546

A K_{HE}-value of 19.1 was used, as it falls within the range of K_{HE}-values most often used in industrial ACHEs. A H_P/d_{FC}-value of 0.4 was employed for all the ACHEs investigated. The latter was based on the results of Chapter 10 that indicate that the $(H_P/d_{FC})_{crit}$-value did not exceed 0.35. A constant volume flow rate of 13 m^3/s was employed as this value coincided with the point of maximum fan static efficiency for the B-fan with a γ_{root}-value of 61°.

The analysis of Chapter 10 was employed to determine K_{source}, K_P and V/V_{cons} from the numerical data for the range of ACHEs investigated.

11.2. Discussion of results

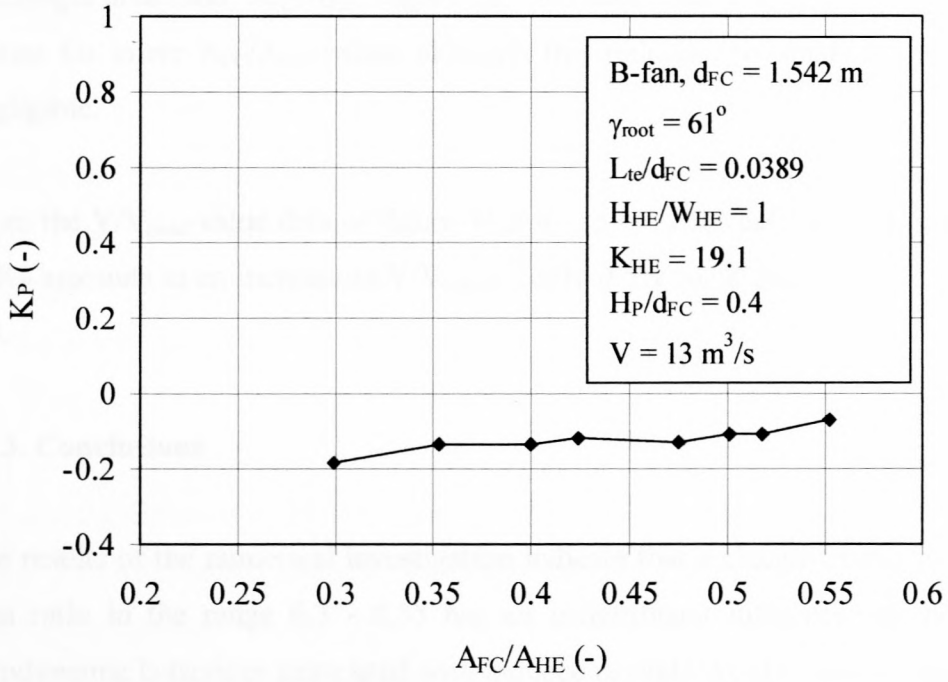

Figure 11.1. K_P plotted as a function A_{FC}/A_{HE} for the range of ACHEs investigated.

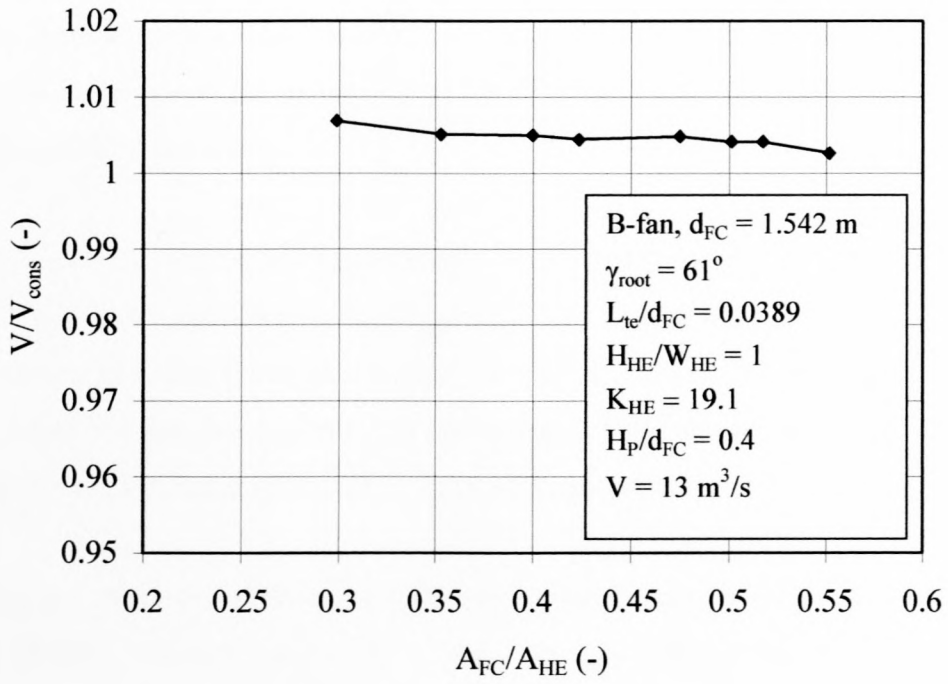

Figure 11.2. V/V_{cons} plotted as a function of A_{FC}/A_{HE} for the range of ACHEs investigated.

Figures 11.1 and 11.2 display K_P and V/V_{cons} respectively as a function of the fan to heat exchanger area ratio, A_{FC}/A_{HE}. Figure 11.1 indicates that there is a slight reduction in the K_P-values for lower A_{FC}/A_{HE}-values although this reduction is small enough to be considered negligible.

From the V/V_{cons}-value data of figure 11.2 it can be seen that the above-mentioned reduction in K_P amounts to an increase in V/V_{cons} of only 0.5% for a decrease in A_{FC}/A_{HE} from 0.55 to 0.3.

11.3. Conclusions

The results of the numerical investigation indicate that a change in the fan to heat exchanger area ratio in the range 0.3 - 0.55 has an insignificant influence on the plenum chamber aerodynamic behaviour associated with induced draught ACHEs and consequently also on the ACHE performance characteristics.

CHAPTER 12 - The influence of axial flow fan operation on the plenum chamber aerodynamic behaviour associated with induced draught ACHEs

In popular texts concerned with the design of induced draught ACHE [92AP1, 86AI1, 83PA1] the type of axial flow fan used and its ensuing influence on induced draught ACHE performance characteristics are limited entirely to the information contained in the fan performance characteristics as determined in a code fan test facility according to the specifications set in, for example, BS 848 [80BS1] of the British Standards Organisation.

Fortunately this state of affairs is not the result of gross ignorance on the part of investigators concerned with ACHE performance characteristics, but rather based on the close similarity that exists between the fan installation in a code fan test facility and an induced draught ACHE. In the code fan test facility shown schematically in figure C.1 in Appendix C the settling chamber and mesh screens at the settling chamber inlet perform the same task as the plenum chamber and heat exchanger respectively in an induced draught ACHE.

However Russell and Berryman [88RU1] in their comparison of three sets of induced draught ACHE performance data note that some of the differences observed in the experimental data can be attributed to the sensitivity of the different axial flow fans used to flow distortions at the respective fan inlets.

In Chapter 10 of this text mention was made that the axial flow fan of an induced draught ACHE with a relatively low A_{FC}/A_{HE}-value was in all probability subject to a larger degree of distortion of its fan inlet velocity field than ACHEs utilising higher A_{FC}/A_{HE}-values. It should be noted that the last statement is applicable only where the plenum chamber height is less than the critical value indicated by the $(H_P/d_{FC})_{crit}$-value.

From the above it is clear that the fan performance characteristics as determined in a code fan test facility, do not necessarily contain enough information to describe the performance characteristics of the same fan in an induced draught ACHE accurately. Indications are, however, that the inadequacy of the standard fan performance characteristics are only

significant in induced draught ACHEs where either plenum chamber height and/or fan to heat exchanger area ratio values fall outside the recommended ranges. The object of the current numerical investigation was therefore to determine whether changes to the axial flow fan geometry and operation used in an induced draught ACHE with plenum chamber height and fan to heat exchanger area ratio that fall within the specified ranges could have a detrimental affect on induced draught ACHE performance characteristics.

12.1. Numerical procedure

As mentioned earlier, the performance of an axial flow fan can be affected through a change in either the volume flow rate and/or a change of the blade setting indicated by the γ_{root}-value. The influence of the axial flow fan on ACHE performance can therefore be isolated by keeping the geometrical characteristics of the range of ACHEs tested as well as the associated heat exchanger bundle K_{HE}-values constant whilst treating the operating point volume flow rate and the γ_{root}-value as variable.

An A_{FC}/A_{HE}-, H_{PL}/d_{FC}- and K_{HE}-values of 0.517, 0.4 and 19 were used. These values fall within the respective acceptable ranges set for these variables.

Table 12.1 lists the ACHEs that were numerically investigated.

Table 12.1. The range of induced draught ACHEs numerically investigated.

No. (-)	γ_{root} (°)	d_{FC} (m)	L_{te}/d_{FC} (-)	H_{HE} (m)	H_{HE}/W_{HE} (-)	K_{HE} (-)	H_P/d_{FC} (-)	A_{FC}/A_{HE} (-)	V (m^3/s)	K_{source} (-)
1	63.5	1.54	0.0389	1.9	1	18.91	0.4	0.517	12.00	-15.986
2	63.5	1.54	0.0389	1.9	1	18.89	0.4	0.517	13.00	-7.508
3	63.5	1.54	0.0389	1.9	1	18.89	0.4	0.517	14.00	-0.827
4	63.5	1.54	0.0389	1.9	1	18.89	0.4	0.517	15.00	5.196
5	63.5	1.54	0.0389	1.9	1	18.89	0.4	0.517	16.00	10.105
6	63.5	1.54	0.0389	1.9	1	18.89	0.4	0.517	17.00	14.105
7	61	1.54	0.0389	1.9	1	18.91	0.4	0.517	12.00	-23.063
8	61	1.54	0.0389	1.9	1	18.90	0.4	0.517	13.00	-14.857
9	61	1.54	0.0389	1.9	1	18.90	0.4	0.517	14.00	-7.723
10	61	1.54	0.0389	1.9	1	18.90	0.4	0.517	15.00	-1.796
11	61	1.54	0.0389	1.9	1	18.89	0.4	0.517	16.00	2.743
12	61	1.54	0.0389	1.9	1	18.89	0.4	0.517	17.00	7.154
13	58	1.54	0.0389	1.9	1	18.91	0.4	0.517	12.00	-27.940
14	58	1.54	0.0389	1.9	1	18.90	0.4	0.517	14.00	-12.721
15	58	1.54	0.0389	1.9	1	18.89	0.4	0.517	15.00	-7.251
16	58	1.54	0.0389	1.9	1	18.89	0.4	0.517	16.00	-2.648
17	58	1.54	0.0389	1.9	1	18.89	0.4	0.517	17.00	1.439

12.2. Discussion of results

Figures 12.1 and 12.2 display K_{PL} and V/V_{cons} respectively as a function of the operating point volume flow rate of the range of induced draught ACHEs investigated. The numerical results indicate that a change in the fan blade root stagger angle and the operating point volume flow rate have a negligible influence on both the K_P- and V/V_{cons}-value data.

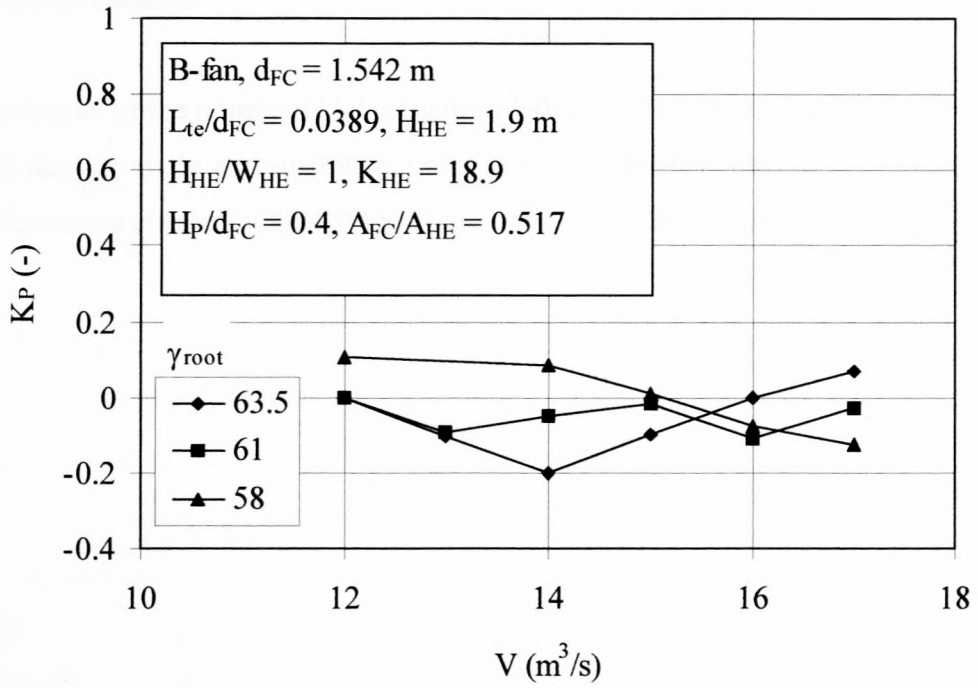

Figure 12.1. K_P as a function of V for the range of ACHEs investigated.

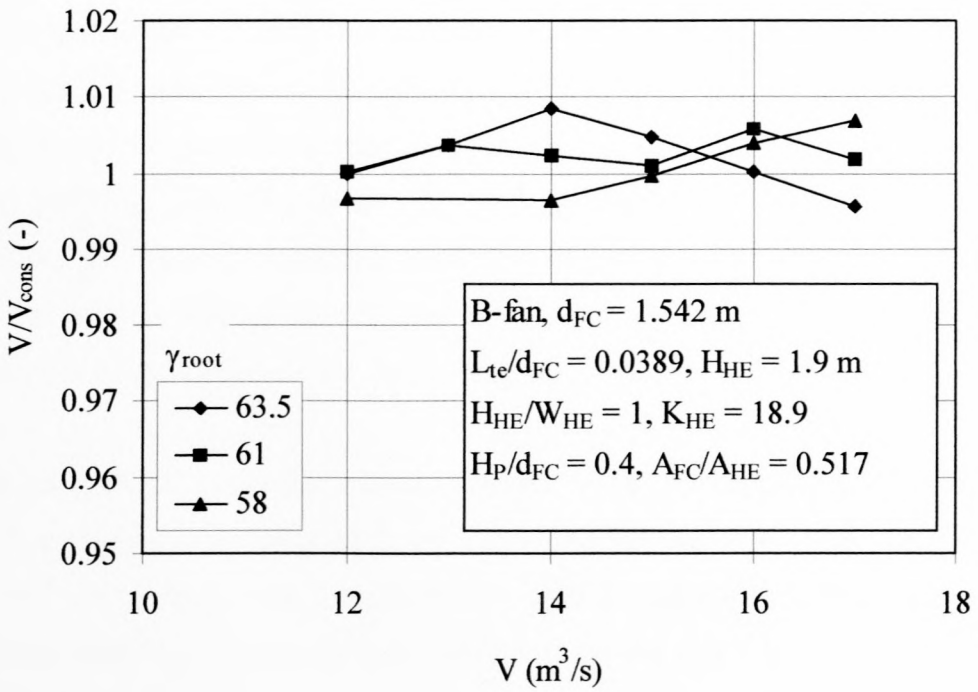

Figure 12.2. V/V_{cons} as a function of V for the range of ACHEs investigated.

12.3. Conclusions

The results of the numerical investigation indicates that any change to the axial flow fan blade root stagger angle and operating point volume flow rate have a negligible influence on the performance characteristics of the range of induced draught ACHEs investigated.

CHAPTER 13 - The influence of the axial flow fan position within the fan ring on the plenum chamber aerodynamic behaviour associated with induced draught ACHEs

In the discussion concerned with the influence of axial flow fan position within the fan ring on forced draught ACHE performance characteristics contained in Chapter 9 of this text mention was made of two distinctly different areas of influence. The first area of influence was concerned with flow disturbances associated with the type of inlet used at the fan ring. Depending on the location of the axial flow fan within the fan ring these flow disturbances could influence fan performance characteristics and consequently that of the ACHE adversely. The second area of influence was concerned with the additional diffusive effect in the plenum chamber of a forced draught ACHE associated with the rotational component of the velocity field at the fan rotor exit plane. It follows that the latter could only influence induced draught ACHE performance should the fan ring exit be furnished with a diffuser.

The Engineering Design Handbook of the United States Army [75US1] states that, although the optimum fan position should best be determined experimentally, it is recommended in general that two-thirds of the projected width of the axial flow fan should penetrate into the fan shroud for induced draught ACHEs. The same observations were made by Taylor and Chu [76TA1], following an investigation into the performance characteristics of a range of induced draught ACHEs utilised for automotive engine cooling purposes. As noted in Chapter 9, the ACHEs used in military and automotive applications are in general associated with short fan casings due to space limitations.

Kröger [98KR1] states that induced draught ACHE performance characteristics are invariant with a change in the location of the axial flow fan within the fan ring, provided that a bell mouth type inlet is used in combination with a sufficiently long fan ring. As noted earlier Kröger [98KR1] refers to the combination of the fan ring inlet section and the fan ring as the fan casing and specifies a fan casing axial length of at least 1/6 fan diameter.

The objective of the current investigation was to evaluate numerically the performance characteristics of a range of induced draught ACHEs that differ only in the location of the axial flow fan within the fan ring. The range of ACHEs investigated were furnished with bell mouth type inlets at the fan ring and the latter was of sufficient length according to the specifications by Kröger [98KR1].

13.1. Numerical procedure

Figure 10.1 of Chapter 10 indicates that the position of the axial flow fan within the fan casing is characterised by the L_{te}/d_{FC}-value. The influence of the latter on induced draught ACHE performance characteristics was isolated by treating all other variable values used to characterise the ACHE as constant, whilst evaluating different values of L_{te}/d_{FC}. Table 13.1 lists the two induced draught ACHEs numerically investigated.

The particular K_{HE}- and A_{FC}/A_{HE}-values used were chosen so as to fall within the range of values used in induced draught ACHEs used in industry, whilst the operating point volume flow rate was chosen to ensure operation close to the point of maximum fan static efficiency.

The analysis described in Chapter 10 was employed to determine K_{source}, K_P, and V/V_{cons} from the numerical data for the range of ACHEs investigated.

Table 13.1. Range of induced draught ACHEs numerically investigated.

No. (-)	γ_{root} (deg)	d_{FC} (m)	L_{te}/d_{FC} (-)	H_{HE} (m)	H_{HE}/W_{HE} (-)	K_{HE} (-)	H_P/d_{FC} (-)	A_{FC}/A_{HE} (-)	V (m^3/s)	K_{source} (-)
1	61	1.542	0.0389	1.9	1	19.09	0.4	0.517	13.00	-14.73
2	61	1.542	0.0043	1.9	1	18.90	0.4	0.517	13.00	-15.00

13.2. Discussion of results

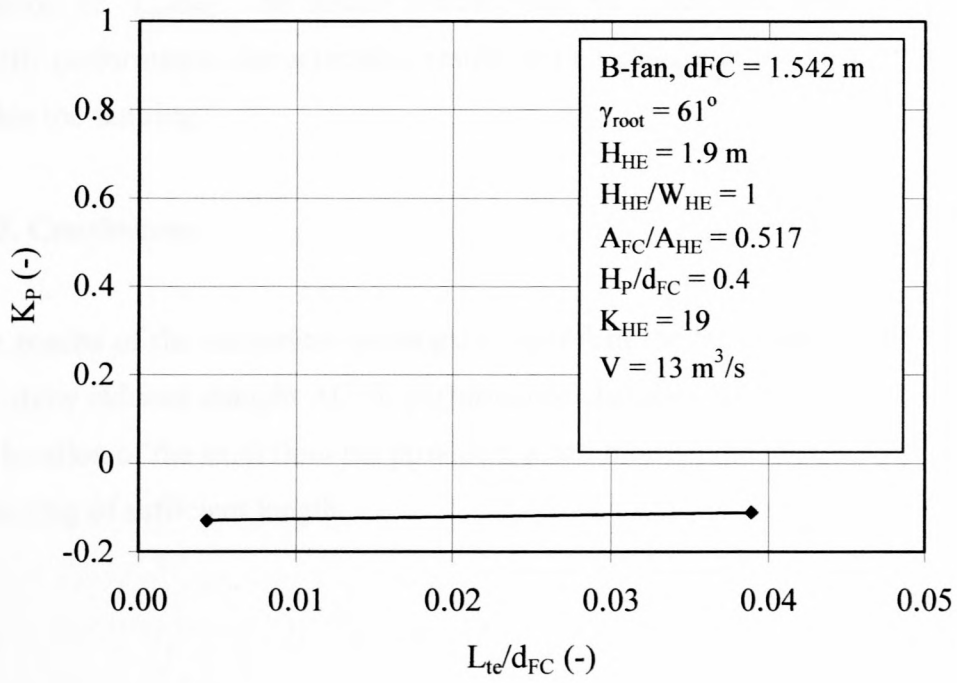

Figure 13.1. Plenum pressure loss as a function of the position of the axial flow fan.

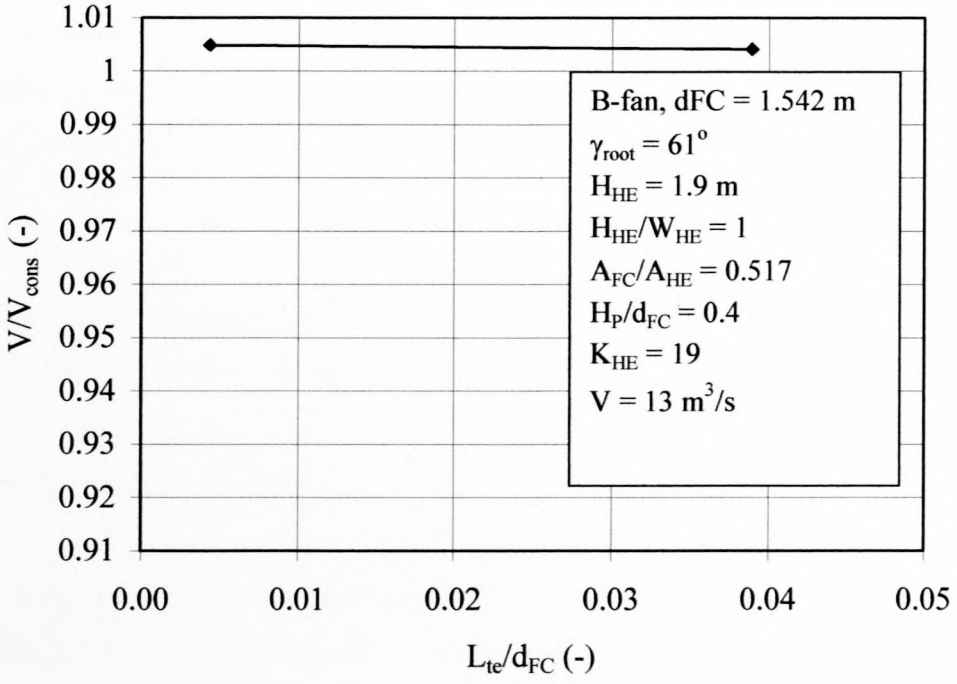

Figure 13.2. V/V_{cons} plotted as a function of the position of the axial flow fan.

Figures 13.1 - 13.2 display the K_P- and V/V_{cons}-values of the ACHEs investigated as a function of L_{te}/d_{FC}. The results indicate that no observable influence on induced draught ACHE performance characteristics results with a change in the location of the axial flow fan within the fan ring.

13.3. Conclusions

The results of the numerical investigation confirm the statements made by Kröger [98KR1] and show induced draught ACHE performance characteristics to be invariant with a change in the location of the axial flow fan provided, a bell mouth type inlet is used in combination with a fan ring of sufficient length.

CHAPTER 14 - The influence of heat exchanger bundle flow resistance on the plenum chamber aerodynamic behaviour associated with induced draught ACHEs

One of the advantages associated with the use of induced as opposed to forced draught ACHEs is that the heat exchanger bundle is not subject to flow maldistribution [60RU1], where the latter is said to affect the heat transfer performance characteristics of the heat exchanger bundle [98ME1] adversely.

Earlier mention was made of the close similarity that exists between the fan installation in a typical induced draught ACHE and that in a code fan test facility, such as that described in BS 848 [80BS1] of the British Standards Organisation and shown in figure C.1. In the code fan test facility a uniform velocity field at the fan inlet is ensured with the fitting of several mesh screens at the settling chamber inlet. The heat exchanger bundle in a typical induced draught ACHE fulfills a similar function as the mesh screens. Due to the orientation of the finned surfaces of the finned tubes used to build up a heat exchanger bundle, the flow issuing from a heat exchanger irrespective of the magnitude of its flow resistance value will most probably be orientated in the fan axial direction As a result it is very unlikely that the heat exchanger bundle resistance could have a marked influence on the system effect associated with induced draught ACHEs.

The objective of the current numerical investigation was to numerically investigate the plenum chamber aerodynamic behaviour associated with a range of induced draught ACHEs that were identical but for the heat exchanger bundle flow resistance value used.

14.1. Numerical procedure

The influence of the heat exchanger bundle resistance on induced draught ACHE performance characteristics was determined by numerically investigating a range of ACHEs where the variable values used to characterise uniquely a particular induced draught ACHE as

demonstrated in Chapter 10, were kept constant, whilst treating K_{HE} as variable. Table 14.1 lists the range of induced draught ACHEs numerically investigated.

An A_{FC}/A_{HE}-value of 0.517 was used, as it falls midway in the range of A_{FC}/A_{HE}-values typically used in industrial induced draught ACHEs. An operating point volume flow rate of 13 m^3/s was used as it is close to the point of maximum fan static efficiency. A H_P/d_{FC}-value of 0.4 was employed as this is higher than the $(H_P/d_{FC})_{crit}$-value of 0.3 indicated in Chapter 10.

The analysis described in Chapter 10 was employed to determine K_{source}, K_{PL} and V/V_{cons} from the numerical data for the range of ACHEs investigated.

Table 14.1. Range of induced draught ACHEs numerically investigated.

No. (-)	γ_{root} (°)	d_{FC} (m)	L_{te}/d_{FC} (-)	H_{HE} (m)	H_{HE}/W_{HE} (-)	K_{HE} (-)	H_P/d_{FC} (-)	A_{FC}/A_{HE} (-)	V (m^3/s)	K_{source} (-)
1	61	1.542	0.0389	1.9	1	4.78	0.4	0.517	13.00	-28.992
2	61	1.542	0.0389	1.9	1	9.51	0.4	0.517	13.00	-24.252
3	61	1.542	0.0389	1.9	1	14.22	0.4	0.517	13.00	-19.544
4	61	1.542	0.0389	1.9	1	19.09	0.4	0.517	13.00	-14.735
5	61	1.542	0.0389	1.9	1	23.57	0.4	0.517	13.00	-10.190

14.2. Discussion of results

Figures 14.1 and 14.2 display K_P and V/V_{cons} as a function of the heat exchanger K_{HE}-value. The numerical results indicate that a change in K_{HE} has no observable influence on the system effect associated with induced draught ACHEs. It should however be noted that the latter is only applicable where the plenum chamber height is higher than the value indicated by the $(H_P/d_{FC})_{crit}$-value.

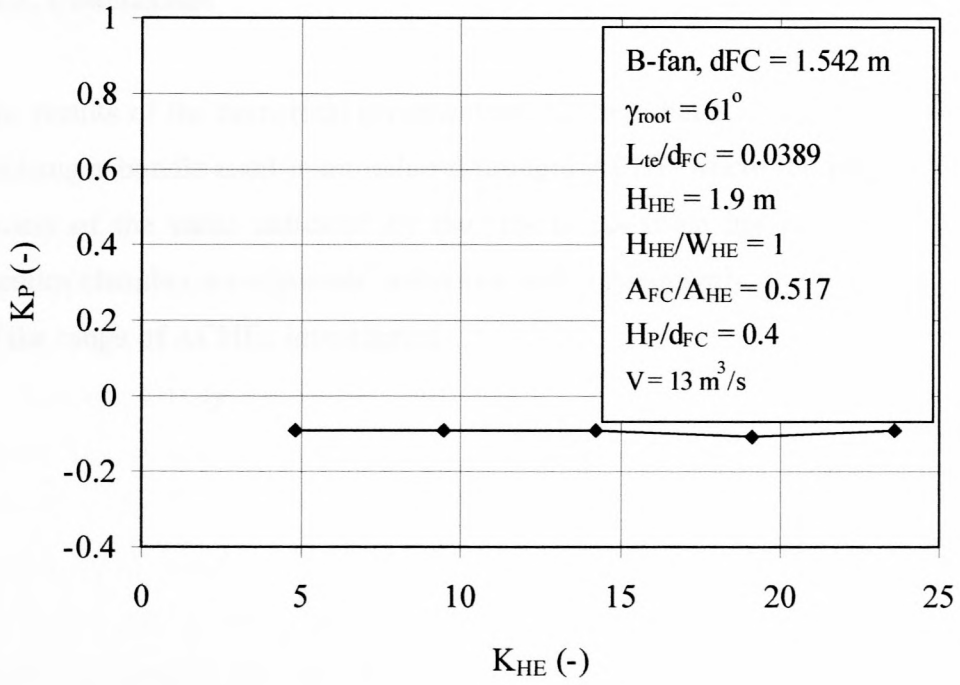

Figure 14.1. K_P as a function of K_{HE} for the range of ACHEs investigated.

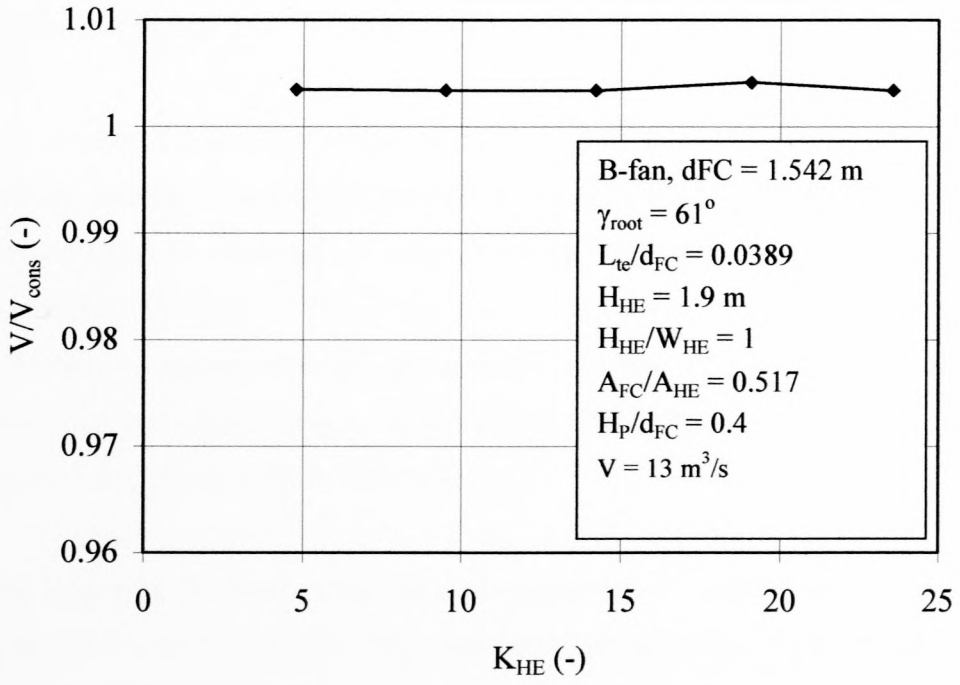

Figure 14.2. V/V_{cons} as a function of K_{HE} for the range of ACHEs investigated.

14.3. Conclusions

The results of the numerical investigation indicate that a change in the K_{HE}-value of the heat exchanger bundle used in an induced draught ACHE where the plenum chamber height is in excess of the value indicated by the $(H_P/d_{FC})_{crit}$-value has no observable influence on the plenum chamber aerodynamic behaviour and consequently on the performance characteristics of the range of ACHEs investigated.

CHAPTER 15 - Closure

A review of the limited number of publications concerned with the design and function of mechanical draught ACHEs indicate that relatively little consideration is given to the aerodynamic features as opposed to structural aspects of mechanical draught ACHEs. A sound knowledge of the aerodynamic behaviour of mechanical draught ACHEs is desirable, as designs that are aerodynamically inefficient can be avoided and the accuracy with which the ACHE operating point can be determined can be increased.

Although all current methods used to predict the operating point of mechanical draught ACHEs make use of both the axial flow fan and heat exchanger performance characteristics, the aerodynamic behaviour of the plenum chamber is often neglected. The plenum chamber occupies a very strategic position within both forced and induced draught ACHEs as its aerodynamic behaviour is influenced by not only its geometrical characteristics, but also by the aerodynamic interaction with both the axial flow fan and the heat exchanger bundle. This suggests that the plenum chamber aerodynamic behaviour plays an important part in mechanical draught ACHE performance characteristics.

This dissertation is an effort to address the need for not only a better understanding of the plenum chamber aerodynamic behaviour of both forced and induced draught ACHEs, but also the need for the quantitative inclusion of plenum chamber aerodynamic behaviour into the mechanical draught ACHE design process. During the course of the investigation the influence of component and geometrical changes on the plenum chamber aerodynamic behaviour and consequently of the performance characteristics of a range of forced and induced draught ACHEs is determined.

Due largely to flexibility, cost and time constraints a numerical as opposed to an experimental approach to the investigation was taken. For this purpose a commercially available CFD-code augmented with user-defined models to include the effect of the axial flow fan and heat exchanger bundle on the ACHE flow field was utilised to investigate the performance characteristics of a range of forced and induced draught ACHEs. Detail pertaining to the user-defined axial flow fan and heat exchanger model as well as the numerical techniques

employed by the CFD-code to resolve the flow fields through the range of ACHEs investigated can be found in Chapter 4.

15.1. Conclusions and recommendations

In Chapter 3 the draught equations formulated in Chapter 2 were used to investigate the sensitivity of forced and induced draught ACHE performance characteristics to a change in the plenum chamber aerodynamic behaviour, expressed as $d(V/V_{cons})/dK_{rec}$ and the absolute value of $d(V/V_{cons})/dK_P$ respectively. The V/V_{cons}-value is used as an indication of the magnitude of the plenum chamber aerodynamic behaviour associated with a particular forced or induced draught ACHE. This contrasts the operating point volume flow rate yielded by the draught equation when no provision is made for the plenum chamber aerodynamic behaviour, with the operating point volume flow rate predicted when the plenum chamber aerodynamic behaviour is taken into account.

The analysis indicates that for forced draught ACHEs the sensitivity of V/V_{cons} to a change in K_{rec} remains virtually unchanged over the range of K_{rec}-values considered whilst at a constant K_{rec}-value the sensitivity of V/V_{cons} increases for a decrease in the K_{HE}- and A_{FC}/A_{HE}-values and an increase in the a- and b-values.

For induced draught ACHEs the sensitivity of V/V_{cons} to a change in K_P remains virtually unchanged over the range of K_P-values considered, whilst at a constant K_P-value the sensitivity of V/V_{cons} increases for a decrease in the K_{HE}- and A_{FC}/A_{HE}-values and an increase in the a- and b-values.

In Chapter 5 the influence of the axial flow fan used on the plenum chamber aerodynamic behaviour associated with forced draught ACHEs was investigated. The flow patterns within a forced draught ACHE plenum chamber are also compared to those observed by other investigators. As the investigation was limited to the use of one particular axial flow fan it is shown that the fan performance characteristics can be altered through specification of the ACHE operating point volume flow rate as well as the fan blade root stagger angle, γ_{root}.

The results indicate that transition from one flow pattern to another within the ACHE plenum chamber is associated with changes in both the operating point volume flow rate as well as the fan blade root stagger angle of the axial flow fan. These changes result in K_{rec}-values ranging from 0.4 - 0.8 which span nearly 50% of the observed K_{rec}-value range. It is clear from these results that the type of axial flow fan used can have a dramatic effect on the plenum chamber aerodynamic behaviour and hence the performance characteristics of forced draught ACHEs.

The results also indicate that the maximum K_{rec}-values associated with each of the blade root stagger angles investigated do not coincide with the volume flow rate associated with the point of maximum fan static efficiency of the particular blade root stagger angle considered. In fact, all K_{rec}-values are seen to increase for an increase in operating point volume flow rate in excess of that associated with the point of maximum fan static efficiency. These results confirm the statements made earlier to the effect that the operation of an axial flow fan within a forced draught ACHE is not necessarily comparable to that observed in a code fan test facility. It follows that the general design guideline that requires the ACHE operating point volume flow rate to coincide with the point of maximum fan static efficiency does not necessarily ensure optimum axial flow fan performance within a forced draught ACHE.

The α_{eHE}-value data shows that there exits a linear relationship between the kinetic energy coefficient at the axial flow fan exit, α_{eF} and α_{eHE}. The latter is also seen to decrease exponentially with an increase in the operating point volume flow rate.

Visualisation of the flow patterns within the plenum chambers of the ACHEs investigated indicate that the numerically determined flow patterns compare favourably with those observed by other investigators.

The high level of complexity associated with the influence of axial flow fan operation on forced draught ACHE performance characteristics makes it difficult to formulate any form of design guideline based on the results obtained using a solitary axial flow fan. As a result the recommendation by Meyer and Kröger [98ME1] that a K_{rec}-value of 0.3 be used throughout, is proposed as a conservative means with which to include the system effect into the forced draught ACHE design process.

In Chapter 6 the influence of a change in the plenum chamber height on the plenum chamber aerodynamic behaviour of a range of forced draught ACHEs was investigated and the results are compared to available experimental data. Meyer and Kröger [98ME1] define the critical plenum chamber height to fan diameter ratio, $(H_P/d_{FC})_{crit}$, as the minimum plenum chamber height that still allows a forced draught ACHE to perform in a manner that is comparable to the performance at larger plenum chamber heights. The numerical results indicate a $(H_P/d_{FC})_{crit}$ -value of 0.35, as opposed to a value of 0.3, as indicated by Meyer and Kröger [98ME1].

The numerically determined K_{rec}-values are also elevated above those reported by Meyer and Kröger [98ME1]. The discrepancies between the numerical and experimental results are thought to be the result of the differences between the axial flow fans used in the numerical and experimental investigations as well as modelling errors introduced by the various numerical strategies employed in the CFD-code to resolve the flow field through an ACHE.

Relatively good agreement is obtained between the numerically and experimentally determined α_{eHE} - values. The latter is seen to increase with a decrease in the H_P/d_{FC} - value.

The influence of a change in the heat exchanger bundle flow resistance as well as the fan to heat exchanger area ratio on the $(H_P/d_{FC})_{crit}$ -value is also shown to be negligible. Although Meyer and Kröger [98ME1] report an increase in the $(H_P/d_{FC})_{crit}$ -value at lower heat exchanger bundle flow resistances, the latter is thought to be the result of cross-flow effects through the heat exchanger bundle used in the experimental investigation.

Based on the results of the numerical investigation, a $(H_P/d_{FC})_{crit}$ -value of 0.3, as proposed by Meyer and Kröger [98ME1], is recommended for design purposes.

Chapter 7 is concerned with the influence of the fan to heat exchanger area ratio on forced draught ACHE performance characteristics. The numerical results show that K_{rec} increases in a linear fashion with an increase in A_{FC}/A_{HE}. The latter is thought to be the result of the effect of the plenum chamber walls on the tangential component of the velocity field at the fan exit. The plenum chamber walls are believed to act in a manner similar to that of fan exit guide vanes. The α_{eHE} - values are seen to increase for a reduction in A_{FC}/A_{HE}.

A high A_{FC}/A_{HE}-value, in combination with a plenum chamber utilising a square cross-sectional area, is recommended for design purposes.

Chapter 8 indicates that an increase in the heat exchanger bundle flow resistance is associated with a very slight and linear increase in K_{rec}, whilst α_{eHE} is seen to decrease with an increase in heat exchanger bundle flow resistance.

Chapter 9 concludes the investigation of forced draught ACHE performance characteristics and reports that a change in the location of the axial flow fan within the fan casing has a negligible influence on K_{rec} as well as α_{eHE}, provided that a bell mouth type inlet is used at the fan ring and that the axial length of the bell mouth fan ring combination is at least 1/6 of the fan diameter according to the recommendations of Kröger [98KR1].

Appendix G of this text contains a correlation for both K_{rec} and α_{eHE} based on the results of the numerical investigations of Chapters 5 to 8. It should however be noted that these correlations are not necessarily applicable to forced draught ACHEs making use of different types of axial flow fans and heat exchanger bundles than those used for this investigation. The use of the correlations contained in Appendix G for general design purposes is strongly discouraged.

In Chapter 10 the effect of a change of the plenum chamber height, H_P on the plenum chamber aerodynamic behaviour associated with induced draught ACHEs was investigated. The numerical results indicate that induced draught ACHE performance characteristics are unaffected by a decrease in plenum chamber height until a critical plenum chamber height denoted by the $(H_P/d_{FC})_{crit}$-value is reached. A further reduction in plenum chamber height is associated with a rapid deterioration of ACHE performance characteristics and a consequent increase in K_P. The results indicate a $(H_P/d_{FC})_{crit}$-value of 0.3 for the range of induced draught ACHEs investigated. The results further show that the $(H_P/d_{FC})_{crit}$-value is unaffected by a change in the A_{FC}/A_{HE}-value although the manner in which K_P increases with a decrease in plenum chamber height below the $(H_P/d_{FC})_{crit}$-value is seen to be affected by the A_{FC}/A_{HE}-value.

A K_P-value of zero is recommended for design purposes, provided that the plenum chamber depth is not reduced beyond the value suggested by a $(H_P/d_{FC})_{crit}$-value of 0.3.

The results of the numerical investigations of Chapters 11 to 14 indicate that the influence of the fan to heat exchanger area ratio, the axial flow fan operation, the position of the axial flow fan within the fan ring and the heat exchanger bundle flow resistance respectively on the plenum chamber aerodynamic behaviour associated with induced draught ACHEs is negligible.

15.2. Future research

The relatively small number of publications concerned with the aerodynamic behaviour of mechanical draught ACHEs suggests that any further research directed at a better understanding of any one of the aspects touched upon in this dissertation will be well worth the effort.

Of particular importance to further research is the demonstrated ability of obtaining valuable data through the near exclusive use of a commercially available CFD code. Use of the latter is an especially attractive option when considering the near prohibitive time and cost constraints associated with an experimental investigation of the aerodynamic behaviour of a wide range of mechanical draught ACHEs.

Although attractive, it should be remembered that the accuracy and reliability of commercially available CFD codes have as yet not progressed beyond the point where all experimental investigation can be considered obsolete. As a result a combined approach that include both numerical and experimental techniques is recommended for future research.

The influence of the axial flow fan on the plenum chamber aerodynamic behaviour of forced draught ACHEs is probably the most significant area highlighted by the investigation for future research. As noted earlier, the results indicate that changes to a single type of fan affects a change in K_{rec} that spans nearly 50% of the observed K_{rec}-value range. The manner in which the geometrical and operating characteristics of different axial flow fans influence

the velocity profile at the fan exit plane and the influence of the latter on the plenum chamber aerodynamic behaviour is as yet undetermined and warrants further investigation.

Closely related to the influence exerted on the plenum chamber aerodynamic behaviour of forced draught ACHEs by the axial flow fan, is the influence of the fan to heat exchanger area ratio. It was speculated that the walls of the plenum chamber act in a manner similar to guide vanes upon the velocity field at the fan exit plane in that a portion of the energy associated with the tangential component of the velocity field is recovered. The latter indicates that the addition of fan exit guide vanes could improve the plenum chamber aerodynamic behaviour of forced draught ACHEs and consequently suggests further investigation.

APPENDIX A - Heat exchanger inlet flow losses

Forced draught ACHEs have in the past been employed as condenser units in power stations [81KO1 and 93GO1] where the large size of these units and space limitations have popularised the idea of arranging the heat exchanger finned tube bundles in V-styled arrays. It was however noted that the use of this arrangement is characterised by an increase in the heat exchanger air flow losses, especially in instances where the semi-apex angle, θ, of the "V" is small [84MO1]. Increased heat exchanger bundle flow resistance as a result of air entering the heat exchanger bundle at an oblique angle is also associated with forced draught ACHEs, where the heat exchanger bundle is perpendicular to the axial flow fan axis [96ME1].

This increase in heat exchanger air flow losses has prompted a number of theoretical and/or experimental investigations. A number of investigations focussed on air flow losses associated with the flow field downstream of heat exchangers [79MO1, 86KO1, 93VA1] whilst another group of investigators focussed their attention on the flow losses incurred when air enters the heat exchanger at an oblique angle [72PR1, 77MO1, 84FI1, 84MO1, 98ME1] .

Although mainly concerned with changes in heat transfer characteristics, Fisher [84FI1] reports a progressive increase in heat exchanger flow losses as a result of a decrease in the semi-apex angle, θ of a range of heat exchangers. Note that $\theta = 90°$ refers to the instance where the air approaches the face of the heat exchanger at a right angle. Preece and Hitchcock [72PR1] reports a 7% to 28% difference in the static pressure differences measured across heat exchangers inclined at a θ-value of 11.5° with a change in the orientation of the finned surfaces of the heat exchangers. Mohandes et al. [84MO1] showed that this high degree of variation encountered by Preece and Hitchcock [72PR1] was markedly reduced when total pressure rather than static pressure changes were considered.

In their investigation Mohandes et al. [84MO1] focussed attention on the heat exchanger inlet air flow losses in an effort to relate the latter to the θ - value of the heat exchanger. Apart from proposing an approximate method with which to predict the increase in heat exchanger inlet losses Mohandes et al. [84MO1] conclude that the difference in heat exchanger inlet air flow

losses due to a change in the orientation of the finned surfaces of the heat exchanger finned tubes with respect to the inlet flow field are small compared to the change in inlet losses due to a change of the θ - value of the heat exchanger.

Based on experimental results, Meyer and Kröger [98ME1] reported the dramatic effect that differences in heat exchanger inlet air flow losses resulting from different orientations of the finned surfaces of the heat exchanger finned tubes have on the performance characteristics of a forced draught ACHEs.

The aim of this appendix is to resolve some of the issues raised in the preceding paragraphs by evaluating the isothermal performance characteristics of a wide range of V-styled heat exchangers through experiment. The influence of a change in orientation of the heat exchanger finned surfaces on the heat exchanger performance characteristics over a range of semi-apex angles are investigated. The method proposed by Mohandes et al. [77MO1] with which to determine the heat exchanger inlet flow losses is critically evaluated and an alternative method is proposed.

A.1. Analysis

In section 2.4 of Chapter 2 a dimensionless isothermal total pressure loss coefficient, K, is defined as

$$K = \frac{\Delta p_t}{1/2 \cdot \rho \cdot v^2} \qquad (A.1)$$

where Δp is the total pressure loss, ρ the air density and v a characteristic velocity.

According to figure A.1, the total isothermal pressure loss coefficient of a heat exchanger, K_θ, based on the average velocity through the heat exchanger cross-sectional area can be expressed as

$$K_\theta = K_{i\theta} + K_f + K_e + K_o \qquad (A.2)$$

where $K_{i\theta}$, K_f, K_e and K_o are the inlet, frictional, exit and outlet loss coefficient respectively.

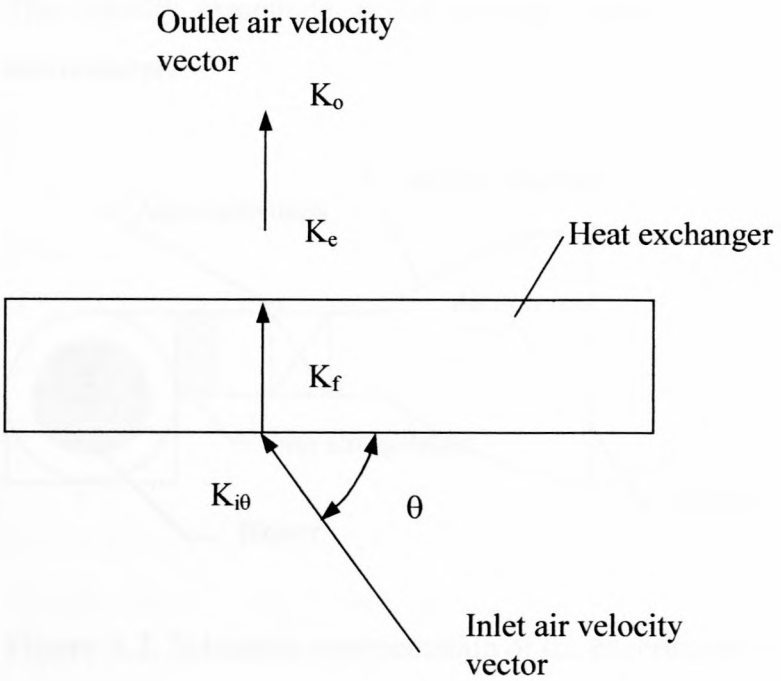

Figure A.1. Flow losses through a heat exchanger.

In section 4.6 of Chapter 4 a characteristic flow parameter, Ry, is defined as

$$Ry = \rho \cdot v/\mu \qquad (A.3)$$

where v is a characteristic velocity, ρ the fluid density and μ the fluid dynamic viscosity.

A.2. Experimental equipment

A schematic representation of the experimental set-up and detail pertaining to the test section are shown in figures A.2 and A.3 respectively. A blower forces ambient air through the wind tunnel and is immediately followed by a flow straightener that serves to smooth the exiting air from the blower. The mass flow rate through the wind tunnel is controlled via a set of adjustable flaps downstream of the flow straighteners. After passing through the adjustable

flaps, the air enters into a settling chamber furnished with a set of mesh screens. The exit of the settling chamber forms a smooth contraction that, together with the set of mesh screens within the settling chamber ensures a smooth and uniform velocity profile at the settling chamber exit. The velocity magnitude at the settling chamber exit is measured with a propeller-type anemometer.

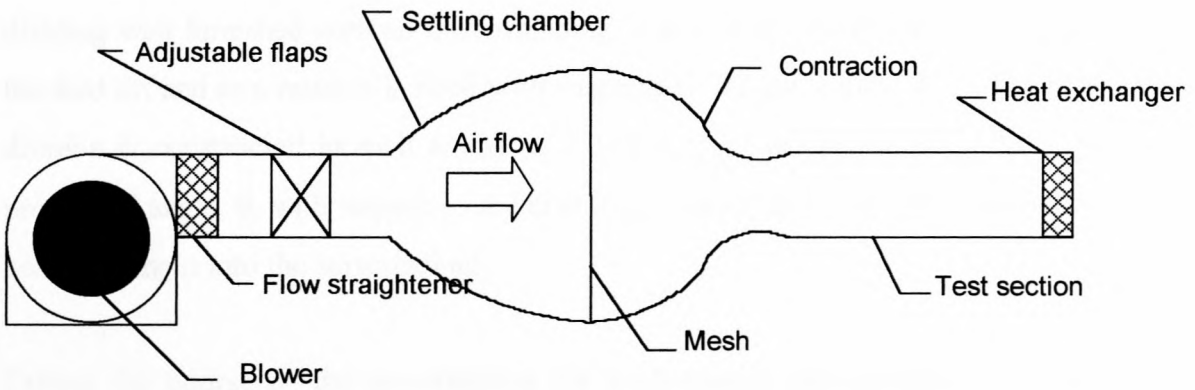

Figure A.2. Schematic representation of the experimental set-up (side elevation).

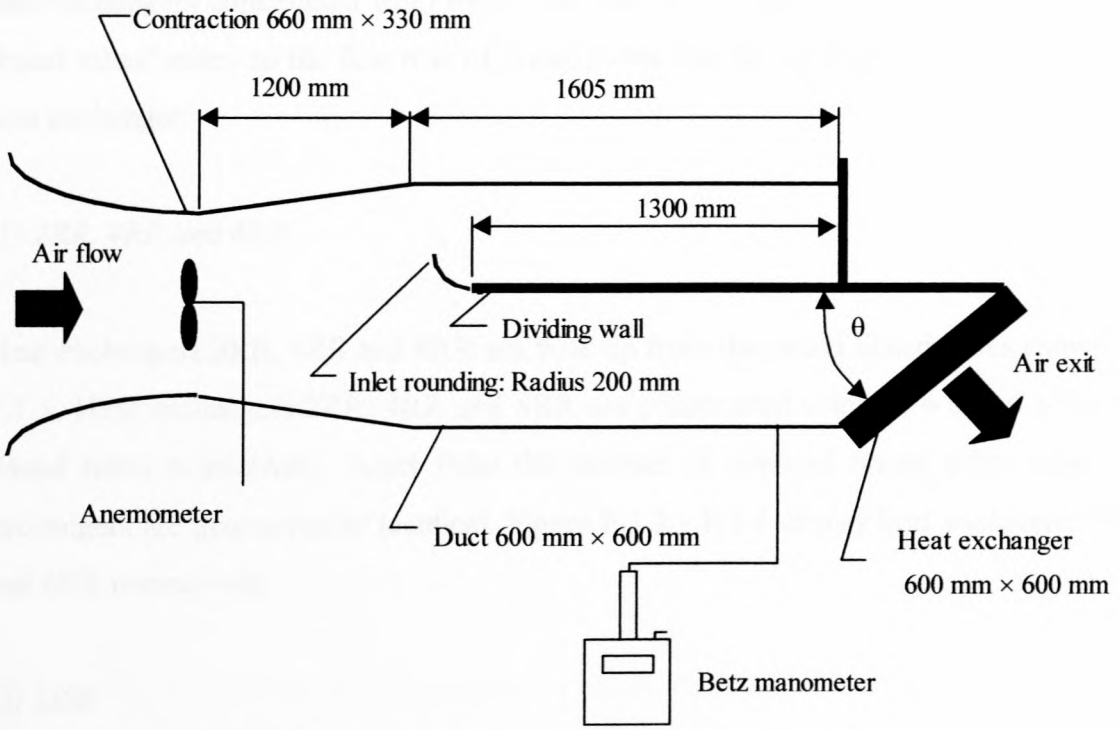

Figure A.3. Cross-sectional view of the test section (top view).

The heat exchanger test section is connected to the settling chamber exit via a length of ducting that serves as a cross-over piece between the rectangular cross-section of the settling chamber exit (0.33 m × 0.66 m) and the square cross-section of the test section (0.6 m × 0.6 m).

The test section is divided into two parts along the direction of air flow by an adjustable dividing wall furnished with an inlet rounding. The exit of one of the two divisions is totally blocked off and as a result it is filled with stagnant air during testing. The exit of the remaining division is constructed in such a way as to allow the heat exchanger to be positioned at a prescribed angle, θ, with respect to the inlet air as shown in figure A.4. The air exits from the heat exchanger into the surroundings.

During the course of the investigation the performance characteristics of 9 different heat exchangers, each with a frontal area of 600 mm × 600 mm, were evaluated. A brief description of the different heat exchangers are given below. Detailed parts and assembly drawings of the respective heat exchangers are displayed in Appendix F. It should be noted that, in the case of heat exchangers constructed from more than one row of finned tubes, the term "first row of finned tubes" refers to the first row of finned tubes that the air encounters as it flows into the heat exchanger.

(1) 2RR, 4RR and 6RR

Heat exchangers 2RR, 4RR and 6RR are built up from the round finned tubes shown in figure F.1.5. Heat exchangers 2RR, 4RR and 6RR are constructed using 2, 4 and 6 rows of round finned tubes respectively. Apart from the number of rows of finned tubes used, the heat exchangers are geometrically identical. Figure F.1.2 - F.1.4 display heat exchanger 2RR, 4RR and 6RR respectively.

(2) MSF

Heat exchanger MSF displayed in figure F.2.1 is built up of a single row of plate finned elliptical tubes of the type shown in figure F.2.3.

(3) MDC

Heat exchanger MDC, shown in figure F.2.2, is constructed using two rows of plate-finned elliptical tubes. The second row is constructed of the same finned tubes used in the construction of heat exchanger MSF. Apart from using a coarser fin pitch of 4 mm, the finned tubes in the first row of heat exchanger MDC are identical to those used in the second row. It should be noted that the finned tubes in the second row are staggered with respect to the finned tubes in the first row.

(4) SM

Heat exchanger SM, shown in figure F.3.1, is a double row heat exchanger constructed from the plate finned-elliptical tubes shown in figure F.3.2. Figure F.3.1 shows the staggered position of the second row of finned tubes with respect to those in the first row.

(5) LUM

Heat exchanger LUM is a single-row heat exchanger constructed from the plate-finned tubes shown in figure F.4.1. The plate fins exhibit a wave pattern in the direction of air flow.

(6) HUNG

Heat exchanger HUNG is constructed from a heat exchanger core as opposed to individual heat exchanger finned tubes. Figure F.5.1 shows the heat exchanger core in detail.

(7) RAD

Similar to the previous heat exchanger, heat exchanger RAD is constructed from a heat exchanger core. This particular heat exchanger core shown in figure F.6.1 finds application in automotive engine cooling systems.

A.3. Experimental procedure

After mounting a particular heat exchanger in the test section of the wind tunnel as shown in figure A.4, the static pressure drop across the heat exchanger was measured over a range of volume flow rates. The different volume flow rates were chosen so as to yield a velocity, based on the cross-sectional area of the heat exchanger, ranging from 1 to 6 m/s. This velocity range is representative of the heat exchanger velocities encountered in most industrial applications.

The procedure described in the previous paragraph was repeated for every individual heat exchanger over a range of θ-values. Both orientations of the heat exchanger were considered for every θ-value tested. The latter refers to the position of the heat exchanger finned surfaces with respect to the inlet air flow field. The finned surfaces can either be parallel or inclined to the incoming air flow field, as shown schematically in figure A.4.

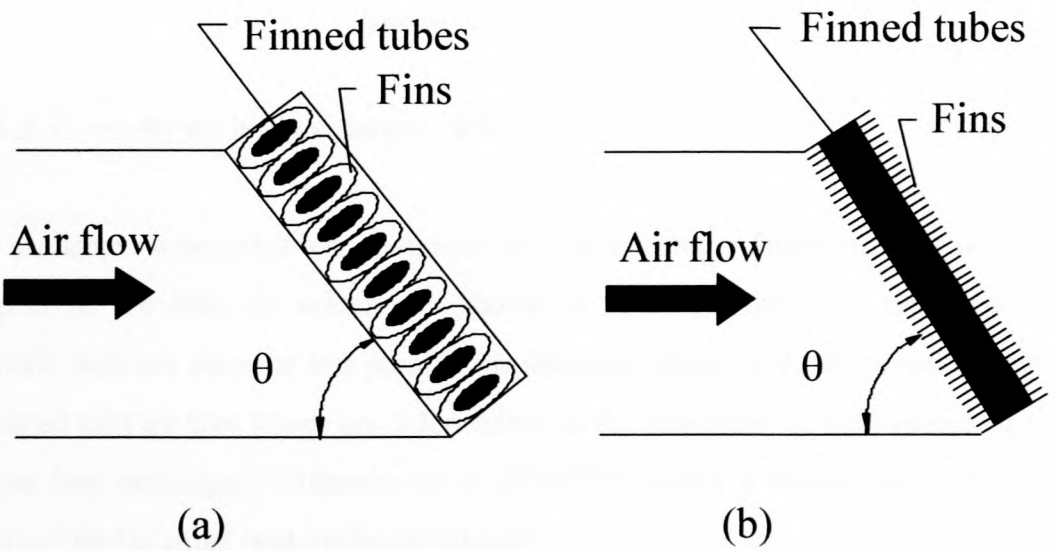

Figure A.4. Cross-sectional view through a heat exchanger inclined at an angle θ to the approaching air velocity with the finned surfaces of the finned tubes a) parallel and b) at an angle to the flow velocity.

A.4. Discussion of results

Figure A.5 displays a plot of K_θ vs. Ry for heat exchanger 6RR at different inclinations to the flow field denoted by the differing values of θ.

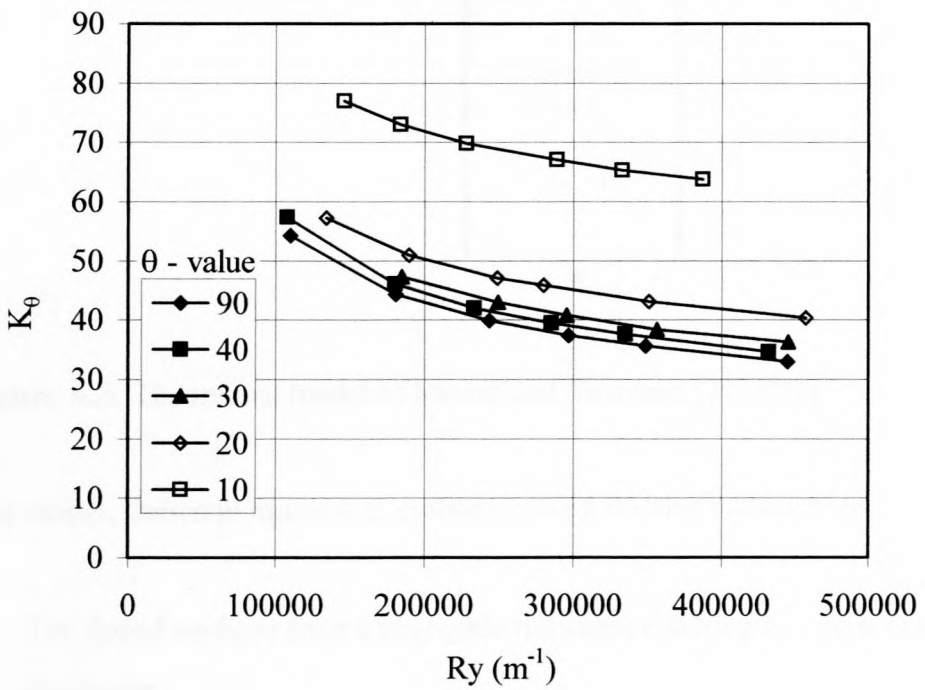

Figure A.5. K_θ vs. Ry for heat exchanger 6RR.

The heat exchanger orientation was such that the heat exchanger finned surfaces were inclined with respect to the inlet air velocity as shown in figure A.4(b). It is observed that the characteristic lines are more or less parallel for different values of θ, which would imply that the associated inlet air flow losses are independent of the magnitude of the average air velocity through the heat exchanger. Mohandes et al. [84MO1] reports a similar result. This trend is also observed for the other heat exchangers tested.

In order to relate the inlet loss coefficient, $K_{i\theta}$, in equation (A.2) to the inclination of the heat exchanger with respect to the inlet flow field, Moore and Torrance [77MO1] developed a simplified model of the flow between a set of parallel plates.

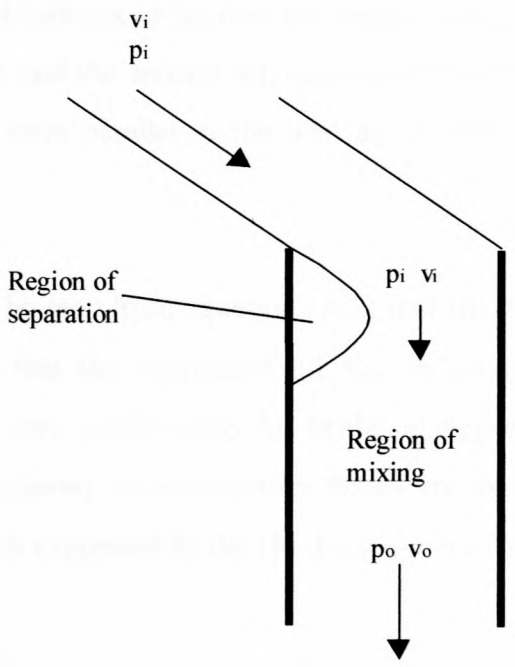

Figure A.6. Theoretical model of Moore and Torrence [77MO1].

The model, shown in figure A.6, embodies the following assumptions

- The finned surfaces have a negligible thickness resulting in a zero solidity ratio for the heat exchanger.
- Upon entering the space between the finned surfaces flow separation occurs. The pressure within the separated region equals that of the inlet air and as a result the initial velocity between the finned surfaces equals the inlet velocity.
- Downstream of the separated region the air expands to fill the space between the finned surfaces.

The following expression for the inlet loss results

$$K_{i\theta} = (1/\sin\theta - 1)^2 \qquad (A.4)$$

Figures A.7 - A.15 compares the (K_θ- $K_{\theta=90°}$) - values for the heat exchangers tested with $K_{i\theta}$, calculated according to equation (A.3) over a range of θ-values. Two sets of experimental data points are displayed in these figures. The first set, denoted by the letter A, refers to the instance

where the finned surfaces of the heat exchanger finned tubes were orientated at an angle to the inlet air velocity and the second set, denoted by the letter P refers to the instance where the finned surfaces were parallel to the inlet air velocity as shown in figure A.4(a) and A.4(b) respectively.

Although it can be seen from equation (A.2) that (K_θ-$K_{\theta=90°}$) is not equivalent to $K_{i\theta}$, it should be remembered that the expression for $K_{i\theta}$, as displayed in equation (A.2), embodies the assumption of a zero solidity ratio due to the negligible thickness of the heat exchanger finned surfaces. Consequently no contraction losses are accounted for in equation (A.2). This is essentially what is expressed by the (K_θ-$K_{\theta=90°}$)-values of figures A.7 - A.15.

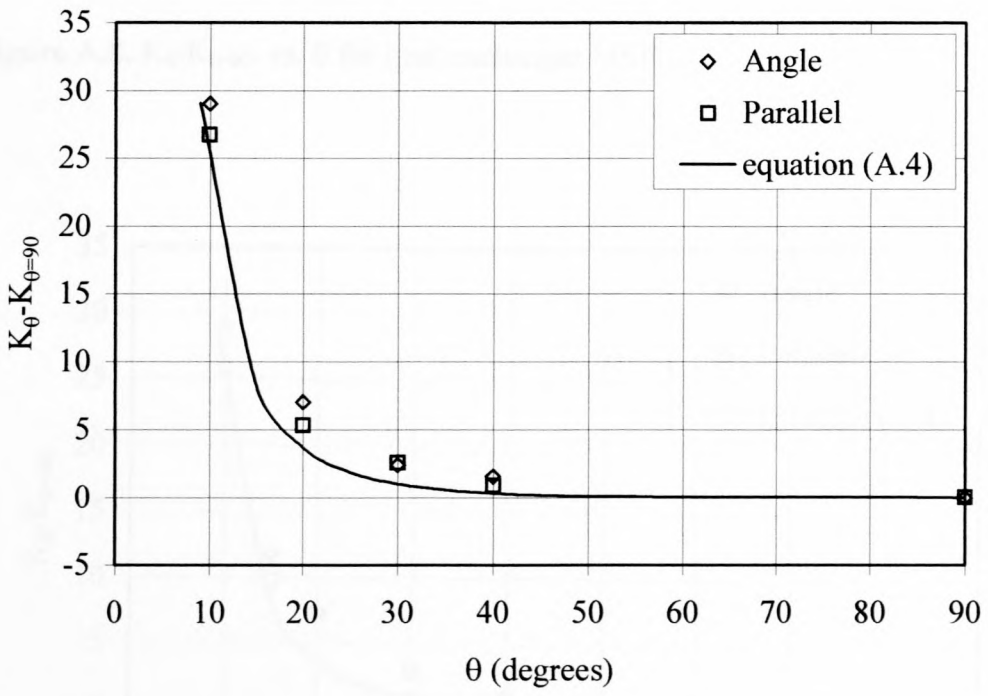

Figure A.7. K_θ-$K_{\theta=90°}$ vs. θ for heat exchanger MDC.

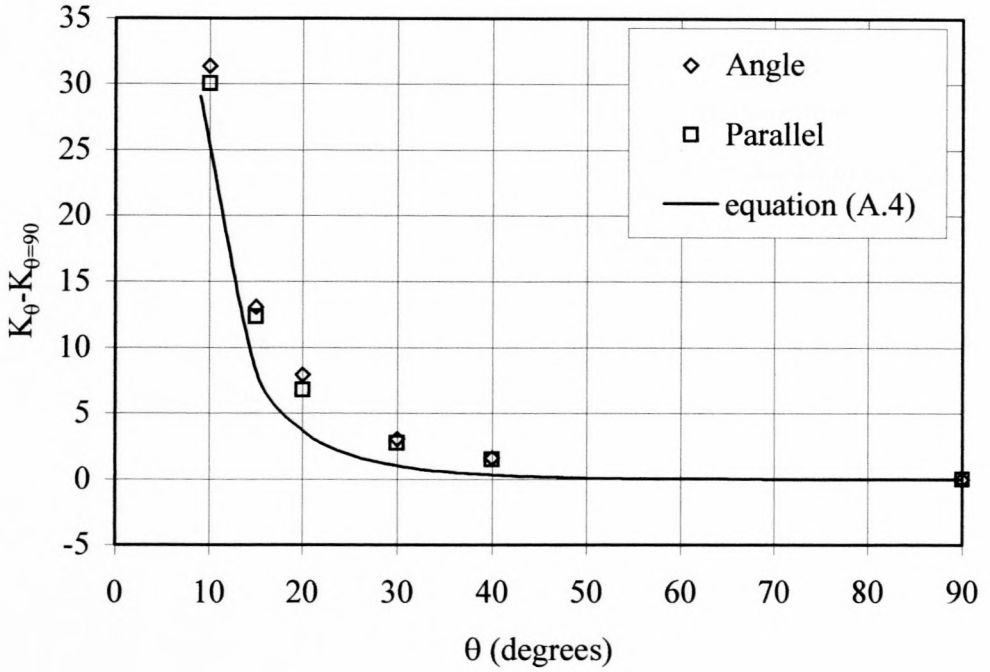

Figure A.8. K_θ-$K_{\theta=90°}$ vs. θ for heat exchanger MSF.

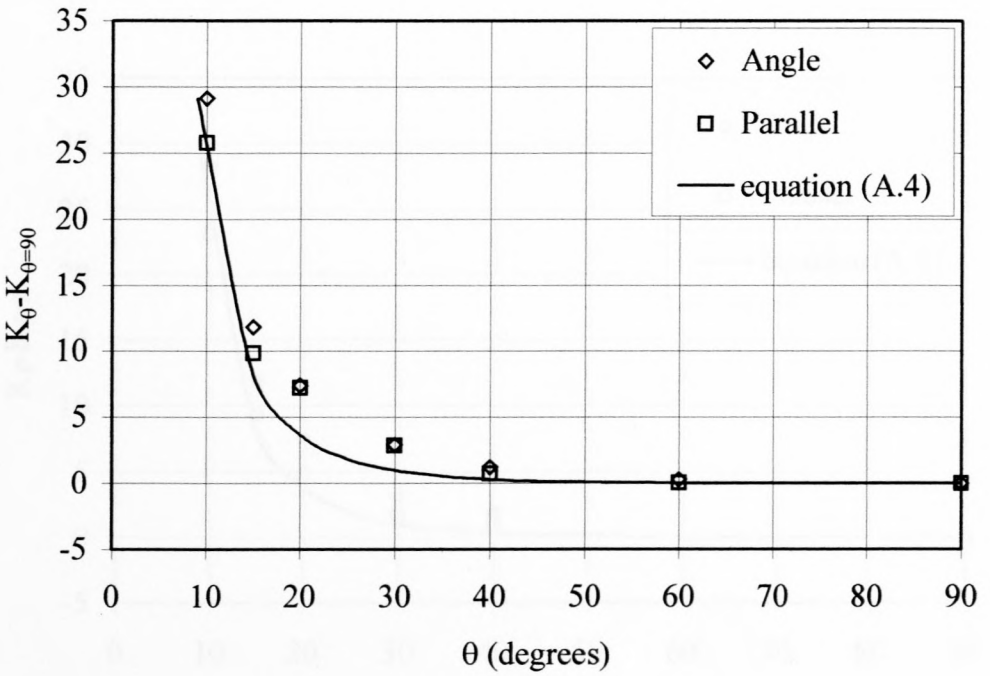

Figure A.9. K_θ-$K_{\theta=90°}$ vs. θ for heat exchanger SM.

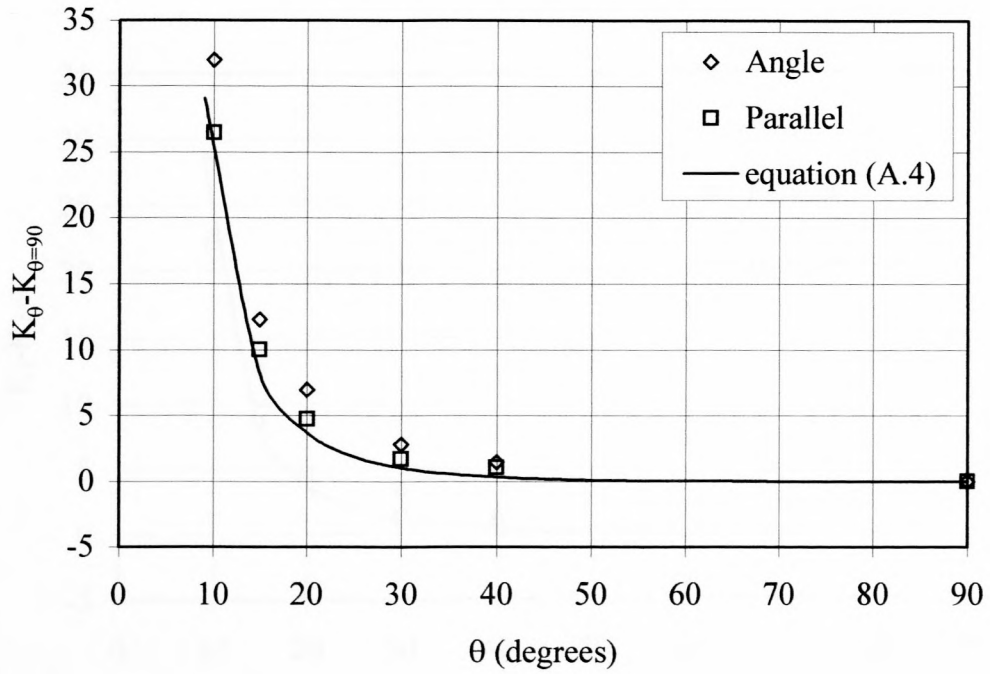

Figure A.10. K_θ-$K_{\theta=90°}$ vs. θ for heat exchanger 2RR.

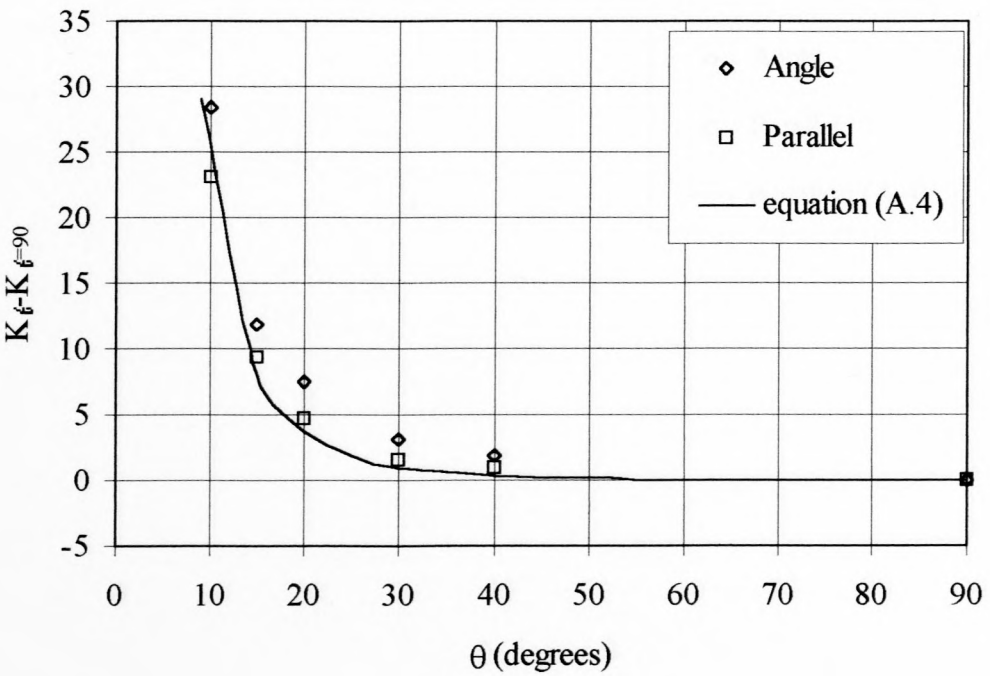

Figure A.11. K_θ-$K_{\theta=90°}$ vs. θ for heat exchanger 4RR.

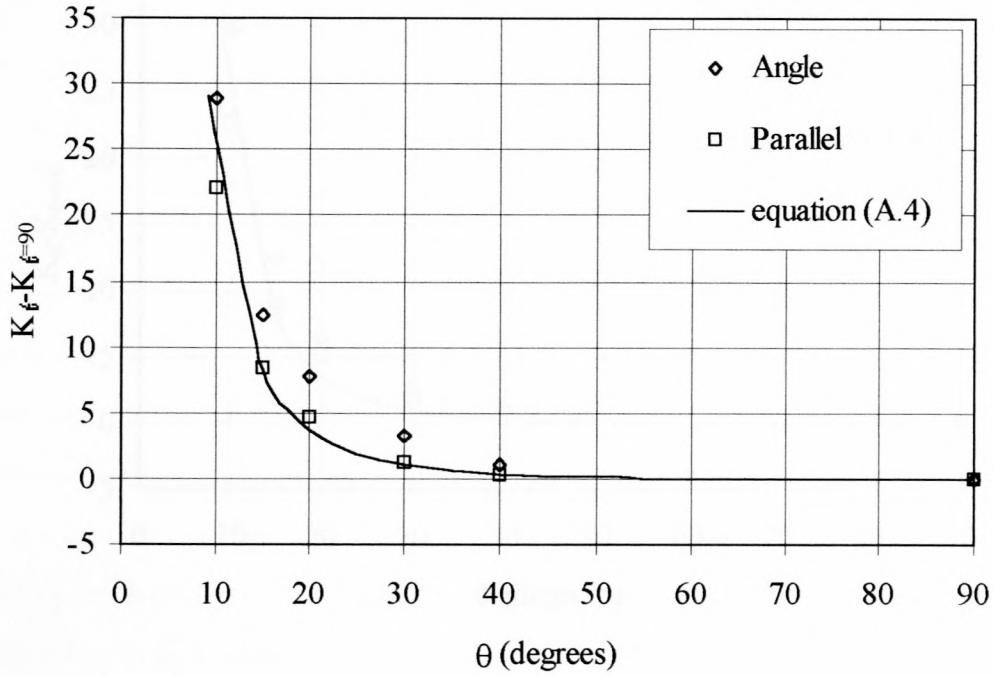

Figure A.12. K_θ-$K_{\theta=90°}$ vs. θ for heat exchanger 6RR.

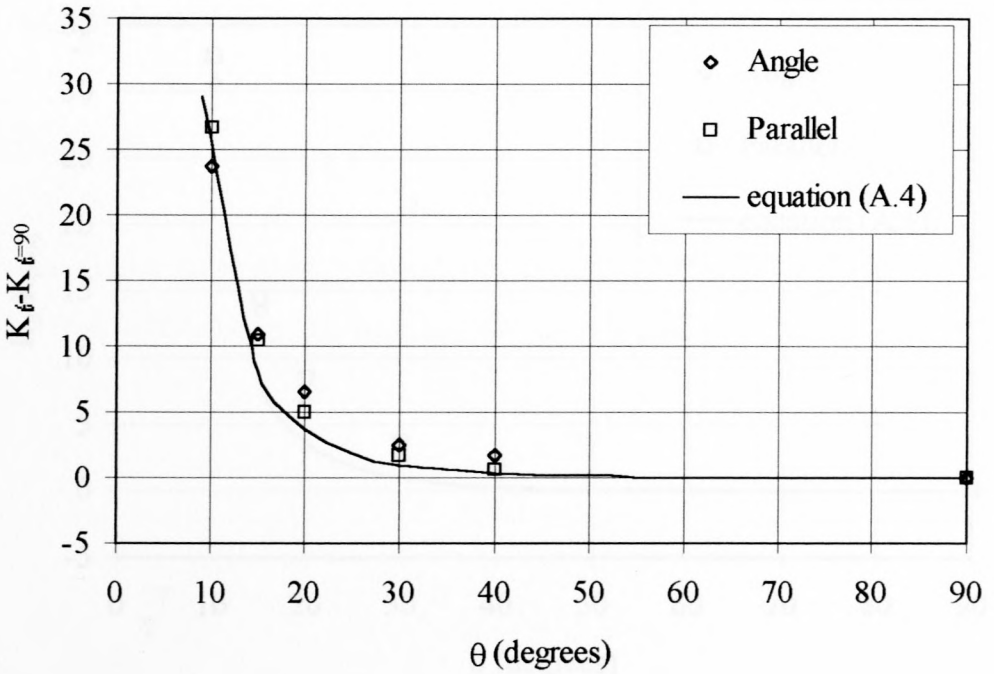

Figure A.13. K_θ-$K_{\theta=90°}$ vs. θ for heat exchanger LUM

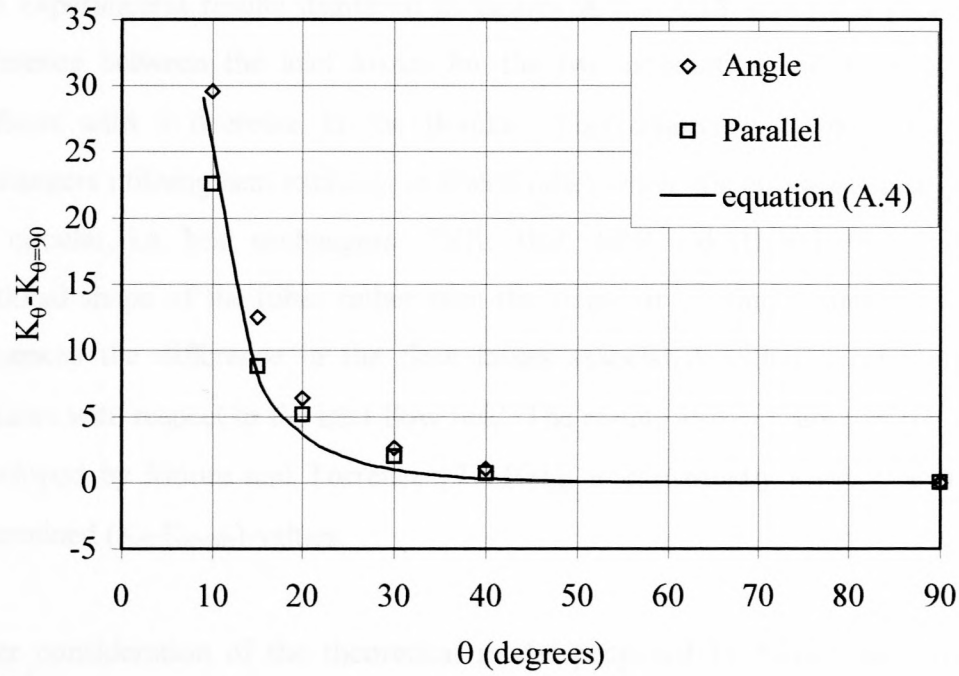

Figure A.14. K_θ-$K_{\theta=90°}$ vs. θ for heat exchanger HUNG.

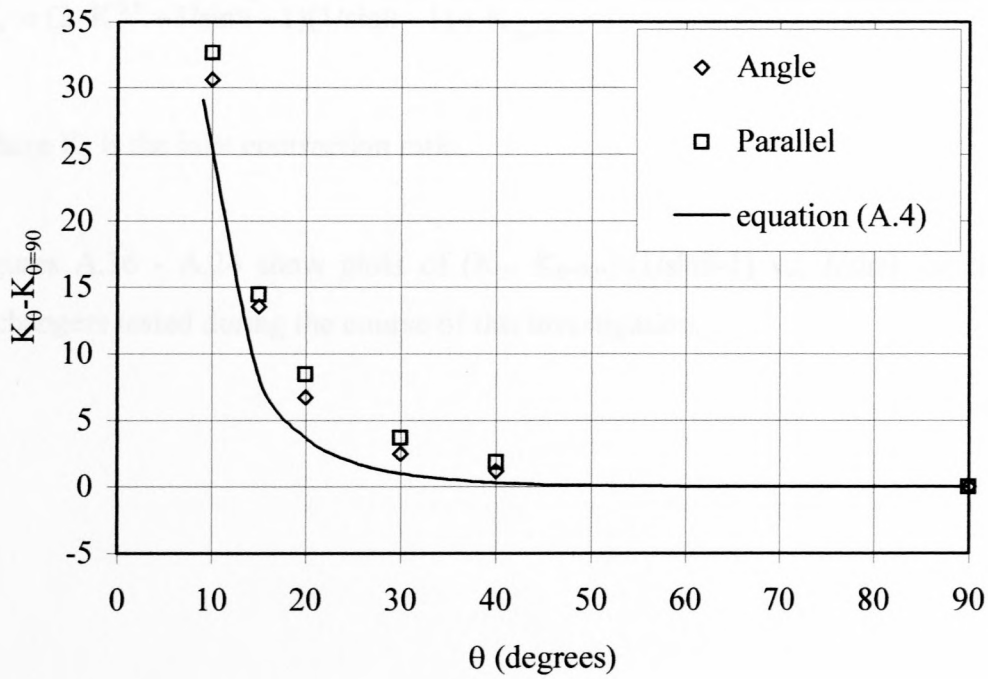

Figure A.15. K_θ-$K_{\theta=90°}$ vs. θ for heat exchanger RAD.

The experimental results displayed in figures A.7 - A.15 indicate a general increase in the difference between the inlet losses for the two orientations of the heat exchanger finned surfaces with a decrease in the θ-value. This difference is more pronounced for heat exchangers utilising heat exchangers finned tubes where the cross-sectional profile of the tubes are circular, i.e. heat exchangers 2RR, 4RR, 6RR and HUNG. It follows that the cross-sectional shape of the tubes rather than the shape of the finned surfaces of the finned tubes influences the difference in the flow losses associated with the orientation of the finned surfaces with respect to the inlet flow field. The results also indicate that the expression for $K_{i\theta}$, developed by Moore and Torrence [77MO1], is consistently lower than the experimentally determined $(K_\theta - K_{\theta=90^\circ})$-values.

After consideration of the theoretical model proposed by Moore and Torrence [77MO1], Mohandes et al. [84MO1] observed that plots of $(K_\theta - K_{\theta=90^\circ})/(1/\sin\theta - 1)$ vs. $1/\sin\theta$ produced straight lines with gradients close to unity for a range of perforated sheets and also for sets of parallel plates inclined to the inlet air velocity. Mohandes et al. [84MO1] subsequently proposed the following expression for K_θ

$$K_\theta = (2 \cdot K_c^{0.5} + 1/\sin\theta - 1)(1/\sin\theta - 1) + K_{\theta=90^\circ} \qquad \text{(A.5)}$$

where K_c is the inlet contraction ratio.

Figures A.16 - A.24 show plots of $(K_\theta - K_{\theta=90^\circ})/(1/\sin\theta - 1)$ vs. $1/\sin\theta$ for the different heat exchangers tested during the course of this investigation.

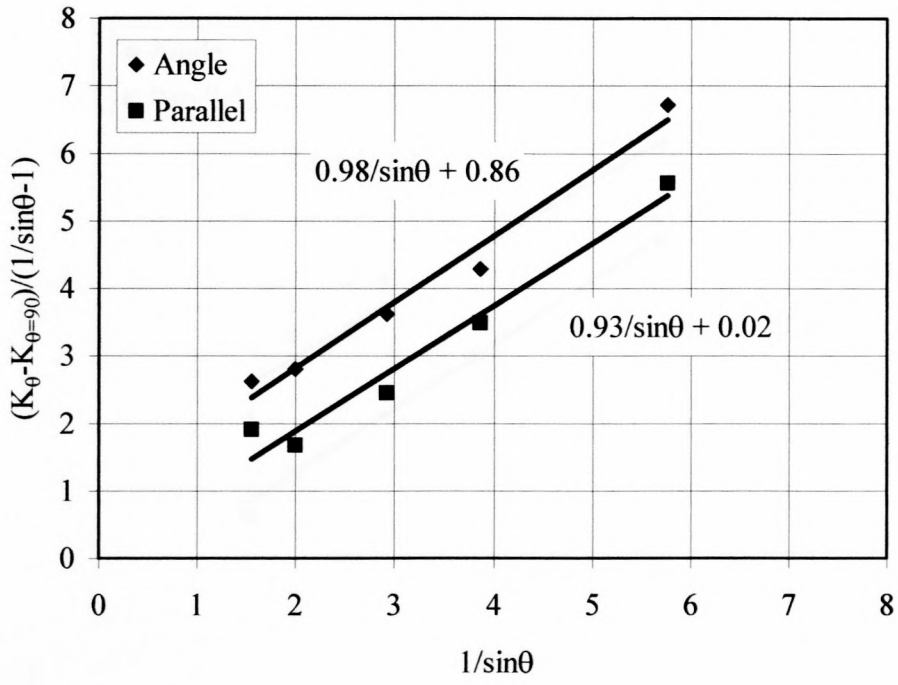

Figure A.16. $(K_\theta - K_{\theta=90^\circ})/(1/\sin\theta - 1)$ vs. $1/\sin\theta$ for heat exchanger 2RR.

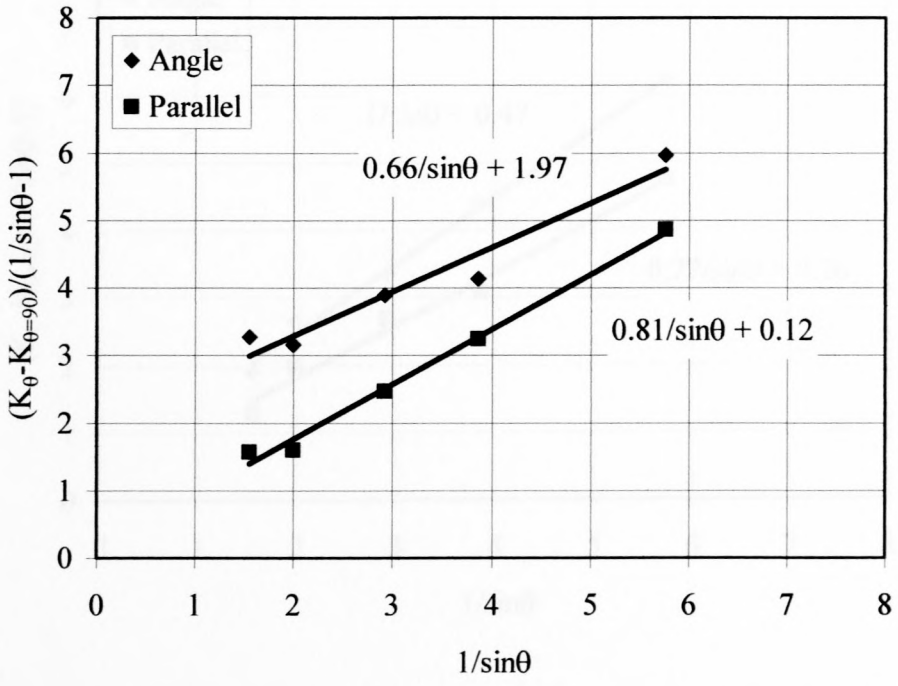

Figure A.17. $(K_\theta - K_{\theta=90^\circ})/(1/\sin\theta - 1)$ vs. $1/\sin\theta$ for heat exchanger 4RR.

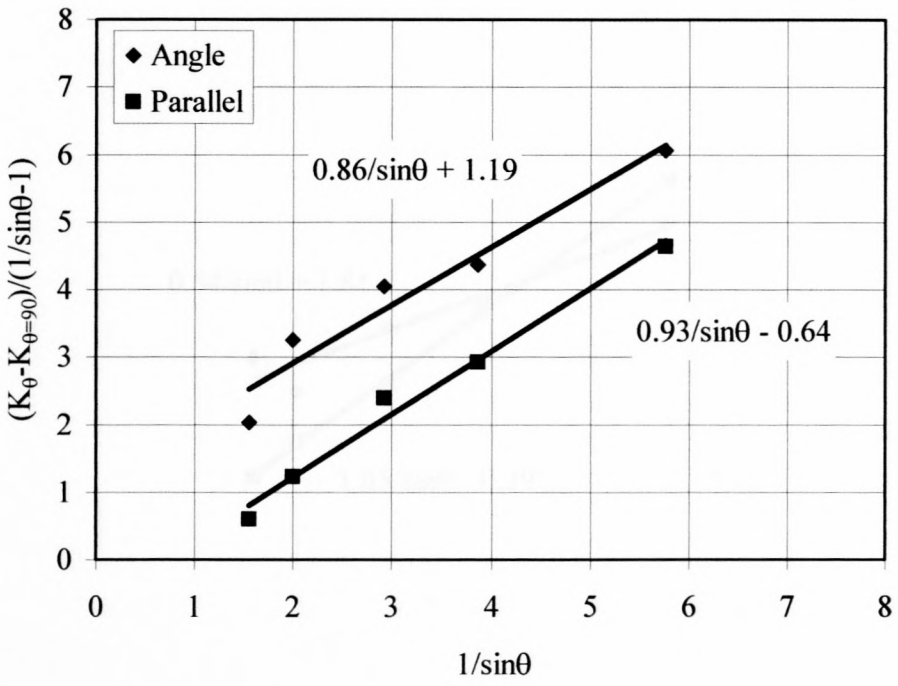

Figure A.18. $(K_\theta - K_{\theta=90^\circ})/(1/\sin\theta - 1)$ vs. $1/\sin\theta$ for heat exchanger 6RR.

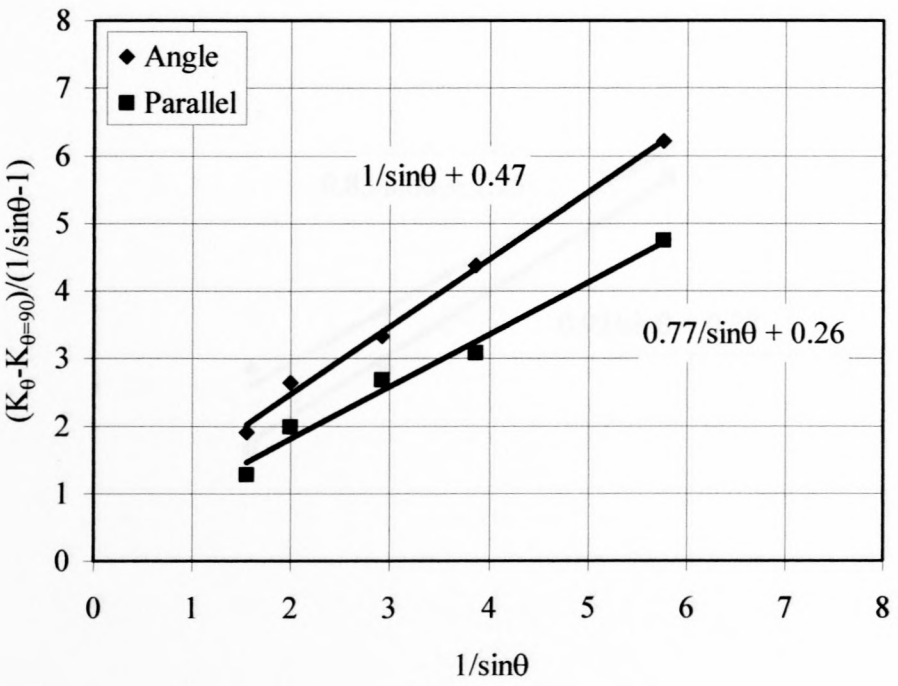

Figure A.19. $(K_\theta - K_{\theta=90^\circ})/(1/\sin\theta - 1)$ vs. $1/\sin\theta$ for heat exchanger HUNG.

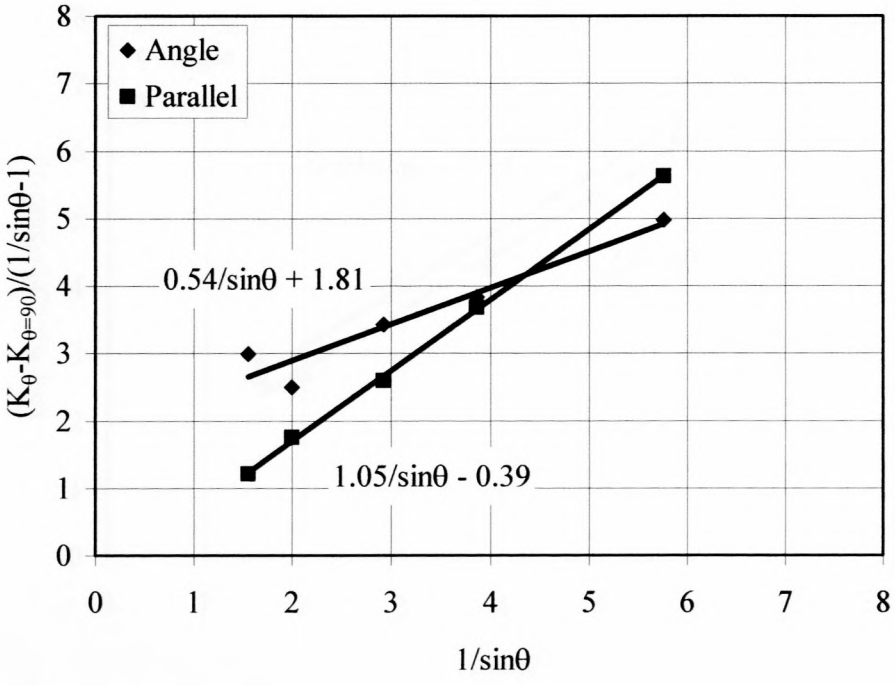

Figure A.20. $(K_\theta - K_{\theta=90^\circ})/(1/\sin\theta - 1)$ vs. $1/\sin\theta$ for heat exchanger LUM.

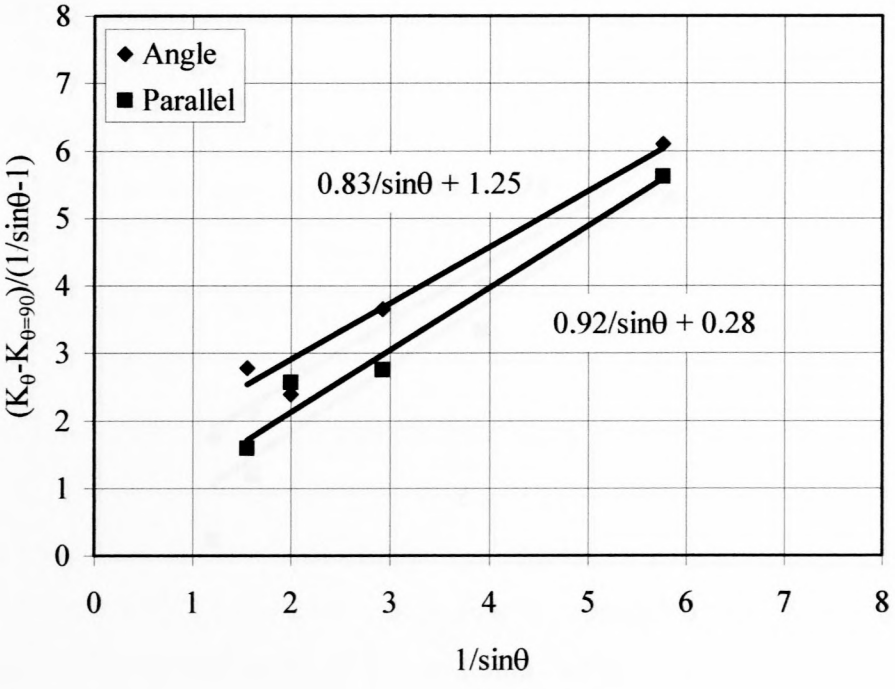

Figure A.21. $(K_\theta - K_{\theta=90^\circ})/(1/\sin\theta - 1)$ vs. $1/\sin\theta$ for heat exchanger MDC.

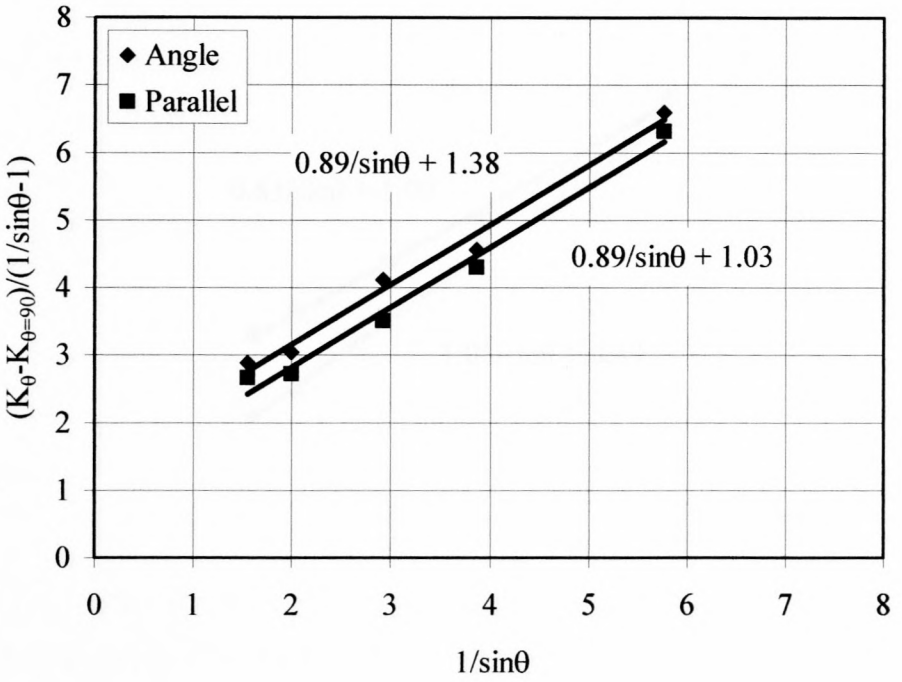

Figure A.22. $(K_\theta - K_{\theta=90^\circ})/(1/\sin\theta - 1)$ vs. $1/\sin\theta$ for heat exchanger MSF.

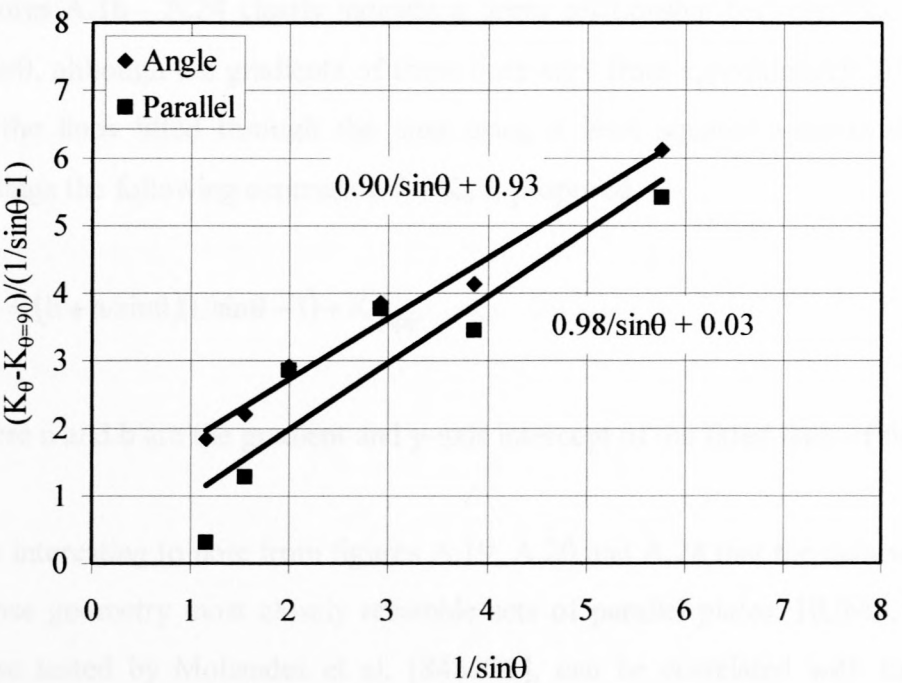

Figure A.23. $(K_\theta - K_{\theta=90^\circ})/(1/\sin\theta - 1)$ vs. $1/\sin\theta$ for heat exchanger SM.

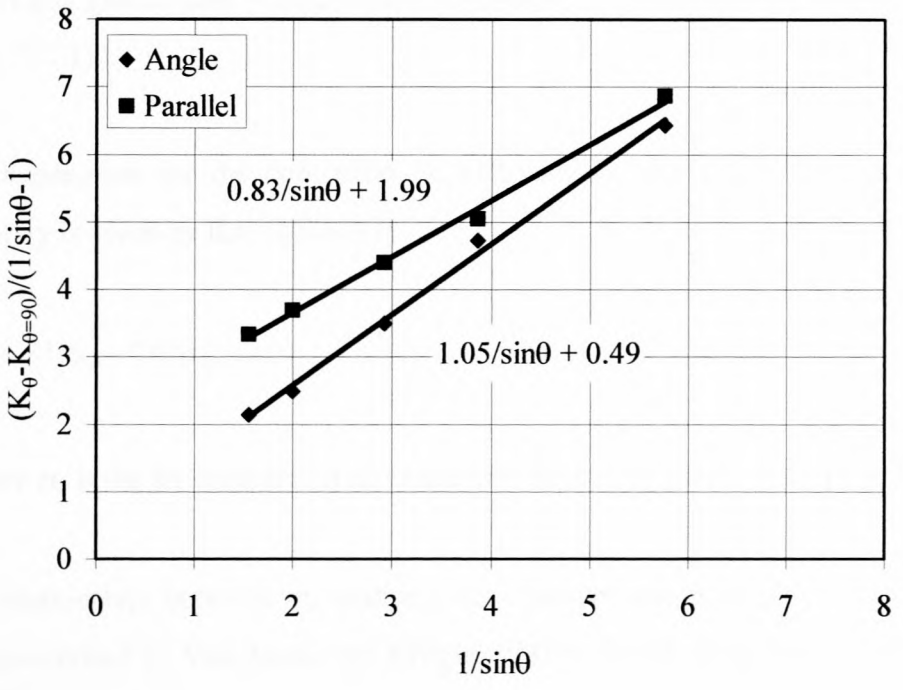

Figure A.24. $(K_\theta - K_{\theta=90^\circ})/(1/\sin\theta - 1)$ vs. $1/\sin\theta$ for heat exchanger RAD.

Figures A.16 - A.24 clearly indicate a linear relationship between $(K_\theta - K_{\theta=90^\circ})/(1/\sin\theta - 1)$ and $1/\sin\theta$, although the gradients of these lines vary from approximately 0.54 to 1.0, as indicated by the lines fitted through the data using a least squares approximation. Based on these findings the following expression for K_θ is proposed

$$K_\theta = (b + a/\sin\theta)(1/\sin\theta - 1) + K_{\theta=90^\circ} \qquad \text{(A.6)}$$

where a and b are the gradient and y-axis intercept of the fitted lines of figures A.16 - A.24.

It is interesting to note from figures A.19, A.20 and A.24 that the data sets of heat exchangers whose geometry most closely resemble sets of parallel plates: HUNG, RAD and LUM, like those tested by Mohandes et al. [84MO1], can be correlated with straight lines exhibiting gradients close to unity. In the case of heat exchangers HUNG and RAD the finned surfaces were at an angle to the inlet flow field, as opposed to heat exchanger LUM where the finned surfaces were parallel to the inlet flow field. In case of the latter the flat profiled tubes of the finned tubes acted as sets of parallel plates. These results would seem to indicate that equation

(A.5) is a special case of equation (A.6) where the gradient a = 1 and the y-axis intercept b = $(2K_c^{0.5} - 1)$.

An expression for the contraction coefficient, K_c, for plate fins based on the free stream velocity is given by Kays [50KA1]

$$K_c = (1/\sigma_c - 1)^2 / \sigma_{21}^2 \qquad (A.6)$$

where σ_c is the jet contraction ratio and σ_{21} the solidity ratio of the plate fins.

A relationship between σ_c and σ_{21} for parallel plates is given by Rouse [46RO1] and parameterised by Van Aarde and Kröger [93VA1] with the following expression

$$\begin{aligned}\sigma_c = {} & 0.6144517 + 0.04566493\,\sigma_{21} - 0.336651\,\sigma_{21}^2 + 0.4082743\,\sigma_{21}^3 \\ & + 2.672041\,\sigma_{21}^4 - 5.963169\,\sigma_{21}^5 + 3.558944\,\sigma_{21}^6\end{aligned} \qquad (A.7)$$

By means of equations (A.6) and (A.7) it is possible to calculate theoretical K_c-values for heat exchangers HUNG and RAD and according to White [86WH1] a theoretical K_c-value of approximately 0.04 is applicable for heat exchanger LUM. These theoretical K_c-values are compared in table A.1 with the K_c-values calculated from the lines fitted through the relevant experimental data points of figures A.19, A.20 and A.24, using the assumption made by Mohandes et al. [84MO1] that a = 1 and b = $(2K_c^{0.5} - 1)$ in equation (A.4).

Table A.1. Comparison of theoretically and experimentally determined K_c-values.

Heat Exchanger	K_c	
	Theoretical	Experimental
HUNG	0.14	0.54
RAD	0.05	0.55
LUM	0.04	0.09

Table A.1 indicates that the theoretically determined K_c-values are consistently lower than those determined from the experimental data for the relevant heat exchangers.

Of all the fitted lines shown in figures A.16 - A.24 the line that displays the smallest gradient correlates the data points for heat exchanger LUM in figure A.20 where the finned surfaces of the finned tubes were at an angle to the inlet flow field. The small gradient could be attributed to the wave pattern of the finned surfaces in the vicinity of the heat exchanger inlet. These curved surfaces could act as inlet guides for the air flowing into the passages between the finned surfaces resulting in a diminished inlet loss.

The experimental data of heat exchanger RAD displayed in figure A.24 is also of interest. Unlike the data of the other heat exchangers, the measured inlet losses in the case where the finned surfaces of the heat exchanger were parallel to the inlet flow field are higher than when the finned surfaces were oriented at an angle to the flow field. This phenomenon can be attributed to the unique staggered configuration used for the position of the heat exchanger finned tubes that would cause the angle of incidence between the inlet flow field and a line running through the centre of a finned tube in the first row and the corresponding finned tube in the last row to differ from the angle of incidence experienced for a different configuration.

Heat exchangers 2RR, 4RR and 6RR are near identical and differ only in the number of rows of finned tubes used which are 2, 4 and 6 respectively. It is expected that these heat exchangers

will exhibit identical inlet losses in the case where the finned surfaces of the finned tubes are at an angle to the incoming flow field. Figures A.16 - A.18 however, indicate that this is not the case. The differences in inlet losses can be attributed to distortion of the air flow field exiting from the heat exchanger for θ-values of 30° and lower. These outlet flow field distortions were most noticeable for heat exchanger 2RR and to a lesser degree for heat exchanger 4RR. In the case of heat exchanger 6RR no outlet flow field distortions were observed for both orientations of the heat exchanger over the range of θ-values tested.

A.5. Conclusions

The experimental results show that the inlet air flow losses are independent of the average air velocity approaching the heat exchanger. The results further indicate an increase in the difference between the inlet air flow losses of a particular heat exchanger as a result of a change in the orientation of the finned surfaces of the heat exchanger finned tubes as the θ-value is decreased. There are strong indications that the difference in inlet air flow losses as a result of different heat exchanger orientations is related to the cross-sectional profile of the tubes of the heat exchanger finned tubes and found to be more pronounced for finned tubes using round tubes as opposed to finned tubes utilising flat or elliptical tubes

The dimensionless total pressure loss coefficient, K_θ, is best expressed by equation (A.6) where coefficients a and b are determined experimentally. The expression proposed by Mohandes et al. [84MO1] is shown to be not only a special case of equation (A.6), applicable to heat exchangers characterised by finned surfaces closely resembling sets of parallel plates, but also to under-estimate heat exchanger inlet losses.

The empirical constants a and b displayed in equation (A.5) are shown to be sensitive to the geometrical characteristics of the heat exchangers tested. The large degree of variation in the values of constant a and b for the heat exchangers tested, would seem to indicate that these values should best be determined experimentally depending on the degree of accuracy required.

APPENDIX B – Experimental and calculated results of heat exchanger inlet flow losses

In this appendix the experimental and calculated results of the experimental investigation described in Appendix A are presented.

B.1. Sample calculation

Table B.2.1.2 displays the experimental and calculated results of heat exchanger 2RR in the instance where $\theta = 40°$. The heat exchanger orientation was such that the finned surfaces of the heat exchanger finned tubes were at an angle to the inlet air flow field. Consider the 5th data set of table B.2.1.2 where the following measured values are obtained

The ambient temperature and pressure

$T_{amb} = 19\ °C\ (292.15\ K)$

$P_{amb} = 101310\ N/m^2$

The air velocity in the venturi of the wind tunnel shown in figure A.1 of Appendix A

$v_{venturi} = 4.081\ m/s$

The static pressure drop across the heat exchanger

$\Delta p_{sHE} = 58\ N/m^2$

The air density in the test section directly upstream of the heat exchanger can be calculated from the perfect gas relation

$$\rho_a = p/(R \cdot T) = (p_{amb} + \Delta p_{sHE})/(R \cdot T) = (101310 + 58)/(287.08 \times 292.15) = 1.209\ kg/m^3 \qquad (B.1)$$

The dynamic viscosity of dry air, μ_a, at standard atmospheric pressure (101325 N/m^2) and at a temperature of 292.15 K is given by Kröger [98KR1] as

$$\mu_a = 1.811\times10^{-5} \text{ kg/(m.s)}$$

The average air velocity at and normal to the heat exchanger outlet, v_o, can be calculated from continuity as follows

$$\begin{aligned} v_o &= v_{venturi} \cdot \left(A_{venturi}/A_o\right) \\ &= 4.081 \cdot \left(\left(330\times660\right)/\left(600^2\right)\right) = 2.469 \text{ m/s} \end{aligned} \tag{B.2}$$

where $A_{venturi}$ and A_o are the areas at the wind tunnel venturi and heat exchanger outlet respectively.

It should be noted that the assumption is made that the air exits the heat exchanger in a direction perpendicular to the heat exchanger surface.

The heat exchanger oblique inlet air velocity, v_i, is calculated in a similar manner

$$\begin{aligned} v_i &= v_o \cdot \left(A_o/A_i\right) = v_o/\sin(\theta) \\ &= 2.469/\sin(40^\circ) = 3.841 \text{ m/s} \end{aligned} \tag{B.3}$$

The sum of the total pressure loss across the heat exchanger and the kinetic energy loss at the heat exchanger exit, Δp_θ, is given as

$$\begin{aligned} \Delta p_\theta &= \left(p_i + \rho_a v_i^2/2\right) - p_o = \Delta p_{sHE} + \rho_a v_i^2/2 \\ &= 58 + 1.209 \cdot 3.841^2/2 = 66.917 \text{ N/m}^2 \end{aligned} \tag{B.4}$$

From the above the dimensionless loss coefficient, K_θ, is given as

$$\begin{aligned} K_\theta &= \Delta p_\theta/(0.5 \cdot \rho_a v_o^2) \\ &= 66.917/(0.5 \cdot 1.209 \cdot 2.469^2) = 18.164 \end{aligned} \tag{B.5}$$

The characteristic flow parameter, Ry, is calculated according to

$$\begin{aligned} Ry &= v_o \cdot \rho_a / \mu_a \\ &= 2.469 \cdot 1.209 / (1.811 \times 10^{-5}) = 164817.4 \end{aligned} \tag{B.6}$$

B.2.1. Experimental and calculated results of heat exchangers 2RR, 4RR and 6RR

Table B.2.1.1 Heat exchanger 2RR with $\theta = 90°$.

$V_{venturi}$ (m/s)	Δp_{sHE} (N/m^2)	ρ_a (kg/m^3)	μ_a (kg/(ms))	v_i (m/s)	v_o (m/s)	Δp_{tHE} (N/m^2)	Ry (m^{-1})	K_θ
2.421	26.00	1.208	1.804E-05	1.464	1.464	27.296	98120.8	21.064
4.128	60.00	1.209	1.804E-05	2.497	2.497	63.769	167376.3	16.918
6.206	118.50	1.210	1.804E-05	3.754	3.754	127.025	251791.8	14.900
7.785	174.00	1.210	1.804E-05	4.710	4.710	187.423	316030.3	13.963
8.566	205.00	1.211	1.804E-05	5.183	5.183	221.259	347866.6	13.609
10.115	275.00	1.211	1.804E-05	6.120	6.120	297.685	411045.7	13.123

Table B.2.1.2 Heat exchanger 2RR with finned surfaces at angle to the inlet flow and $\theta = 40°$.

$v_{venturi}$ (m/s)	Δp_{sHE} (N/m^2)	ρ_a (kg/m^3)	μ_a (kg/(ms))	v_i (m/s)	v_o (m/s)	Δp_{tHE} (N/m^2)	Ry (m^{-1})	K_θ
10.815	309.00	1.212	1.811E-05	10.180	6.543	371.776	437863.7	14.334
9.475	246.00	1.211	1.811E-05	8.918	5.733	294.155	383378.9	14.784
7.175	151.00	1.210	1.811E-05	6.754	4.341	178.589	290051.2	15.667
6.133	116.00	1.209	1.811E-05	5.772	3.710	136.147	247817.0	16.356
4.081	58.00	1.209	1.811E-05	3.841	2.469	66.917	164817.4	18.164
2.334	24.00	1.208	1.811E-05	2.197	1.412	26.916	94240.3	22.339

Table B.2.1.3 Heat exchanger 2RR with finned surfaces parallel to the inlet flow and $\theta = 40°$.

$v_{venturi}$ (m/s)	Δp_{sHE} (N/m^2)	ρ_a (kg/m^3)	μ_a (kg/(ms))	v_i (m/s)	v_o (m/s)	Δp_{tHE} (N/m^2)	Ry (m^{-1})	K_θ
10.441	276.00	1.222	1.799E-05	9.827	6.317	334.988	428958.4	13.744
8.813	208.00	1.221	1.799E-05	8.295	5.332	250.003	361846.9	14.406
7.201	147.00	1.220	1.799E-05	6.778	4.357	175.026	295488.2	15.115
5.840	103.00	1.220	1.799E-05	5.497	3.534	121.427	239548.5	15.948
4.624	70.00	1.219	1.799E-05	4.353	2.798	81.549	189609.7	17.090
2.334	34.00	1.219	1.799E-05	2.197	1.412	36.942	95676.6	30.395

Table B.2.1.4 Heat exchanger 2RR with finned surfaces at angle to the inlet flow and $\theta = 30°$.

$v_{venturi}$ (m/s)	Δp_{sHE} (N/m^2)	ρ_a (kg/m^3)	μ_a (kg/(ms))	v_i (m/s)	v_o (m/s)	Δp_{tHE} (N/m^2)	Ry (m^{-1})	K_θ
11.200	326.00	1.200	1.815E-05	13.552	6.776	436.204	448000.2	15.833
9.136	227.00	1.199	1.815E-05	11.054	5.527	300.260	365088.5	16.394
7.729	171.00	1.198	1.815E-05	9.352	4.676	223.408	308705.3	17.051
6.214	118.00	1.198	1.815E-05	7.518	3.759	151.853	248042.8	17.943
4.053	59.00	1.197	1.815E-05	4.904	2.452	73.393	161691.2	20.396
2.341	26.00	1.197	1.815E-05	2.832	1.416	30.800	93360.3	25.666

Table B.2.1.5 Heat exchanger 2RR with finned surfaces parallel to the inlet flow and $\theta = 30°$.

$v_{venturi}$ (m/s)	Δp_{sHE} (N/m^2)	ρ_a (kg/m^3)	μ_a (kg/(ms))	v_i (m/s)	v_o (m/s)	Δp_{tHE} (N/m^2)	Ry (m^{-1})	K_θ
2.340	23.50	1.197	1.815E-05	2.831	1.415	28.295	93307.2	23.604
3.843	50.00	1.197	1.815E-05	4.650	2.325	62.942	153316.7	19.453
6.086	104.50	1.198	1.815E-05	7.365	3.682	136.976	242930.7	16.871
7.729	156.00	1.198	1.815E-05	9.352	4.676	208.396	308645.7	15.909
9.344	214.00	1.199	1.815E-05	11.306	5.653	290.622	373349.6	15.172
11.521	301.00	1.200	1.815E-05	13.940	6.970	417.583	460726.0	14.327

Table B.2.1.6 Heat exchanger 2RR with finned surfaces at angle to the inlet flow and $\theta = 20°$.

$v_{venturi}$ (m/s)	Δp_{sHE} (N/m^2)	ρ_a (kg/m^3)	μ_a (kg/(ms))	v_i (m/s)	v_o (m/s)	Δp_{tHE} (N/m^2)	Ry (m^{-1})	K_θ
9.946	255.00	1.230	1.790E-05	17.594	6.017	445.331	413487.8	20.002
8.793	205.00	1.229	1.790E-05	15.554	5.320	353.687	365374.1	20.335
7.870	171.00	1.229	1.790E-05	13.922	4.761	290.077	326920.4	20.825
5.941	106.00	1.228	1.790E-05	10.510	3.595	173.818	246638.4	21.910
4.651	71.00	1.228	1.790E-05	8.227	2.814	112.544	193004.0	23.159
2.900	36.00	1.227	1.790E-05	5.130	1.755	52.150	120317.9	27.604

Table B.2.1.7 Heat exchanger 2RR with finned surfaces parallel to the inlet flow and $\theta = 20°$.

$v_{venturi}$ (m/s)	Δp_{sHE} (N/m^2)	ρ_a (kg/m^3)	μ_a (kg/(ms))	v_i (m/s)	v_o (m/s)	Δp_{tHE} (N/m^2)	Ry (m^{-1})	K_θ
2.914	29.00	1.229	1.787E-05	5.154	1.763	45.328	121238.4	23.731
4.315	54.00	1.230	1.787E-05	7.632	2.610	89.808	179561.0	21.440
5.849	87.00	1.230	1.787E-05	10.346	3.539	152.825	243494.0	19.847
8.115	147.00	1.231	1.787E-05	14.354	4.909	273.779	338022.3	18.461
9.115	176.00	1.231	1.787E-05	16.123	5.514	336.000	379789.5	17.952
10.377	216.00	1.231	1.787E-05	18.356	6.278	423.467	432556.5	17.449

Table B.2.1.8 Heat exchanger 2RR with finned surfaces at angle to the inlet flow and $\theta = 15°$.

$v_{venturi}$ (m/s)	Δp_{sHE} (N/m^2)	ρ_a (kg/m^3)	μ_a (kg/(ms))	v_i (m/s)	v_o (m/s)	Δp_{tHE} (N/m^2)	Ry (m^{-1})	K_θ
2.266	23.00	1.214	1.801E-05	5.297	1.371	40.028	92377.8	35.092
3.841	50.00	1.214	1.801E-05	8.979	2.324	98.947	156643.6	30.177
5.071	77.00	1.214	1.801E-05	11.855	3.068	162.331	206852.8	28.399
7.265	139.00	1.215	1.801E-05	16.983	4.395	314.237	296519.0	26.769
8.452	180.00	1.216	1.801E-05	19.758	5.114	417.278	345109.3	26.253
9.898	235.00	1.216	1.801E-05	23.137	5.988	560.572	404360.8	25.703

Table B.2.1.9 Heat exchanger 2RR with finned surfaces parallel to the inlet flow and $\theta = 15°$.

$v_{venturi}$ (m/s)	Δp_{sHE} (N/m^2)	ρ_a (kg/m^3)	μ_a (kg/(ms))	v_i (m/s)	v_o (m/s)	Δp_{tHE} (N/m^2)	Ry (m^{-1})	K_θ
10.520	198.00	1.218	1.799E-05	24.591	6.365	566.275	430911.5	22.954
9.126	159.00	1.218	1.799E-05	21.333	5.521	436.044	373673.7	23.496
7.711	123.00	1.217	1.799E-05	18.025	4.665	320.707	315611.0	24.216
5.316	68.00	1.216	1.799E-05	12.426	3.216	161.903	217451.6	25.738
4.089	45.00	1.216	1.799E-05	9.558	2.474	100.551	167231.3	27.021
2.293	19.00	1.216	1.799E-05	5.359	1.387	36.460	93744.3	31.173

Table B.2.1.10 Heat exchanger 2RR with finned surfaces at angle to the inlet flow and θ = 10°.

$v_{venturi}$ (m/s)	Δp_{sHE} (N/m^2)	ρ_a (kg/m^3)	μ_a (kg/(ms))	v_i (m/s)	v_o (m/s)	Δp_{tHE} (N/m^2)	Ry (m^{-1})	K_θ
2.891	32.00	1.206	1.808E-05	10.074	1.749	93.191	116662.5	50.506
4.166	57.00	1.206	1.808E-05	14.513	2.520	184.036	168114.3	48.044
5.914	105.00	1.207	1.808E-05	20.603	3.578	361.148	238775.2	46.758
7.004	143.00	1.207	1.808E-05	24.402	4.237	502.442	282904.5	46.357
8.444	201.00	1.208	1.808E-05	29.420	5.109	723.793	341283.4	45.914
10.459	297.00	1.209	1.808E-05	36.440	6.328	1099.779	423111.0	45.433

Table B.2.1.11 Heat exchanger 2RR with finned surfaces parallel to the inlet flow and θ = 10°.

$v_{venturi}$ (m/s)	Δp_{sHE} (N/m^2)	ρ_a (kg/m^3)	μ_a (kg/(ms))	v_i (m/s)	v_o (m/s)	Δp_{tHE} (N/m^2)	Ry (m^{-1})	K_θ
10.108	147.00	1.209	1.806E-05	35.217	6.115	896.972	409531.5	39.664
8.513	111.00	1.209	1.806E-05	29.660	5.150	642.794	344793.5	40.086
7.194	87.00	1.209	1.806E-05	25.063	4.352	466.628	291283.0	40.764
6.149	68.00	1.208	1.806E-05	21.422	3.720	345.284	248918.4	41.296
4.380	41.00	1.208	1.806E-05	15.261	2.650	181.679	177276.5	42.829
2.938	23.00	1.208	1.806E-05	10.236	1.777	86.278	118884.4	45.218

Table B.2.1.12 Heat exchanger 4RR with θ = 90°.

$v_{venturi}$ (m/s)	Δp_{sHE} (N/m^2)	ρ_a (kg/m^3)	μ_a (kg/(ms))	v_i (m/s)	v_o (m/s)	Δp_{tHE} (N/m^2)	Ry (m^{-1})	K_θ
10.643	554.00	1.219	1.799E-05	6.439	6.439	579.270	436306.8	22.923
9.270	438.00	1.218	1.799E-05	5.608	5.608	457.149	379594.1	23.873
7.148	282.00	1.216	1.799E-05	4.325	4.325	293.369	292264.8	25.803
5.621	187.00	1.215	1.799E-05	3.401	3.401	194.024	229615.5	27.622
4.111	112.00	1.214	1.799E-05	2.487	2.487	115.754	167797.1	30.835
2.322	46.00	1.213	1.799E-05	1.405	1.405	47.197	94724.1	39.427

Table B.2.1.13 Heat exchanger 4RR with finned surfaces at angle to the inlet flow and θ = 40°.

$v_{venturi}$ (m/s)	Δp_{sHE} (N/m^2)	ρ_a (kg/m^3)	μ_a (kg/(ms))	v_i (m/s)	v_o (m/s)	Δp_{tHE} (N/m^2)	Ry (m^{-1})	K_θ
9.574	463.00	1.195	1.824E-05	9.011	5.792	511.533	379510.8	25.510
8.839	403.00	1.195	1.824E-05	8.320	5.348	444.347	350186.3	26.010
7.460	302.00	1.194	1.824E-05	7.021	4.513	331.420	295243.6	27.265
6.054	212.00	1.192	1.824E-05	5.699	3.663	231.362	239410.4	28.921
4.517	131.00	1.192	1.824E-05	4.251	2.733	141.767	178462.7	31.866
2.830	63.00	1.191	1.824E-05	2.664	1.712	67.225	111759.9	38.505

Table B.2.1.14 Heat exchanger 4RR with finned surfaces parallel to the inlet flow and θ = 40°.

$v_{venturi}$ (m/s)	Δp_{sHE} (N/m^2)	ρ_a (kg/m^3)	μ_a (kg/(ms))	v_i (m/s)	v_o (m/s)	Δp_{tHE} (N/m^2)	Ry (m^{-1})	K_θ
2.822	62.00	1.193	1.822E-05	2.656	1.707	66.207	111749.2	38.090
4.341	121.00	1.193	1.822E-05	4.086	2.626	130.961	172008.9	31.819
5.947	203.00	1.194	1.822E-05	5.597	3.598	221.710	235831.4	28.680
7.223	281.00	1.195	1.822E-05	6.798	4.370	308.621	286651.1	27.043
8.624	375.00	1.196	1.822E-05	8.117	5.217	414.412	342573.0	25.449
10.189	495.00	1.198	1.822E-05	9.590	6.164	550.083	405229.8	24.170

Table B.2.1.15 Heat exchanger 4RR with finned surfaces at angle to the inlet flow and θ = 30°.

$v_{venturi}$ (m/s)	Δp_{sHE} (N/m^2)	ρ_a (kg/m^3)	μ_a (kg/(ms))	v_i (m/s)	v_o (m/s)	Δp_{tHE} (N/m^2)	Ry (m^{-1})	K_θ
9.676	467.00	1.202	1.815E-05	11.708	5.854	549.369	387581.9	26.678
8.646	387.00	1.201	1.815E-05	10.462	5.231	452.725	346079.7	27.553
7.534	306.00	1.200	1.815E-05	9.116	4.558	355.858	301303.7	28.550
5.620	188.00	1.199	1.815E-05	6.801	3.400	215.716	224515.6	31.132
4.047	109.00	1.198	1.815E-05	4.897	2.449	123.360	161543.5	34.362
1.688	30.00	1.197	1.815E-05	2.042	1.021	32.495	67309.5	52.096

Table B.2.1.16 Heat exchanger 4RR with finned surfaces parallel to the inlet flow and θ = 30°.

$v_{venturi}$ (m/s)	Δp_{sHE} (N/m^2)	ρ_a (kg/m^3)	μ_a (kg/(ms))	v_i (m/s)	v_o (m/s)	Δp_{tHE} (N/m^2)	Ry (m^{-1})	K_θ
1.682	28.00	1.195	1.818E-05	2.035	1.018	30.474	66881.2	49.273
3.859	97.00	1.195	1.818E-05	4.669	2.334	110.030	153542.4	33.778
5.528	173.00	1.196	1.818E-05	6.689	3.344	199.760	220124.8	29.859
7.674	297.00	1.198	1.818E-05	9.285	4.643	348.635	305958.8	27.008
8.758	370.00	1.199	1.818E-05	10.597	5.298	437.304	349436.9	25.990
9.499	423.00	1.199	1.818E-05	11.493	5.747	502.211	379189.9	25.361

Table B.2.1.17 Heat exchanger 4RR with finned surfaces at angle to the inlet flow and θ = 20°.

$v_{venturi}$ (m/s)	Δp_{sHE} (N/m^2)	ρ_a (kg/m^3)	μ_a (kg/(ms))	v_i (m/s)	v_o (m/s)	Δp_{tHE} (N/m^2)	Ry (m^{-1})	K_θ
10.208	512.00	1.216	1.811E-05	18.057	6.176	710.173	414629.0	30.635
8.243	355.00	1.214	1.811E-05	14.580	4.987	484.008	334280.1	32.073
7.046	273.00	1.213	1.811E-05	12.464	4.263	367.195	285522.9	33.325
5.716	193.00	1.212	1.811E-05	10.111	3.458	254.938	231439.0	35.186
4.335	122.00	1.211	1.811E-05	7.668	2.622	157.597	175391.8	37.847
2.807	62.00	1.210	1.811E-05	4.965	1.698	76.915	113499.2	44.084

Table B.2.1.18 Heat exchanger 4RR with finned surfaces parallel to the inlet flow and θ = 20°.

$v_{venturi}$ (m/s)	Δp_{sHE} (N/m^2)	ρ_a (kg/m^3)	μ_a (kg/(ms))	v_i (m/s)	v_o (m/s)	Δp_{tHE} (N/m^2)	Ry (m^{-1})	K_θ
2.258	41.00	1.214	1.806E-05	3.995	1.366	50.687	91850.1	44.732
4.192	105.00	1.215	1.806E-05	7.415	2.536	138.401	170610.4	35.423
5.661	171.00	1.216	1.806E-05	10.013	3.425	231.945	230535.4	32.534
7.250	256.00	1.217	1.806E-05	12.825	4.386	356.064	295521.8	30.419
8.771	347.00	1.218	1.806E-05	15.515	5.306	493.568	357819.2	28.788
10.592	469.00	1.219	1.806E-05	18.735	6.408	682.990	432614.6	27.285

Table B.2.1.19 Heat exchanger 4RR with finned surfaces at angle to the inlet flow and θ = 15°.

$v_{venturi}$ (m/s)	Δp_{sHE} (N/m^2)	ρ_a (kg/m^3)	μ_a (kg/(ms))	v_i (m/s)	v_o (m/s)	Δp_{tHE} (N/m^2)	Ry (m^{-1})	K_θ
2.519	51.00	1.214	1.801E-05	5.889	1.524	72.051	102726.6	51.095
4.023	104.00	1.215	1.801E-05	9.404	2.434	157.719	164145.1	43.829
6.206	208.00	1.216	1.801E-05	14.507	3.755	335.957	253465.6	39.195
7.474	283.00	1.217	1.801E-05	17.471	4.522	468.715	305472.1	37.676
8.516	351.00	1.218	1.801E-05	19.906	5.152	592.251	348279.9	36.648
10.397	489.00	1.219	1.801E-05	24.302	6.290	849.080	425783.6	35.201

Table B.2.1.20 Heat exchanger 4RR with finned surfaces parallel to the inlet flow and θ = 15°.

$v_{venturi}$ (m/s)	Δp_{sHE} (N/m^2)	ρ_a (kg/m^3)	μ_a (kg/(ms))	v_i (m/s)	v_o (m/s)	Δp_{tHE} (N/m^2)	Ry (m^{-1})	K_θ
10.720	436.00	1.219	1.801E-05	25.059	6.486	818.655	438813.4	31.937
8.606	312.00	1.217	1.801E-05	20.117	5.207	558.314	351848.2	33.837
7.446	251.00	1.217	1.801E-05	17.406	4.505	435.290	304250.0	35.260
6.357	195.00	1.216	1.801E-05	14.860	3.846	329.241	259598.7	36.613
4.236	102.00	1.215	1.801E-05	9.902	2.563	161.552	172825.1	40.497
2.539	47.00	1.214	1.801E-05	5.935	1.536	68.384	103534.6	47.739

Table B.2.1.21 Heat exchanger 4RR with finned surfaces at angle to the inlet flow and θ = 10°.

$v_{venturi}$ (m/s)	Δp_{sHE} (N/m^2)	ρ_a (kg/m^3)	μ_a (kg/(ms))	v_i (m/s)	v_o (m/s)	Δp_{tHE} (N/m^2)	Ry (m^{-1})	K_θ
3.498	76.00	1.224	1.790E-05	12.188	2.116	166.931	144777.0	60.881
4.473	111.00	1.225	1.790E-05	15.585	2.706	259.724	185186.1	57.915
5.731	164.00	1.225	1.790E-05	19.966	3.467	408.239	237377.7	55.432
7.033	231.00	1.226	1.790E-05	24.502	4.255	599.046	291492.5	53.978
8.655	323.00	1.227	1.790E-05	30.155	5.236	880.971	359070.0	52.361
10.422	439.00	1.229	1.790E-05	36.312	6.306	1249.034	432885.7	51.136

Table B.2.1.22 Heat exchanger 4RR with finned surfaces parallel to the inlet flow and θ = 10°.

$v_{venturi}$ (m/s)	Δp_{sHE} (N/m^2)	ρ_a (kg/m^3)	μ_a (kg/(ms))	v_i (m/s)	v_o (m/s)	Δp_{tHE} (N/m^2)	Ry (m^{-1})	K_θ
10.405	305.00	1.229	1.787E-05	36.252	6.295	1112.657	432904.3	45.687
8.621	240.00	1.228	1.787E-05	30.035	5.216	794.049	358437.4	47.529
7.243	190.00	1.228	1.787E-05	25.235	4.382	580.924	301007.8	49.282
5.888	142.00	1.227	1.787E-05	20.513	3.562	400.196	244570.1	51.402
4.622	100.00	1.227	1.787E-05	16.103	2.796	259.049	191912.8	54.015
3.545	67.00	1.226	1.787E-05	12.352	2.145	160.544	147155.6	56.916

Table B.2.1.23 Heat exchanger 6RR with θ = 90°.

$v_{venturi}$ (m/s)	Δp_{sHE} (N/m^2)	ρ_a (kg/m^3)	μ_a (kg/(ms))	v_i (m/s)	v_o (m/s)	Δp_{tHE} (N/m^2)	Ry (m^{-1})	K_θ
2.720	87.00	1.207	1.806E-05	1.645	1.645	88.634	109978.1	54.245
4.472	191.50	1.208	1.806E-05	2.705	2.705	195.922	181021.4	44.304
6.011	311.00	1.210	1.806E-05	3.637	3.637	319.000	243616.5	39.876
7.316	432.00	1.211	1.806E-05	4.426	4.426	443.867	296885.6	37.405
8.581	566.00	1.213	1.806E-05	5.192	5.192	582.346	348672.7	35.627
10.922	848.00	1.216	1.806E-05	6.608	6.608	874.553	445018.2	32.936

Table B.2.1.24 Heat exchanger 6RR with finned surfaces at angle to the inlet flow and θ = 40°.

$v_{venturi}$ (m/s)	Δp_{sHE} (N/m^2)	ρ_a (kg/m^3)	μ_a (kg/(ms))	v_i (m/s)	v_o (m/s)	Δp_{tHE} (N/m^2)	Ry (m^{-1})	K_θ
2.635	85.00	1.217	1.801E-05	2.480	1.594	88.744	107735.3	57.367
4.407	189.00	1.219	1.801E-05	4.148	2.666	199.481	180348.8	46.064
5.698	287.00	1.220	1.801E-05	5.363	3.447	304.539	233414.6	42.024
6.954	400.00	1.221	1.801E-05	6.545	4.207	426.155	285195.1	39.434
8.157	524.00	1.223	1.801E-05	7.678	4.935	560.035	334957.1	37.614
10.495	795.00	1.226	1.801E-05	9.878	6.350	854.805	432087.9	34.594

Table B.2.1.25 Heat exchanger 6RR with finned surfaces parallel to the inlet flow and θ = 40°.

$v_{venturi}$ (m/s)	Δp_{sHE} (N/m^2)	ρ_a (kg/m^3)	μ_a (kg/(ms))	v_i (m/s)	v_o (m/s)	Δp_{tHE} (N/m^2)	Ry (m^{-1})	K_θ
10.579	790.00	1.224	1.804E-05	9.957	6.400	850.658	434213.6	33.942
7.995	495.00	1.220	1.804E-05	7.525	4.837	529.543	327199.8	37.102
7.303	427.00	1.219	1.804E-05	6.873	4.418	455.802	298672.1	38.302
5.224	244.00	1.217	1.804E-05	4.917	3.161	258.713	213279.4	42.557
4.211	172.00	1.216	1.804E-05	3.963	2.548	181.553	171792.7	45.998
2.703	87.00	1.215	1.804E-05	2.544	1.635	90.932	110175.5	55.967

Table B.2.1.26 Heat exchanger 6RR with finned surfaces at angle to the inlet flow and θ = 30°.

$v_{venturi}$ (m/s)	Δp_{sHE} (N/m^2)	ρ_a (kg/m^3)	μ_a (kg/(ms))	v_i (m/s)	v_o (m/s)	Δp_{tHE} (N/m^2)	Ry (m^{-1})	K_θ
10.819	848.00	1.224	1.799E-05	13.092	6.546	952.899	445401.8	36.336
8.673	577.00	1.221	1.799E-05	10.495	5.247	644.234	356108.9	38.328
7.206	426.00	1.219	1.799E-05	8.720	4.360	472.344	295435.4	40.768
6.089	322.00	1.218	1.799E-05	7.368	3.684	355.057	249385.2	42.963
4.522	197.00	1.216	1.799E-05	5.472	2.736	215.208	184973.3	47.277
1.599	41.00	1.214	1.799E-05	1.934	0.967	43.272	65285.1	76.192

Table B.2.1.27 Heat exchanger 6RR with finned surfaces parallel to the inlet flow and θ = 30°.

$v_{venturi}$ (m/s)	Δp_{sHE} (N/m^2)	ρ_a (kg/m^3)	μ_a (kg/(ms))	v_i (m/s)	v_o (m/s)	Δp_{tHE} (N/m^2)	Ry (m^{-1})	K_θ
1.593	40.00	1.212	1.801E-05	1.928	0.964	42.253	64871.1	75.026
4.420	181.00	1.214	1.801E-05	5.348	2.674	198.359	180202.0	45.709
6.130	310.00	1.216	1.801E-05	7.417	3.708	343.433	250246.6	41.089
7.134	396.00	1.217	1.801E-05	8.632	4.316	441.323	291489.5	38.949
8.391	519.00	1.218	1.801E-05	10.153	5.077	581.785	343286.8	37.065
10.891	795.00	1.221	1.801E-05	13.178	6.589	901.058	446775.8	33.984

Table B.2.1.28 Heat exchanger 6RR with finned surfaces at angle to the inlet flow and θ = 20°.

$v_{venturi}$ (m/s)	Δp_{sHE} (N/m^2)	ρ_a (kg/m^3)	μ_a (kg/(ms))	v_i (m/s)	v_o (m/s)	Δp_{tHE} (N/m^2)	Ry (m^{-1})	K_θ
11.222	895.00	1.220	1.811E-05	19.850	6.789	1135.389	457518.6	40.376
8.638	575.00	1.216	1.811E-05	15.281	5.226	717.006	351095.4	43.163
6.902	395.00	1.214	1.811E-05	12.209	4.176	485.496	280028.1	45.862
6.141	323.00	1.213	1.811E-05	10.863	3.715	394.585	248969.6	47.121
4.693	207.00	1.212	1.811E-05	8.301	2.839	248.758	190044.2	50.926
3.320	119.00	1.211	1.811E-05	5.872	2.008	139.876	134314.8	57.278

Table B.2.1.29 Heat exchanger 6RR with finned surfaces parallel to the inlet flow and θ = 20°.

$v_{venturi}$ (m/s)	Δp_{sHE} (N/m^2)	ρ_a (kg/m^3)	μ_a (kg/(ms))	v_i (m/s)	v_o (m/s)	Δp_{tHE} (N/m^2)	Ry (m^{-1})	K_θ
2.911	92.00	1.211	1.811E-05	5.149	1.761	108.049	117750.9	57.553
4.290	169.00	1.211	1.811E-05	7.588	2.595	203.878	173652.5	49.971
5.736	271.00	1.213	1.811E-05	10.146	3.470	333.419	232423.8	45.664
7.064	380.00	1.214	1.811E-05	12.495	4.274	474.777	286554.1	42.824
8.835	548.00	1.216	1.811E-05	15.628	5.345	696.492	358976.0	40.097
11.597	848.00	1.220	1.811E-05	20.513	7.016	1104.605	472589.4	36.799

Table B.2.1.30 Heat exchanger 6RR with finned surfaces at angle to the inlet flow and θ = 15°.

$v_{venturi}$ (m/s)	Δp_{sHE} (N/m^2)	ρ_a (kg/m^3)	μ_a (kg/(ms))	v_i (m/s)	v_o (m/s)	Δp_{tHE} (N/m^2)	Ry (m^{-1})	K_θ
11.471	888.00	1.227	1.801E-05	26.815	6.940	1329.146	472761.7	44.978
8.746	563.00	1.223	1.801E-05	20.445	5.291	818.629	359306.1	47.806
7.574	440.00	1.222	1.801E-05	17.704	4.582	631.446	310756.7	49.238
6.110	310.00	1.220	1.801E-05	14.283	3.697	434.457	250397.4	52.112
4.241	171.00	1.218	1.801E-05	9.913	2.566	230.862	173539.8	57.571
1.608	40.00	1.217	1.801E-05	3.758	0.973	48.592	65703.6	84.426

Table B.2.1.31 Heat exchanger 6RR with finned surfaces parallel to the inlet flow and θ = 15°.

$v_{venturi}$ (m/s)	Δp_{sHE} (N/m^2)	ρ_a (kg/m^3)	μ_a (kg/(ms))	v_i (m/s)	v_o (m/s)	Δp_{tHE} (N/m^2)	Ry (m^{-1})	K_θ
1.607	38.00	1.217	1.801E-05	3.756	0.972	46.581	65661.7	81.034
4.139	154.00	1.218	1.801E-05	9.676	2.504	211.030	169370.1	55.240
6.170	291.00	1.220	1.801E-05	14.422	3.733	417.857	252776.2	49.172
7.447	391.00	1.221	1.801E-05	17.407	4.505	575.989	305397.5	46.481
8.521	482.00	1.222	1.801E-05	19.918	5.155	724.434	349771.3	44.608
11.414	758.00	1.225	1.801E-05	26.680	6.905	1194.176	469792.1	40.871

Table B.2.1.32 Heat exchanger 6RR with finned surfaces at angle to the inlet flow and θ = 10°.

$v_{venturi}$ (m/s)	Δp_{sHE} (N/m^2)	ρ_a (kg/m^3)	μ_a (kg/(ms))	v_i (m/s)	v_o (m/s)	Δp_{tHE} (N/m^2)	Ry (m^{-1})	K_θ
3.618	127.00	1.209	1.806E-05	12.606	2.189	223.083	146569.7	76.998
4.545	182.00	1.210	1.806E-05	15.834	2.750	333.661	184194.5	72.961
5.625	257.00	1.211	1.806E-05	19.598	3.403	489.501	228146.3	69.821
7.113	380.00	1.212	1.806E-05	24.781	4.303	752.195	288835.1	67.022
8.182	478.00	1.213	1.806E-05	28.507	4.950	971.027	332590.7	65.316
9.512	615.00	1.215	1.806E-05	33.139	5.755	1282.164	387154.4	63.734

Table B.2.1.33 Heat exchanger 6RR with finned surfaces parallel to the inlet flow and θ = 10°.

$v_{venturi}$ (m/s)	Δp_{sHE} (N/m^2)	ρ_a (kg/m^3)	μ_a (kg/(ms))	v_i (m/s)	v_o (m/s)	Δp_{tHE} (N/m^2)	Ry (m^{-1})	K_θ
9.937	501.00	1.218	1.801E-05	34.621	6.012	1230.860	406452.2	55.928
8.490	401.00	1.217	1.801E-05	29.581	5.137	933.296	346938.0	58.147
7.377	327.00	1.216	1.801E-05	25.702	4.463	728.549	301221.5	60.170
5.727	224.00	1.215	1.801E-05	19.953	3.465	465.764	233610.2	63.890
4.679	164.50	1.214	1.801E-05	16.300	2.831	325.754	190731.7	66.995
3.680	114.50	1.213	1.801E-05	12.822	2.227	214.232	149960.8	71.238

B.2.2. Experimental and calculated results of heat exchanger MDC

Table B.2.2.1 Heat exchanger MDC with $\theta = 90°$.

$v_{venturi}$ (m/s)	Δp_{sHE} (N/m^2)	ρ_a (kg/m^3)	μ_a (kg/(ms))	v_i (m/s)	v_o (m/s)	Δp_{tHE} (N/m^2)	Ry (m^{-1})	K_θ
11.022	466.00	1.225	1.792E-05	6.668	6.668	493.237	455877.3	18.109
9.099	335.00	1.224	1.792E-05	5.505	5.505	353.540	375871.1	19.069
7.093	220.00	1.222	1.792E-05	4.291	4.291	231.253	292663.5	20.551
5.789	158.00	1.221	1.792E-05	3.502	3.502	165.490	238702.2	22.094
4.661	111.00	1.221	1.792E-05	2.820	2.820	115.853	192102.2	23.870
2.900	54.00	1.220	1.792E-05	1.755	1.755	55.878	119466.6	29.752

Table B.2.2.2 Heat exchanger MDC with finned surfaces at angle to the inlet flow and $\theta = 40°$.

$v_{venturi}$ (m/s)	Δp_{sHE} (N/m^2)	ρ_a (kg/m^3)	μ_a (kg/(ms))	v_i (m/s)	v_o (m/s)	Δp_{tHE} (N/m^2)	Ry (m^{-1})	K_θ
2.867	54.00	1.208	1.806E-05	2.698	1.734	58.396	115969.0	32.153
4.461	104.00	1.208	1.806E-05	4.199	2.699	114.650	180558.0	26.055
6.176	177.00	1.209	1.806E-05	5.813	3.737	197.429	250163.1	23.390
7.767	256.00	1.210	1.806E-05	7.310	4.699	288.328	314818.1	21.586
9.151	337.00	1.211	1.806E-05	8.613	5.536	381.919	371239.6	20.578
10.774	445.00	1.212	1.806E-05	10.140	6.518	507.327	437533.6	19.700

Table B.2.2.3 Heat exchanger MDC with finned surfaces parallel to the inlet flow and $\theta = 40°$.

$v_{venturi}$ (m/s)	Δp_{sHE} (N/m^2)	ρ_a (kg/m^3)	μ_a (kg/(ms))	v_i (m/s)	v_o (m/s)	Δp_{tHE} (N/m^2)	Ry (m^{-1})	K_θ
10.829	440.00	1.212	1.806E-05	10.192	6.551	502.960	439738.8	19.334
8.736	305.00	1.211	1.806E-05	8.223	5.285	345.926	354299.9	20.457
7.453	234.00	1.210	1.806E-05	7.015	4.509	263.768	302059.0	21.446
5.955	162.00	1.209	1.806E-05	5.605	3.603	180.989	241165.8	23.068
3.957	85.00	1.208	1.806E-05	3.724	2.394	93.376	160107.6	26.982
2.318	39.00	1.207	1.806E-05	2.182	1.403	41.874	93773.1	35.258

Table B.2.2.4 Heat exchanger MDC with finned surfaces at angle to the inlet flow and θ = 30°.

$v_{venturi}$ (m/s)	Δp_{sHE} (N/m^2)	ρ_a (kg/m^3)	μ_a (kg/(ms))	v_i (m/s)	v_o (m/s)	Δp_{tHE} (N/m^2)	Ry (m^{-1})	K_θ
11.171	473.00	1.211	1.808E-05	13.517	6.758	583.580	452422.0	21.110
9.273	342.00	1.209	1.808E-05	11.220	5.610	418.094	375058.9	21.978
7.781	255.00	1.208	1.808E-05	9.415	4.707	308.532	314444.5	23.054
5.856	160.00	1.207	1.808E-05	7.086	3.543	190.295	236438.4	25.126
4.598	109.00	1.206	1.808E-05	5.564	2.782	127.671	185568.4	27.352
2.871	54.00	1.206	1.808E-05	3.474	1.737	61.273	115784.9	33.700

Table B.2.2.5 Heat exchanger MDC with finned surfaces parallel to the inlet flow and θ = 30°.

$v_{venturi}$ (m/s)	Δp_{sHE} (N/m^2)	ρ_a (kg/m^3)	μ_a (kg/(ms))	v_i (m/s)	v_o (m/s)	Δp_{tHE} (N/m^2)	Ry (m^{-1})	K_θ
2.841	52.00	1.205	1.808E-05	3.437	1.719	59.121	114566.4	33.211
4.368	99.00	1.206	1.808E-05	5.285	2.643	115.844	176247.1	27.510
6.006	163.00	1.207	1.808E-05	7.267	3.634	194.869	242507.4	24.459
7.942	256.00	1.208	1.808E-05	9.609	4.805	311.769	320948.5	22.361
9.060	319.00	1.209	1.808E-05	10.962	5.481	391.625	366367.0	21.570
11.611	488.00	1.211	1.808E-05	14.050	7.025	607.495	470339.0	20.335

Table B.2.2.6 Heat exchanger MDC with finned surfaces at angle to the inlet flow and θ = 20°.

$v_{venturi}$ (m/s)	Δp_{sHE} (N/m^2)	ρ_a (kg/m^3)	μ_a (kg/(ms))	v_i (m/s)	v_o (m/s)	Δp_{tHE} (N/m^2)	Ry (m^{-1})	K_θ
10.166	392.00	1.238	1.783E-05	17.983	6.151	592.170	427107.7	25.290
8.557	292.00	1.237	1.783E-05	15.137	5.177	433.672	359142.0	26.168
7.572	239.00	1.236	1.783E-05	13.394	4.581	349.881	317643.6	26.975
5.631	147.00	1.235	1.783E-05	9.961	3.407	208.272	236017.4	29.058
4.472	103.00	1.234	1.783E-05	7.910	2.705	141.614	187324.2	31.351
2.842	52.00	1.234	1.783E-05	5.027	1.719	67.587	118986.1	37.067

Table B.2.2.7 Heat exchanger MDC with finned surfaces parallel to the inlet flow and θ = 20°.

$v_{venturi}$ (m/s)	Δp_{sHE} (N/m^2)	ρ_a (kg/m^3)	μ_a (kg/(ms))	v_i (m/s)	v_o (m/s)	Δp_{tHE} (N/m^2)	Ry (m^{-1})	K_θ
2.809	50.00	1.236	1.780E-05	4.969	1.699	65.255	117968.0	36.567
4.287	92.00	1.236	1.780E-05	7.584	2.594	127.559	180143.9	30.666
5.499	134.50	1.237	1.780E-05	9.727	3.327	193.016	231138.6	28.198
7.685	228.00	1.238	1.780E-05	13.595	4.650	342.408	323343.2	25.585
9.027	295.00	1.239	1.780E-05	15.968	5.461	452.943	380040.0	24.515
10.627	388.00	1.240	1.780E-05	18.799	6.430	607.106	447821.2	23.687

Table B.2.2.8 Heat exchanger MDC with finned surfaces at angle to the inlet flow and θ = 10°.

$v_{venturi}$ (m/s)	Δp_{sHE} (N/m^2)	ρ_a (kg/m^3)	μ_a (kg/(ms))	v_i (m/s)	v_o (m/s)	Δp_{tHE} (N/m^2)	Ry (m^{-1})	K_θ
2.817	45.00	1.221	1.797E-05	9.814	1.704	103.796	115805.8	58.545
4.376	85.00	1.221	1.797E-05	15.248	2.648	226.979	179992.2	53.018
5.754	129.50	1.222	1.797E-05	20.049	3.481	375.076	236772.0	50.652
7.069	179.00	1.223	1.797E-05	24.630	4.277	549.798	291012.8	49.173
8.866	261.00	1.223	1.797E-05	30.891	5.364	844.768	365290.9	47.991
10.646	362.00	1.225	1.797E-05	37.091	6.441	1204.446	439041.5	47.414

Table B.2.2.9 Heat exchanger MDC with finned surfaces parallel to the inlet flow and θ = 10°.

$v_{venturi}$ (m/s)	Δp_{sHE} (N/m^2)	ρ_a (kg/m^3)	μ_a (kg/(ms))	v_i (m/s)	v_o (m/s)	Δp_{tHE} (N/m^2)	Ry (m^{-1})	K_θ
10.822	312.00	1.220	1.801E-05	37.705	6.547	1179.129	443401.4	45.096
8.991	230.00	1.219	1.801E-05	31.325	5.439	828.019	368075.9	45.918
7.067	156.00	1.218	1.801E-05	24.620	4.275	525.157	289086.2	47.178
5.844	115.00	1.218	1.801E-05	20.362	3.536	367.391	238985.0	48.274
4.509	78.00	1.217	1.801E-05	15.710	2.728	228.191	184321.8	50.386
2.869	42.00	1.217	1.801E-05	9.995	1.736	102.775	117230.5	56.082

B.2.3. Experimental and calculated results of heat exchanger MSF

Table B.2.3.1 Heat exchanger MSF with $\theta = 90°$.

$v_{venturi}$ (m/s)	Δp_{sHE} (N/m^2)	ρ_a (kg/m^3)	μ_a (kg/(ms))	v_i (m/s)	v_o (m/s)	Δp_{tHE} (N/m^2)	Ry (m^{-1})	K_θ
2.368	30.00	1.206	1.806E-05	1.433	1.433	31.238	95709.1	25.229
4.451	72.00	1.207	1.806E-05	2.693	2.693	76.376	179960.0	17.455
6.400	127.00	1.208	1.806E-05	3.872	3.872	136.053	258924.1	15.028
7.566	167.00	1.208	1.806E-05	4.577	4.577	179.657	306211.8	14.194
9.362	238.00	1.209	1.806E-05	5.664	5.664	257.392	379159.0	13.273
10.364	282.00	1.209	1.806E-05	6.270	6.270	305.774	419909.6	12.862

Table B.2.3.2 Heat exchanger MSF with finned surfaces at angle to the inlet flow and $\theta = 40°$.

$v_{venturi}$ (m/s)	Δp_{sHE} (N/m^2)	ρ_a (kg/m^3)	μ_a (kg/(ms))	v_i (m/s)	v_o (m/s)	Δp_{tHE} (N/m^2)	Ry (m^{-1})	K_θ
10.678	298.00	1.223	1.797E-05	10.050	6.460	359.781	439859.7	14.095
8.802	214.00	1.222	1.797E-05	8.284	5.325	255.942	362269.2	14.769
7.575	167.00	1.222	1.797E-05	7.130	4.583	198.053	311646.7	15.436
6.285	123.00	1.221	1.797E-05	5.916	3.803	144.369	258464.7	16.352
4.606	75.00	1.221	1.797E-05	4.336	2.787	86.472	189336.2	18.243
2.944	39.00	1.220	1.797E-05	2.771	1.781	43.683	120947.0	22.576

Table B.2.3.3 Heat exchanger MSF with finned surfaces parallel to the inlet flow and $\theta = 40°$.

$v_{venturi}$ (m/s)	Δp_{sHE} (N/m^2)	ρ_a (kg/m^3)	μ_a (kg/(ms))	v_i (m/s)	v_o (m/s)	Δp_{tHE} (N/m^2)	Ry (m^{-1})	K_θ
2.338	28.00	1.224	1.792E-05	2.200	1.414	30.963	96619.3	25.291
4.373	70.00	1.225	1.792E-05	4.116	2.646	80.374	180825.8	18.751
6.085	118.00	1.225	1.792E-05	5.727	3.681	138.098	251740.6	16.631
7.591	166.00	1.226	1.792E-05	7.145	4.593	197.295	314213.2	15.258
8.783	213.00	1.227	1.792E-05	8.266	5.314	254.908	363690.4	14.722
10.713	296.00	1.228	1.792E-05	10.083	6.481	358.405	443991.1	13.900

Table B.2.3.4 Heat exchanger MSF with finned surfaces at angle to the inlet flow and θ = 30°.

$v_{venturi}$ (m/s)	Δp_{sHE} (N/m^2)	ρ_a (kg/m^3)	μ_a (kg/(ms))	v_i (m/s)	v_o (m/s)	Δp_{tHE} (N/m^2)	Ry (m^{-1})	K_θ
9.421	241.00	1.207	1.806E-05	11.400	5.700	319.453	381075.7	16.288
8.599	207.00	1.207	1.806E-05	10.405	5.203	272.340	347716.0	16.672
7.196	154.00	1.206	1.806E-05	8.707	4.353	199.729	290814.2	17.471
5.940	114.00	1.206	1.806E-05	7.187	3.594	145.146	239958.4	18.641
4.308	68.00	1.205	1.806E-05	5.212	2.606	84.375	173948.0	20.611
2.634	33.00	1.205	1.806E-05	3.187	1.593	39.119	106316.5	25.572

Table B.2.3.5 Heat exchanger MSF with finned surfaces parallel to the inlet flow and θ = 30°.

$v_{venturi}$ (m/s)	Δp_{sHE} (N/m^2)	ρ_a (kg/m^3)	μ_a (kg/(ms))	v_i (m/s)	v_o (m/s)	Δp_{tHE} (N/m^2)	Ry (m^{-1})	K_θ
2.617	33.00	1.199	1.813E-05	3.166	1.583	39.009	104683.8	25.967
4.071	62.00	1.199	1.813E-05	4.925	2.463	76.545	162887.1	21.051
6.217	118.00	1.200	1.813E-05	7.523	3.761	151.949	248925.7	17.903
7.828	170.00	1.200	1.813E-05	9.472	4.736	223.853	313597.8	16.627
9.284	226.00	1.201	1.813E-05	11.233	5.617	301.780	372104.7	15.929
10.031	257.00	1.201	1.813E-05	12.137	6.069	345.494	402173.2	15.617

Table B.2.3.6 Heat exchanger MSF with finned surfaces at angle to the inlet flow and θ = 20°.

$v_{venturi}$ (m/s)	Δp_{sHE} (N/m^2)	ρ_a (kg/m^3)	μ_a (kg/(ms))	v_i (m/s)	v_o (m/s)	Δp_{tHE} (N/m^2)	Ry (m^{-1})	K_θ
2.845	38.50	1.233	1.785E-05	5.032	1.721	54.113	118899.0	29.629
4.413	73.00	1.234	1.785E-05	7.806	2.670	110.579	184492.4	25.155
6.099	120.50	1.234	1.785E-05	10.789	3.690	192.325	255122.3	22.890
7.781	179.00	1.235	1.785E-05	13.763	4.707	295.961	325652.5	21.632
8.690	215.00	1.235	1.785E-05	15.373	5.258	360.962	363857.8	21.141
11.017	322.00	1.237	1.785E-05	19.488	6.665	556.809	461739.6	20.272

Table B.2.3.7 Heat exchanger MSF with finned surfaces parallel to the inlet flow and $\theta = 20°$.

$v_{venturi}$ (m/s)	Δp_{sHE} (N/m^2)	ρ_a (kg/m^3)	μ_a (kg/(ms))	v_i (m/s)	v_o (m/s)	Δp_{tHE} (N/m^2)	Ry (m^{-1})	K_θ
10.930	284.00	1.232	1.790E-05	19.335	6.613	514.247	455162.4	19.093
8.872	200.00	1.231	1.790E-05	15.693	5.367	351.557	369128.5	19.830
7.920	166.00	1.230	1.790E-05	14.011	4.792	286.762	329445.3	20.300
6.323	116.00	1.230	1.790E-05	11.185	3.826	192.928	262876.9	21.439
4.642	72.00	1.229	1.790E-05	8.211	2.808	113.441	192898.8	23.401
2.877	36.00	1.229	1.790E-05	5.090	1.741	51.917	119529.8	27.883

Table B.2.3.8 Heat exchanger MSF with finned surfaces at angle to the inlet flow and $\theta = 15°$.

$v_{venturi}$ (m/s)	Δp_{sHE} (N/m^2)	ρ_a (kg/m^3)	μ_a (kg/(ms))	v_i (m/s)	v_o (m/s)	Δp_{tHE} (N/m^2)	Ry (m^{-1})	K_θ
1.660	18.00	1.214	1.801E-05	3.879	1.004	27.132	67648.8	44.353
3.824	55.00	1.214	1.801E-05	8.939	2.314	103.507	155942.1	31.855
5.754	101.00	1.215	1.801E-05	13.450	3.481	210.870	234745.5	28.651
7.218	144.00	1.215	1.801E-05	16.873	4.367	316.995	294623.6	27.354
8.432	184.00	1.216	1.801E-05	19.709	5.101	420.119	344272.1	26.561
9.856	239.00	1.216	1.801E-05	23.039	5.963	561.822	402657.4	25.980

Table B.2.3.9 Heat exchanger MSF with finned surfaces parallel to the inlet flow and $\theta = 15°$.

$v_{venturi}$ (m/s)	Δp_{sHE} (N/m^2)	ρ_a (kg/m^3)	μ_a (kg/(ms))	v_i (m/s)	v_o (m/s)	Δp_{tHE} (N/m^2)	Ry (m^{-1})	K_θ
9.770	218.00	1.216	1.801E-05	22.838	5.911	535.140	399056.6	25.190
8.512	174.00	1.216	1.801E-05	19.898	5.150	414.648	347540.7	25.722
7.293	136.00	1.215	1.801E-05	17.048	4.412	312.571	297641.5	26.426
5.908	98.00	1.215	1.801E-05	13.811	3.575	213.846	241041.9	27.557
4.023	55.00	1.214	1.801E-05	9.403	2.434	108.680	164046.5	30.223
1.675	18.00	1.214	1.801E-05	3.915	1.013	27.301	68271.0	43.820

Table B.2.3.10 Heat exchanger MSF with finned surfaces at angle to the inlet flow and θ = 10°.

$v_{venturi}$ (m/s)	Δp_{sHE} (N/m^2)	ρ_a (kg/m^3)	μ_a (kg/(ms))	v_i (m/s)	v_o (m/s)	Δp_{tHE} (N/m^2)	Ry (m^{-1})	K_θ
11.132	296.50	1.224	1.792E-05	38.785	6.735	1216.959	459944.2	43.846
8.652	190.00	1.223	1.792E-05	30.144	5.235	745.448	357105.0	44.508
7.305	143.00	1.222	1.792E-05	25.450	4.419	538.745	301356.7	45.147
6.176	108.50	1.222	1.792E-05	21.517	3.736	391.271	254692.7	45.888
4.267	61.00	1.221	1.792E-05	14.868	2.582	195.944	175903.0	48.155
2.879	34.50	1.221	1.792E-05	10.030	1.742	95.899	118636.9	51.798

Table B.2.3.11 Heat exchanger MSF with finned surfaces parallel to the inlet flow and θ = 10°.

$v_{venturi}$ (m/s)	Δp_{sHE} (N/m^2)	ρ_a (kg/m^3)	μ_a (kg/(ms))	v_i (m/s)	v_o (m/s)	Δp_{tHE} (N/m^2)	Ry (m^{-1})	K_θ
2.896	30.00	1.216	1.797E-05	10.089	1.752	91.903	118606.3	49.235
4.187	51.00	1.217	1.797E-05	14.586	2.533	180.423	171515.4	46.232
6.247	96.50	1.217	1.797E-05	21.765	3.780	384.809	256049.3	44.264
7.452	130.00	1.218	1.797E-05	25.963	4.508	540.365	305528.2	43.669
8.741	170.50	1.218	1.797E-05	30.453	5.288	735.301	358509.9	43.175
11.245	267.00	1.219	1.797E-05	39.177	6.803	1202.651	461654.8	42.627

B.2.4. Experimental and calculated results of heat exchanger SM

Table B.2.4.1 Heat exchanger SM with $\theta = 90°$.

$v_{venturi}$ (m/s)	Δp_{sHE} (N/m^2)	ρ_a (kg/m^3)	μ_a (kg/(ms))	v_i (m/s)	v_o (m/s)	Δp_{tHE} (N/m^2)	Ry (m^{-1})	K_θ
2.534	47.00	1.237	1.783E-05	1.533	1.533	48.455	106433.3	33.312
5.144	139.00	1.239	1.783E-05	3.112	3.112	144.999	216242.2	24.171
6.867	220.00	1.240	1.783E-05	4.155	4.155	230.699	288898.7	21.563
8.260	298.00	1.241	1.783E-05	4.997	4.997	313.489	347744.8	20.239
9.644	387.00	1.242	1.783E-05	5.835	5.835	408.134	406374.1	19.312
11.331	510.00	1.243	1.783E-05	6.855	6.855	539.209	478032.3	18.460

Table B.2.4.2 Heat exchanger SM with finned surfaces at angle to the inlet flow and $\theta = 60°$.

$v_{venturi}$ (m/s)	Δp_{sHE} (N/m^2)	ρ_a (kg/m^3)	μ_a (kg/(ms))	v_i (m/s)	v_o (m/s)	Δp_{tHE} (N/m^2)	Ry (m^{-1})	K_θ
10.908	477.00	1.225	1.801E-05	7.620	6.599	512.560	448727.8	19.218
9.018	343.00	1.223	1.801E-05	6.300	5.456	367.275	370505.6	20.173
7.336	242.00	1.222	1.801E-05	5.125	4.439	258.050	301118.7	21.437
6.395	194.00	1.221	1.801E-05	4.467	3.869	206.189	262346.6	22.555
5.139	137.00	1.221	1.801E-05	3.590	3.109	144.866	210691.7	24.556
3.211	66.00	1.220	1.801E-05	2.243	1.943	69.069	131562.0	30.006

Table B.2.4.3 Heat exchanger SM with finned surfaces parallel to the inlet flow and $\theta = 60°$.

$v_{venturi}$ (m/s)	Δp_{sHE} (N/m^2)	ρ_a (kg/m^3)	μ_a (kg/(ms))	v_i (m/s)	v_o (m/s)	Δp_{tHE} (N/m^2)	Ry (m^{-1})	K_θ
3.206	65.00	1.215	1.806E-05	2.240	1.940	68.047	130455.8	29.779
4.947	127.00	1.215	1.806E-05	3.456	2.993	134.258	201406.3	24.665
6.210	183.00	1.216	1.806E-05	4.338	3.757	194.441	252947.3	22.660
7.692	262.00	1.217	1.806E-05	5.373	4.653	279.568	313561.1	21.218
8.846	331.00	1.218	1.806E-05	6.180	5.352	354.254	360881.1	20.312
9.960	404.00	1.219	1.806E-05	6.958	6.026	433.499	406602.2	19.594

Table B.2.4.4 Heat exchanger SM with finned surfaces at angle to the inlet flow and $\theta = 40°$.

$v_{venturi}$ (m/s)	Δp_{sHE} (N/m^2)	ρ_a (kg/m^3)	μ_a (kg/(ms))	v_i (m/s)	v_o (m/s)	Δp_{tHE} (N/m^2)	Ry (m^{-1})	K_θ
2.260	38.00	1.201	1.813E-05	2.127	1.367	40.716	90550.1	36.280
4.421	106.00	1.201	1.813E-05	4.161	2.675	116.402	177262.5	27.083
5.740	162.00	1.202	1.813E-05	5.402	3.472	179.541	230249.0	24.773
7.221	236.00	1.203	1.813E-05	6.796	4.369	263.782	289877.3	22.980
9.035	342.00	1.204	1.813E-05	8.504	5.466	385.542	363086.4	21.431
10.326	428.00	1.205	1.813E-05	9.719	6.247	484.927	415339.6	20.617

Table B.2.4.5 Heat exchanger SM with finned surfaces parallel to the inlet flow and $\theta = 40°$.

$v_{venturi}$ (m/s)	Δp_{sHE} (N/m^2)	ρ_a (kg/m^3)	μ_a (kg/(ms))	v_i (m/s)	v_o (m/s)	Δp_{tHE} (N/m^2)	Ry (m^{-1})	K_{tHE}
9.748	381.50	1.214	1.811E-05	9.175	5.897	432.601	395468.2	20.489
8.175	285.00	1.213	1.811E-05	7.695	4.946	320.908	331351.2	21.630
6.706	206.00	1.212	1.811E-05	6.312	4.057	230.146	271607.1	23.069
5.510	150.00	1.211	1.811E-05	5.186	3.334	166.291	223035.5	24.705
3.941	88.00	1.211	1.811E-05	3.709	2.384	96.327	159407.0	27.999
2.273	39.00	1.210	1.811E-05	2.140	1.375	41.770	91920.0	36.495

Table B.2.4.6 Heat exchanger SM with finned surfaces at angle to the inlet flow and $\theta = 30°$.

$v_{venturi}$ (m/s)	Δp_{sHE} (N/m^2)	ρ_a (kg/m^3)	μ_a (kg/(ms))	v_i (m/s)	v_o (m/s)	Δp_{tHE} (N/m^2)	Ry (m^{-1})	K_θ
10.282	428.00	1.217	1.804E-05	12.441	6.220	522.152	419599.3	22.183
8.743	324.00	1.215	1.804E-05	10.579	5.289	392.005	356426.3	23.057
7.474	250.00	1.215	1.804E-05	9.044	4.522	299.666	304487.8	24.134
5.655	159.00	1.213	1.804E-05	6.843	3.421	187.407	230175.6	26.389
4.592	114.00	1.213	1.804E-05	5.557	2.778	132.724	186830.7	28.354
2.852	54.00	1.212	1.804E-05	3.451	1.726	61.219	115971.3	33.922

Table B.2.4.7 Heat exchanger SM with finned surfaces parallel to the inlet flow and $\theta = 30°$.

$v_{venturi}$ (m/s)	Δp_{sHE} (N/m^2)	ρ_a (kg/m^3)	μ_a (kg/(ms))	v_i (m/s)	v_o (m/s)	Δp_{tHE} (N/m^2)	Ry (m^{-1})	K_θ
2.837	54.00	1.210	1.806E-05	3.433	1.716	61.131	115015.0	34.291
4.380	106.00	1.211	1.806E-05	5.300	2.650	123.005	177656.7	28.934
6.045	177.00	1.212	1.806E-05	7.314	3.657	209.408	245343.5	25.847
7.422	245.00	1.212	1.806E-05	8.981	4.490	293.891	301445.8	24.045
8.506	308.00	1.213	1.806E-05	10.292	5.146	372.249	345673.7	23.175
10.311	426.00	1.215	1.806E-05	12.477	6.238	520.531	419537.1	22.026

Table B.2.4.8 Heat exchanger SM with finned surfaces at angle to the inlet flow and $\theta = 20°$.

$v_{venturi}$ (m/s)	Δp_{sHE} (N/m^2)	ρ_a (kg/m^3)	μ_a (kg/(ms))	v_i (m/s)	v_o (m/s)	Δp_{tHE} (N/m^2)	Ry (m^{-1})	K_θ
10.165	421.00	1.225	1.799E-05	17.981	6.150	619.038	418772.7	26.722
8.838	330.00	1.224	1.799E-05	15.634	5.347	479.578	363784.2	27.409
7.284	240.00	1.223	1.799E-05	12.884	4.407	341.495	299529.1	28.763
5.911	170.00	1.222	1.799E-05	10.456	3.576	236.801	242918.1	30.304
4.841	124.00	1.221	1.799E-05	8.564	2.929	168.787	198858.2	32.217
2.829	54.00	1.221	1.799E-05	5.003	1.711	69.278	116106.5	38.763

Table B.2.4.9 Heat exchanger SM with finned surfaces parallel to the inlet flow and $\theta = 20°$.

$v_{venturi}$ (m/s)	Δp_{sHE} (N/m^2)	ρ_a (kg/m^3)	μ_a (kg/(ms))	v_i (m/s)	v_o (m/s)	Δp_{tHE} (N/m^2)	Ry (m^{-1})	K_θ
2.789	53.00	1.227	1.792E-05	4.933	1.687	67.926	115505.9	38.904
4.657	116.00	1.228	1.792E-05	8.238	2.817	157.654	193016.5	32.356
5.799	165.00	1.228	1.792E-05	10.257	3.508	229.611	240450.9	30.380
7.305	238.00	1.229	1.792E-05	12.922	4.420	340.627	303152.3	28.374
8.865	327.00	1.230	1.792E-05	15.680	5.363	478.243	368176.6	27.032
10.223	416.00	1.231	1.792E-05	18.084	6.185	617.332	424977.3	26.212

Table B.2.4.10 Heat exchanger SM with finned surfaces at angle to the inlet flow and θ = 15°.

$v_{venturi}$ (m/s)	Δp_{sHE} (N/m^2)	ρ_a (kg/m^3)	μ_a (kg/(ms))	v_i (m/s)	v_o (m/s)	Δp_{tHE} (N/m^2)	Ry (m^{-1})	K_θ
9.660	356.00	1.233	1.794E-05	22.580	5.844	670.436	401720.8	31.830
8.734	301.00	1.233	1.794E-05	20.415	5.284	557.895	363010.3	32.419
7.440	230.00	1.232	1.794E-05	17.392	4.501	416.315	309039.3	33.357
5.599	146.00	1.231	1.794E-05	13.088	3.387	251.425	232371.9	35.602
4.275	96.00	1.230	1.794E-05	9.992	2.586	157.414	177312.7	38.263
2.246	37.00	1.230	1.794E-05	5.250	1.359	53.943	93106.5	47.527

Table B.2.4.11 Heat exchanger SM with finned surfaces parallel to the inlet flow and θ = 15°.

$v_{venturi}$ (m/s)	Δp_{sHE} (N/m^2)	ρ_a (kg/m^3)	μ_a (kg/(ms))	v_i (m/s)	v_o (m/s)	Δp_{tHE} (N/m^2)	Ry (m^{-1})	K_θ
2.242	34.00	1.223	1.801E-05	5.241	1.356	50.796	92101.5	45.147
4.150	83.00	1.224	1.801E-05	9.702	2.511	140.594	170590.4	36.442
5.848	139.00	1.224	1.801E-05	13.670	3.538	253.395	240485.2	33.067
7.904	222.00	1.225	1.801E-05	18.477	4.782	431.174	325324.2	30.772
8.962	271.00	1.226	1.801E-05	20.948	5.422	540.004	369016.2	29.967
9.768	311.00	1.226	1.801E-05	22.834	5.910	630.726	402383.9	29.449

Table B.2.4.12 Heat exchanger SM with finned surfaces at angle to the inlet flow and θ = 10°.

$v_{venturi}$ (m/s)	Δp_{sHE} (N/m^2)	ρ_a (kg/m^3)	μ_a (kg/(ms))	v_i (m/s)	v_o (m/s)	Δp_{tHE} (N/m^2)	Ry (m^{-1})	K_θ
11.164	422.00	1.211	1.799E-05	38.895	6.754	1338.236	454761.8	48.438
8.667	274.00	1.210	1.799E-05	30.195	5.243	825.374	352520.4	49.644
7.555	218.00	1.209	1.799E-05	26.322	4.571	636.770	307134.2	50.427
5.931	148.00	1.208	1.799E-05	20.665	3.588	405.926	240955.3	52.193
4.652	101.00	1.207	1.799E-05	16.208	2.815	259.600	188903.2	54.283
2.827	48.00	1.207	1.799E-05	9.849	1.710	106.530	114725.8	60.361

Table B.2.4.13 Heat exchanger SM with finned surfaces parallel to the inlet flow and $\theta = 10°$.

$v_{venturi}$ (m/s)	Δp_{sHE} (N/m^2)	ρ_a (kg/m^3)	μ_a (kg/(ms))	v_i (m/s)	v_o (m/s)	Δp_{tHE} (N/m^2)	Ry (m^{-1})	K_θ
2.848	41.00	1.203	1.804E-05	9.923	1.723	100.208	114889.3	56.128
4.607	82.00	1.203	1.804E-05	16.051	2.787	236.968	185907.9	50.712
6.237	130.00	1.204	1.804E-05	21.729	3.773	414.144	251796.6	48.336
7.478	172.00	1.204	1.804E-05	26.055	4.524	580.722	302054.6	47.119
8.555	212.00	1.205	1.804E-05	29.807	5.176	747.125	345689.1	46.302
11.054	321.00	1.206	1.804E-05	38.512	6.688	1215.304	447132.2	45.067

B.2.5. Experimental and calculated results of heat exchanger LUM

Table B.2.5.1 Heat exchanger LUM with $\theta = 90°$.

$v_{venturi}$ (m/s)	Δp_{sHE} (N/m^2)	ρ_a (kg/m^3)	μ_a (kg/(ms))	v_i (m/s)	v_o (m/s)	Δp_{tHE} (N/m^2)	Ry (m^{-1})	K_θ
10.499	503.00	1.210	1.808E-05	6.352	6.352	527.413	425065.1	21.604
8.641	362.00	1.208	1.808E-05	5.228	5.228	378.512	349338.2	22.923
7.619	292.00	1.208	1.808E-05	4.609	4.609	304.828	307808.4	23.762
5.880	189.00	1.206	1.808E-05	3.557	3.557	196.633	237313.2	25.761
4.614	125.00	1.206	1.808E-05	2.792	2.792	129.697	186109.4	27.610
2.331	40.00	1.205	1.808E-05	1.410	1.410	41.197	93922.2	34.407

Table B.2.5.2 Heat exchanger LUM with finned surfaces at angle to the inlet flow and $\theta = 40°$.

$v_{venturi}$ (m/s)	Δp_{sHE} (N/m^2)	ρ_a (kg/m^3)	μ_a (kg/(ms))	v_i (m/s)	v_o (m/s)	Δp_{tHE} (N/m^2)	Ry (m^{-1})	K_θ
2.823	58.00	1.215	1.801E-05	2.657	1.708	62.288	115200.4	35.155
4.355	119.00	1.216	1.801E-05	4.099	2.635	129.216	177860.4	30.613
5.956	199.00	1.217	1.801E-05	5.606	3.603	218.119	243412.5	27.612
7.311	279.00	1.218	1.801E-05	6.882	4.423	307.836	299053.7	25.838
8.478	357.00	1.219	1.801E-05	7.979	5.129	395.800	347029.0	24.689
10.857	542.00	1.221	1.801E-05	10.219	6.569	605.752	445236.9	22.997

Table B.2.5.3 Heat exchanger LUM with finned surfaces parallel to the inlet flow and $\theta = 40°$.

$v_{venturi}$ (m/s)	Δp_{sHE} (N/m^2)	ρ_a (kg/m^3)	μ_a (kg/(ms))	v_i (m/s)	v_o (m/s)	Δp_{tHE} (N/m^2)	Ry (m^{-1})	K_θ
10.731	508.00	1.218	1.804E-05	10.100	6.492	570.144	438569.8	22.205
8.600	350.00	1.217	1.804E-05	8.094	5.203	389.854	350945.1	23.675
7.481	276.00	1.216	1.804E-05	7.041	4.526	306.132	305040.0	24.589
5.414	162.00	1.214	1.804E-05	5.095	3.275	177.764	220512.5	27.292
4.115	103.00	1.214	1.804E-05	3.873	2.490	112.104	167523.7	29.804
2.192	36.00	1.213	1.804E-05	2.063	1.326	38.582	89185.8	36.167

Table B.2.5.4 Heat exchanger LUM with finned surfaces at angle to the inlet flow and θ = 30°.

$v_{venturi}$ (m/s)	Δp_{sHE} (N/m^2)	ρ_a (kg/m^3)	μ_a (kg/(ms))	v_i (m/s)	v_o (m/s)	Δp_{tHE} (N/m^2)	Ry (m^{-1})	K_θ
10.334	482.00	1.217	1.802E-05	12.504	6.252	577.104	421969.1	24.273
8.835	371.00	1.215	1.802E-05	10.691	5.345	440.443	360376.6	25.370
7.270	268.00	1.214	1.802E-05	8.797	4.399	314.975	296249.0	26.821
5.913	190.00	1.213	1.802E-05	7.155	3.577	221.049	240758.6	28.477
4.511	122.00	1.212	1.802E-05	5.459	2.729	140.062	183564.1	31.019
2.282	41.00	1.211	1.802E-05	2.762	1.381	45.619	92790.2	39.507

Table B.2.5.5 Heat exchanger LUM with finned surfaces parallel to the inlet flow and θ = 30°.

$v_{venturi}$ (m/s)	Δp_{sHE} (N/m^2)	ρ_a (kg/m^3)	μ_a (kg/(ms))	v_i (m/s)	v_o (m/s)	Δp_{tHE} (N/m^2)	Ry (m^{-1})	K_θ
2.267	39.00	1.210	1.804E-05	2.744	1.372	43.555	92046.1	38.249
4.335	111.00	1.211	1.804E-05	5.246	2.623	127.664	176119.5	30.644
5.935	185.00	1.212	1.804E-05	7.182	3.591	216.253	241280.0	27.678
7.712	285.00	1.213	1.804E-05	9.332	4.666	337.825	313843.8	25.581
8.690	346.00	1.214	1.804E-05	10.515	5.258	413.112	353852.6	24.622
10.232	455.00	1.215	1.804E-05	12.381	6.190	548.132	417066.7	23.542

Table B.2.5.6 Heat exchanger LUM with finned surfaces at angle to the inlet flow and θ = 20°.

$v_{venturi}$ (m/s)	Δp_{sHE} (N/m^2)	ρ_a (kg/m^3)	μ_a (kg/(ms))	v_i (m/s)	v_o (m/s)	Δp_{tHE} (N/m^2)	Ry (m^{-1})	K_θ
2.816	56.00	1.216	1.804E-05	4.982	1.704	71.093	114907.2	40.266
4.633	126.00	1.217	1.804E-05	8.195	2.803	166.876	189163.8	34.900
5.997	192.00	1.218	1.804E-05	10.609	3.628	260.544	245037.1	32.494
7.346	269.00	1.219	1.804E-05	12.994	4.444	371.912	300360.5	30.894
8.838	365.00	1.220	1.804E-05	15.634	5.347	514.102	361706.4	29.476
10.666	502.00	1.222	1.804E-05	18.866	6.453	719.430	437086.2	28.286

Table B.2.5.7 Heat exchanger LUM with finned surfaces parallel to the inlet flow and θ = 20°.

$v_{venturi}$ (m/s)	Δp_{sHE} (N/m^2)	ρ_a (kg/m^3)	μ_a (kg/(ms))	v_i (m/s)	v_o (m/s)	Δp_{tHE} (N/m^2)	Ry (m^{-1})	K_θ
10.873	472.00	1.219	1.806E-05	19.234	6.578	697.536	444138.8	26.439
8.796	332.00	1.218	1.806E-05	15.560	5.322	479.400	358807.2	27.803
7.520	255.00	1.217	1.806E-05	13.303	4.550	362.656	306525.4	28.797
6.201	184.00	1.216	1.806E-05	10.969	3.752	257.142	252569.3	30.054
4.838	123.00	1.215	1.806E-05	8.558	2.927	167.497	196939.0	32.179
2.832	51.50	1.214	1.806E-05	5.009	1.713	66.731	115179.5	37.454

Table B.2.5.8 Heat exchanger LUM with finned surfaces at angle to the inlet flow and θ = 15°.

$v_{venturi}$ (m/s)	Δp_{sHE} (N/m^2)	ρ_a (kg/m^3)	μ_a (kg/(ms))	v_i (m/s)	v_o (m/s)	Δp_{tHE} (N/m^2)	Ry (m^{-1})	K_θ
3.444	72.00	1.219	1.799E-05	8.051	2.084	111.521	141241.1	42.125
5.108	135.00	1.220	1.799E-05	11.940	3.090	221.977	209596.1	38.099
6.610	204.00	1.221	1.799E-05	15.450	3.999	349.725	271390.9	35.826
7.942	274.00	1.222	1.799E-05	18.565	4.805	484.543	326324.1	34.356
8.736	321.00	1.222	1.799E-05	20.421	5.285	575.871	359119.5	33.730
10.676	444.00	1.224	1.799E-05	24.956	6.459	825.085	439391.8	32.321

Table B.2.5.9 Heat exchanger LUM with finned surfaces parallel to the inlet flow and θ = 15°.

$v_{venturi}$ (m/s)	Δp_{sHE} (N/m^2)	ρ_a (kg/m^3)	μ_a (kg/(ms))	v_i (m/s)	v_o (m/s)	Δp_{tHE} (N/m^2)	Ry (m^{-1})	K_θ
10.691	441.00	1.226	1.797E-05	24.990	6.468	823.798	441323.2	32.126
8.646	311.00	1.224	1.797E-05	20.210	5.231	561.033	356445.4	33.496
7.805	262.00	1.224	1.797E-05	18.244	4.722	465.657	321617.1	34.133
6.667	202.00	1.223	1.797E-05	15.585	4.034	350.533	274582.7	35.230
5.269	137.00	1.222	1.797E-05	12.316	3.188	229.703	216854.3	36.990
3.456	69.50	1.221	1.797E-05	8.078	2.091	109.351	142133.6	40.963

Table B.2.5.10 Heat exchanger LUM with finned surfaces at angle to the inlet flow and θ = 10°.

$v_{venturi}$ (m/s)	Δp_{sHE} (N/m^2)	ρ_a (kg/m^3)	μ_a (kg/(ms))	v_i (m/s)	v_o (m/s)	Δp_{tHE} (N/m^2)	Ry (m^{-1})	K_θ
10.605	316.00	1.214	1.804E-05	36.950	6.416	1144.403	431698.4	45.814
8.646	232.00	1.213	1.804E-05	30.123	5.231	782.123	351648.8	47.149
7.284	178.00	1.212	1.804E-05	25.377	4.407	568.227	296088.9	48.291
5.722	123.00	1.211	1.804E-05	19.936	3.462	363.706	232481.5	50.110
3.910	68.00	1.211	1.804E-05	13.624	2.366	180.343	158781.4	53.237
1.640	19.00	1.210	1.804E-05	5.714	0.992	38.750	66559.5	65.067

Table B.2.5.11 Heat exchanger LUM with finned surfaces parallel to the inlet flow and θ = 10°.

$v_{venturi}$ (m/s)	Δp_{sHE} (N/m^2)	ρ_a (kg/m^3)	μ_a (kg/(ms))	v_i (m/s)	v_o (m/s)	Δp_{tHE} (N/m^2)	Ry (m^{-1})	K_θ
1.635	20.00	1.208	1.806E-05	5.698	0.989	39.606	66173.9	66.993
3.750	72.00	1.209	1.806E-05	13.063	2.268	175.119	151800.7	56.319
5.825	149.00	1.209	1.806E-05	20.296	3.524	398.108	236027.8	53.000
7.128	207.00	1.210	1.806E-05	24.833	4.312	580.140	288954.5	51.561
8.498	273.00	1.211	1.806E-05	29.606	5.141	803.710	344717.9	50.223
10.407	372.00	1.212	1.806E-05	36.258	6.296	1168.755	422581.0	48.647

B.2.6. Experimental and calculated results of heat exchanger HUNG

Table B.2.6.1 Heat exchanger HUNG with $\theta = 90°$.

$v_{venturi}$ (m/s)	Δp_{sHE} (N/m^2)	ρ_a (kg/m^3)	μ_a (kg/(ms))	v_i (m/s)	v_o (m/s)	Δp_{tHE} (N/m^2)	Ry (m^{-1})	K_θ
2.308	41.50	1.207	1.806E-05	1.397	1.397	42.677	93303.2	36.272
4.405	118.50	1.208	1.806E-05	2.665	2.665	122.788	178190.3	28.635
5.805	191.00	1.208	1.806E-05	3.512	3.512	198.452	234981.9	26.632
7.489	297.00	1.210	1.806E-05	4.531	4.531	309.417	303493.4	24.918
8.887	399.00	1.211	1.806E-05	5.377	5.377	416.501	360488.1	23.798
10.109	500.00	1.212	1.806E-05	6.116	6.116	522.668	410466.3	23.058

Table B.2.6.2 Heat exchanger HUNG with finned surfaces at angle to the inlet flow and $\theta = 40°$.

$v_{venturi}$ (m/s)	Δp_{sHE} (N/m^2)	ρ_a (kg/m^3)	μ_a (kg/(ms))	v_i (m/s)	v_o (m/s)	Δp_{tHE} (N/m^2)	Ry (m^{-1})	K_θ
2.177	38.00	1.211	1.806E-05	2.049	1.317	40.542	88299.9	38.605
3.702	89.00	1.211	1.806E-05	3.485	2.240	96.354	150235.3	31.711
5.585	179.00	1.212	1.806E-05	5.257	3.379	195.753	226854.2	28.280
6.947	261.00	1.213	1.806E-05	6.539	4.203	286.942	282407.5	26.771
8.006	331.00	1.214	1.806E-05	7.535	4.843	365.470	325646.2	25.661
9.409	436.00	1.216	1.806E-05	8.856	5.692	483.664	383131.4	24.559

Table B.2.6.3 Heat exchanger HUNG with finned surfaces parallel to the inlet flow and $\theta = 40°$.

$v_{venturi}$ (m/s)	Δp_{sHE} (N/m^2)	ρ_a (kg/m^3)	μ_a (kg/(ms))	v_i (m/s)	v_o (m/s)	Δp_{tHE} (N/m^2)	Ry (m^{-1})	K_θ
10.087	482.00	1.222	1.799E-05	9.494	6.103	537.050	414363.7	23.611
8.299	345.00	1.220	1.799E-05	7.811	5.021	382.215	340460.5	24.858
7.404	283.00	1.219	1.799E-05	6.968	4.479	312.600	303544.0	25.560
5.761	184.00	1.218	1.799E-05	5.422	3.485	201.904	235959.0	27.294
4.109	103.00	1.217	1.799E-05	3.867	2.486	112.099	168146.8	29.817
2.065	34.00	1.216	1.799E-05	1.943	1.249	36.296	84439.3	38.258

Table B.2.6.4 Heat exchanger HUNG with finned surfaces at angle to the inlet flow and θ = 30°.

$v_{venturi}$ (m/s)	Δp_{sHE} (N/m^2)	ρ_a (kg/m^3)	μ_a (kg/(ms))	v_i (m/s)	v_o (m/s)	Δp_{tHE} (N/m^2)	Ry (m^{-1})	K_θ
9.891	475.00	1.215	1.804E-05	11.968	5.984	562.051	403262.2	25.826
8.718	382.00	1.214	1.804E-05	10.549	5.274	449.561	355099.6	26.616
7.529	297.00	1.213	1.804E-05	9.110	4.555	347.342	306395.9	27.599
5.487	173.00	1.212	1.804E-05	6.639	3.320	199.707	223032.1	29.911
4.268	113.00	1.211	1.804E-05	5.164	2.582	129.149	173377.2	31.990
2.579	49.00	1.210	1.804E-05	3.120	1.560	54.892	104690.7	37.267

Table B.2.6.5 Heat exchanger HUNG with finned surfaces parallel to the inlet flow and θ = 30°.

$v_{venturi}$ (m/s)	Δp_{sHE} (N/m^2)	ρ_a (kg/m^3)	μ_a (kg/(ms))	v_i (m/s)	v_o (m/s)	Δp_{tHE} (N/m^2)	Ry (m^{-1})	K_θ
2.558	47.00	1.210	1.804E-05	3.095	1.548	52.798	103850.6	36.427
4.547	123.00	1.211	1.804E-05	5.502	2.751	141.332	184736.1	30.838
6.086	201.00	1.212	1.804E-05	7.364	3.682	233.862	247433.9	28.466
7.430	281.00	1.213	1.804E-05	8.991	4.495	330.031	302356.7	26.924
8.567	357.00	1.214	1.804E-05	10.366	5.183	422.219	348846.8	25.895
10.087	471.00	1.215	1.804E-05	12.205	6.102	561.521	411213.0	24.813

Table B.2.6.6 Heat exchanger HUNG with finned surfaces at angle to the inlet flow and θ = 20°.

$v_{venturi}$ (m/s)	Δp_{sHE} (N/m^2)	ρ_a (kg/m^3)	μ_a (kg/(ms))	v_i (m/s)	v_o (m/s)	Δp_{tHE} (N/m^2)	Ry (m^{-1})	K_θ
2.820	55.00	1.212	1.808E-05	4.988	1.706	70.083	114375.3	39.721
4.609	125.00	1.213	1.808E-05	8.152	2.788	165.311	187047.0	35.057
5.970	194.00	1.214	1.808E-05	10.560	3.612	261.676	242440.2	33.054
7.295	272.00	1.215	1.808E-05	12.903	4.413	373.133	296482.9	31.541
8.765	370.00	1.216	1.808E-05	15.504	5.303	516.148	356582.3	30.191
10.531	507.00	1.218	1.808E-05	18.629	6.371	718.271	429017.8	29.063

Table B.2.6.7 Heat exchanger HUNG with finned surfaces parallel to the inlet flow and θ = 20°.

$v_{venturi}$ (m/s)	Δp_{sHE} (N/m^2)	ρ_a (kg/m^3)	μ_a (kg/(ms))	v_i (m/s)	v_o (m/s)	Δp_{tHE} (N/m^2)	Ry (m^{-1})	K_θ
10.774	487.00	1.215	1.811E-05	19.058	6.518	707.705	437512.4	27.412
8.671	342.00	1.214	1.811E-05	15.338	5.246	484.743	351602.1	29.030
7.375	261.00	1.213	1.811E-05	13.045	4.462	364.175	298806.1	30.174
6.128	192.00	1.212	1.811E-05	10.841	3.708	263.204	248146.1	31.600
4.798	127.00	1.211	1.811E-05	8.487	2.903	170.614	194145.7	33.442
2.807	53.00	1.210	1.811E-05	4.966	1.698	67.920	113513.4	38.915

Table B.2.6.8 Heat exchanger HUNG with finned surfaces at angle to the inlet flow and θ = 15°.

$v_{venturi}$ (m/s)	Δp_{sHE} (N/m^2)	ρ_a (kg/m^3)	μ_a (kg/(ms))	v_i (m/s)	v_o (m/s)	Δp_{tHE} (N/m^2)	Ry (m^{-1})	K_θ
2.739	52.00	1.214	1.801E-05	6.403	1.657	76.885	111692.8	46.122
4.730	129.00	1.215	1.801E-05	11.057	2.862	203.281	193044.0	40.853
6.241	205.00	1.216	1.801E-05	14.589	3.776	334.396	254884.0	38.579
7.508	280.00	1.217	1.801E-05	17.550	4.542	467.405	306854.8	37.232
8.541	349.00	1.218	1.801E-05	19.966	5.168	591.709	349327.8	36.394
10.415	485.00	1.219	1.801E-05	24.344	6.301	846.317	426506.0	34.966

Table B.2.6.9 Heat exchanger HUNG with finned surfaces parallel to the inlet flow and θ = 15°.

$v_{venturi}$ (m/s)	Δp_{sHE} (N/m^2)	ρ_a (kg/m^3)	μ_a (kg/(ms))	v_i (m/s)	v_o (m/s)	Δp_{tHE} (N/m^2)	Ry (m^{-1})	K_θ
10.832	418.00	1.219	1.801E-05	25.319	6.553	808.573	443291.0	30.905
8.765	300.00	1.217	1.801E-05	20.488	5.303	555.454	358295.1	32.460
7.517	237.00	1.216	1.801E-05	17.570	4.548	424.756	307076.8	33.772
6.455	186.00	1.216	1.801E-05	15.089	3.905	324.400	263577.9	34.991
4.969	124.00	1.215	1.801E-05	11.615	3.006	205.962	202774.9	37.513
2.760	48.00	1.214	1.801E-05	6.451	1.670	73.260	112528.6	43.295

Table B.2.6.8 Heat exchanger HUNG with finned surfaces at angle to the inlet flow and θ = 10°.

$v_{venturi}$ (m/s)	Δp_{sHE} (N/m^2)	ρ_a (kg/m^3)	μ_a (kg/(ms))	v_i (m/s)	v_o (m/s)	Δp_{tHE} (N/m^2)	Ry (m^{-1})	K_θ
10.487	465.00	1.217	1.801E-05	36.538	6.345	1277.621	428801.8	52.140
8.745	341.00	1.216	1.801E-05	30.468	5.291	905.382	357135.9	53.201
7.356	255.00	1.215	1.801E-05	25.630	4.451	654.032	300169.4	54.356
5.811	171.00	1.214	1.801E-05	20.246	3.516	419.793	236919.7	55.957
4.562	114.00	1.213	1.801E-05	15.894	2.760	267.235	185882.7	57.836
2.797	51.00	1.212	1.801E-05	9.746	1.692	108.576	113905.2	62.539

Table B.2.6.9 Heat exchanger HUNG with finned surfaces parallel to the inlet flow and θ = 10°.

$v_{venturi}$ (m/s)	Δp_{sHE} (N/m^2)	ρ_a (kg/m^3)	μ_a (kg/(ms))	v_i (m/s)	v_o (m/s)	Δp_{tHE} (N/m^2)	Ry (m^{-1})	K_θ
2.842	43.00	1.212	1.801E-05	9.902	1.719	102.434	115723.9	57.157
4.609	88.00	1.213	1.801E-05	16.058	2.788	244.382	187757.4	51.825
6.197	135.00	1.213	1.801E-05	21.589	3.749	417.793	252545.3	48.995
7.727	186.50	1.214	1.801E-05	26.922	4.675	626.471	315084.8	47.221
9.161	240.00	1.215	1.801E-05	31.917	5.542	858.719	373746.4	46.027
10.656	300.00	1.215	1.801E-05	37.125	6.447	1137.596	434987.0	45.042

B.2.7. Experimental and calculated results of heat exchanger RAD

Table B.2.7.1 Heat exchanger RAD with $\theta = 90°$.

$v_{venturi}$ (m/s)	Δp_{sHE} (N/m^2)	ρ_a (kg/m^3)	μ_a (kg/(ms))	v_i (m/s)	v_o (m/s)	Δp_{tHE} (N/m^2)	Ry (m^{-1})	K_θ
10.318	87.00	1.205	1.808E-05	6.242	6.242	110.479	415998.1	4.706
8.440	63.50	1.205	1.808E-05	5.106	5.106	79.205	340195.0	5.043
7.340	50.50	1.205	1.808E-05	4.440	4.440	62.376	295813.9	5.252
5.540	33.00	1.204	1.808E-05	3.352	3.352	39.766	223253.7	5.877
4.308	22.50	1.204	1.808E-05	2.606	2.606	26.589	173560.6	6.502
3.063	14.00	1.204	1.808E-05	1.853	1.853	16.067	123393.1	7.772

Table B.2.7.2 Heat exchanger RAD with finned surfaces at angle to the inlet flow and $\theta = 40°$.

$v_{venturi}$ (m/s)	Δp_{sHE} (N/m^2)	ρ_a (kg/m^3)	μ_a (kg/(ms))	v_i (m/s)	v_o (m/s)	Δp_{tHE} (N/m^2)	Ry (m^{-1})	K_θ
2.988	12.00	1.214	1.804E-05	2.812	1.808	16.802	121709.1	8.468
4.648	24.00	1.214	1.804E-05	4.375	2.812	35.622	189351.3	7.418
5.904	34.00	1.215	1.804E-05	5.557	3.572	52.755	240552.1	6.808
7.515	49.00	1.215	1.804E-05	7.073	4.547	79.388	306214.5	6.323
9.846	75.00	1.215	1.804E-05	9.267	5.957	127.172	401284.1	5.900
11.814	100.00	1.215	1.804E-05	11.120	7.148	175.139	481638.0	5.641

Table B.2.7.3 Heat exchanger RAD with finned surfaces parallel to the inlet flow and $\theta = 40°$.

$v_{venturi}$ (m/s)	Δp_{sHE} (N/m^2)	ρ_a (kg/m^3)	μ_a (kg/(ms))	v_i (m/s)	v_o (m/s)	Δp_{tHE} (N/m^2)	Ry (m^{-1})	K_θ
11.580	119.00	1.216	1.804E-05	10.899	7.006	191.196	472155.7	6.410
9.969	92.00	1.215	1.804E-05	9.383	6.031	145.498	406384.3	6.582
8.429	70.00	1.215	1.804E-05	7.933	5.100	108.236	343524.9	6.851
6.556	47.00	1.215	1.804E-05	6.171	3.967	70.128	267143.9	7.339
4.849	29.00	1.215	1.804E-05	4.563	2.933	41.646	197523.7	7.970
3.031	14.00	1.214	1.804E-05	2.853	1.834	18.942	123473.0	9.276

Table B.2.7.4 Heat exchanger RAD with finned surfaces at angle to the inlet flow and θ = 30°.

$v_{venturi}$ (m/s)	Δp_{sHE} (N/m^2)	ρ_a (kg/m^3)	μ_a (kg/(ms))	v_i (m/s)	v_o (m/s)	Δp_{tHE} (N/m^2)	Ry (m^{-1})	K_θ
11.409	89.00	1.211	1.804E-05	13.805	6.902	204.374	463368.8	7.086
9.003	60.00	1.210	1.804E-05	10.893	5.447	131.815	365525.4	7.342
7.453	45.00	1.210	1.804E-05	9.018	4.509	94.209	302551.3	7.658
5.696	30.00	1.210	1.804E-05	6.893	3.446	58.746	231223.2	8.175
4.531	21.00	1.210	1.804E-05	5.483	2.742	39.188	183916.4	8.618
3.327	14.00	1.210	1.804E-05	4.025	2.013	23.802	135012.3	9.713

Table B.2.7.5 Heat exchanger RAD with finned surfaces parallel to the inlet flow and θ = 30°.

$v_{venturi}$ (m/s)	Δp_{sHE} (N/m^2)	ρ_a (kg/m^3)	μ_a (kg/(ms))	v_i (m/s)	v_o (m/s)	Δp_{tHE} (N/m^2)	Ry (m^{-1})	K_θ
3.304	17.00	1.210	1.804E-05	3.998	1.999	26.670	134097.8	11.032
4.255	25.00	1.210	1.804E-05	5.149	2.575	41.041	172721.9	10.234
5.944	42.00	1.210	1.804E-05	7.192	3.596	73.303	241305.0	9.367
8.192	71.00	1.211	1.804E-05	9.913	4.956	130.479	332671.0	8.775
9.551	90.00	1.211	1.804E-05	11.556	5.778	170.849	387891.7	8.453
11.156	117.00	1.211	1.804E-05	13.499	6.749	227.341	453210.7	8.241

Table B.2.7.6 Heat exchanger RAD with finned surfaces at angle to the inlet flow and θ = 20°.

$v_{venturi}$ (m/s)	Δp_{sHE} (N/m^2)	ρ_a (kg/m^3)	μ_a (kg/(ms))	v_i (m/s)	v_o (m/s)	Δp_{tHE} (N/m^2)	Ry (m^{-1})	K_θ
2.983	11.00	1.225	1.792E-05	5.277	1.805	28.050	123341.1	14.064
4.461	19.50	1.225	1.792E-05	7.890	2.699	57.628	184453.2	12.921
6.230	31.50	1.225	1.792E-05	11.021	3.769	105.895	257667.9	12.168
7.564	42.50	1.225	1.792E-05	13.380	4.576	152.162	312852.0	11.862
9.258	58.00	1.225	1.792E-05	16.376	5.601	222.302	382971.5	11.566
10.548	70.50	1.225	1.792E-05	18.659	6.382	283.813	436395.1	11.374

Table B.2.7.7 Heat exchanger RAD with finned surfaces parallel to the inlet flow and θ = 20°.

$v_{venturi}$ (m/s)	Δp_{sHE} (N/m^2)	ρ_a (kg/m^3)	μ_a (kg/(ms))	v_i (m/s)	v_o (m/s)	Δp_{tHE} (N/m^2)	Ry (m^{-1})	K_θ
10.126	107.50	1.224	1.794E-05	17.911	6.126	303.800	417801.7	13.230
9.002	87.00	1.224	1.794E-05	15.923	5.446	242.111	371353.4	13.343
7.603	65.00	1.223	1.794E-05	13.449	4.600	175.632	313588.1	13.571
6.345	48.00	1.223	1.794E-05	11.224	3.839	125.042	261665.1	13.875
4.650	29.00	1.223	1.794E-05	8.226	2.813	70.372	191732.7	14.541
2.969	15.00	1.223	1.794E-05	5.252	1.796	31.860	122389.5	16.154

Table B.2.7.8 Heat exchanger RAD with finned surfaces at angle to the inlet flow and θ = 15°.

$v_{venturi}$ (m/s)	Δp_{sHE} (N/m^2)	ρ_a (kg/m^3)	μ_a (kg/(ms))	v_i (m/s)	v_o (m/s)	Δp_{tHE} (N/m^2)	Ry (m^{-1})	K_θ
10.319	78.00	1.221	1.797E-05	24.122	6.243	433.146	424179.2	18.207
9.128	63.00	1.221	1.797E-05	21.337	5.522	340.834	375151.1	18.313
7.033	41.00	1.220	1.797E-05	16.440	4.255	205.906	288991.5	18.640
5.777	30.00	1.220	1.797E-05	13.504	3.495	141.243	237344.6	18.954
4.699	21.50	1.220	1.797E-05	10.985	2.843	95.104	193052.5	19.289
2.934	11.00	1.220	1.797E-05	6.859	1.775	39.693	120528.9	20.651

Table B.2.7.9 Heat exchanger RAD with finned surfaces parallel to the inlet flow and θ = 15°.

$v_{venturi}$ (m/s)	Δp_{sHE} (N/m^2)	ρ_a (kg/m^3)	μ_a (kg/(ms))	v_i (m/s)	v_o (m/s)	Δp_{tHE} (N/m^2)	Ry (m^{-1})	K_θ
2.865	13.00	1.216	1.801E-05	6.697	1.733	40.260	116975.9	22.047
4.443	25.00	1.216	1.801E-05	10.385	2.688	90.565	181424.8	20.620
5.723	38.00	1.216	1.801E-05	13.378	3.462	146.811	233735.0	20.142
6.794	51.00	1.216	1.801E-05	15.880	4.110	204.347	277493.8	19.893
8.958	81.00	1.217	1.801E-05	20.940	5.420	347.716	366019.6	19.462
10.442	106.00	1.217	1.801E-05	24.408	6.317	468.449	426733.5	19.294

Table B.2.7.10 Heat exchanger RAD with finned surfaces at angle to the inlet flow and θ = 10°.

$v_{venturi}$ (m/s)	Δp_{sHE} (N/m^2)	ρ_a (kg/m^3)	μ_a (kg/(ms))	v_i (m/s)	v_o (m/s)	Δp_{tHE} (N/m^2)	Ry (m^{-1})	K_θ
1.669	5.00	1.208	1.797E-05	5.816	1.010	25.438	67925.9	41.277
4.340	16.00	1.208	1.797E-05	15.122	2.626	154.171	176623.9	37.004
6.294	27.00	1.209	1.797E-05	21.930	3.808	317.618	256168.3	36.245
7.674	36.00	1.209	1.797E-05	26.735	4.643	467.990	312334.9	35.927
8.931	45.00	1.209	1.797E-05	31.117	5.403	630.259	363561.0	35.713
10.228	54.00	1.209	1.797E-05	35.634	6.188	821.562	416370.0	35.497

Table B.2.7.11 Heat exchanger RAD with finned surfaces parallel to the inlet flow and θ = 10°.

$v_{venturi}$ (m/s)	Δp_{sHE} (N/m^2)	ρ_a (kg/m^3)	μ_a (kg/(ms))	v_i (m/s)	v_o (m/s)	Δp_{tHE} (N/m^2)	Ry (m^{-1})	K_θ
10.054	98.00	1.218	1.787E-05	35.028	6.083	845.161	414466.8	37.513
8.776	78.00	1.218	1.787E-05	30.577	5.310	647.242	361732.8	37.708
7.441	59.00	1.217	1.787E-05	25.925	4.502	468.125	306638.3	37.946
6.228	43.00	1.217	1.787E-05	21.698	3.768	329.530	256595.4	38.140
4.458	24.50	1.217	1.787E-05	15.532	2.697	171.289	183641.3	38.699
1.673	6.00	1.217	1.787E-05	5.828	1.012	26.665	68897.5	42.792

APPENDIX C - Fan performance characteristics: experimental

The performance characteristics of an axial flow fan is usually determined in a code fan test facility. Changes made to the code fan test facility that are not covered by the particular test standard could influence the fan performance characteristics.

The purpose of this appendix is to determine the sensitivity of the performance characteristics of two axial flow fans to changes made to a standard test facility. The latter was largely motivated by the following:

- Tests conducted by Meyer[96ME1] on a range of forced draught ACHEs indicated that the axial flow fan performance characteristics had a significant influence on ACHE performance. The performance characteristics of the axial flow fans used by Meyer [96ME1], were determined with the fan drive and support structure mounted on the downstream side of the axial flow fan, whilst the drive and support structure was located on the fan upstream side for the ACHEs tests due to space limitations. In light of the above it becomes important to determine to what extent the fan performance characteristics are influenced by the location of the fan drive and support structure.
- The Type A configuration for fan tests as defined in BS 848 [80BS1], requires that the air exits from the fan directly into the atmosphere. Numerical simulation of a Type A fan test configuration utilising a CFD-code is problematic largely due to complexities associated with boundary conditions for the free atmosphere. In order to do away with the free atmosphere in the numerical simulation, an annular pipe section is added to the fan exit in the numerical model. Before the numerically determined fan performance characteristics can be compared to those determined experimentally, it is necessary to ascertain to what extent the addition of an annular pipe section at the fan exit influences the experimentally-determined fan performance characteristics.

The performance characteristics of two types of axial flow fans were determined in a code fan test facility constructed according to the specifications set in BS 848 [80BS1] of the British Standards Organisation. Changes made to the standard test installation included installation of

the fan drive on the up- and the downstream side of the axial flow fan as well as the installation of an annular pipe section at the fan outlet.

C.1. Experimental equipment

Code fan test facility

Fan tests were conducted in a fan test facility designed according to the specifications of the British Standards Organization BS 848 [80BS1] for type A tests (free inlet, free outlet). Figure C.1 is a schematic representation of the fan test facility.

The volume flow rate is measured at the calibrated inlet bell mouth (1) having a diameter of 1008 mm. The volume flow rate through the facility is controlled by means of a throttling device (3) with flow straighteners installed upstream (2) and downstream (4) thereof. Testing over a wider range of air volume flow rates is made possible with the use of a six-bladed auxiliary fan (5) with an outside diameter of 1 540 mm located downstream of the throttling device. A third flow straightener (6) is located downstream of the auxiliary fan to remove the air rotational velocity component induced by the fan rotor. Flow guide vanes (7) are installed at the inlet of the settling chamber (8) to distribute the air more evenly. The settling chamber inside dimensions are 4 m × 4 m × 7 m. A set of 3 stainless steel mesh screens (9) is installed within the settling chamber to insure a uniform velocity profile at the test fan (10) inlet.

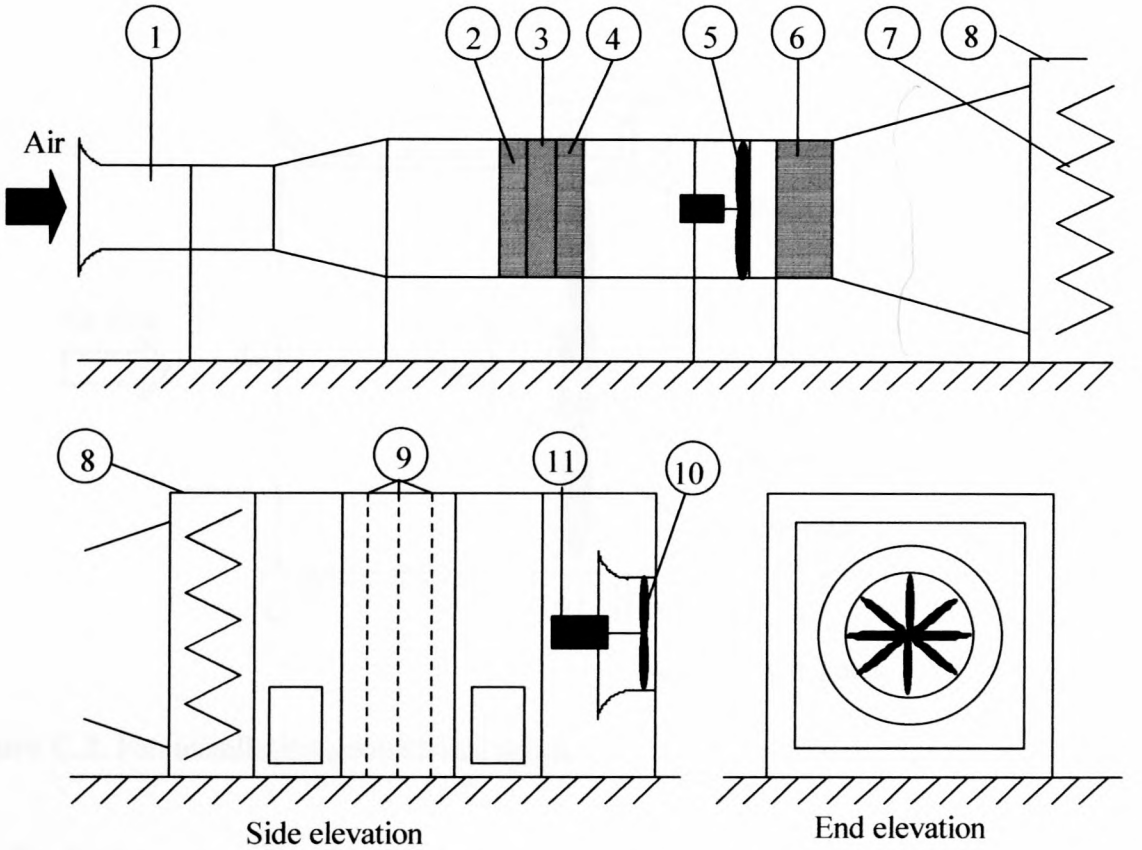

Figure C.1. Schematic representation of the code fan test facility [80BS1].

The outlet of the settling chamber takes on the form of a 2.5 m × 2.5 m square opening in which fan inlets can be installed for free outlet tests. The test fan (10) is driven by means of a hydraulic motor (11).

Axial flow fans

During the course of the investigation two axial flow fans referred to as the B-fan and the DL-fan, were tested. Figure C.2 shows the fan set-up in detail. Due to physical restrictions it was not possible to mount the fan blade trailing edge flush with the exit plane of the fan casing and the fan rotor was mounted a distance of L_{te} away from the exit plane of the fan casing.

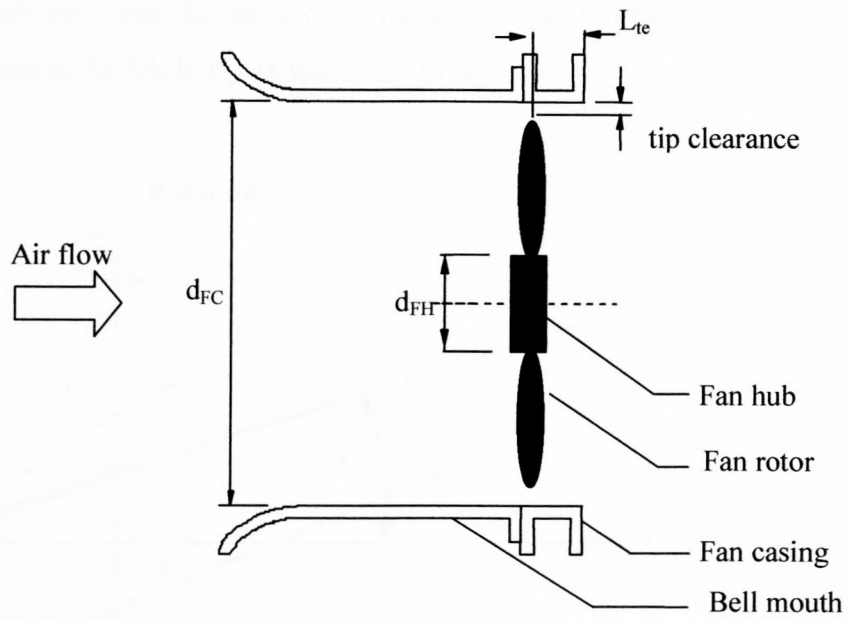

Figure C.2. Fan installation geometrical detail.

The fan blades were set within the hub at a specific angle with respect to the fan axis. No standardised procedure for fan blade setting exists. The B-fan blade angles were set at the root of the fan blades in the way indicated in figure C.3.

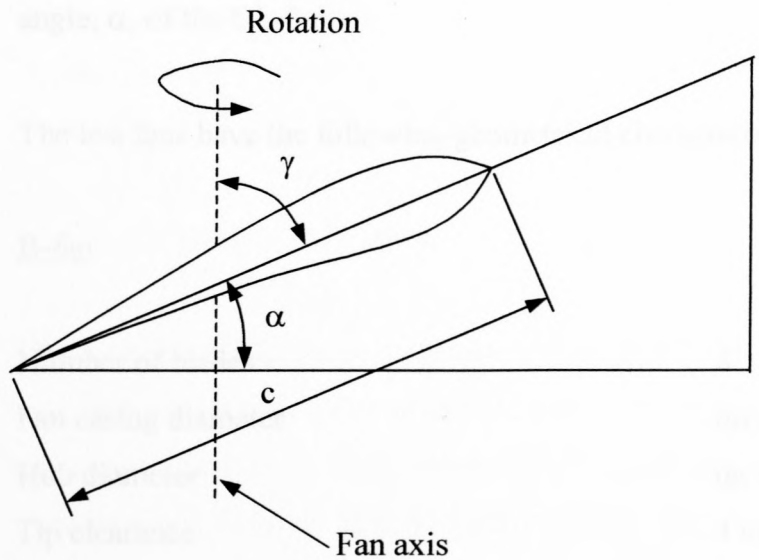

Figure C.3. Definition of fan blade root angle for the B-fan.

The blade root stagger angle, γ, was measured between the chord of the fan blade profile at the blade root and the fan axis of rotation. The fan blade tip angle, α, for the DL-fan was measured at the blade tip as indicated in figure C.4.

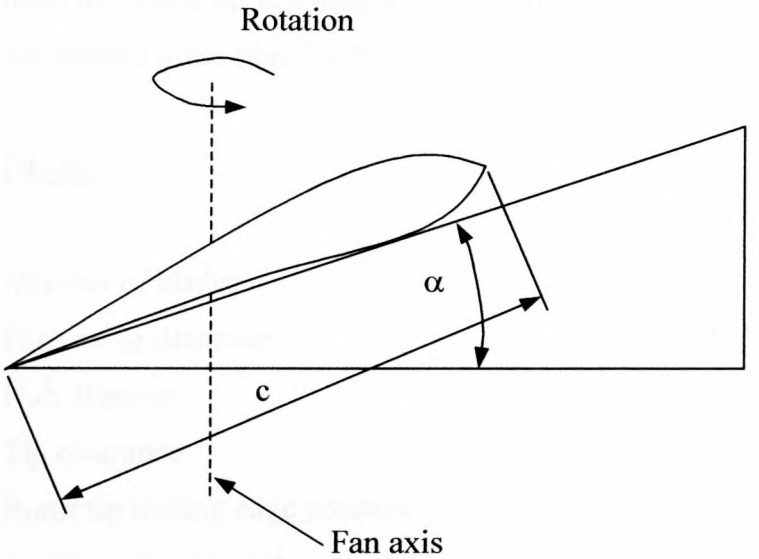

Figure C.4. Definition of fan blade tip angle for the DL-fan.

A digital protractor was used to measure the blade root angle, γ, of the B-fan and the blade tip angle, α, of the DL-fan.

The test fans have the following geometrical characteristics.

<u>B-fan</u>

Number of blades	8
Fan casing diameter	d_{FC} = 1.542 m
Hub diameter	d_H = 0.4 m
Tip clearance	4 mm
Rotor tip trailing edge position	L_{te} = 16 mm
Average chord length	c = 170 mm

The B-fan was designed at the University of Stellenbosch by Bruneau [94BR1] and makes use of a NACA LS blade cross-sectional profile. Detail pertaining to the blade and cross-section profiles and design criteria for the fan can be found in the Bruneau thesis [94BR1]. In general the fan can be described as a medium chord fan with both the blade chord and twist increasing from the blade tip reaching a maximum at the blade root close to the hub. The B-fan blades are molded glass fibre blades with a very smooth surface finish.

DL-fan

Number of blades	8
Fan casing diameter	$d_{FC} = 1.542$ m
Hub diameter	$d_H = 0.480$ m
Tip clearance	4 mm
Rotor tip trailing edge position	$L_{te} = 30$ mm
Average chord length	$c = 260$ mm

Annular pipe sections

Two annular pipe sections with a length of 3.5 m were constructed. The outside diameter of both annular pipe sections corresponds to the fan casing diameter of the test fans whilst the inside diameter of the pipe sections corresponds to the hub diameter of the B-fan and DL-fan respectively.

C.2. Experimental procedure

The B-fan and DL-fan performance characteristics were determined with the axial flow fan and hydraulic motor drive in the position indicated in figure C.5(a). The performance tests were repeated after the installation of the respective annular pipe sections at the exit of the test fans shown in figure C.5(b). The annular pipe sections were removed and the hydraulic motor drive was installed at the fan exit in the position indicated in figure C.5(c). The fan performance characteristics for both fans were repeated.

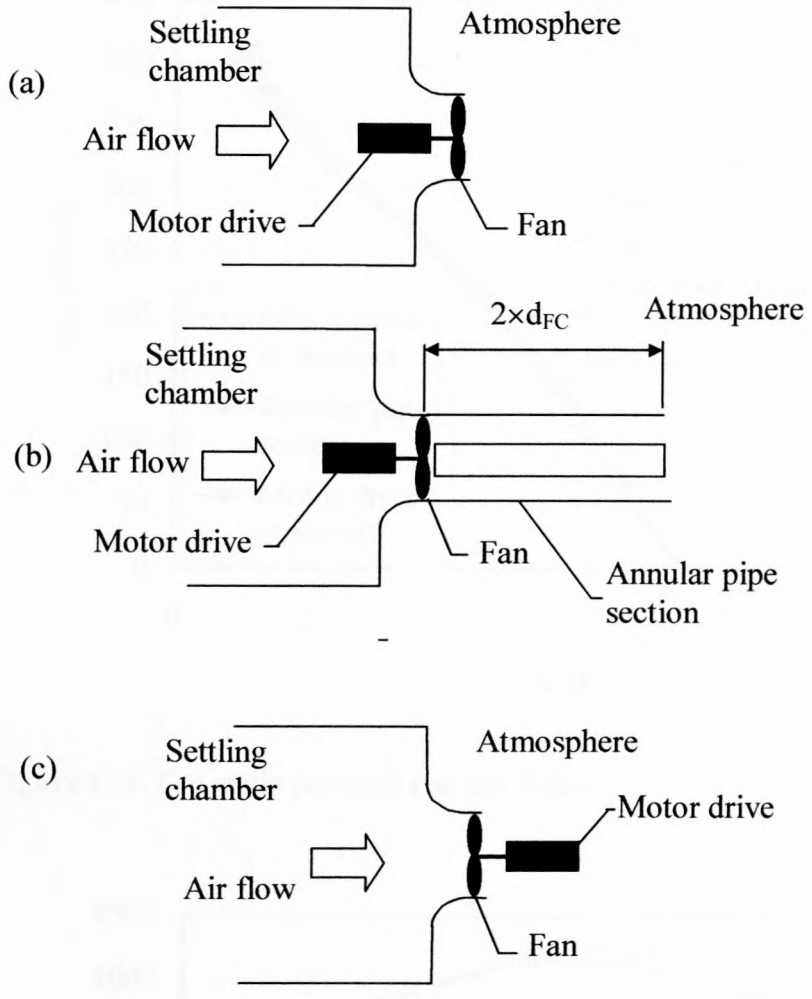

Figure C.5. The different configurations of the fan test facility.

C.3. Results and discussion

Figures C.6 - C.8 display the fan static pressure rise, fan power consumption and fan static efficiency respectively for the B-fan for the different configurations tested. Figure C.6 indicates that the fan static pressure rise characteristics are near identical for the configurations tested, although the values obtained in the case where the hydraulic motor drive was mounted at the fan exit, is slightly lower than those obtained for the other two configurations at higher volume flow rates. This discrepancy is most likely due to experimental scatter in the data.

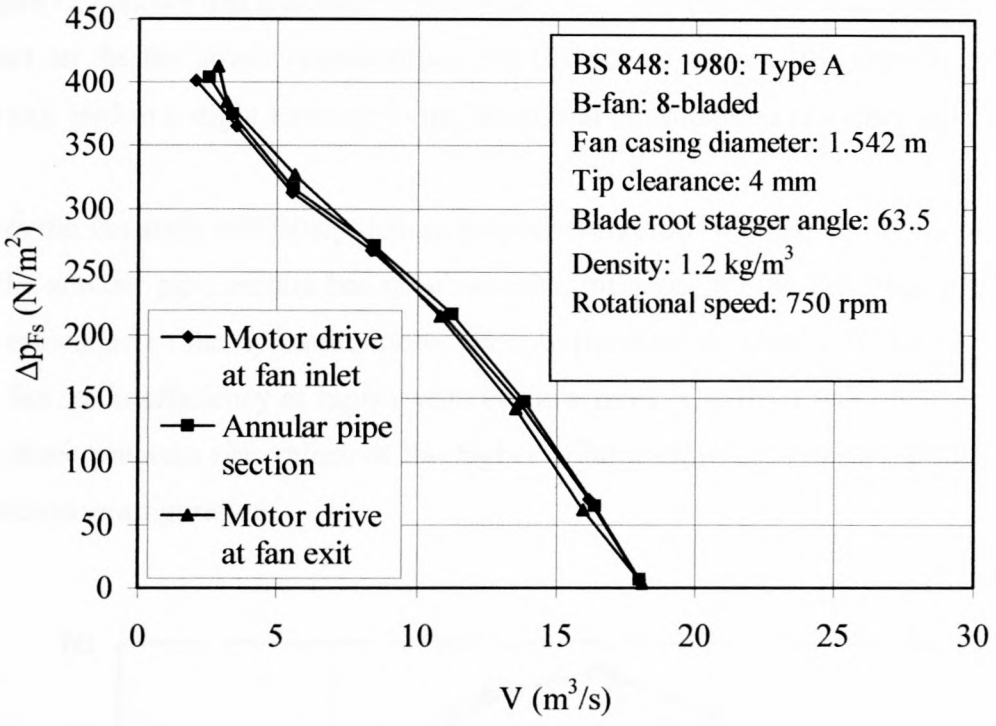

Figure C.6. Fan static pressure rise for B-fan.

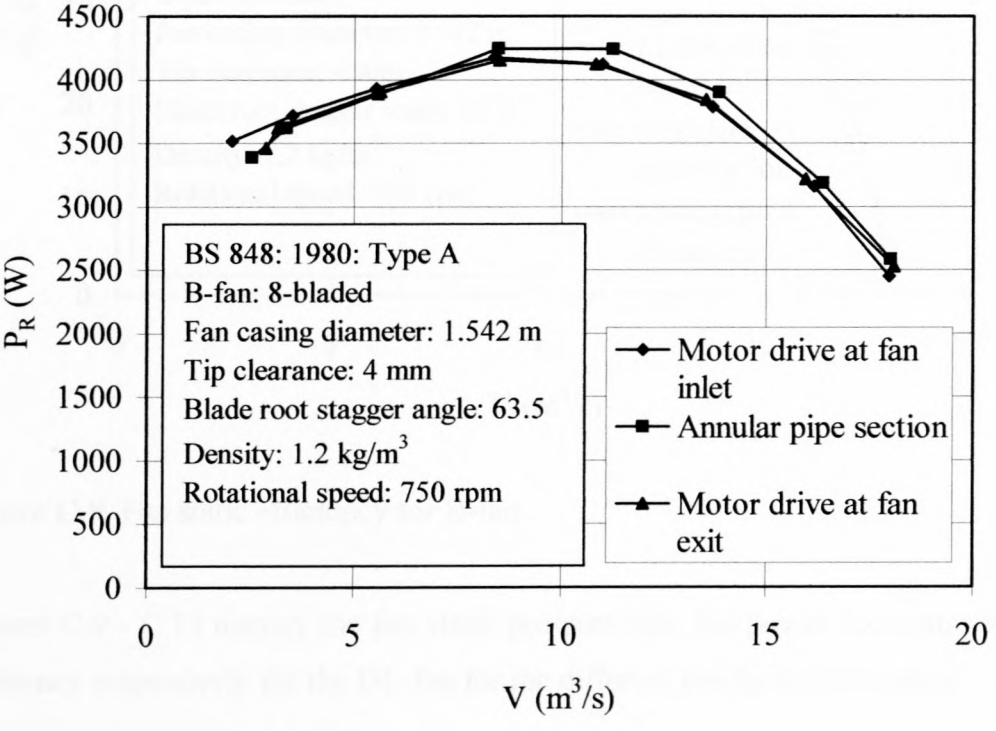

Figure C.7. Fan power consumption for B-fan.

Figure C.7 shows that a change in the position of the hydraulic motor drive has no discernable effect on the fan power consumption, but that the addition of the annular pipe section at the fan exit lead to a slight increase in the fan power consumption at higher volume flow rates.

From the fan static efficiency data displayed in figure C.8 it can be observed that the addition of the annular pipe section has no observable influence on the fan static efficiency, although the relocation of the hydraulic motor drive to the fan exit is seen to effect a slight decrease in the fan static efficiency at higher volume flow rates. The latter is a direct result of the lower fan static pressure rise values at the higher volume flow rates observed in figure C.6 for the particular configuration.

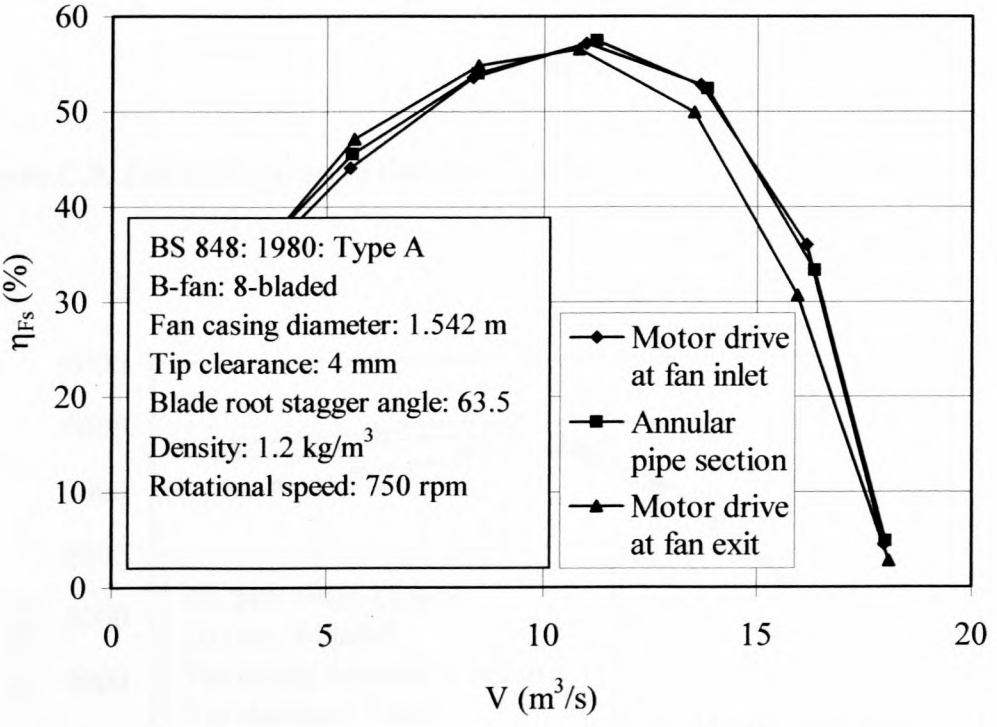

Figure C.8. Fan static efficiency for B-fan.

Figures C.9 - C.11 display the fan static pressure rise, fan power consumption and fan static efficiency respectively for the DL-fan for the different configurations tested.

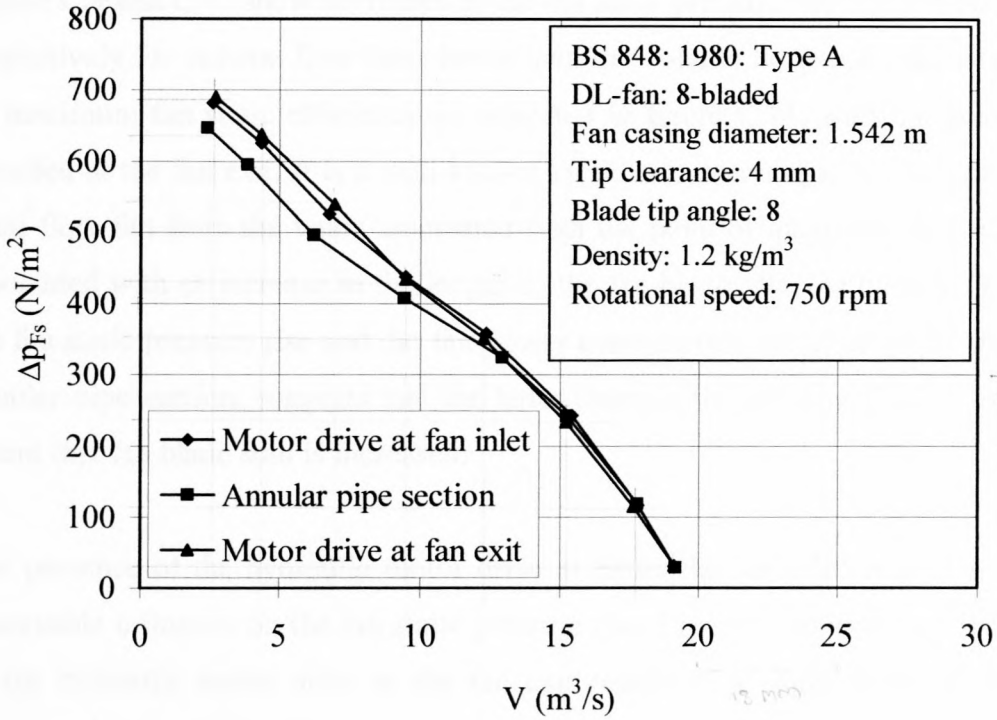

Figure C.9. Fan static pressure rise for DL-fan.

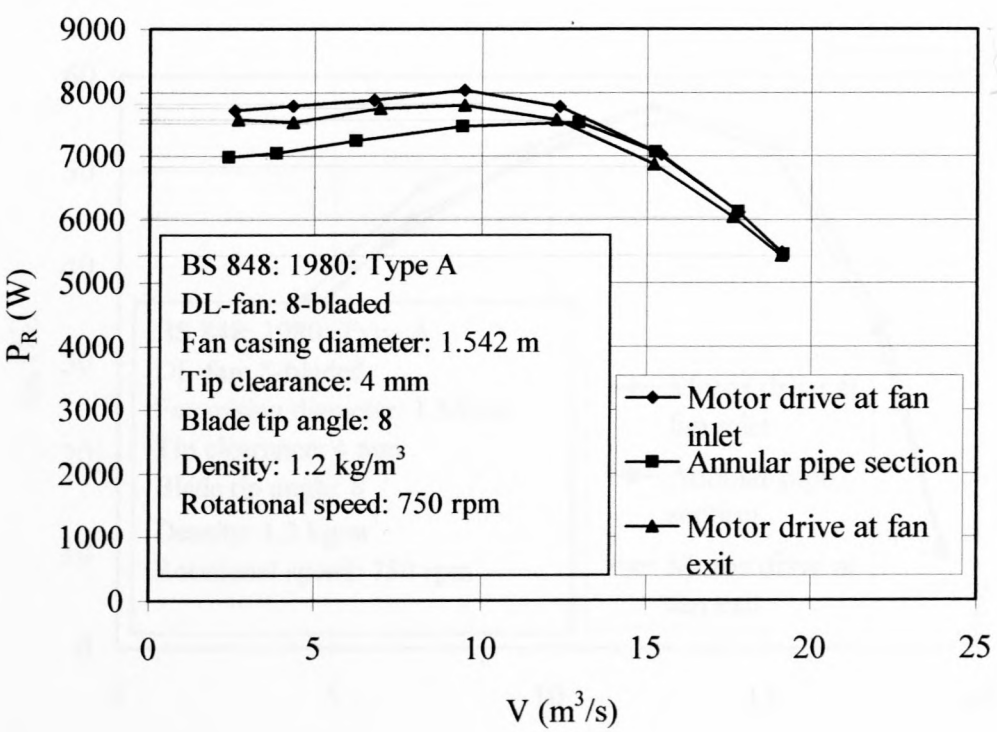

Figure C.10. Fan power consumption for DL-fan.

Figure C.9 and C.10 show decreases in the fan static pressure rise and fan power consumption respectively for volume flow rates lower than the volume flow rate associated with the point of maximum fan static efficiency as indicated in figure C.11, with the annular pipe section installed at the fan exit. It is a well-known fact that a decrease in the volume flow rate of an axial flow fan from the value associated with the point of maximum fan static efficiency is associated with an increase in the length of the fan blade affected by stall. The fact that both the fan static pressure rise and the fan power consumption are affected by the addition of the annular pipe section, suggests that the latter changes the velocity field at the fan exit to the extent that fan blade stall is increased.

The presence of the hydraulic motor drive at either the fan inlet or exit is seen to have no observable influence on the fan static pressure rise. Figure C.10 indicates that the installation of the hydraulic motor drive at the fan exit results in a slight decrease in the fan power consumption.

Figure C.11 indicates that the fan static efficiencies for the different configurations tested are near identical.

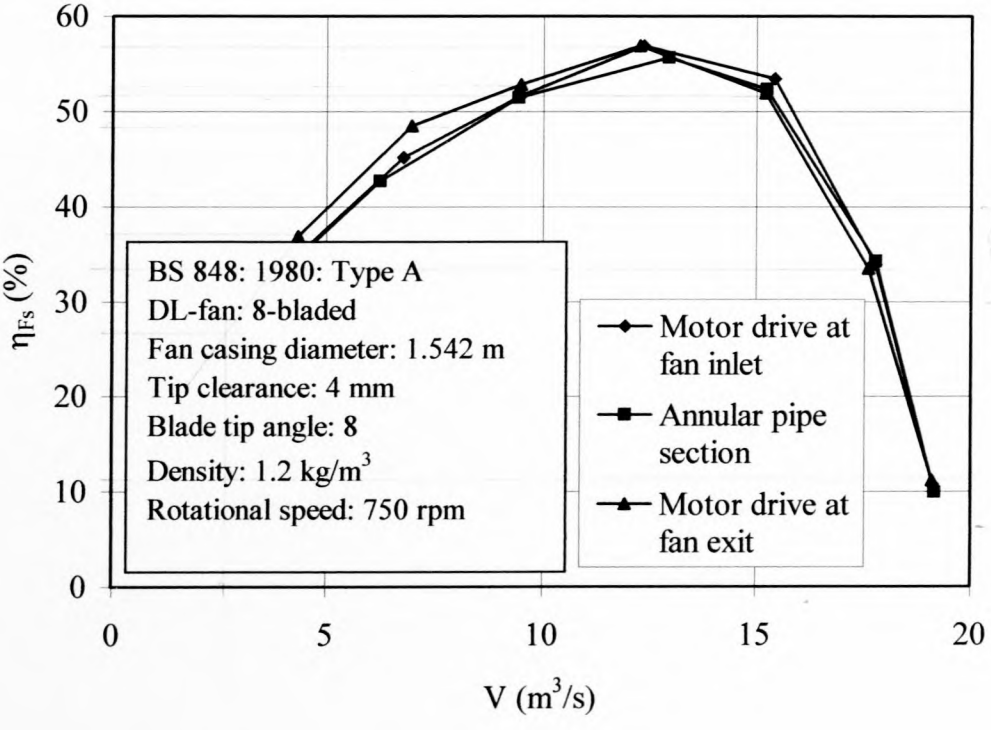

Figure C.11. Fan static efficiency for DL-fan.

C.4. Conclusions

The experimental results indicate that the influence of the position of the hydraulic motor drive as well as a the installation of an annular pipe section at the fan exit has either no or very little influence on the fan performance characteristics. The most notable effect is the lowering of the fan pressure rise and fan power consumption characteristics at lower volume flow rates of the DL-fan with the annular pipe section installed at the fan exit. The latter is thought to be the result of an increase in fan blade stall due to an alteration of the velocity field at the fan exit.

APPENDIX D – Experimental and calculated results of axial flow fan performance characteristics

This appendix contains the experimental and calculated results of the experimental investigation described in Appendix C.

D.1. Sample calculation

Fan characteristic curves are compiled from experimental data obtained from tests conducted in the code fan test facility as described previously. The static pressure differential across the inlet bell mouth and between the settling chamber and the atmosphere was measured as well as the rotational speed of the fan and the input torque transferred to the fan via the fan shaft. Also noted was the time at which sampling commenced for every individual data set. The B-fan will be considered in the sample calculation.

The B-fan blade root stagger angle was set at approximately 63.5°, with a fan tip clearance of 4 mm. The fan tip trailing edge was set 16 mm inward from the fan casing exit plane.

The experimental data and calculated results are listed in tables D.2.1 and D.2.2 respectively.

The 5^{th} data set shown in table D.2.1 produced the following measured values

Static pressure differential across the inlet bell mouth

$\Delta p_{bell} = 114.665\ N/m^2$

Static pressure differential between the settling chamber and the atmosphere

$\Delta p_{sett} = -208.148\ N/m^2$

Shaft input torque

$T = 51.358$ N.m

Fan rotational speed

$N = 750.206$ rpm

The time at which sampling commenced

$t_5 = 9{:}6{:}30$ (h:min:sec)

Barometric air pressure

$p_{bar} = 99859.8$ N/m^2

Ambient air temperature

$T_{amb} = 24.5$ °C

The gas constant is given as

$R = 287.08$ J/kgK

Due to drift associated with the electronic equipment used for data capturing, the data obtained from the experimental measurements tended to become less accurate as time passes. To compensate for this effect, the pressure and torque transducers as well as the speedometer were calibrated before a test. Zero pressure, torque and rotational speed readings were taken before and after the completion of a test. The difference between these zero measurements are an indication of the total drift that occurred during the experimental process. These values were

Total error $\Delta p_{bell} = (-0.495) - (-0.038) = -0.457$ N/m^2

Total error Δp_{sett} = (0.958) - (0.044) = 0.914 N/m^2

Total error T = (0.542) - (0.023) = 0.519 N.m

Total error N = (0.004) - (0.001) = 0.003 rpm

Not only is it assumed that the drift occurs in either the positive or negative direction only but also that it does so in a linear fashion with regard to time. The error due to drift is therefore calculated as follows

$$\text{error}_{\text{drift}} = \text{First zero reading} + \text{Total error} \cdot \frac{t_n - t_{zero}}{t_{total}} \qquad \text{(D.1)}$$

where t_n and t_{zero} refers to the time at which sampling commenced for the data set in question and the first zero measurement respectively. The total time, t_{total}, is the time elapsed between the first and last zero measurement.

It follows that

$$\text{error}(\Delta r_{\text{bell}})_{\text{drift}} = -0.038 + (-0.457) \cdot \frac{(9:6:30 - 8:46:53)}{(9:19:7 - 8:46:53)} = -0.316 \text{ N/m}^2$$

$$\text{error}(\Delta r_{\text{sett}})_{\text{drift}} = 0.044 + 0.914 \cdot \frac{(9:6:30 - 8:46:53)}{(9:19:7 - 8:46:53)} = 0.600 \text{ N/m}^2$$

$$\text{error}(T)_{\text{drift}} = 0.023 + 0.519 \cdot \frac{(9:6:30 - 8:46:53)}{(9:19:7 - 8:46:53)} = 0.339 \text{ Nm}$$

$$\text{error}(N)_{\text{drift}} = 0.001 + 0.003 \cdot \frac{(9:6:30 - 8:46:53)}{(9:19:7 - 8:46:53)} = 0.003 \text{ rpm}$$

The measured experimental values can now be corrected by subtracting the drift-related errors.

$\Delta p_{bell} = 114.665 - (-0.316) = 114.981 \text{ N/m}^2$

$\Delta p_{sett} = -208.148 - (0.600) = -208.748 \text{ N/m}^2$

$T = 51.358 - (0.339) = 51.019 \text{ N.m}$

$N = 750.206 - (0.003) = 750.203 \text{ rpm}$

The density of the ambient air can be calculated from the perfect gas relation

$$\rho_{amb} = \frac{p_{amb}}{RT_{amb}} = \frac{99859.8}{287.08 \times (24.5 + 273.15)} = 1.169 \text{ kg/m}^3 \qquad \text{(D.4)}$$

Assuming that $\rho_{bell} = \rho_{amb}$, the mass flow rate through the wind tunnel is given by

$$m = \alpha \, \varepsilon \, \frac{\pi \, d_{bell}^2}{4} \sqrt{2\rho_{bell} \Delta \, p_{bell}} \qquad \text{(D.5)}$$

$$= 0.9803 \frac{\pi \, (1.008)^2}{4} \sqrt{2(1.169)(114.981)} = 12.824 \text{ kg/s}$$

where the product of the flow coefficient (α) and the expansibility factor (ε) is known as the compound calibration constant. The $\alpha\varepsilon$-value was determined by calibrating the inlet bell mouth against flow measurements using pitot static tube traverses according to BS 1042 [83BS1]. The calibration constant ($\alpha\varepsilon$) accounts for flow losses due to the actual flow conditions not being isentropic and was found by Venter [90VE1] to be 0.9803.

The pressure in the settling chamber is calculated as

$$p_{sett} = p_{amb} + \Delta \, p_{sett} \qquad \text{(D.6)}$$

$$= 99859.8 - 208.148 = 99651.652 \text{ N/m}^2$$

From the perfect gas relation for air, equation (D.3), the density of the air in the settling chamber can be calculated

$$\rho_{sett} = \frac{p_{sett}}{RT_{sett}} = \frac{99651.652}{287.08 \times (273.15 + 24.5)} = 1.166 \text{ kg/m}^3 \quad \text{(D.7)}$$

The dynamic pressure head in the settling chamber is given as

$$p_{d_{sett}} = \frac{1}{2}\rho_{sett} v_{sett}^2 = \frac{m^2}{2\rho_{sett} A_{sett}^2} = \frac{12.824^2}{2 \cdot 1.166 \cdot 16^2} = 0.275 \text{ N/m}^2 \quad \text{(D.8)}$$

The total pressure at fan inlet is expressed as

$$\Delta p_{t_{sett}} = \Delta p_{s_{sett}} + p_{d_{sett}} = -208.748 + 0.275 = -208.473 \text{ N/m}^2 \quad \text{(D.9)}$$

Fan static pressure is defined as

$$\Delta p_{sF} = -\Delta p_{t_{sett}} = 208.473 \text{ N/m}^2 \quad \text{(D.10)}$$

The shaft power input to the fan rotor is calculated as

$$P_R = \frac{2\pi\pi}{60} T = \frac{2 \cdot \pi \cdot 750.204}{60} \cdot 51.042 = 4008.120 \text{ W} \quad \text{(D.11)}$$

The volume flow rate through the fan is given as

$$V = \frac{m}{\rho_{sett}} = \frac{12.824}{1.166} = 10.997 \text{ m}^3/\text{s} \quad \text{(D.12)}$$

Fan static efficiency is defined as

$$\eta_{sF} = \frac{\Delta p_{sF} V}{P} \times 100 = \frac{208.473 \cdot 10.997}{4008.120} \times 100 = 57.197 \text{ \%} \quad \text{(D.13)}$$

The fan characteristics are transformed to a reference density of 1.2 kg/m^3 and a reference rotational speed of 750 rpm by use of the fan laws

The reference volume flow rate is expressed as

$$V' = V\left(\frac{N'}{N}\right) = 10.997 \cdot \left(\frac{750}{750.203}\right) = 10.994 \quad m^3/s \tag{D.14}$$

The reference fan static pressure is expressed as

$$\Delta p'_{sF} = \Delta p_{sF}\left(\frac{N'}{N}\right)^2\left(\frac{\rho'}{\rho_{sett}}\right) = 208.473 \cdot \left(\frac{750}{750.203}\right)^2\left(\frac{1.2}{1.166}\right) = 214.399 \quad N/m^2 \tag{D.15}$$

Reference fan power consumption is expressed as

$$P' = P\left(\frac{N'}{N}\right)^3\left(\frac{\rho'}{\rho_{sett}}\right) = 4008.1198 \cdot \left(\frac{750}{750.203}\right)^3\left(\frac{1.2}{1.166}\right) = 4120.937 \quad W \tag{D.16}$$

The reference fan static efficiency is expressed as

$$\eta'_{Fs} = \eta_{Fs} = 57.197\ \% \tag{D.17}$$

D.2. Experimental and calculated results of the B-fan

B-fan exits directly into the atmosphere with drive on the fan inlet side

Table D.2.1 Experimental readings.

p_{amb} 99859.8 N/m^2 T_{amb} 24.5 °C					
No (-)	Δp_{bell} (N/m^2)	Δp_{sett} (N/m^2)	T (Nm)	N (rpm)	Time (h:min:sec)
Zero	-0.038	0.044	0.023	0.001	8:46:53
1	3.951	-390.414	43.692	751.524	8:52:24
2	11.590	-352.754	45.928	748.219	8:56:54
3	28.803	-303.026	48.779	749.773	9: 0: 0
4	66.298	-258.819	51.856	749.653	9: 3: 1
5	114.665	-208.148	51.358	750.206	9: 6:30
6	176.942	-141.201	47.025	747.959	9: 9:29
7	247.418	-67.736	39.306	747.610	9:12:17
8	306.930	-5.813	30.688	748.324	9:14:57
9	346.366	29.562	25.764	755.556	9:16:59
Zero	-0.495	0.958	0.542	0.004	9:19: 7

Table D.2.2 Calculated results.

No (-)	V (m^3/s)	Δp_{Fs} (N/m^2)	P_R (W)	η_{Fs} (%)
1	2.068	401.031	3514.139	23.598
2	3.532	365.549	3719.858	34.708
3	5.532	312.653	3929.336	44.019
4	8.375	267.056	4173.955	53.586
5	10.994	214.399	4120.937	57.197
6	13.684	146.260	3787.200	52.846
7	16.173	70.225	3157.352	35.972
8	17.984	6.105	2447.714	4.485
9	18.914	-29.833	2006.452	-28.122

Table D.2.3 Experimental readings (repeat).

P_{amb} 99696.1 N/m^2 T_{amb} 31 °C					
No (-)	Δp_{bell} (N/m^2)	Δp_{sett} (N/m^2)	T (Nm)	N (rpm)	Time (h:min:sec)
Zero	-0.034	0.079	0.076	-0.005	14: 3: 0
1	3.475	-375.421	41.174	749.802	14: 8:14
2	8.718	-347.049	43.613	748.945	14:10:54
3	27.847	-294.004	46.317	748.617	14:13:30
4	64.591	-251.174	49.152	748.535	14:15:36
5	110.868	-203.684	48.941	751.760	14:17:14
6	168.903	-140.443	44.950	749.448	14:19:19
7	242.333	-63.392	37.056	750.347	14:21:13
8	300.338	-2.973	28.264	748.503	14:23:28
9	331.194	30.711	23.072	747.340	14:25:35
Zero	0.014	-0.505	0.745	0.002	14:27:31

Table D.2.4 Calculated results (repeat).

No (-)	V (m^3/s)	Δp_{Fs} (N/m^2)	P_R (W)	η_{Fs} (%)
1	1.944	396.199	3395.129	22.691
2	3.075	366.906	3598.487	31.356
3	5.491	310.798	3818.513	44.694
4	8.359	265.283	4048.469	54.773
5	10.899	212.950	3990.856	58.155
6	13.485	147.275	3677.883	53.998
7	16.120	65.622	3010.554	35.138
8	17.979	1.948	2289.837	1.530
9	18.903	-33.820	1859.906	-34.373

Annular pipe section attached to the B-fan outlet.

Table D.2.5 Experimental readings.

p_{amb} 99798.3 N/m^2 T_{amb} 23 °C					
No (-)	Δp_{bell} (N/m^2)	Δp_{sett} (N/m^2)	T (Nm)	N (rpm)	Time (h:min:sec)
Zero	-0.010	0.006	-0.037	0.003	9:48:14
1	6.192	-393.385	42.065	750.220	9:52:31
2	10.927	-364.954	44.955	749.862	9:54: 6
3	29.579	-306.184	48.035	747.973	9:55:47
4	68.284	-262.935	52.685	748.852	9:57:28
5	120.700	-211.797	52.926	750.548	9:58:35
6	182.509	-143.709	48.511	748.854	10: 0:30
7	257.731	-63.588	40.038	751.674	10: 2:58
8	312.357	-6.827	32.632	751.764	10: 6:37
9	343.867	31.539	26.365	746.607	10: 8:14
Zero	0.002	0.833	0.356	0.014	10: 9:47

Table D.2.6 Calculated results.

No (-)	V (m^3/s)	Δp_{Fs} (N/m^2)	P_R (W)	η_{Fs} (%)
1	2.552	403.673	3385.526	30.427
2	3.390	374.812	3618.453	35.110
3	5.586	315.914	3881.536	45.467
4	8.474	270.541	4243.772	54.020
5	11.235	216.783	4240.180	57.438
6	13.836	147.620	3897.580	52.405
7	16.368	64.713	3183.974	33.267
8	18.006	6.911	2584.195	4.816
9	19.016	-32.577	2109.007	-29.373

Table D.2.7 Experimental readings (repeat).

p_{amb} 100806.8 N/m^2 T_{amb} 22 °C					
No (-)	Δp_{bell} (N/m^2)	Δp_{sett} (N/m^2)	T (Nm)	N (rpm)	Time (h:min:sec)
Zero	-0.056	0.028	-0.016	0.013	12:10: 2
1	6.353	-394.964	42.326	750.794	12:15:47
2	10.541	-367.357	45.118	751.884	12:18: 6
3	30.906	-309.899	47.980	748.934	12:19:44
4	68.518	-265.289	52.543	750.652	12:22:33
5	116.202	-215.942	53.040	751.355	12:23:56
6	180.142	-149.093	48.635	749.007	12:26:46
7	253.220	-67.980	40.144	747.152	12:29:32
8	324.159	1.182	31.673	754.767	12:32:42
Zero	-0.514	2.069	-0.060	0.020	12:34:37

Table D.2.8 Calculated results (repeat).

No (-)	V (m^3/s)	Δp_{Fs} (N/m^2)	P_R (W)	η_{Fs} (%)
1	2.597	399.611	3361.313	30.870
2	3.329	370.720	3571.880	34.552
3	5.686	315.220	3826.340	46.842
4	8.429	268.747	4169.391	54.329
5	10.953	218.411	4199.072	56.969
6	13.666	152.011	3872.633	53.643
7	16.227	70.200	3210.881	35.477
8	18.160	-0.048	2482.067	-0.035

B-fan exits directly into the atmosphere with drive train on the fan outlet side

Table D.2.9 Experimental readings.

p_{amb} 100700 N/m^2 T_{amb} 26 °C					
No (-)	Δp_{bell} (N/m^2)	Δp_{sett} (N/m^2)	T (Nm)	N (rpm)	Time (h:min:sec)
zero	0.116	0.020	0.022	-0.014	15: 2: 5
1	7.959	-400.679	42.586	749.173	15: 7:54
2	9.697	-375.519	44.725	751.425	15:11:04
3	30.277	-319.182	48.208	751.145	15:13:10
4	68.577	-259.732	50.814	748.319	15:16: 6
5	112.168	-210.634	50.825	751.204	15:17:11
6	175.121	-138.605	47.175	750.631	15:20:09
7	243.936	-60.579	39.316	750.295	15:22: 1
8	312.228	-4.064	30.540	748.369	15:23:25
9	349.218	27.137	26.186	754.450	15:24:55
zero	-0.022	0.519	-0.944	-0.006	15:28: 1

Table D.2.10 Calculated results.

No (-)	V (m^3/s)	Δp_{Fs} (N/m^2)	P_R (W)	η_{Fs} (%)
1	2.881	412.705	3459.861	34.371
2	3.176	384.445	3619.665	33.733
3	5.626	326.847	3906.628	47.066
4	8.499	267.818	4153.668	54.799
5	10.824	215.361	4123.971	56.525
6	13.527	141.749	3842.886	49.894
7	15.960	61.799	3217.409	30.656
8	18.093	3.852	2527.932	2.757
9	18.975	-27.817	2145.247	-24.604

D.3. Experimental and calculated results of the DL-fan

DL-fan exits directly into the atmosphere with drive train at fan inlet side

Table D.3.1 Experimental readings.

p_{amb} 100317.8 N/m^2 T_{amb} 28.5 °C					
No (-)	Δp_{bell} (N/m^2)	Δp_{sett} (N/m^2)	T (Nm)	N (rpm)	Time (h:min:sec)
Zero	-0.028	0.021	0.030	0.016	16:21:27
1	6.275	-654.759	94.148	750.289	16:26:53
2	17.719	-598.705	94.701	749.146	16:28:22
3	43.074	-505.709	96.197	750.418	16:30: 8
4	84.505	-422.038	98.164	750.319	16:31:59
5	143.500	-345.634	94.930	749.891	16:34:20
6	225.220	-235.620	85.854	750.941	16:36:58
7	300.643	-114.110	74.794	751.643	16:39: 2
8	344.955	-31.291	66.579	748.972	16:41:27
Zero	361.655	-4.100	64.167	749.257	16:44: 7
	0.245	-0.937	-0.729	0.022	16:46:20

Table D.3.2 Calculated results.

No (-)	V (m^3/s)	Δp_{Fs} (N/m^2)	P_R (W)	η_{Fs} (%)
1	2.584	682.000	7715.509	22.844
2	4.352	625.061	7783.802	34.947
3	6.771	525.512	7876.811	45.176
4	9.480	438.064	8037.478	51.670
5	12.353	358.543	7782.255	56.913
6	15.438	242.892	7020.193	53.415
7	17.800	116.408	6106.754	33.930
8	19.118	30.880	5480.897	10.771
9	19.562	2.475	5285.237	0.916

Annular pipe section attached to the DL-fan outlet.

Table D.3.3 Experimental readings.

p_{amb} 100198.3 N/m^2 T_{amb} 26.5 °C					
No (-)	Δp_{bell} (N/m^2)	Δp_{sett} (N/m^2)	T (Nm)	N (rpm)	Time (h:min:sec)
Zero	-0.039	0.007	0.001	0.018	15:57:45
1	5.357	-627.608	86.551	752.667	16: 4:40
2	13.968	-577.061	87.283	752.089	16: 6:24
3	36.470	-478.936	89.338	750.078	16: 8: 3
4	83.959	-393.848	92.375	750.616	16:10:44
5	157.801	-312.451	92.935	749.184	16:12:46
6	219.618	-233.625	87.355	748.984	16:15:51
7	299.392	-113.857	75.918	748.929	16:17:46
8	349.034	-27.236	67.881	750.073	16:19:34
Zero	365.480	0.494	65.364	749.840	16:22: 2
	-0.225	1.150	0.722	0.026	16:23:46

Table D.3.4 Calculated results.

No (-)	V (m^3/s)	Δp_{Fs} (N/m^2)	P_R (W)	η_{Fs} (%)
1	2.399	646.402	6982.362	22.207
2	3.857	595.036	7044.923	32.574
3	6.229	496.100	7239.133	42.691
4	9.430	407.105	7462.908	51.440
5	12.938	323.930	7526.352	55.684
6	15.254	242.210	7063.693	52.305
7	17.789	117.953	6122.783	34.270
8	19.161	28.198	5444.407	9.924
9	19.608	-0.303	5237.002	-0.114

DL-fan exits directly into the atmosphere with drive train at fan outlet side

Table D.3.5 Experimental readings.

p_{amb} 100740 N/m^2 T_{amb} 26 °C					
No (-)	Δp_{bell} (N/m^2)	Δp_{sett} (N/m^2)	T (Nm)	N (rpm)	Time (h:min:sec)
zero	-0.030	0.040	-0.022	-0.014	6: 1: 51
1	6.696	-669.260	93.395	749.563	6: 7:52
2	17.815	-620.900	93.244	750.937	6:10:54
3	45.703	-524.398	95.732	749.844	6:14:13
4	85.218	-421.837	96.311	749.411	6:15:56
5	142.795	-342.646	93.717	750.129	6:17: 9
6	220.719	-228.836	85.081	750.201	6:19:46
7	296.657	-112.397	74.790	749.692	6:23: 5
8	351.582	-31.858	67.674	752.275	6:24: 5
9	369.963	13.681	62.840	748.637	6:25: 5
zero	-0.426	0.173	-0.266	-0.011	6:28: 12

Table D.3.6 Calculated results.

No (-)	V (m^3/s)	Δp_{Fs} (N/m^2)	P_R (W)	η_{Fs} (%)
1	2.686	690.059	7568.931	24.491
2	4.353	637.542	7527.673	36.866
3	6.959	539.459	7745.938	48.469
4	9.490	433.920	7795.028	52.827
5	12.257	351.355	7565.803	56.921
6	15.216	234.088	6862.704	51.903
7	17.631	114.623	6038.149	33.468
8	19.111	31.702	5424.215	11.169
9	19.690	-14.792	5085.601	-5.727

Table D.3.7 Experimental readings (repeat).

p_{amb} 100850 N/m^2 T_{amb} 22 °C					
No (-)	Δp_{bell} (N/m^2)	Δp_{sett} (N/m^2)	T (Nm)	N (rpm)	Time (h:min:sec)
zero	0.003	-0.012	0.033	-0.011	17: 0: 55
1	7.376	-695.147	95.429	750.833	17: 5: 8
2	15.189	-644.402	95.632	751.436	17: 8:57
3	40.610	-545.609	97.639	751.129	17:15:15
4	87.195	-430.790	98.178	750.830	17:16:53
5	147.214	-351.325	94.980	751.413	17:17:19
6	221.899	-238.031	86.037	750.346	17:18:47
7	306.194	-108.388	75.043	752.115	17:23:15
8	349.721	-27.684	66.611	747.216	17:25: 55
9	380.554	19.286	62.905	751.406	17:27:15
zero	-0.002	0.026	-0.370	-0.004	17:29: 2

Table D.3.8 Calculated results (repeat).

No (-)	V (m^3/s)	Δp_{Fs} (N/m^2)	P_R (W)	η_{Fs} (%)
1	2.770	704.111	7594.065	25.680
2	3.970	651.320	7598.514	34.028
3	6.488	551.317	7763.778	46.069
4	9.499	435.016	7805.744	52.939
5	12.324	353.759	7534.769	57.860
6	15.135	239.802	6840.234	53.058
7	17.714	108.062	5937.794	32.237
8	19.040	27.299	5341.304	9.731
9	19.741	-20.258	4988.678	-8.017

APPENDIX E - Numerical evaluation of the axial flow fan model

The axial flow fan model developed in Chapter 2 is numerically evaluated in this appendix. The evaluation of the fan model also includes the evaluation of two different fan inlet configurations. The first inlet configuration takes the form of a circular duct section, whilst the second includes a geometrically more complex inlet bell mouth as well as a settling chamber. The goal of the investigation is to determine whether the use of a geometrically more complex fan inlet configuration holds any advantage with respect to the accuracy with which the fan performance characteristics can be determined numerically.

The numerically determined fan performance characteristics as well as the velocity field directly up- and down stream of the fan blades are compared to experimental data.

E.1. Computational Model

The fan performance characteristics of the B-fan described in Appendix C are evaluated. Based on the design of the test fan, the lift and drag characteristics of the NASA-LS profile are used in the axial flow fan model. McGhhee et al. [73MC1] experimentally investigated the NASA-LS profile and plotted the dimensionless lift and drag coefficients, C_l and C_d, as a function of the angle of attack, α, for a range of Reynolds numbers. For angle of attack values falling outside of the range tested by McGhhe et al. [73MC1] the lift and drag characteristics for a flat plate are used. According to Hoerner and Borst [75HO1] and Hoerner [65HO1], the dimensionless lift and drag coefficient for a flat plate is given respectively as

$$C_l = C_{d\,max} \cdot \sin\alpha \cdot \cos\alpha \qquad \text{(E.1)}$$

and

$$C_d = C_{d\,max} \cdot \sin^2\alpha \qquad \text{(E.2)}$$

where $C_{d\,max}$=1.98.

A smooth transition between the NASA-LS and flat plate lift and drag characteristics is ensured by the introduction of fourth order polynomial and trigometric functions in the overlap regions.

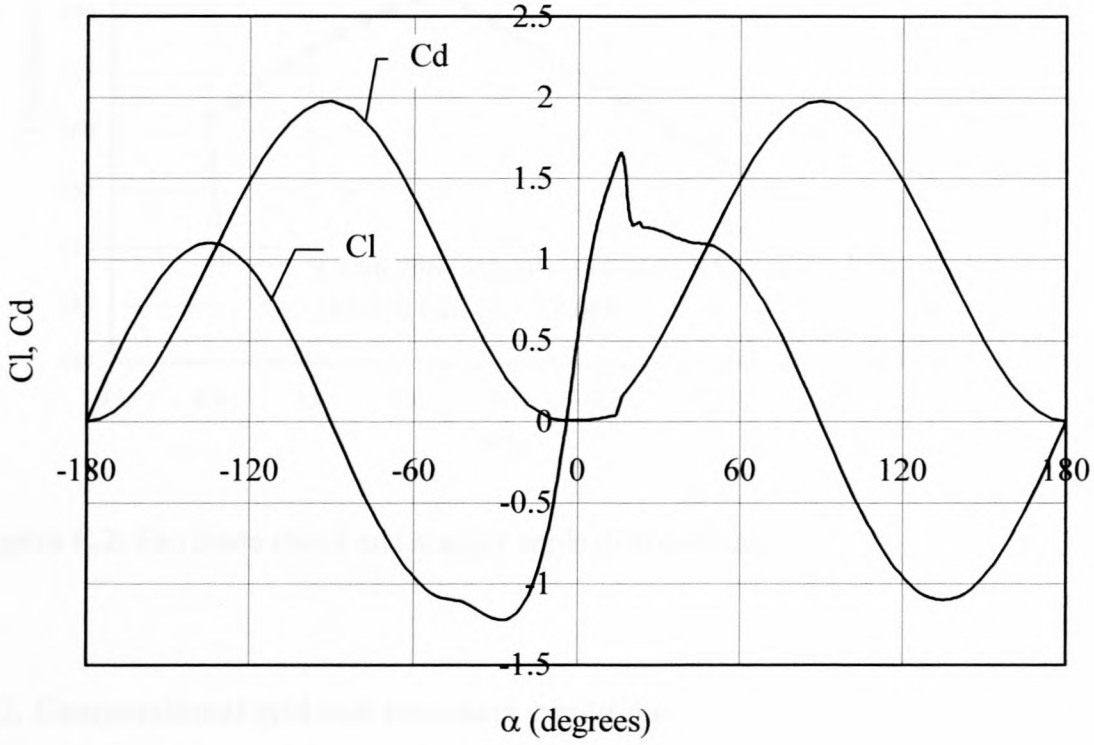

Figure E.1. Composite dimensionless lift and drag coefficient of the fan blade cross-sectional profile with Re = 1.9×10^6.

Figure E.1 displays the composite dimensionless lift and drag coefficient as a function of the angle of attack at a fan blade chord Reynolds number of 1.9×10^6 for the fan model. Linear interpolation is used to determine the C_l and C_d values at other Reynolds numbers.

Figure E.2 shows the chord and stagger angle distribution of the B-fan fan blades as obtained through measurement.

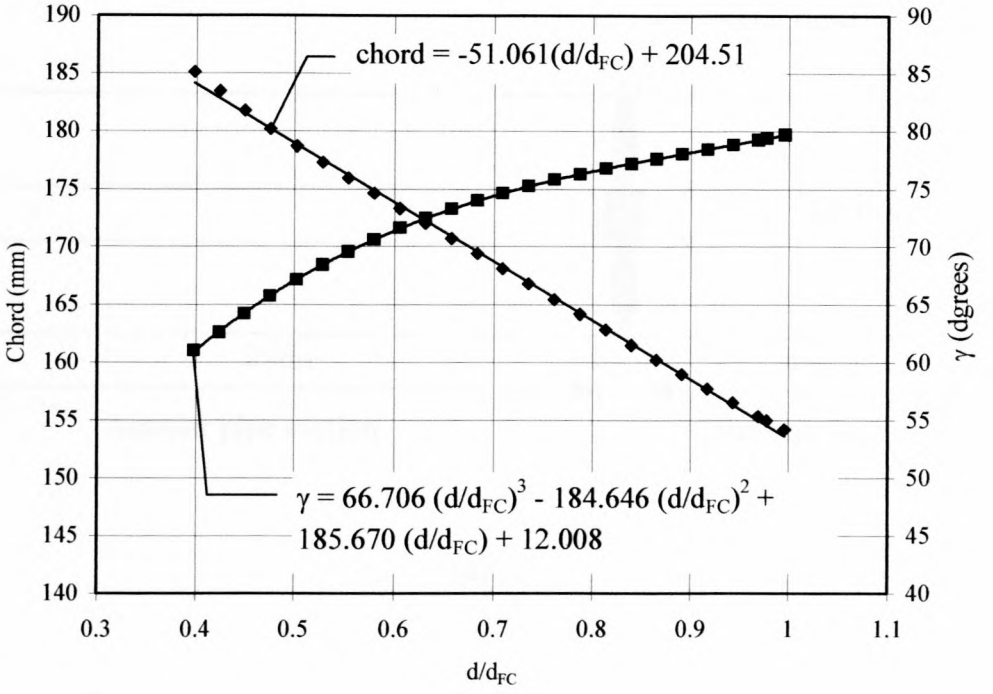

Figure E.2. Fan blade chord and stagger angle distributions.

E.2. Computational grid and boundary conditions

Computational grid

The numerical investigation was an attempt to simulate the operation of the B-fan for the two fan inlet configurations shown schematically in figure E.3. In the configuration shown in figure E.3(a), hereafter referred to as Inlet configuration 1, the B-fan is furnished with an inlet duct of circular cross-section. For Inlet configuration 2, shown in figure E.3(b), the inlet ducting to the fan takes the shape of a settling chamber with a rectangular cross-sectional profile. An inlet bell mouth is installed to ensure a smooth transition between the settling chamber and the axial flow fan inlet. The fan inlet conditions shown in figure E.3(b) corresponds to those prescribed in BS 848 [80BS1].

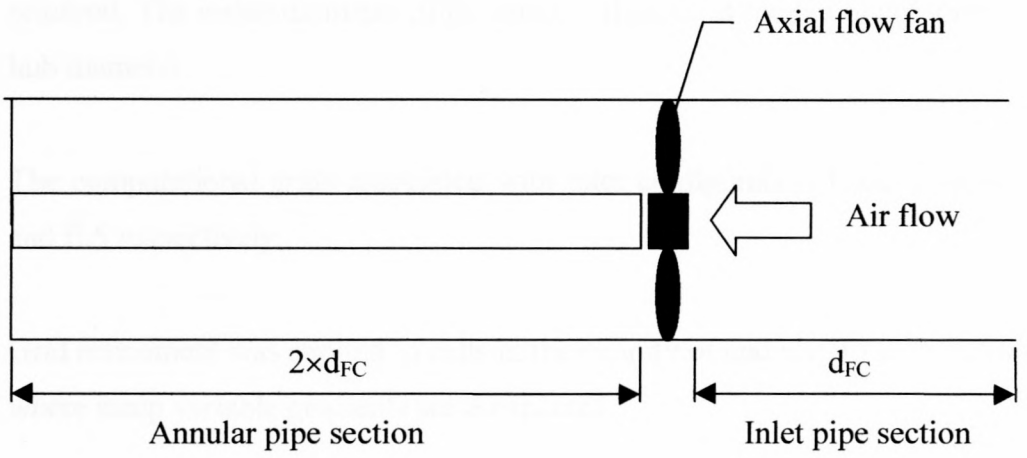

(a)

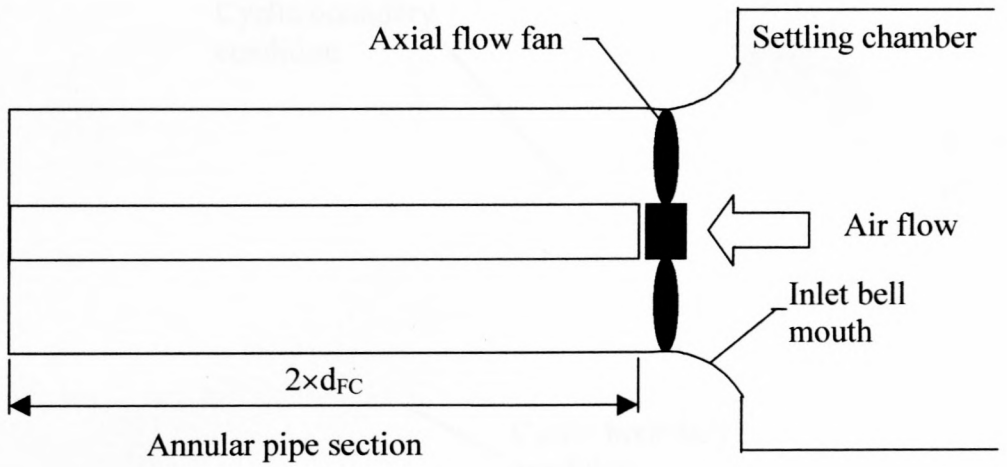

(b)

Figure E.3. Geometry modelled by numerical analysis.

It should also be noted that for the two fan inlet configurations considered an annular pipe section is fitted to the fan exit. This is done so that a free atmosphere at the fan exit need not be simulated as the latter is numerically difficult due to the nature of the boundary conditions

required. The inside diameter of the annular ducting at the fan outlet corresponds to the B-fan hub diameter.

The computational grids associated with inlet configuration 1 and 2 is shown in figures E.4 and E.5 respectively.

Grid refinement was applied to cells in the vicinity of and also to cells within the actuator disc where steep variable gradients were expected.

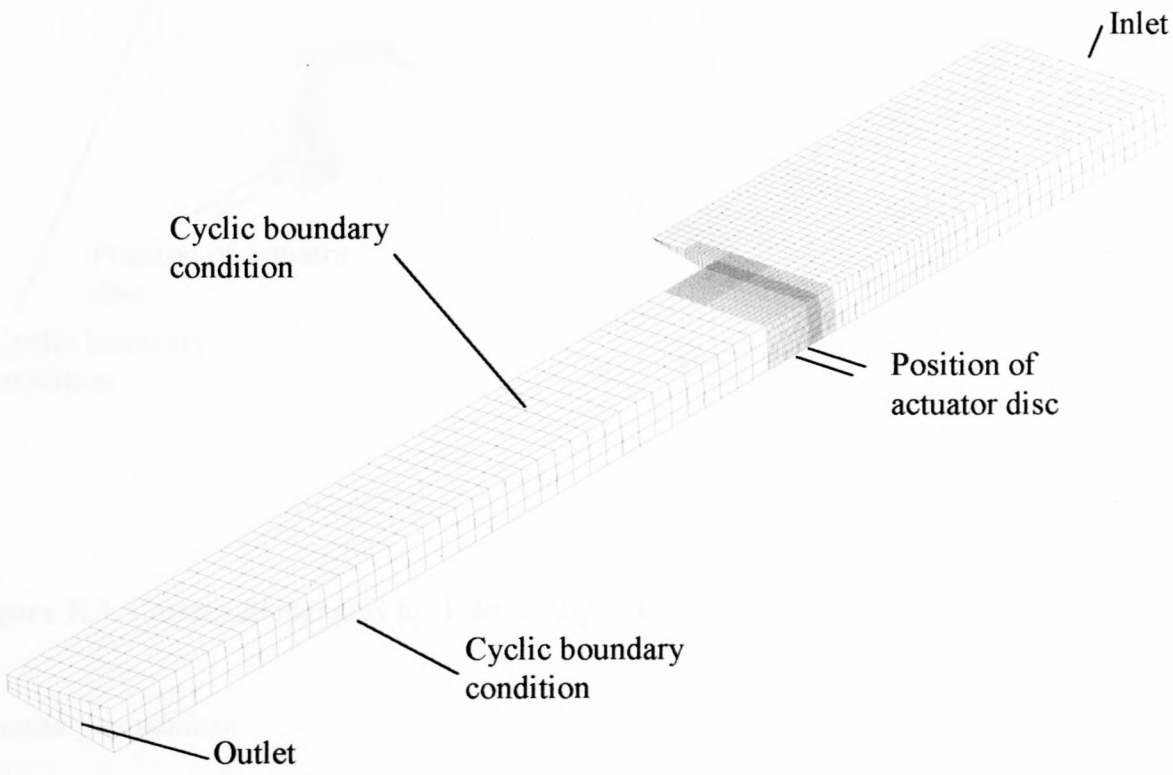

Figure E.4. Computational grid for Inlet configuration 1.

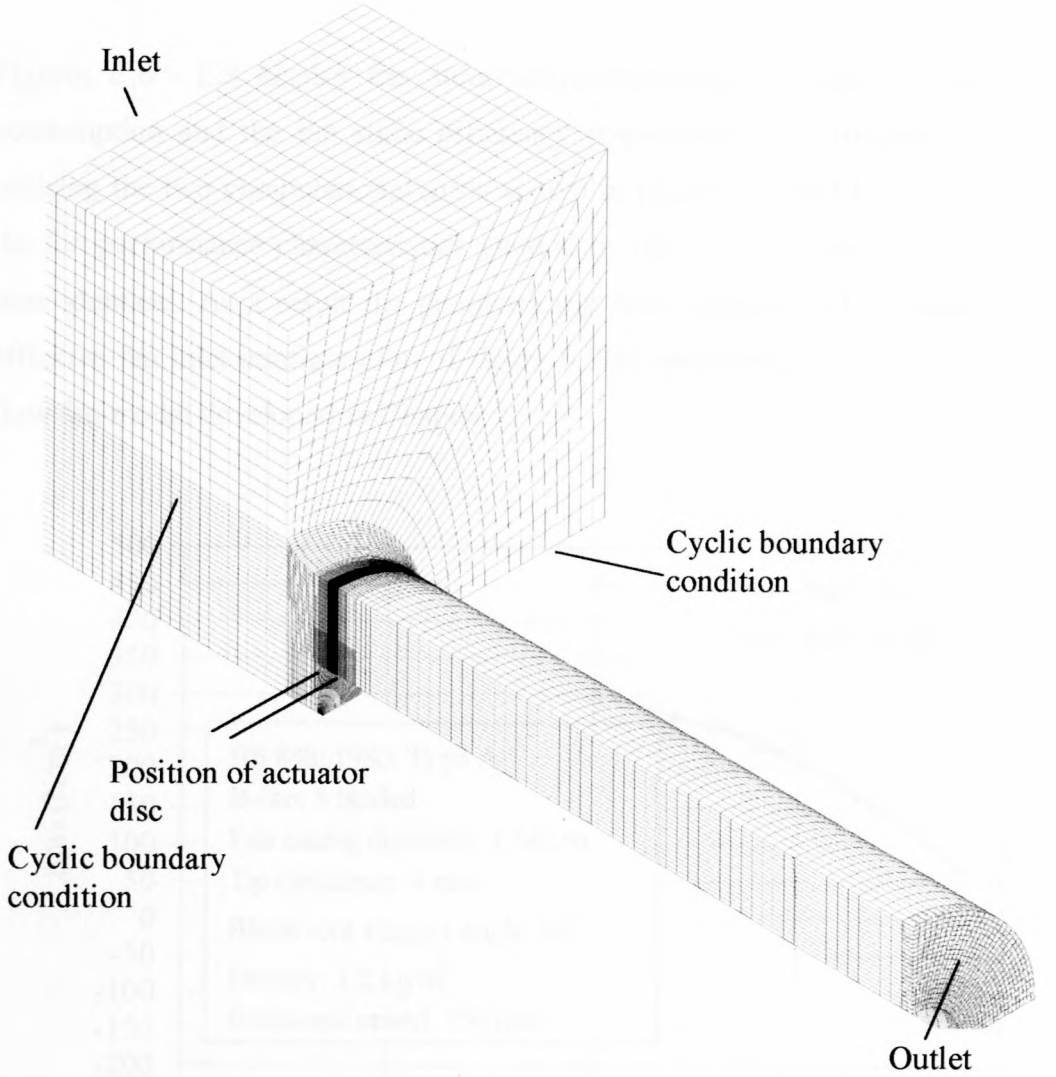

Figure E.5. Computational grid for Inlet configuration 2.

Boundary conditions

The various boundary conditions applied to the cell faces on the exterior of the computational grid, are displayed in figures E.3 and E.4.

Uniform and constant values for the axial velocity field, the turbulent kinetic energy, k, and the dissipation rate of turbulent kinetic energy, ε, were specified at the indicated inlet boundary. Zero variable gradients were specified across the cell faces comprising the outlet boundary. Cyclic boundary conditions were applied to boundary cell faces that faced in the computational grid tangential direction in order to preserve the axisymmetric nature of the flow field. A wall boundary condition was enforced on all other boundary cell faces.

E.3. Results and discussion

Figures E.6 - E.8 display the numerically-determined fan static pressure rise, fan power consumption and the fan static efficiency respectively as a function of volume flow rate utilising the two computational grids shown in figures E.4 and E.5. The results indicate that the fan performance characteristics yielded by the two different fan inlet configurations are near identical. As a result the geometrically less complex and computationally more cost-effective fan inlet configuration of figure E.3(b) was used for further evaluation of the axial flow fan model developed in Chapter 2.

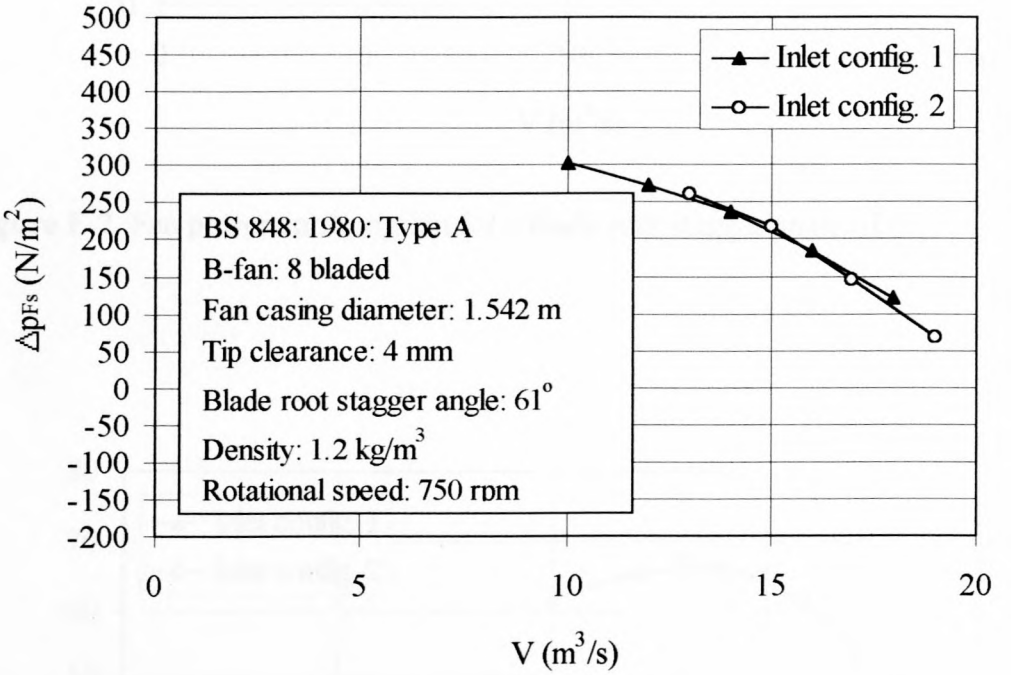

Figure E.6. Fan static pressure rise for a blade root stagger angle of 61°.

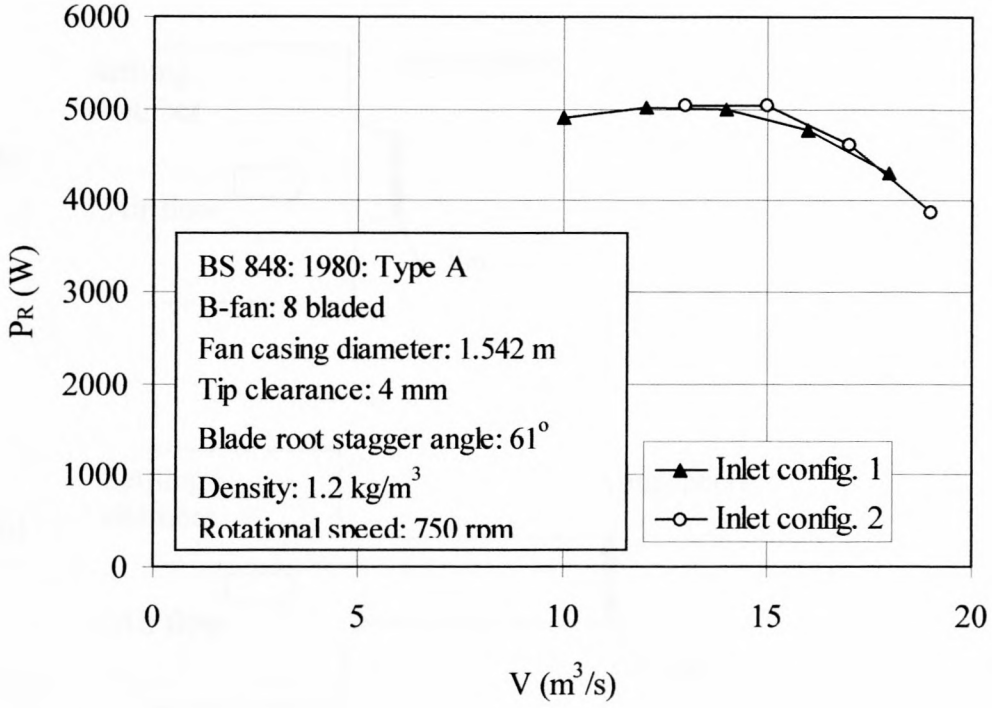

Figure E.7. Fan power consumption for a blade root stagger angle of 60°.

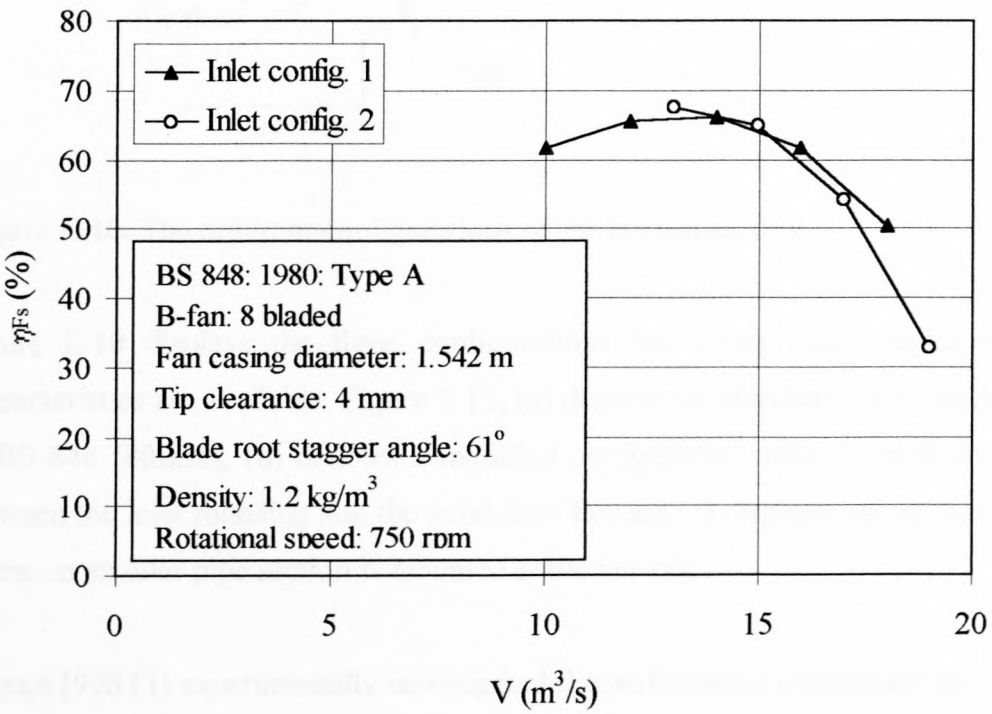

Figure E.9. Fan static efficiency for a blade root stagger angle of 61°.

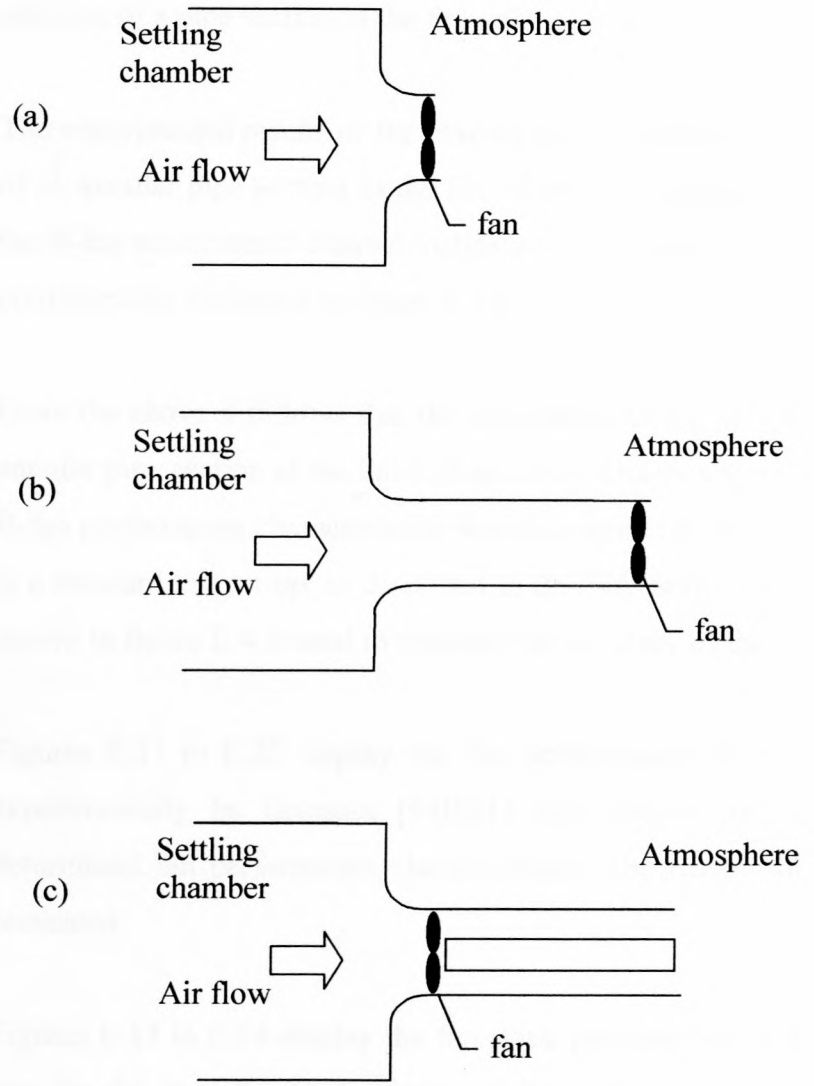

Figure E.10. The different configurations of the fan test facility.

Figure E.10 displays the three configurations for which experimental fan performance characteristics are available. Figure E.10, (a) denotes the standard configurations as described in BS 848 [80BS1], (b) denotes a modified configuration where a pipe section is installed between the inlet rounding and the axial flow fan and (c) displays yet another modified set-up where an annular pipe section is mounted at the fan exit.

Stinnes [99ST1] experimentally investigated the performance characteristics of the B-fan over a range of blade angles in the standard configuration (a) as well as the modified configuration

(b) of figure E.10 and concludes that the fan performance characteristics are unaffected by the addition of a pipe section to the fan inlet.

The experimental results of the investigation contained in Appendix C show that the addition of an annular pipe section to the fan outlet, as displayed in figure E.10(b), also do not affect the B-fan performance characteristics when compared to those obtained utilising the standard configuration displayed in figure E.10(a).

From the above it follows that the installation of a pipe section to the fan inlet as well as an annular pipe section at the fan exit as schematically shown in figure E.3(b) does not alter the B-fan performance characteristics when compared to the performance characteristics obtained in a standard test set-up, as described in BS 848 [80BS1] for a type A test. As a result the grid shown in figure E.4 is used to evaluate the accuracy of the fan model developed in Chapter 2.

Figures E.11 to E.22 display the fan performance characteristics of the B-fan determined experimentally by Bruneau [94BR1] and Stinnes [99ST1] as well as the numerically determined fan performance characteristics. The results for four different blade angles are presented.

Figures E.11 to E.14 display the fan static pressure rise as a function of the air volume flow rate for the four fan blade settings tested. The static pressure rise determined by Stinnes [99ST1] is slightly lower than that determined by Bruneau [94BR1] for all four blade settings at volume flow rates in excess of 15 m^3/s. Stinnes [99ST1] attributes this discrepancy to slight differences in the fan hub geometry. The numerically-determined static pressure characteristics is seen to follow the data of Bruneau [94BR1] to high degree of accuracy.

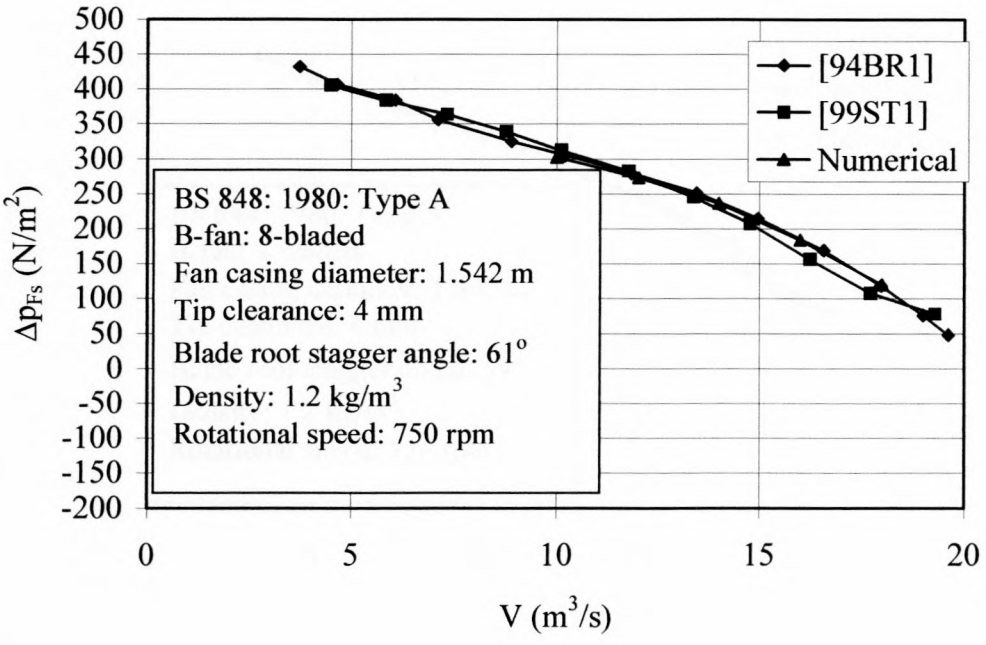

Figure E.11. Fan static pressure rise for a blade root stagger angle of 61°.

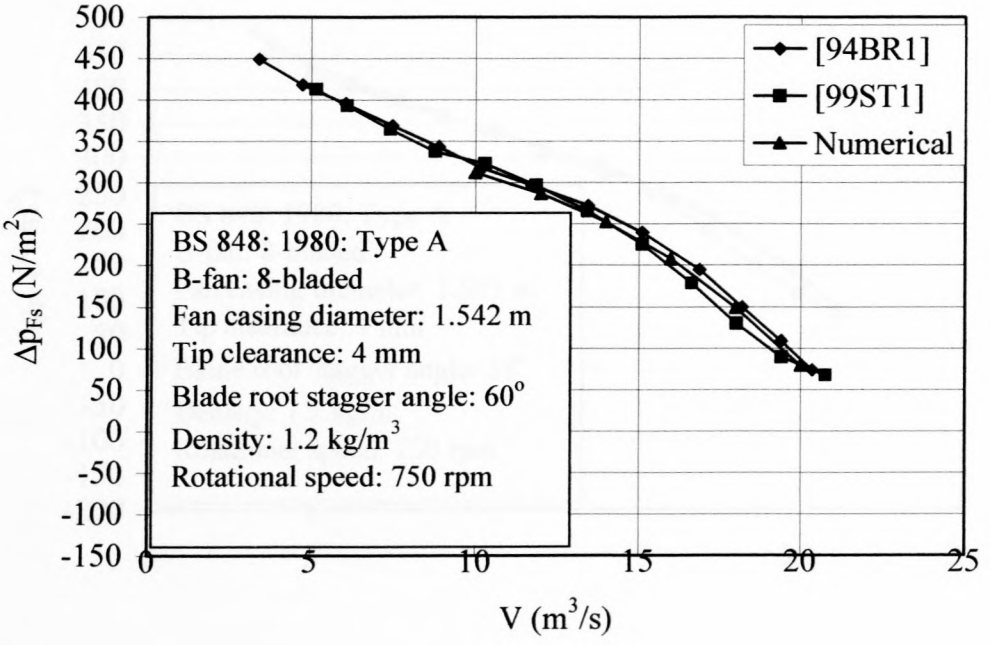

Figure E.12. Fan static pressure rise for a blade root stagger angle of 60°.

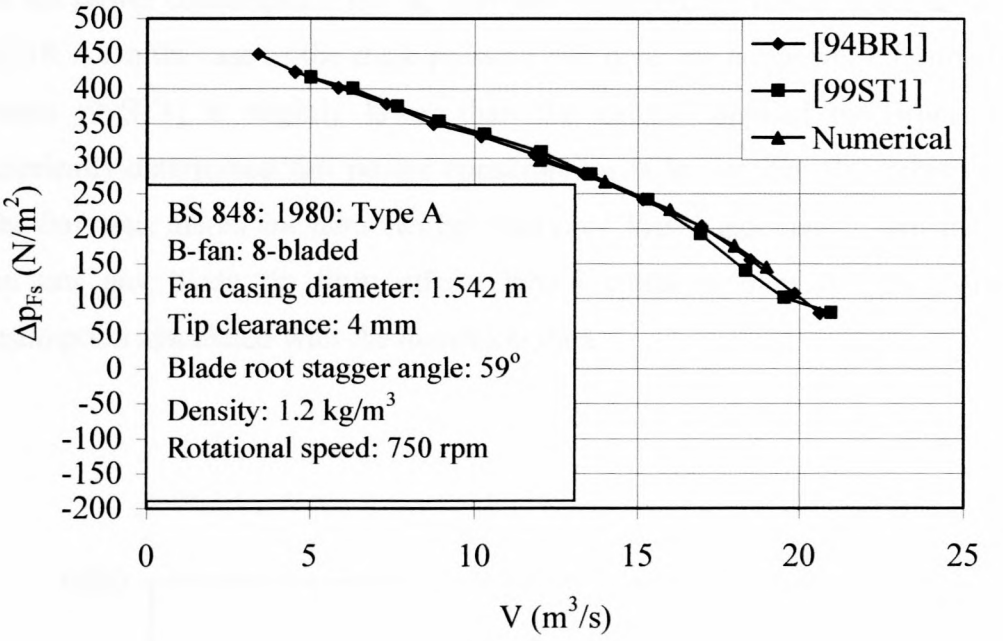

Figure E.13. Fan static pressure rise for a blade root stagger angle of 59°.

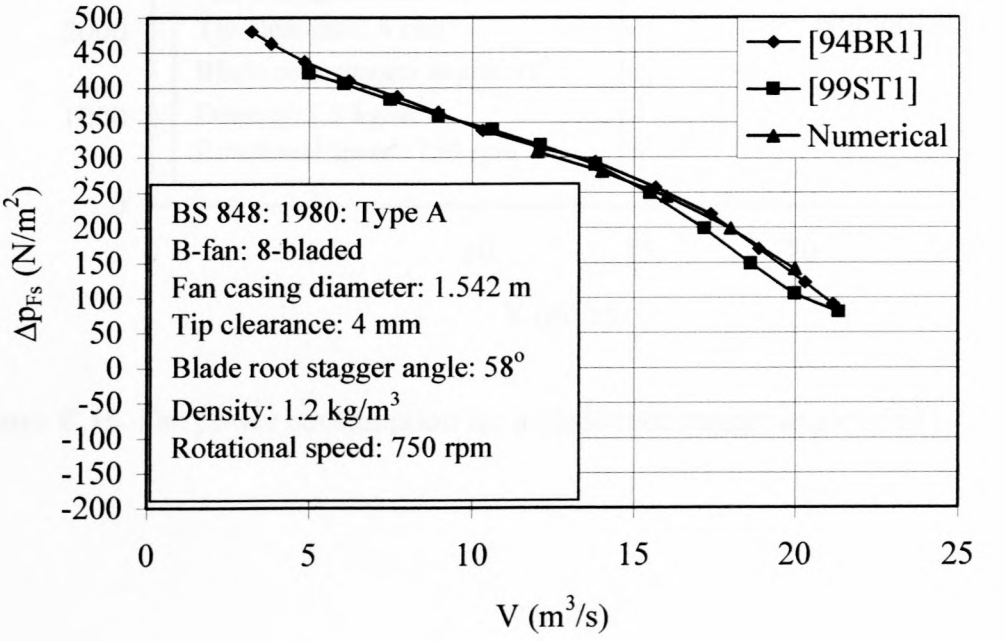

Figure E.14. Fan static pressure rise for a blade root stagger angle of 58°.

The fan power consumption for the four fan blade settings tested is displayed in figures E.15 to E.18. As in the case of the static pressure rise data, the fan power consumption supplied by Stinnes [99ST1] is slightly lower than the values supplied by Bruneau [94BR1]. The numerically-determined fan power consumption is lower than the experimental data. The axial flow fan model includes neither frictional losses associated with the fan motor drive train nor any blade tip flow effects which could account for the reduced fan power consumption associated with the numerical data.

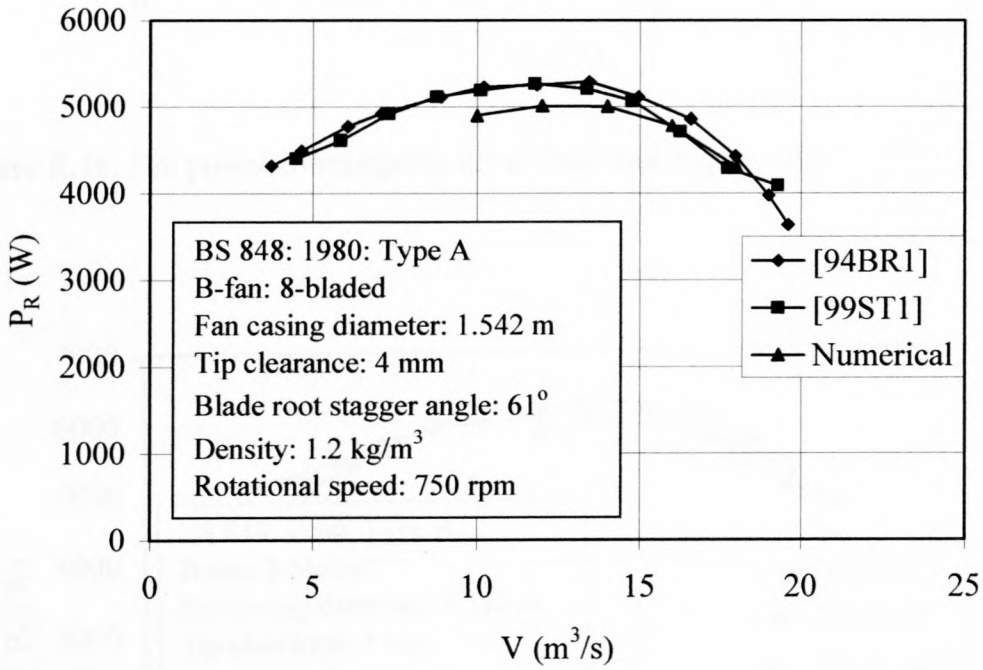

Figure E.15. Fan power consumption for a blade root stagger angle of 61°.

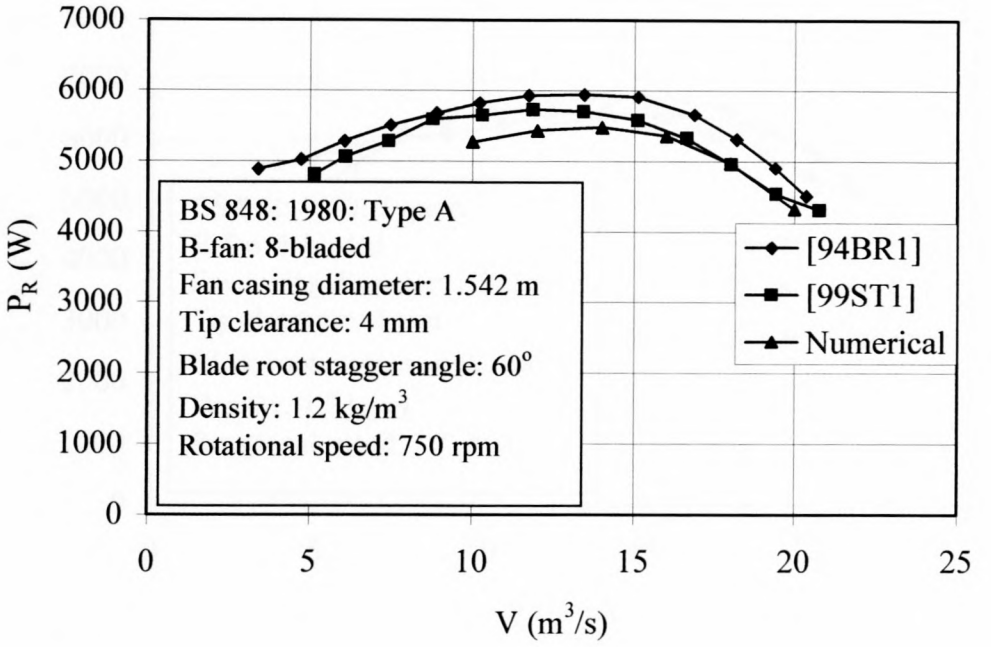

Figure E.16. Fan power consumption for a blade root stagger angle of 60°.

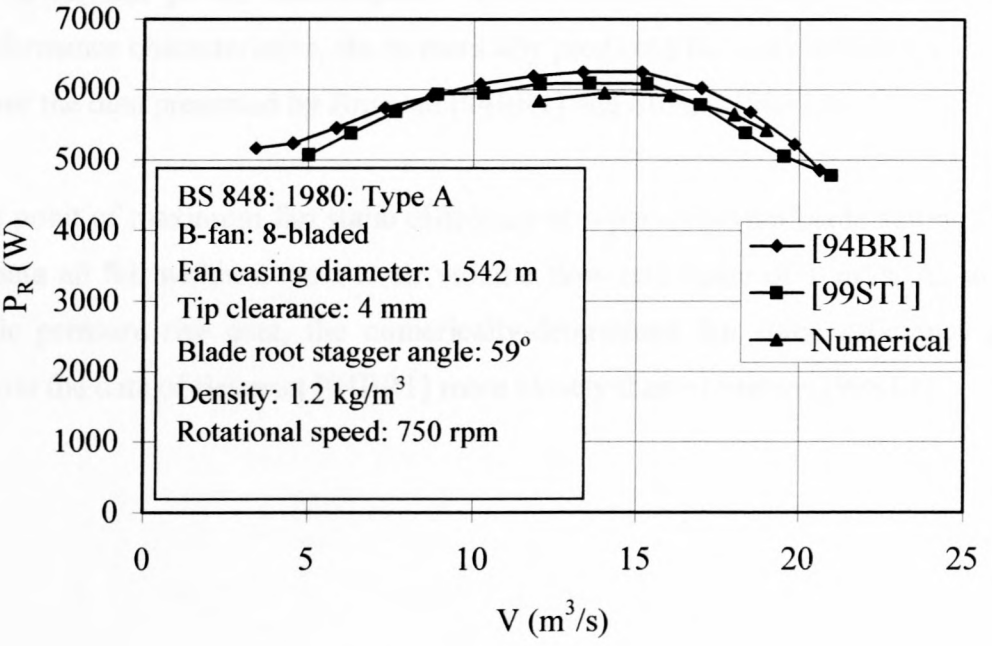

Figure E.17. Fan power consumption for a blade root stagger angle of 59°.

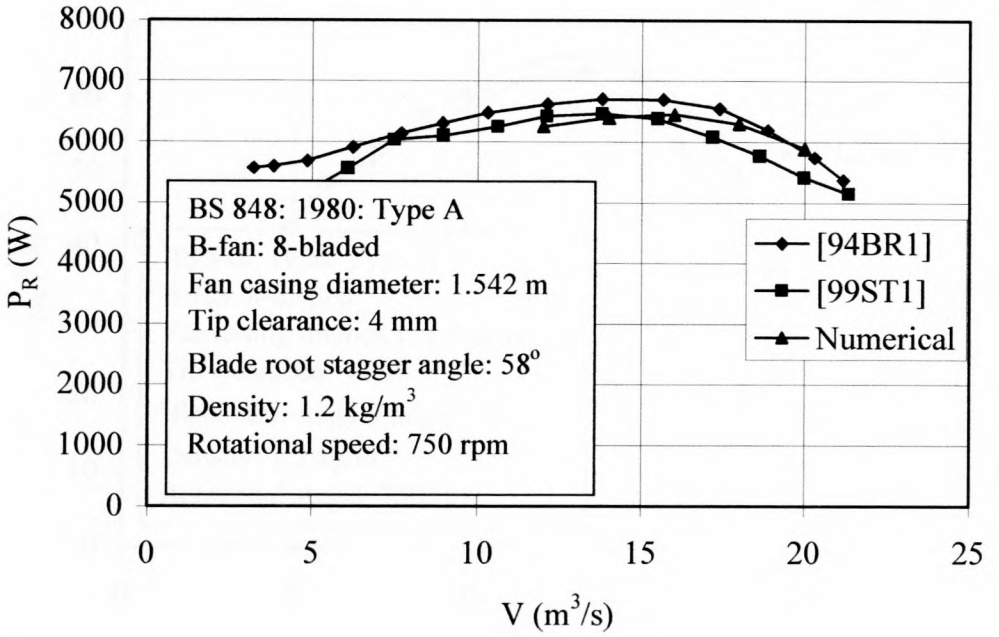

Figure E.18. Fan power consumption for a blade root stagger angle of 58°.

Figures E.19 to E.22 display the fan static efficiency of the fan blade settings tested. Due to the lower fan power consumption values associated with the numerically-predicted fan performance characteristics, the numerically predicted fan static efficiency is slightly elevated above the data presented by Bruneau [94BR1] and Stinnes [99ST1].

The point of maximum fan static efficiency at a particular fan blade setting for the three sets of data all fall within a narrow air volume flow rate range of 1 m^3/s. As in the case of the static pressure rise data, the numerically-determined fan static efficiency curves seem to follow the data of Bruneau [94BR1] more closely than of Stinnes [99ST1].

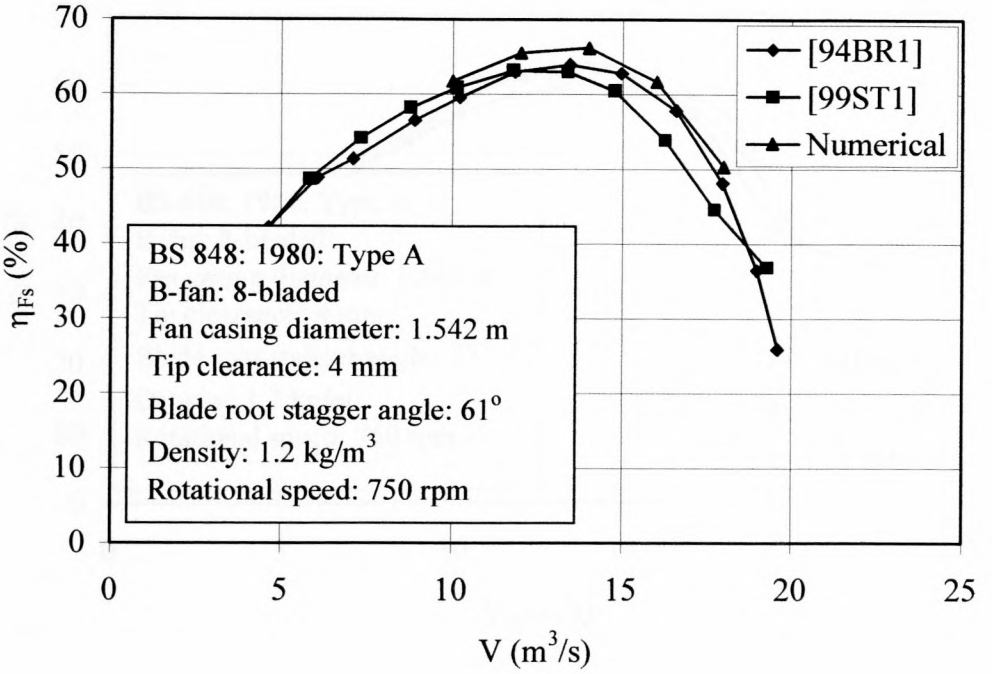

Figure E.19. Fan static efficiency for a blade root stagger angle of 61°.

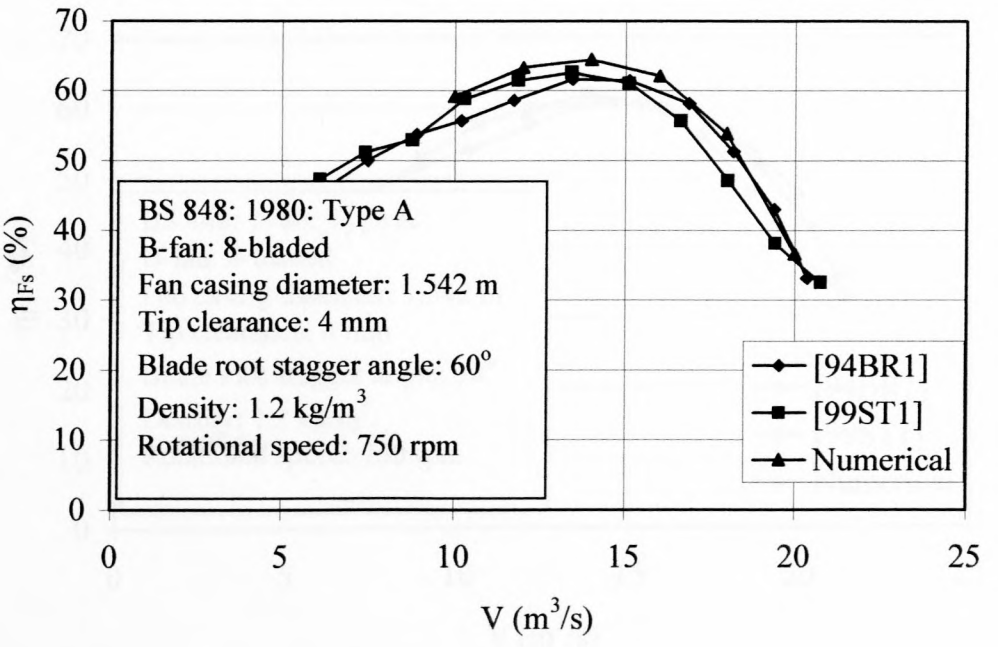

Figure E.20. Fan static efficiency for a blade root stagger angle of 60°.

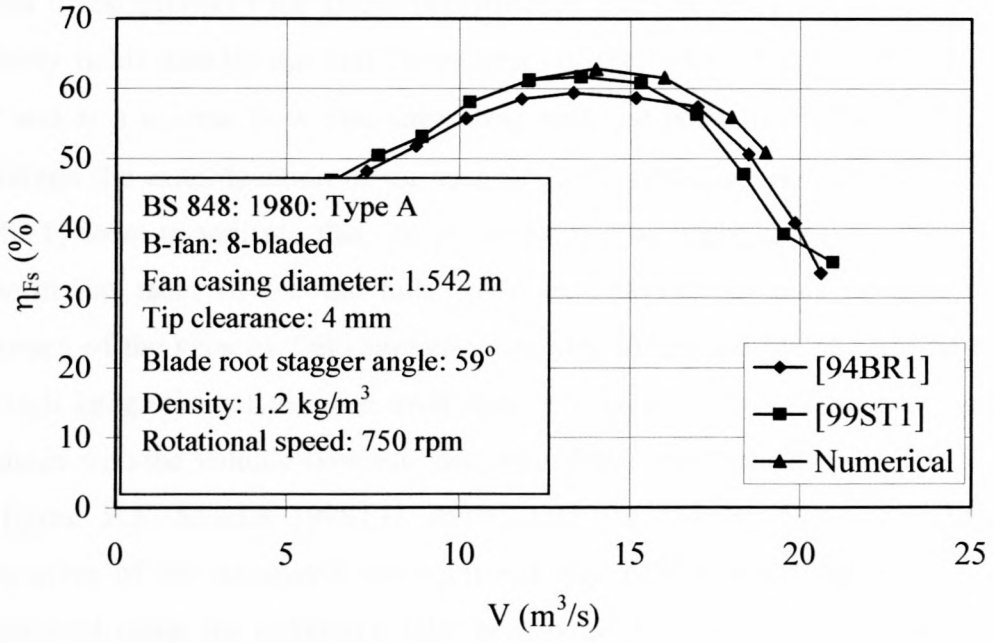

Figure E.21. Fan static efficiency for a blade root stagger angle of 59°.

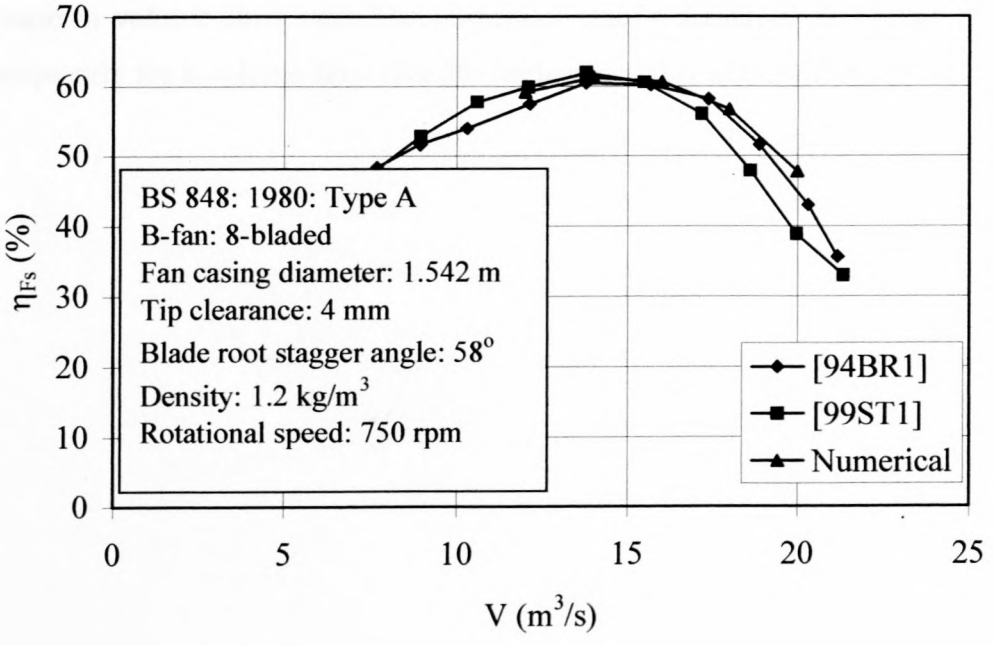

Figure E.22. Fan static efficiency for a blade root stagger angle of 58°.

In his investigation of the B-fan performance characteristics Stinnes [99ST1] measured the velocity fields directly up- and downstream of the B-fan set at a blade root stagger angle of 60° and at a volume flow rate coinciding with the point of maximum fan static efficiency. Although the exact location of the measurement planes are not given, comments by Stinnes [99ST1] seem to indicate that the planes of measurement coincided with the upstream and downstream faces of the fan hub. Stinnes [99ST1] attempts to estimate the degree of accuracy of the velocity field measurements by comparing the volume flow rate determined through integration of the measured upstream axial velocity field using various integration methods with the volume flow rate determined utilising the calibrated inlet bell mouth shown in figure E.5. Stinnes [99ST1] shows that the volume flow rate determined through integration of the measured upstream velocity field over-estimates the volume flow rate determined using the calibrated inlet bell mouth by 4 to 7% depending on the integration technique employed.

Figures E.23 and E.24 contrast the upstream and downstream velocity profiles determined from the results of the numerical analysis with the data of Stinnes [99ST1]. The numerically-determined velocity fields at volume flow rates up to 7% higher than that indicated by Stinnes [99ST1] were also compared. The axial velocity fields alone seemed to be affected by the increase in volume flow rate. The numerical results displayed in figures E.19 and E.20 are subsequently for a volume flow rate 5% higher than that indicated by Stinnes [99ST1].

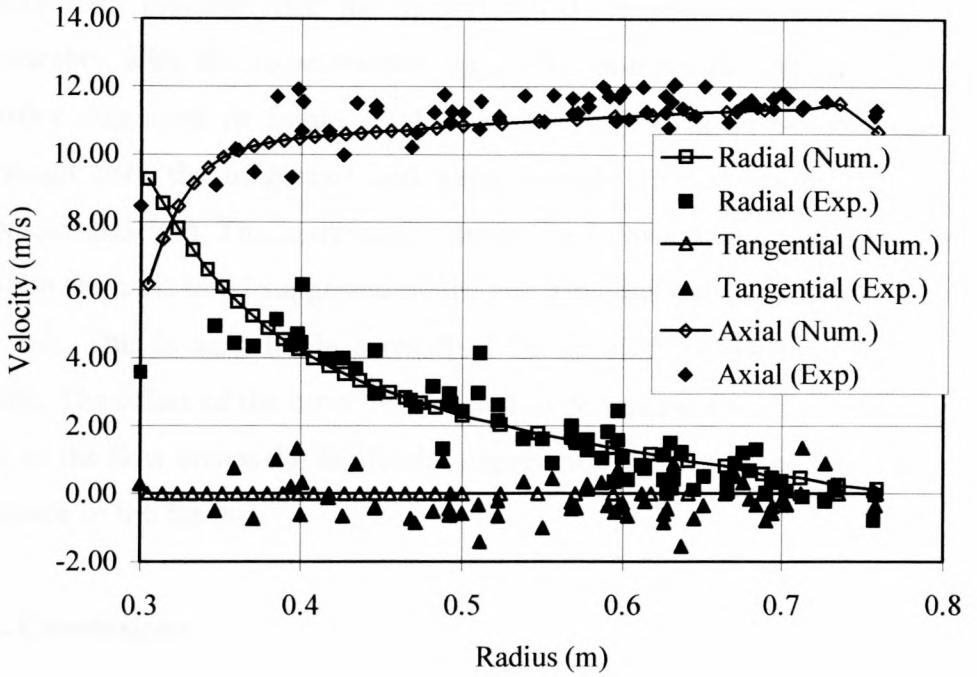

Figure E.23. Velocity profiles directly upstream of the fan blades.

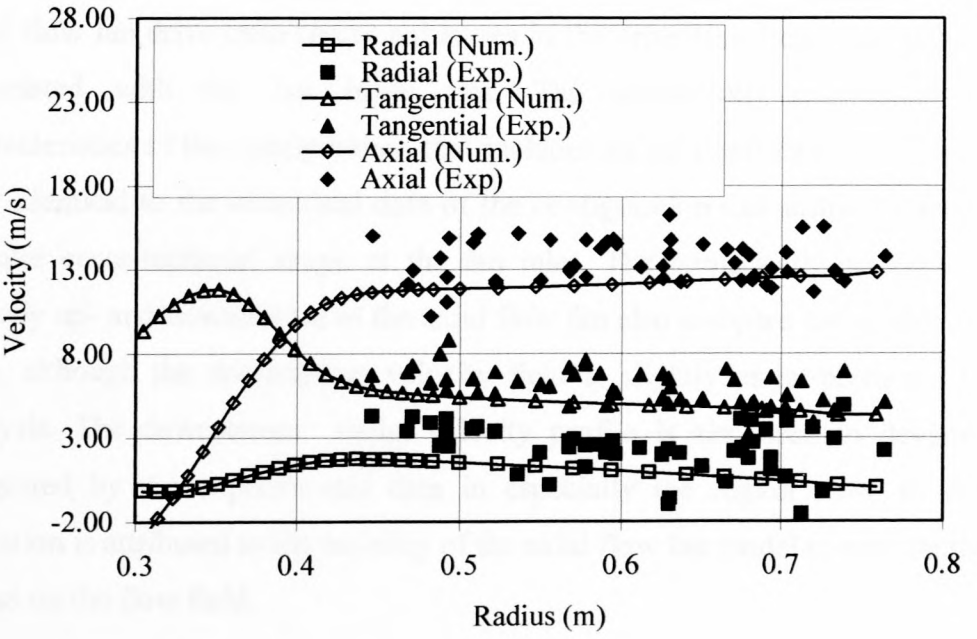

Figure E.24. Velocity profiles directly downstream of the fan blades.

Figure E.23 indicates that the numerically-determined upstream velocity profiles compare favourably with the experimental data. The numerically-determined downstream velocity profiles displayed in figure E.24 seem to slightly under-estimate the experimental data, although both the tangential and axial velocity profiles closely follow the trends of the experimental data. The numerically-determined downstream radial velocity profile is seen to deviate from the trend suggested by the experimental data, especially in the region close to the fan hub. This is most likely a result of the inability of the fan model to account for radial forces. The effect of the latter is expected to be most noticeable in the region close to the fan hub, as the flow across the fan blades experiences a force in the tangential direction due to the presence of the fan hub.

E.4. Conclusions

A comparison of the numerical results with experimental data indicates the accuracy of the fan model in its prediction of the axial flow fan performance characteristics over a range of volume flow rates and blade settings. The numerically-determined fan power consumption is shown to be slightly lower than the experimental data. This discrepancy is thought to be the result of the inability of the numerical analysis to include the resistance associated with the axial flow fan drive train (frictional losses in the drive train bearings) as well as flow effects associated with the fan blade tips. The numerically-determined fan performance characteristics of the configuration that includes an inlet bell mouth and settling chamber are near identical to the numerical data of the configuration that utilises a section of ducting of circular cross-sectional shape at the fan inlet. The numerically-determined velocity fields directly up- and downstream of the axial flow fan also compare favourably with experimental data, although the downstream velocity field is slightly under-predicted by the numerical analysis. The downstream radial velocity profile is also seen to deviate from the trend suggested by the experimental data in especially the region close to the fan hub. This deviation is attributed to the inability of the axial flow fan model to include the effect of radial forces on the flow field.

APPENDIX F - Heat exchanger parts and assembly drawings

This appendix displays parts and assembly drawings of the heat exchangers constructed for use in the experimental investigation described in Appendix A. Heat exchangers LUM, HUNG and RAD were constructed by an unknown researcher and as a result the displayed graphical information concerned with these three heat exchangers is limited to detail pertaining to either the heat exchanger finned tubes or core.

F.1. Heat exchangers 1RR, 2RR, 4RR and 6RR

Figure F.1.1 Heat exchanger 1RR

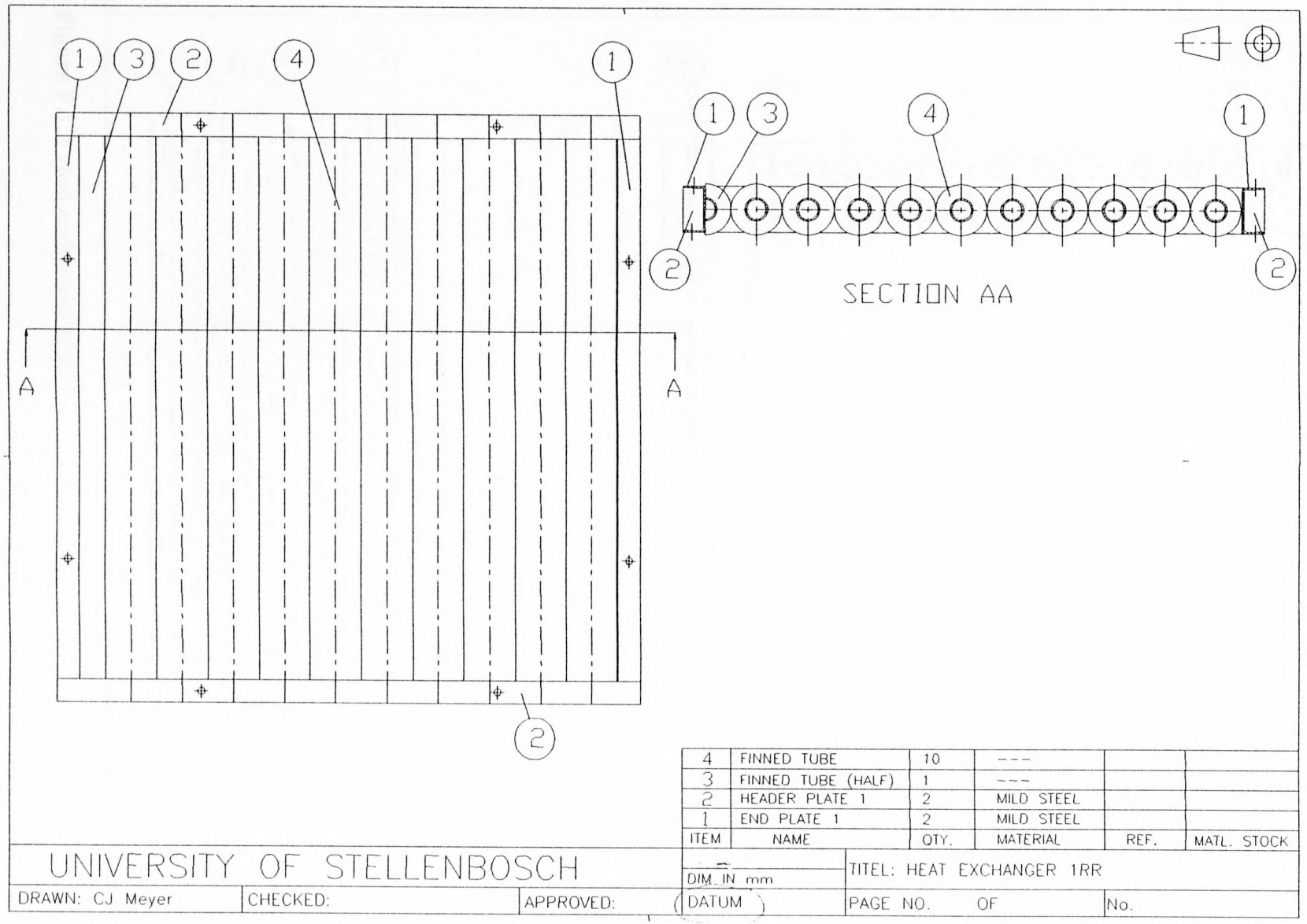

Figure F.1.1 Heat exchanger 1RR.

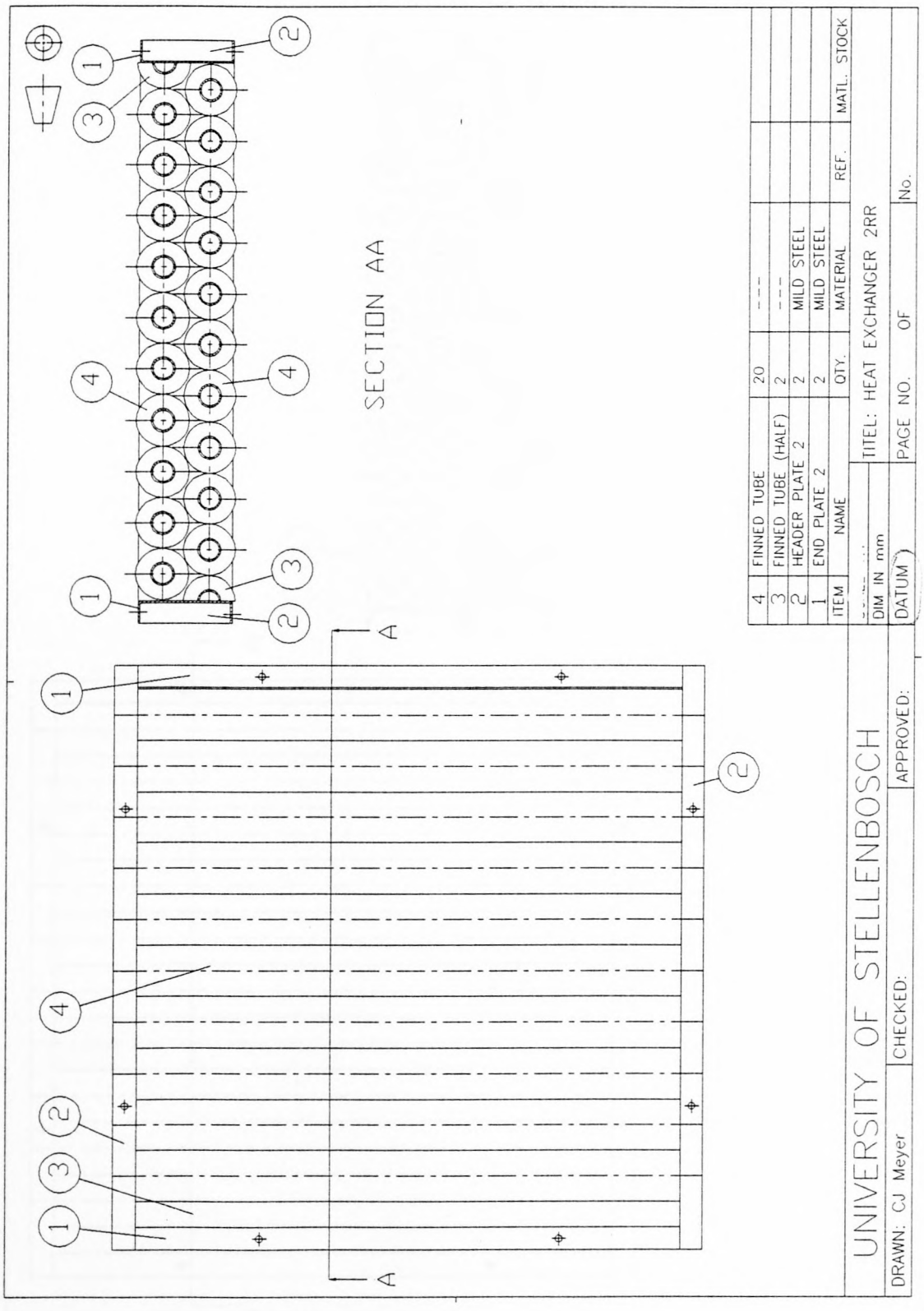

Figure F.1.2 Heat exchanger 2RR.

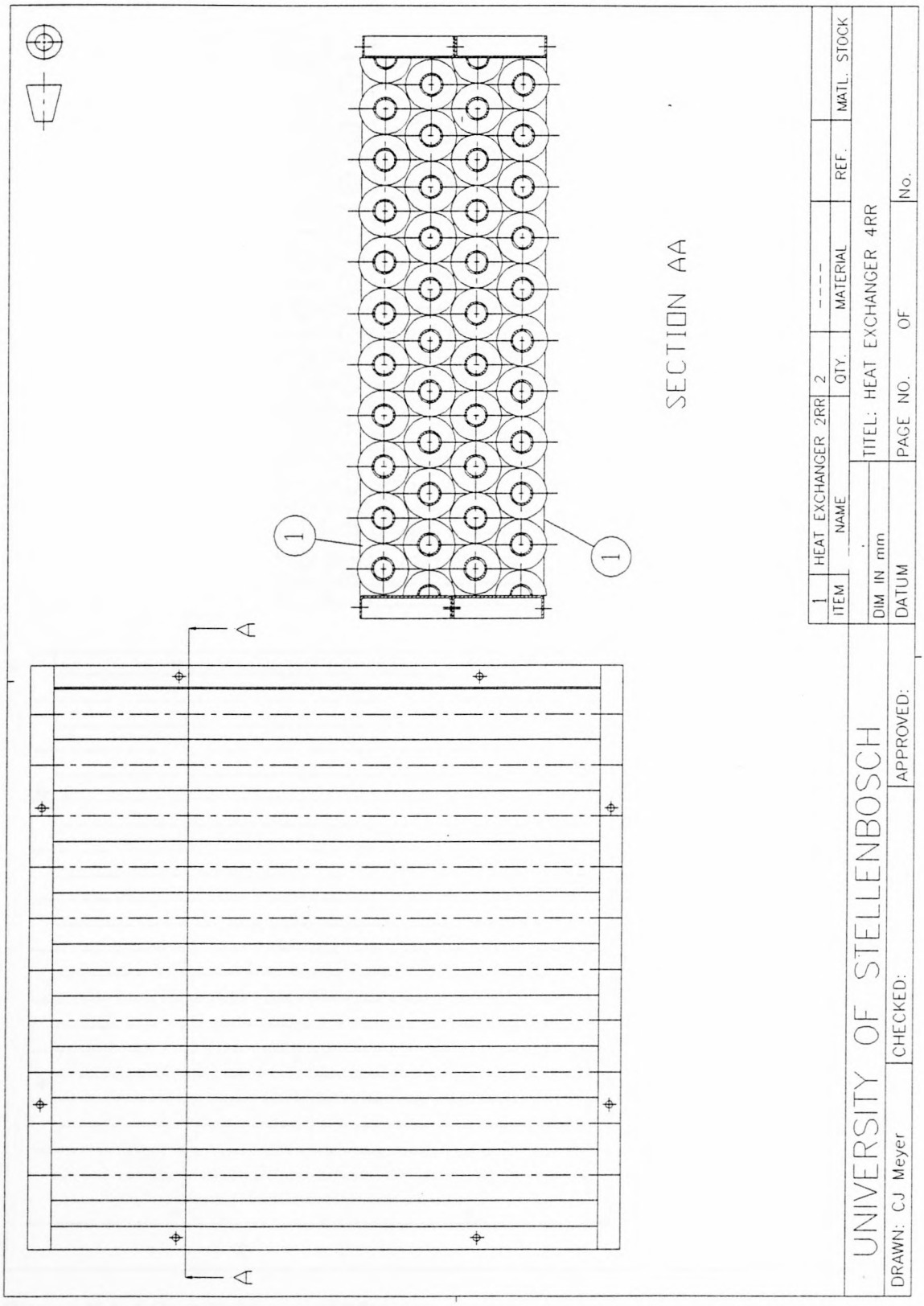

Figure F.1.3 Heat exchanger 4RR.

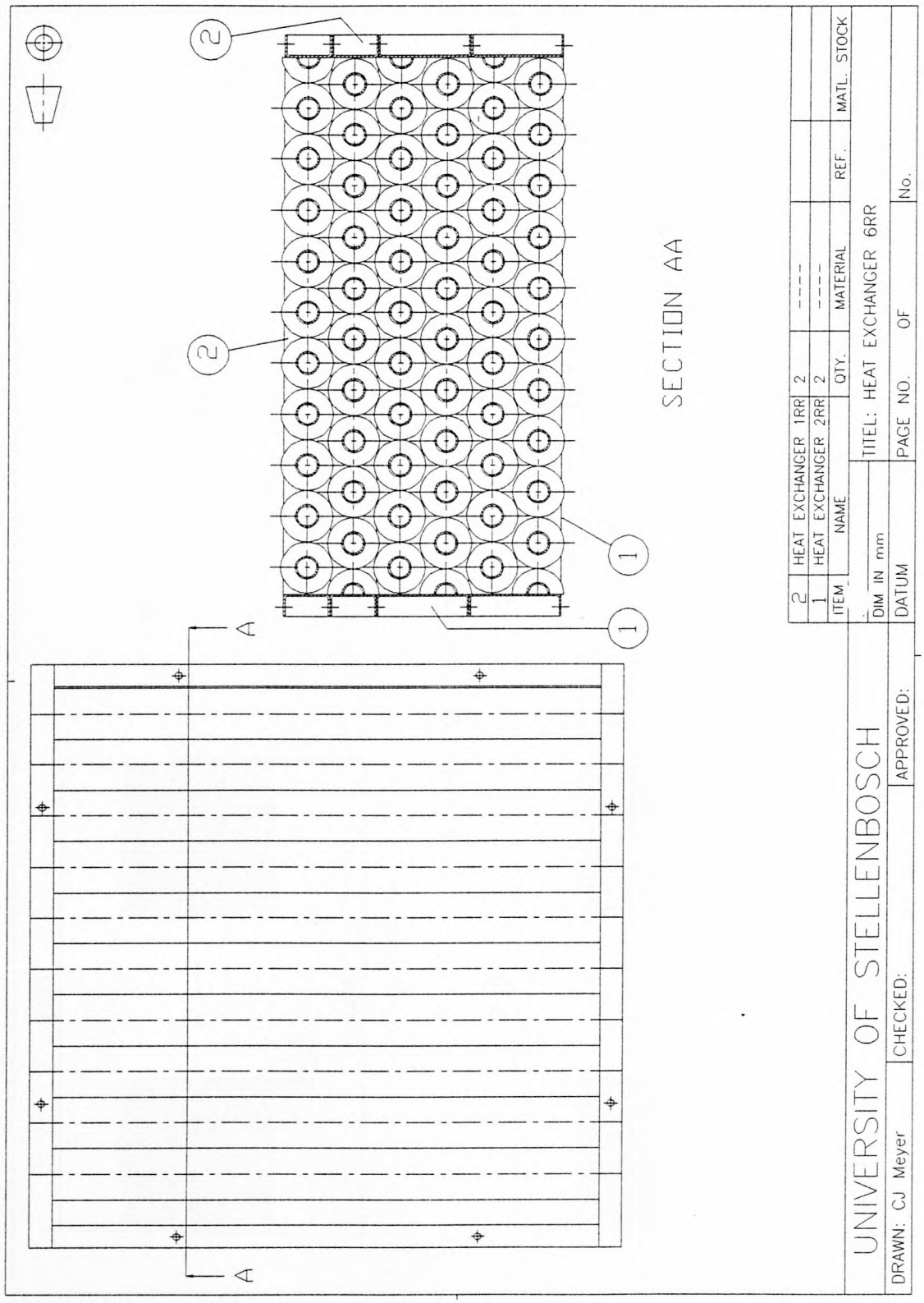

Figure F.1.4 Heat Exchanger 6RR.

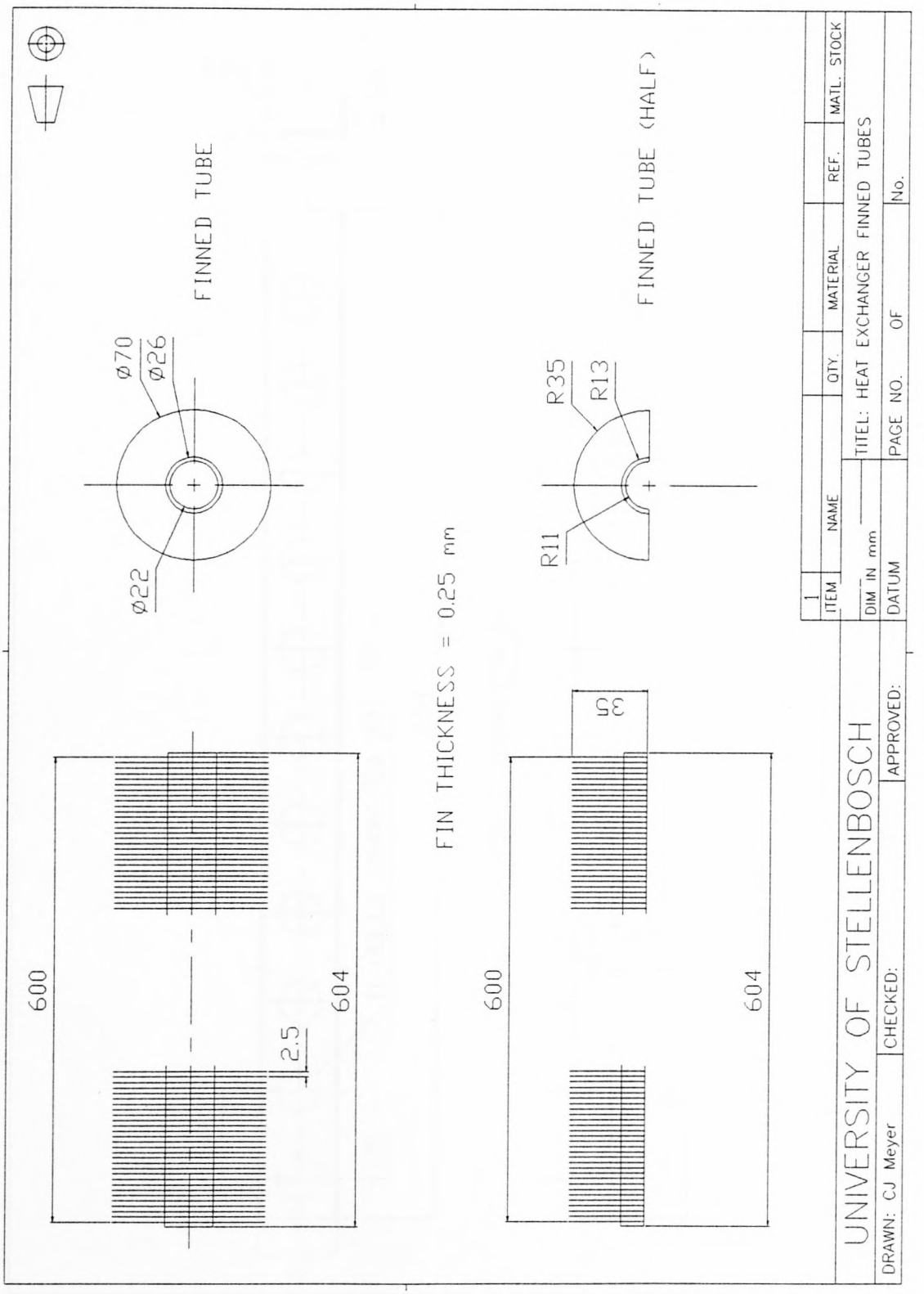

Figure F.1.5 Heat exchanger finned tubes (1RR, 2RR).

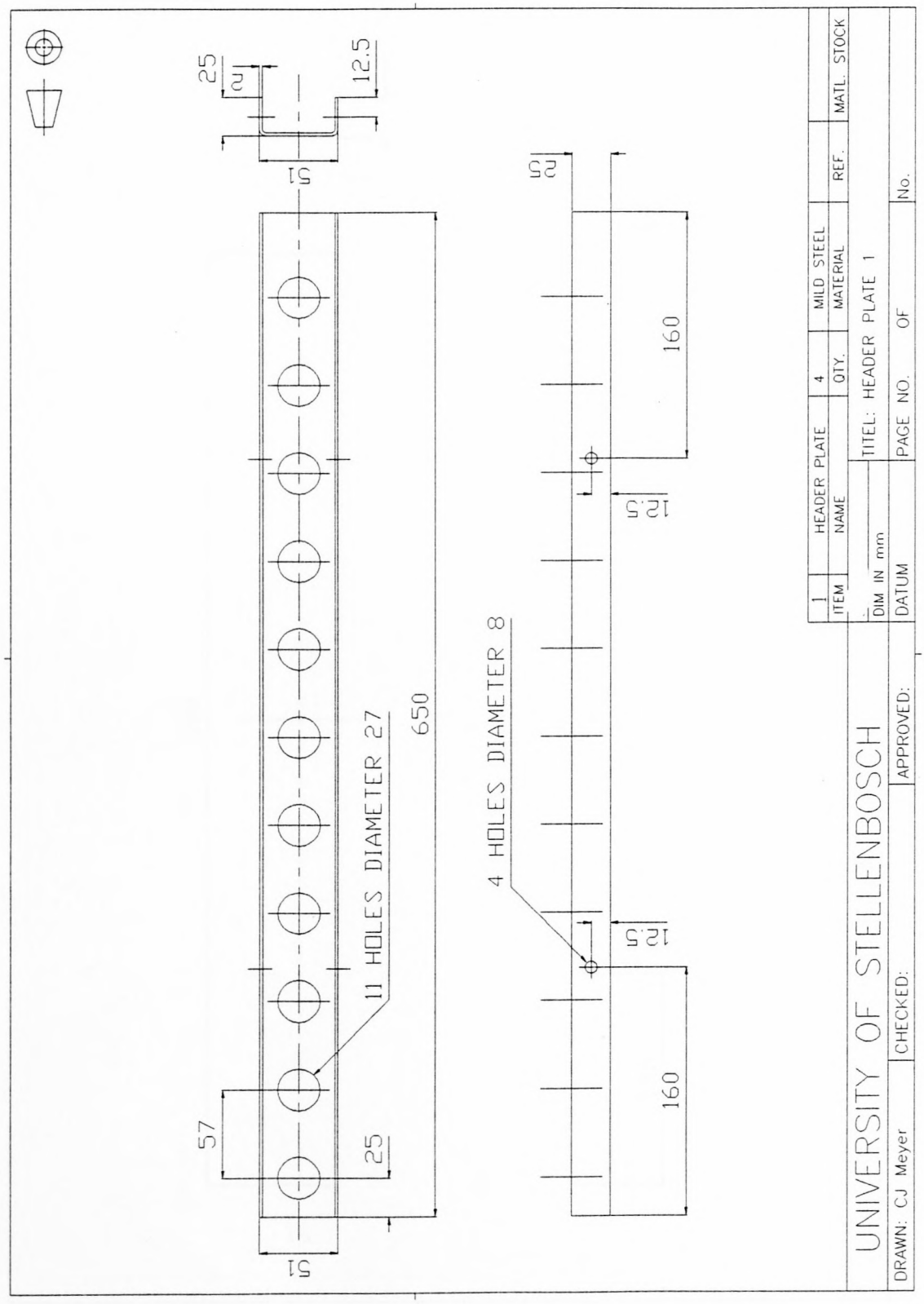

Figure F.1.6 Heat exchanger 1RR header plate 1.

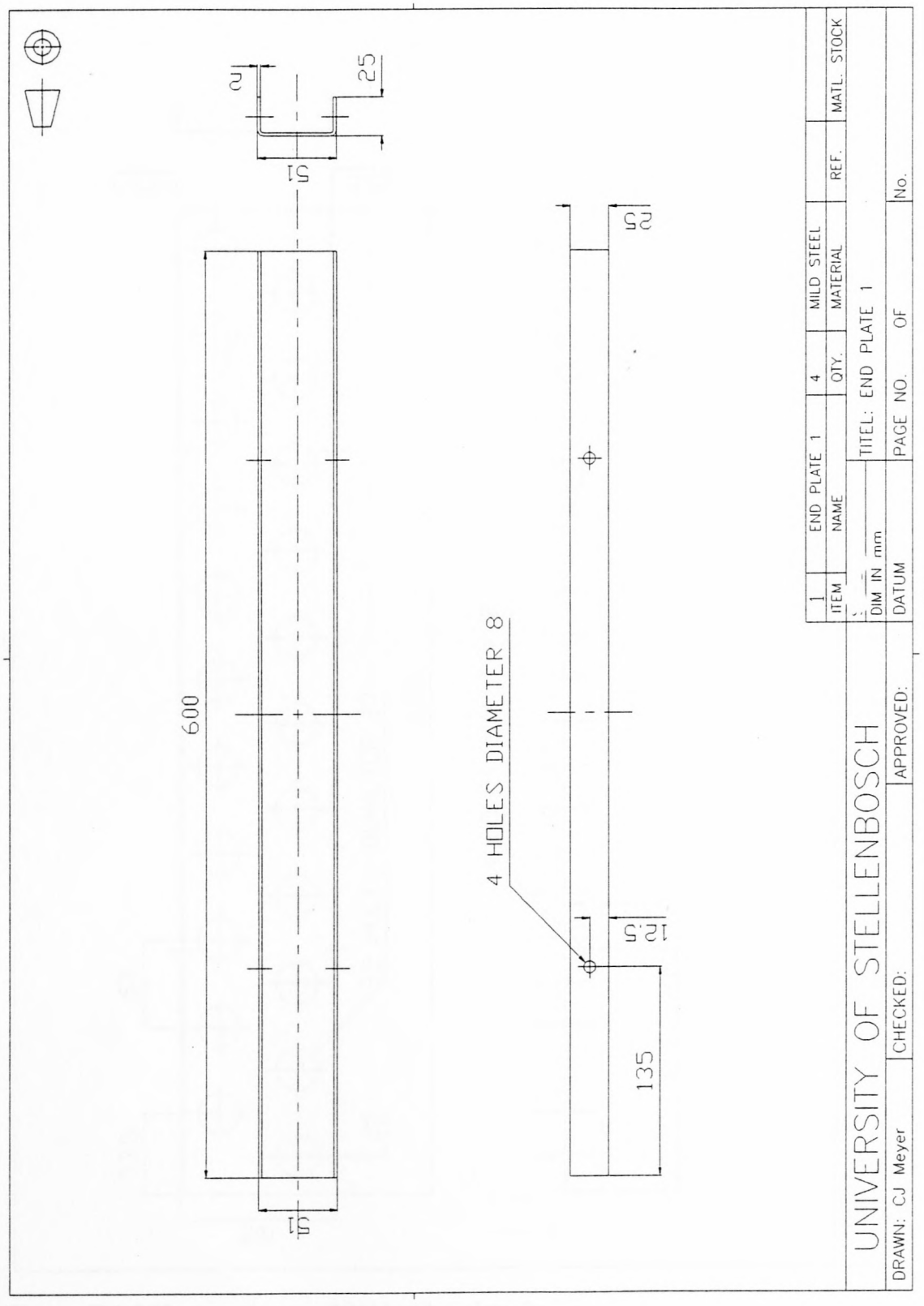

Figure F.1.7 Heat exchanger 1RR end plate 1.

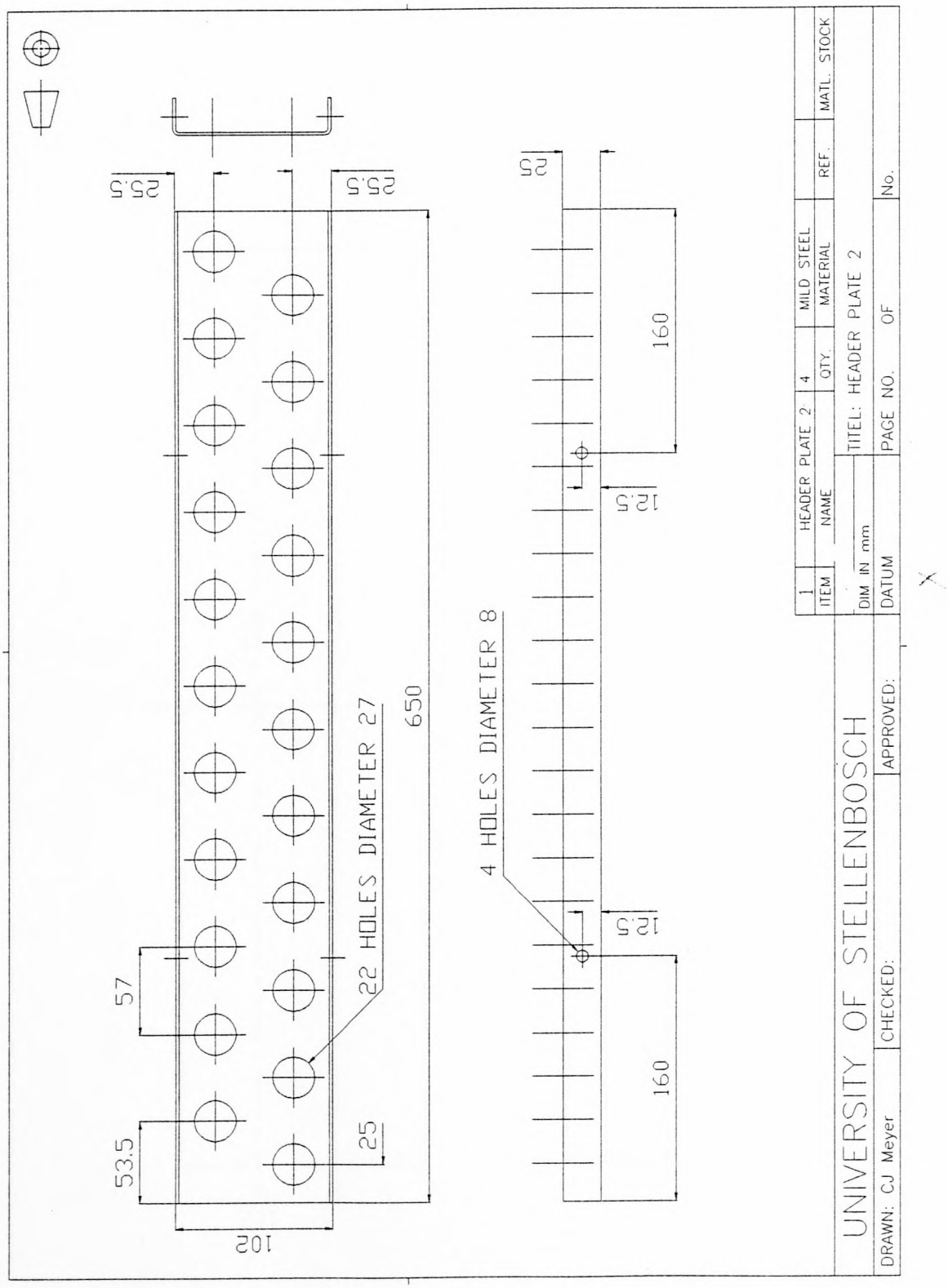

Figure F.1.8 Heat exchanger 2RR header plate 2.

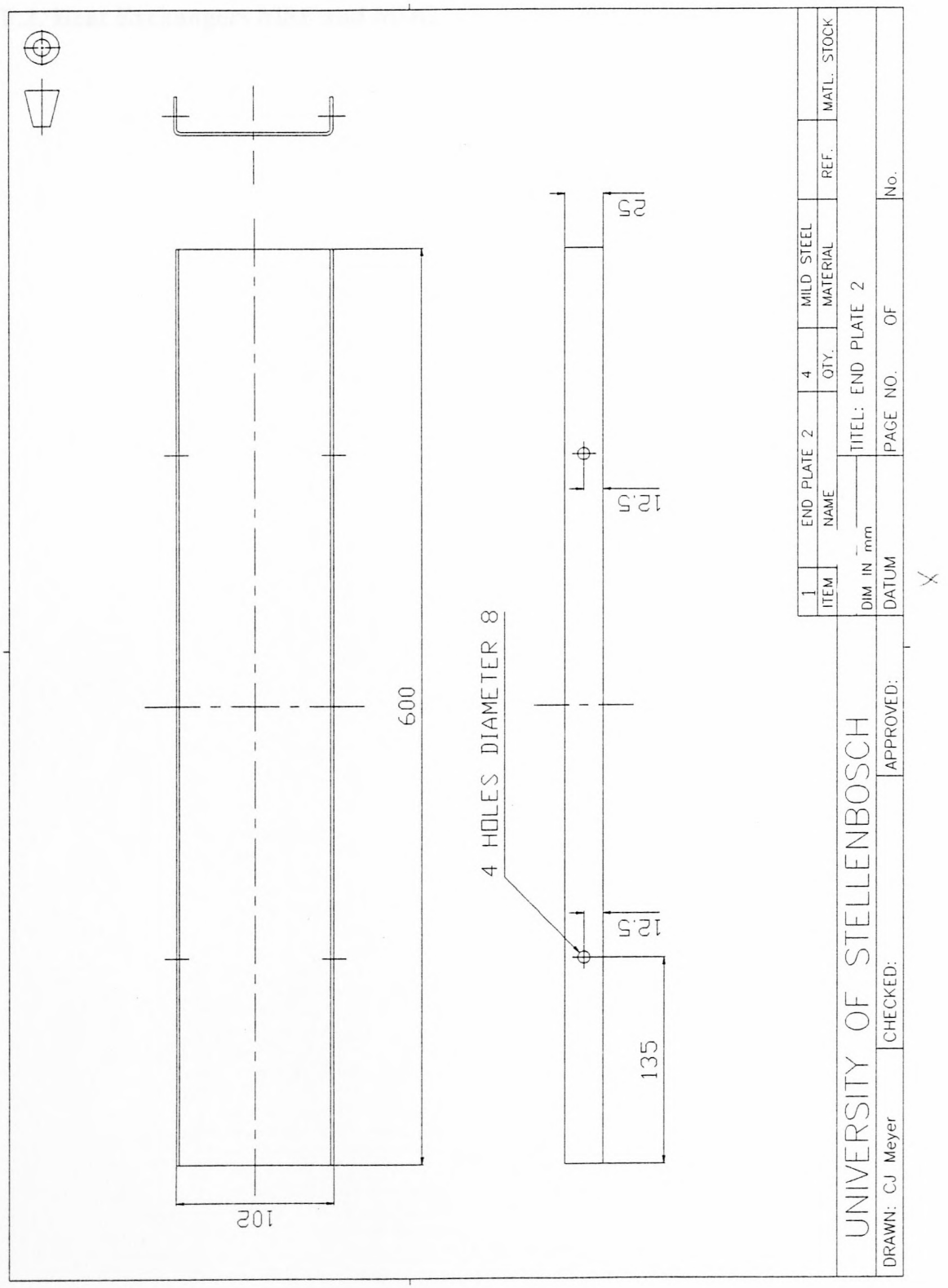

Figure F.1.9 Heat exchanger 2RR end plate 2.

F.2. Heat Exchangers MSF and MDC

Figure F.2.1 Heat exchanger MSF

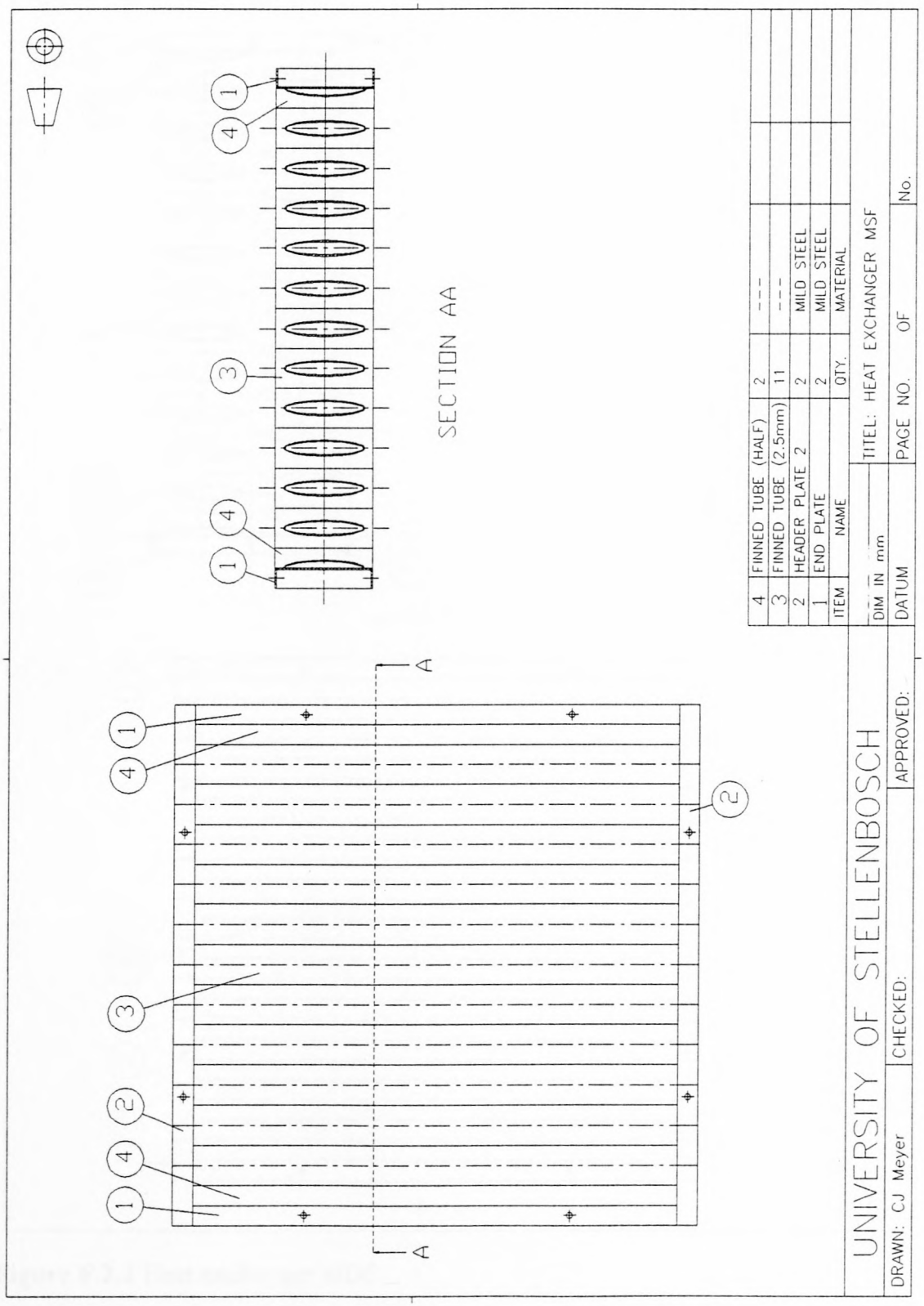

Figure F.2.1 Heat exchanger MSF.

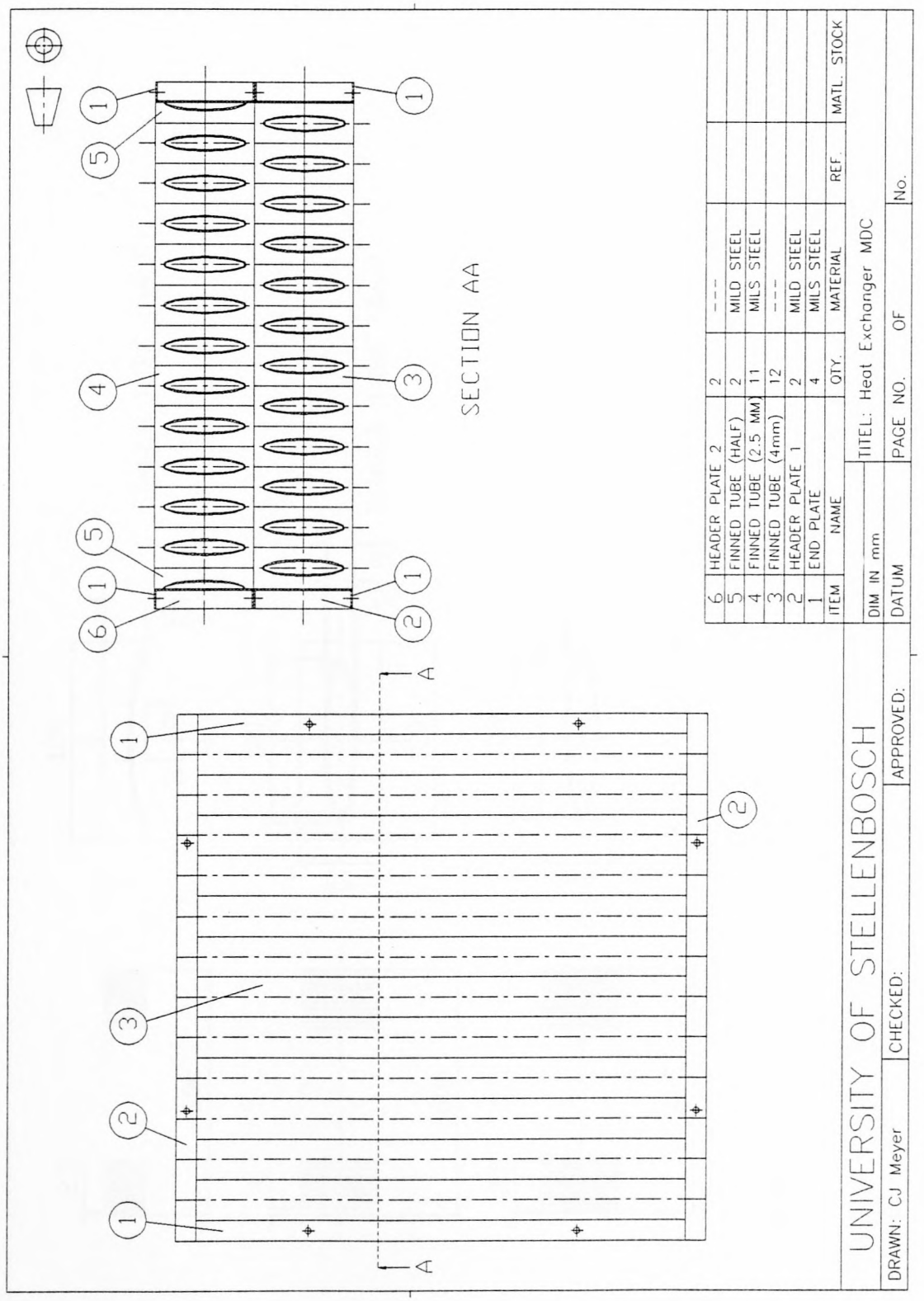

Figure F.2.2 Heat exchanger MDC.

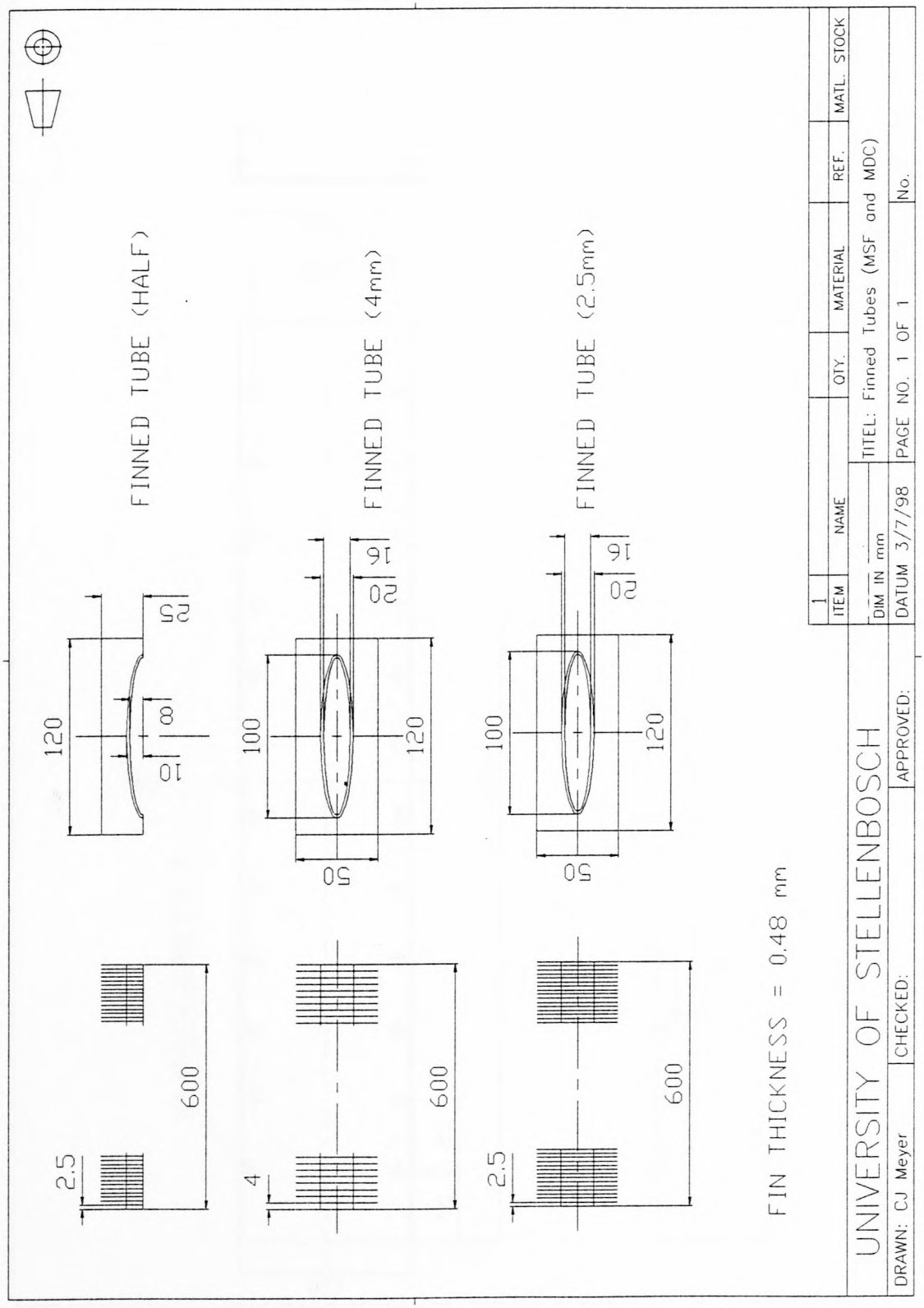

Figure F.2.3 Heat exchanger finned tubes (MSF and MDC).

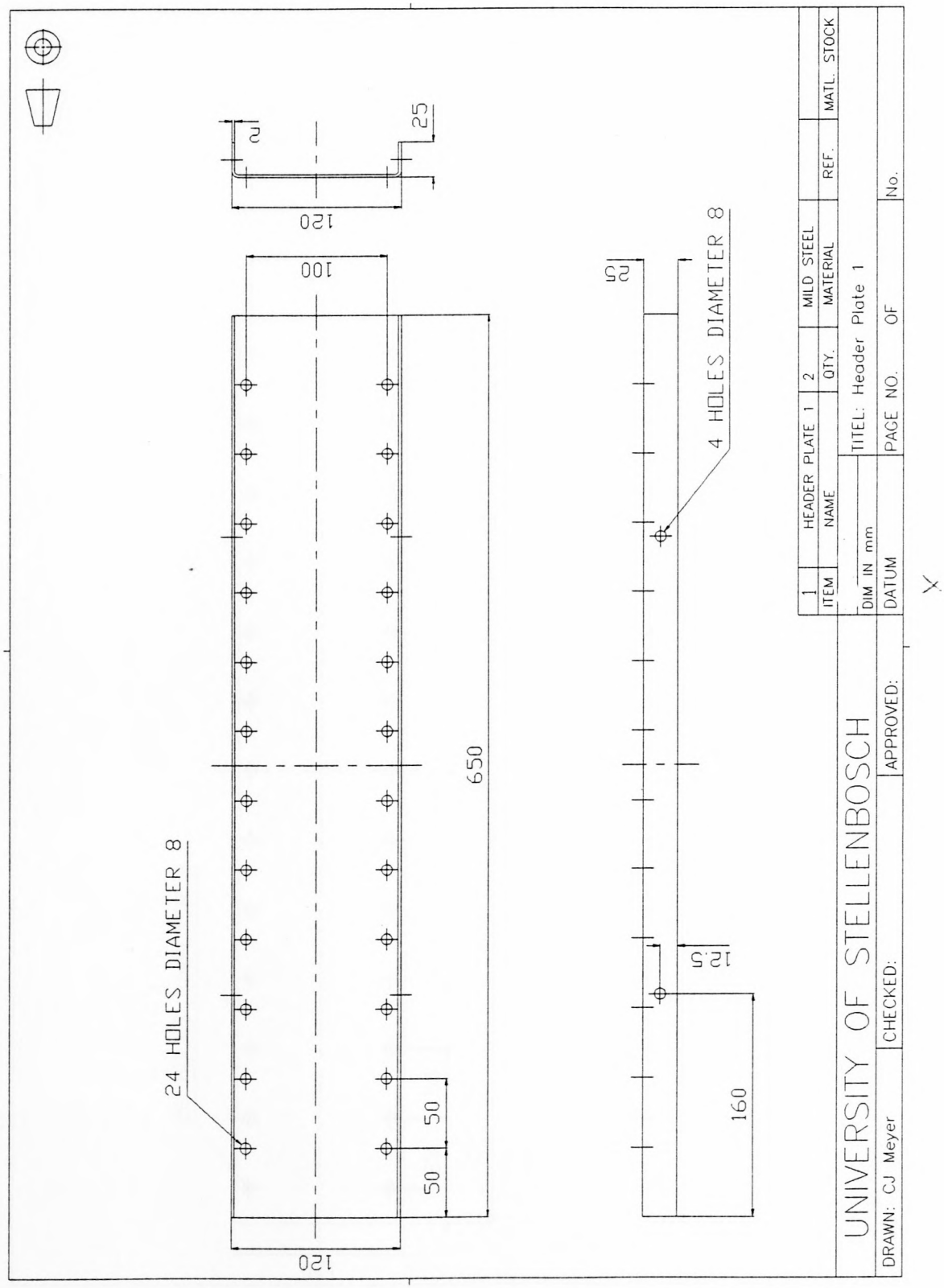

Figure F.2.4 Heat exchanger MDC header plate 1.

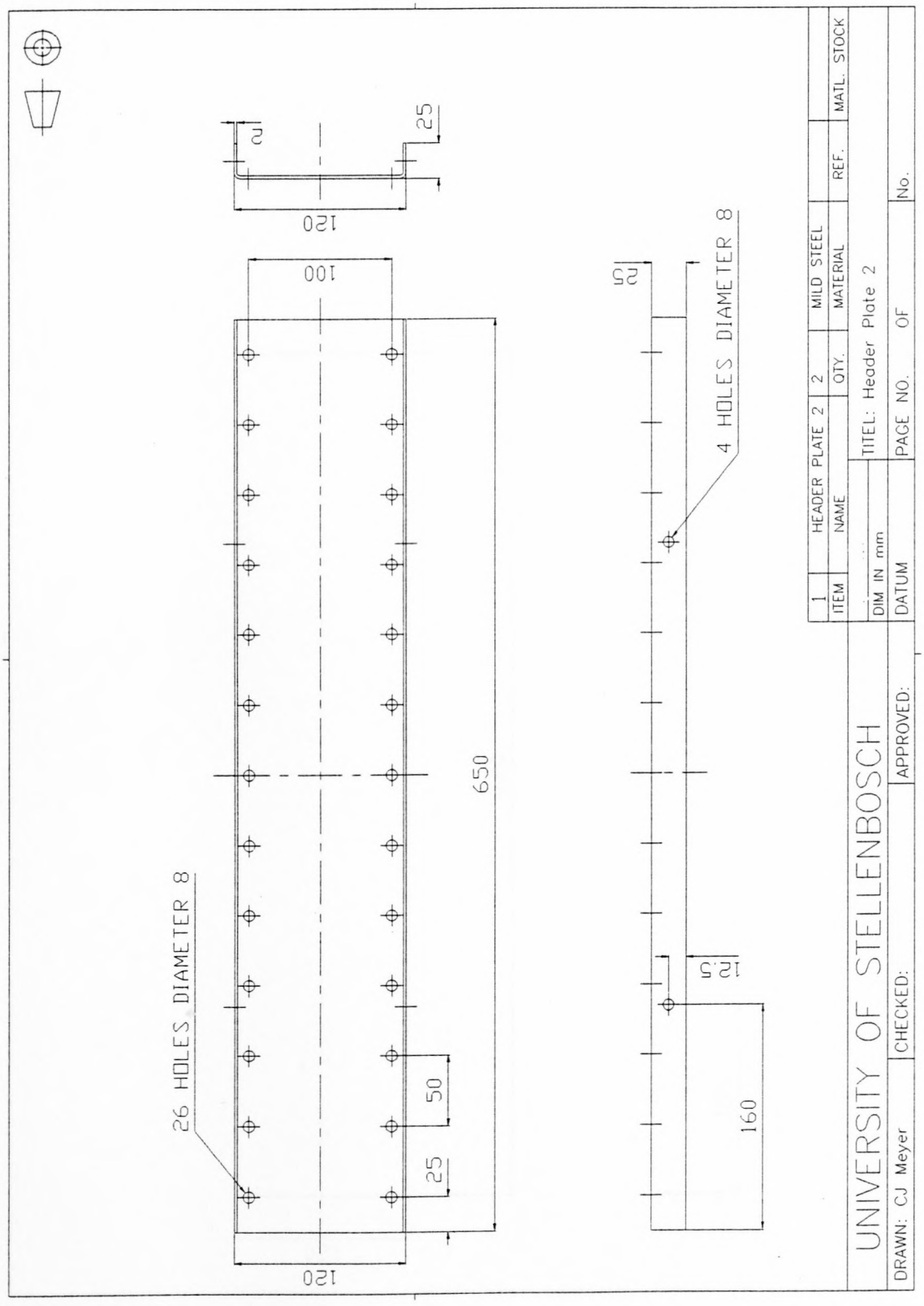

Figure F.2.5 Heat exchangers MSF and MDC header plate 2.

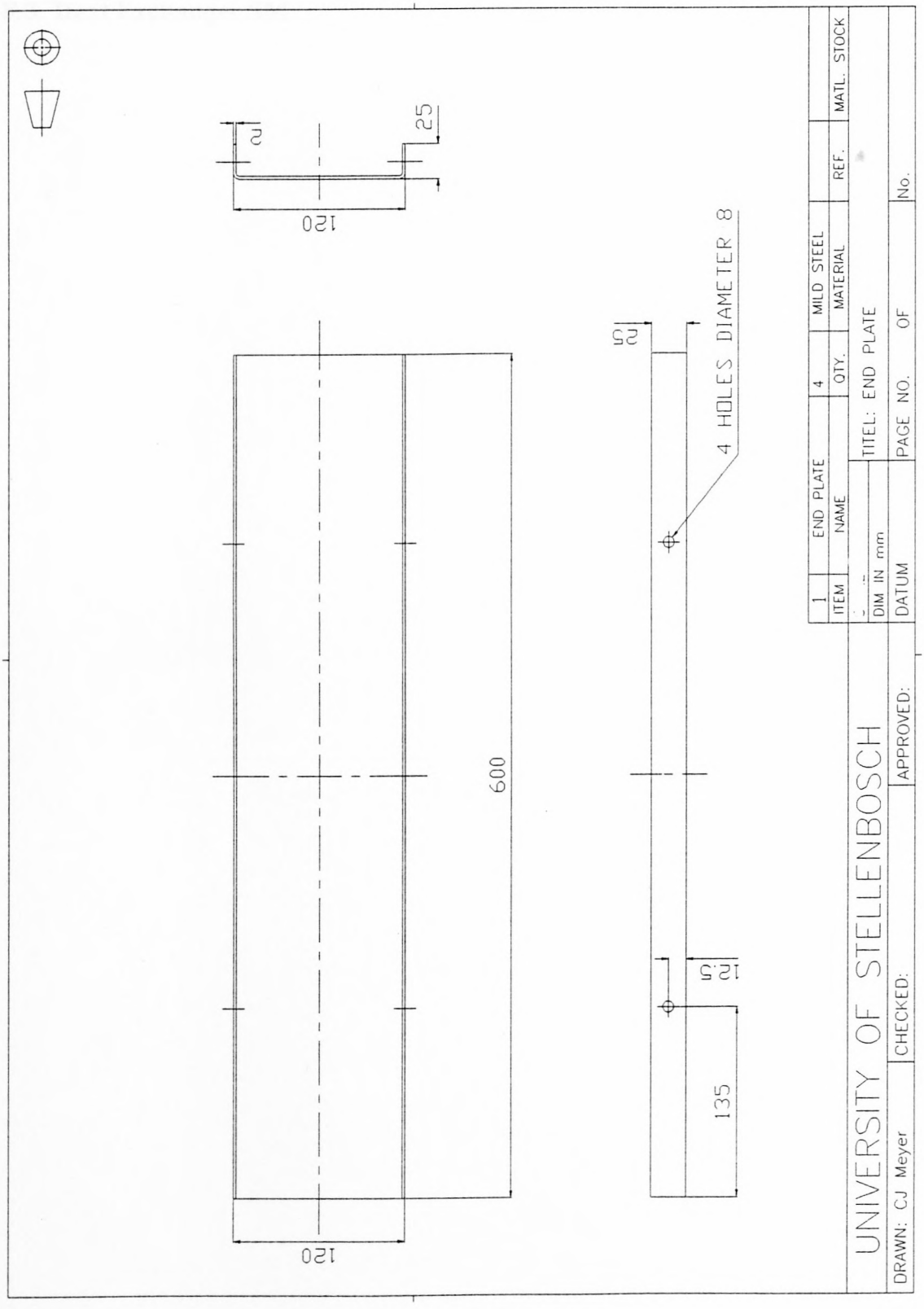

Figure F.2.6 Heat exchangers MSF and MDC end plate.

F.3. Heat Exchanger SM

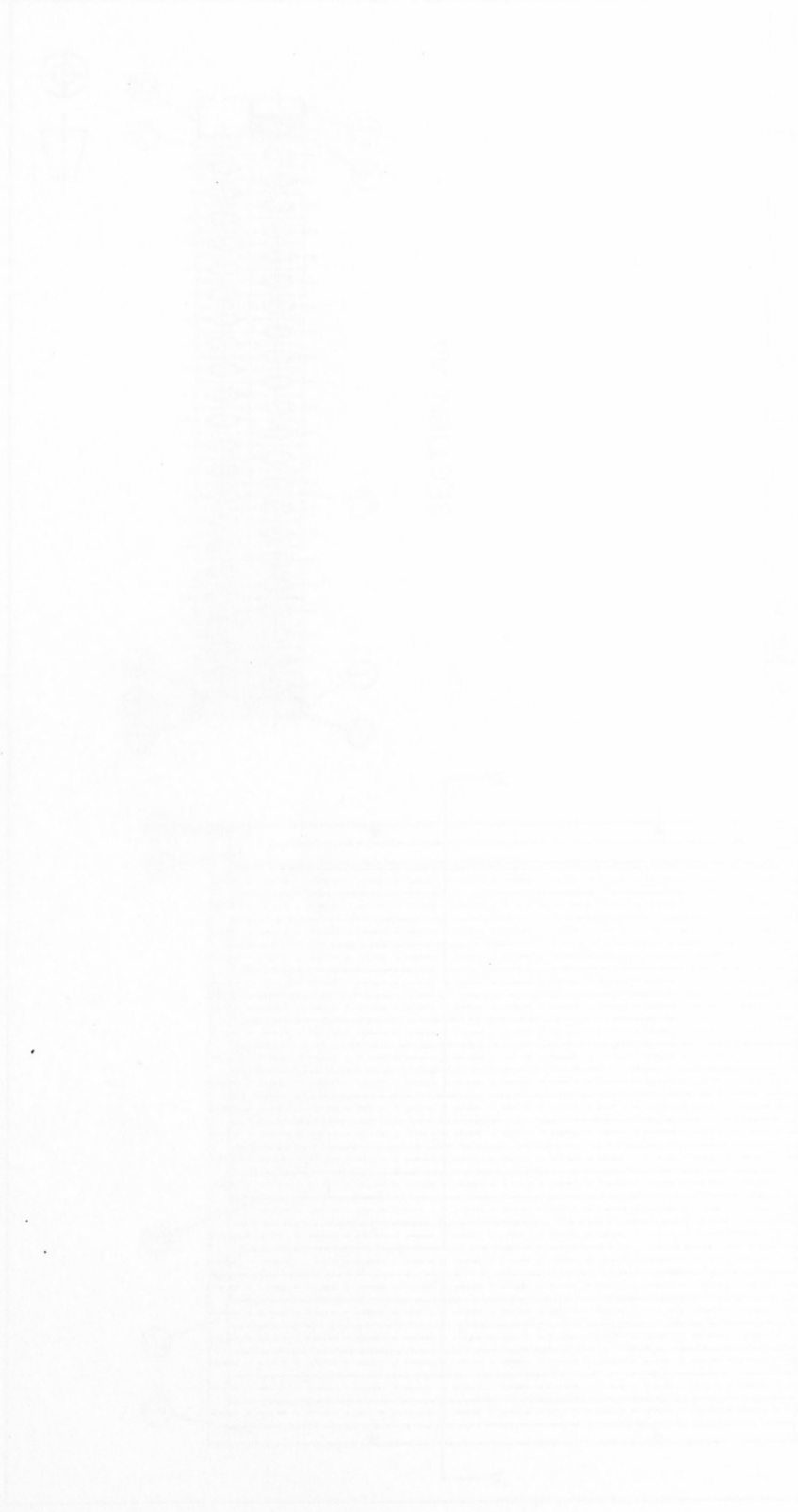

Figure F.3.1 Heat exchanger SM

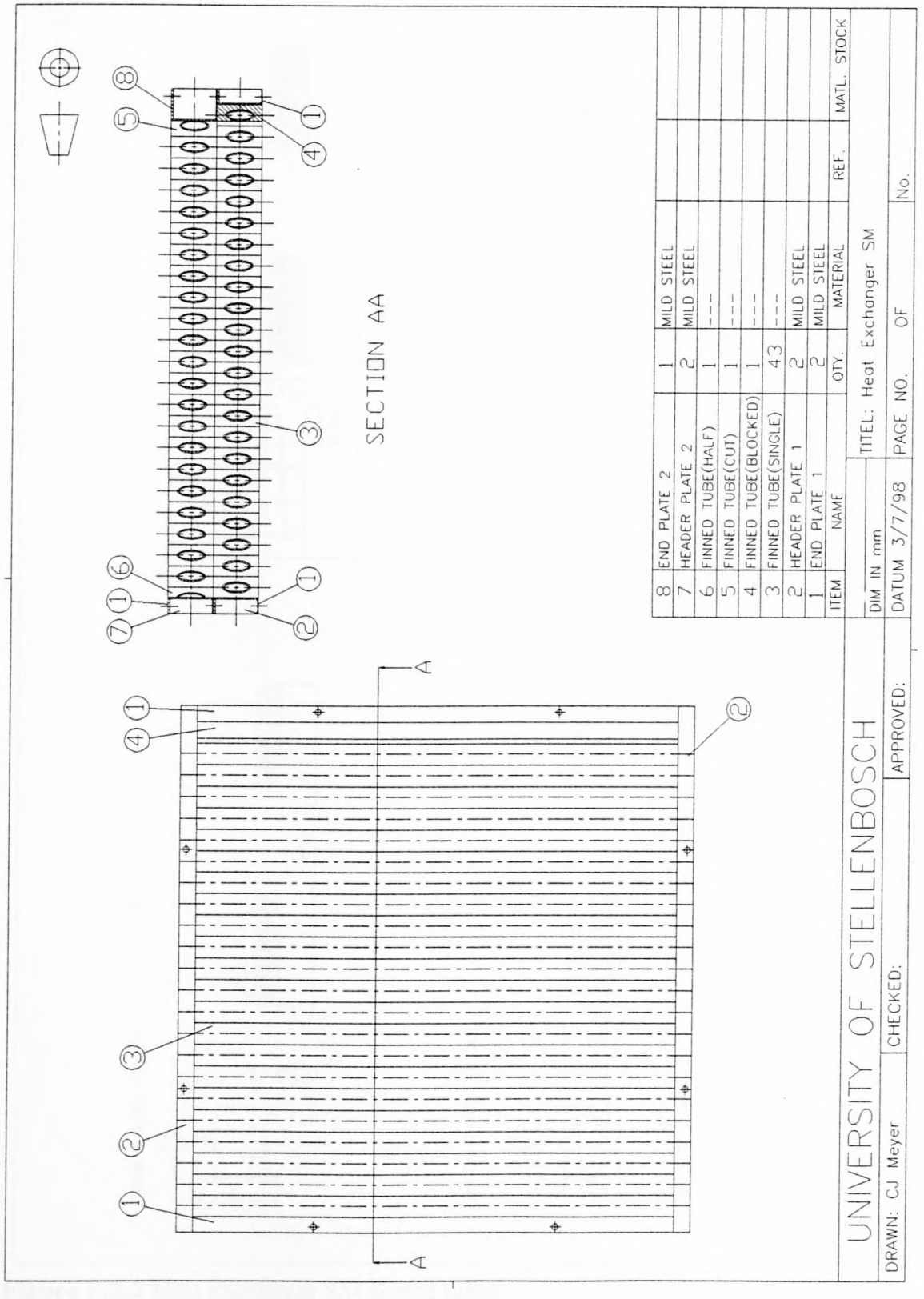

Figure F.3.1 Heat exchanger SM.

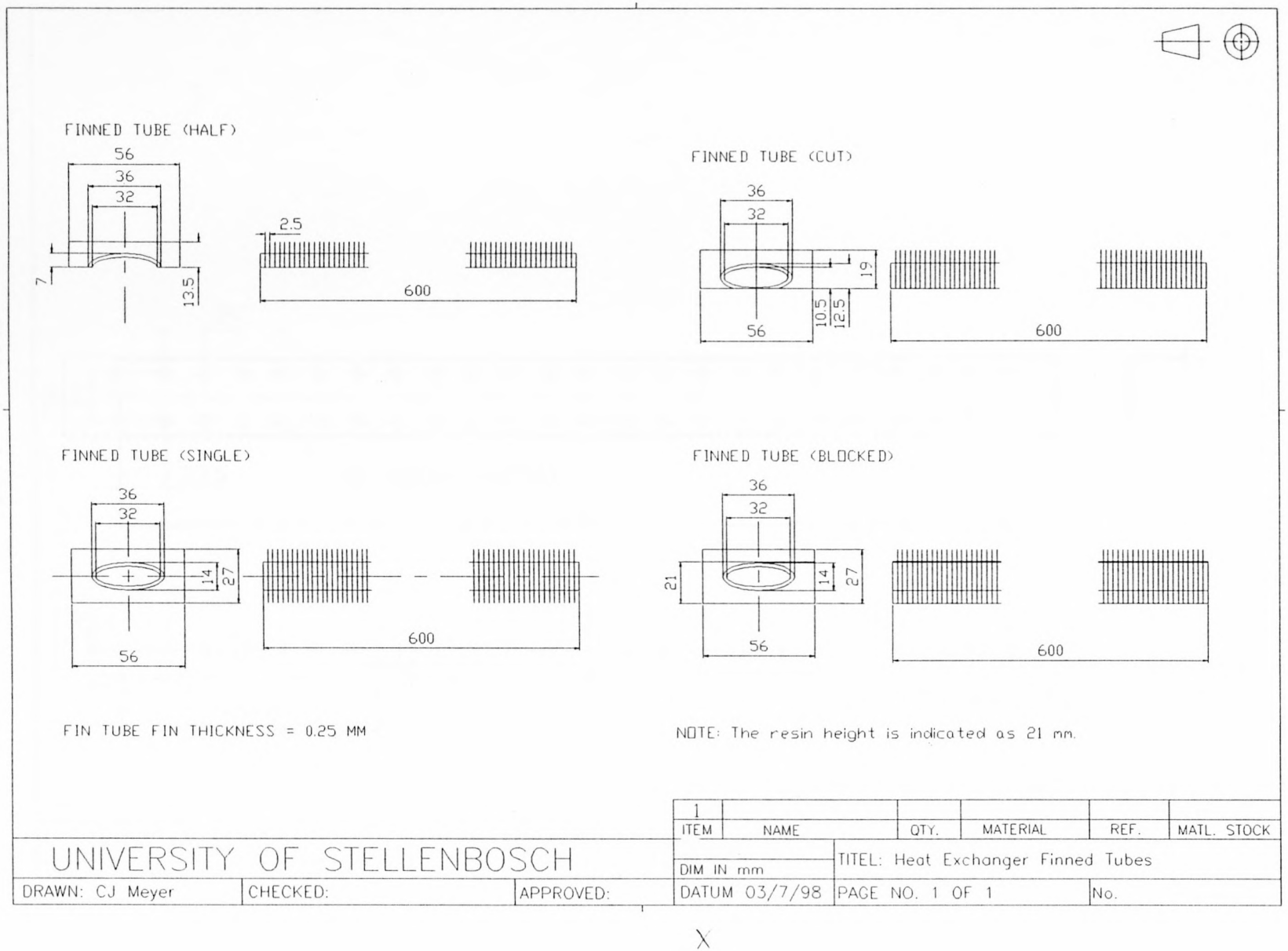

Figure F.3.2 Heat exchanger SM finned tubes.

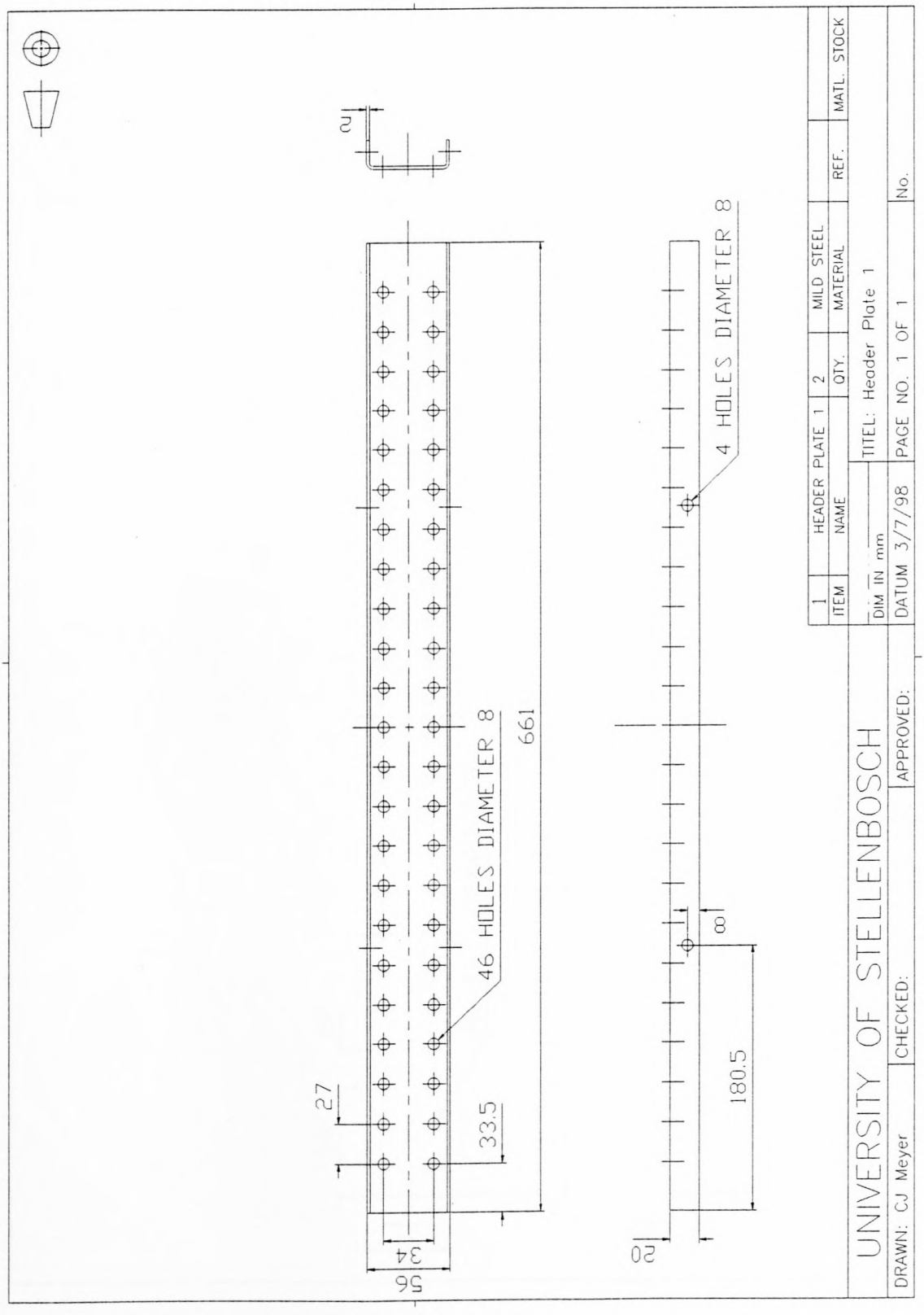

Figure F.3.3 Heat exchanger SM header plate 1.

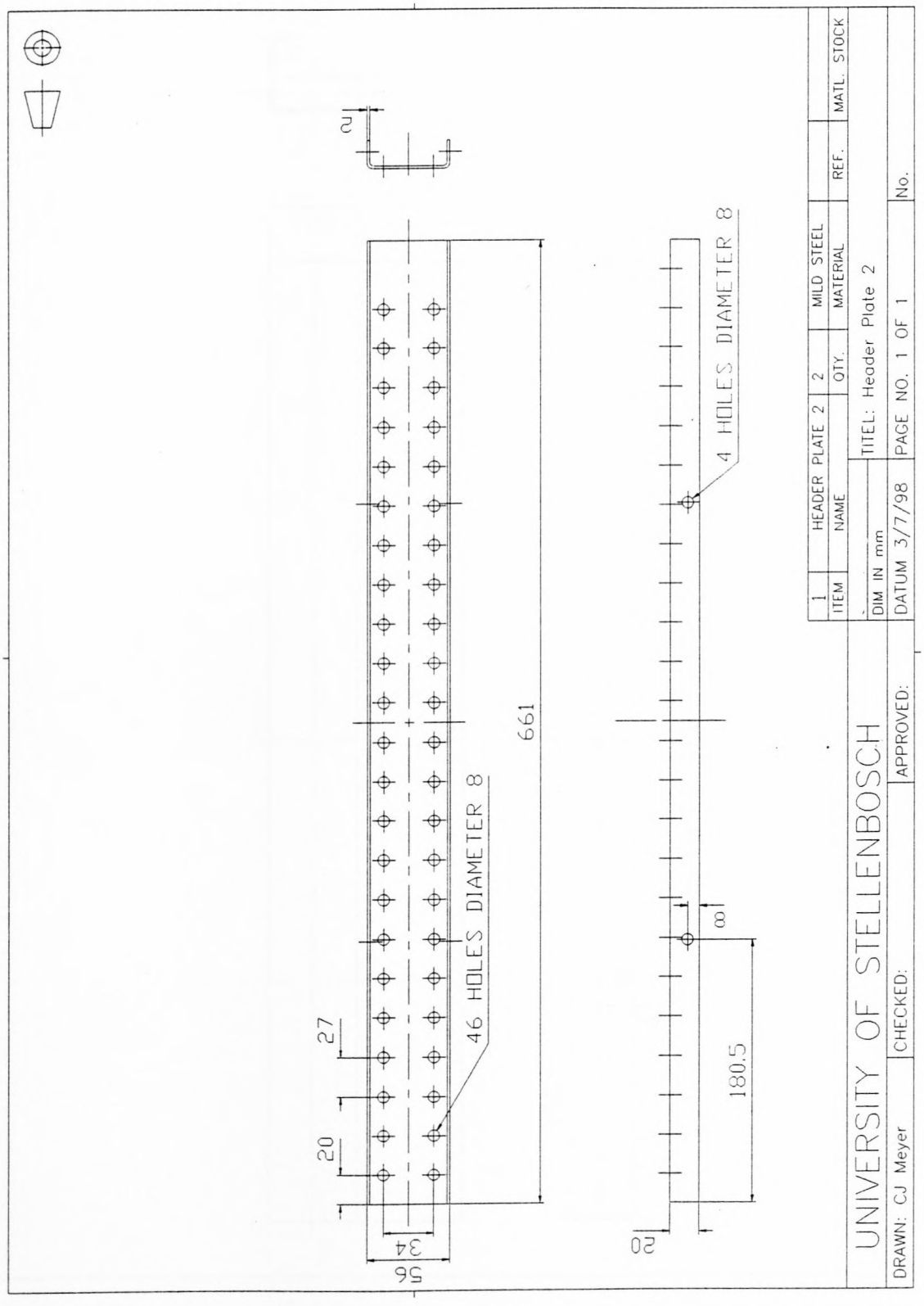

Figure F.3.4 Heat exchanger SM header plate 2.

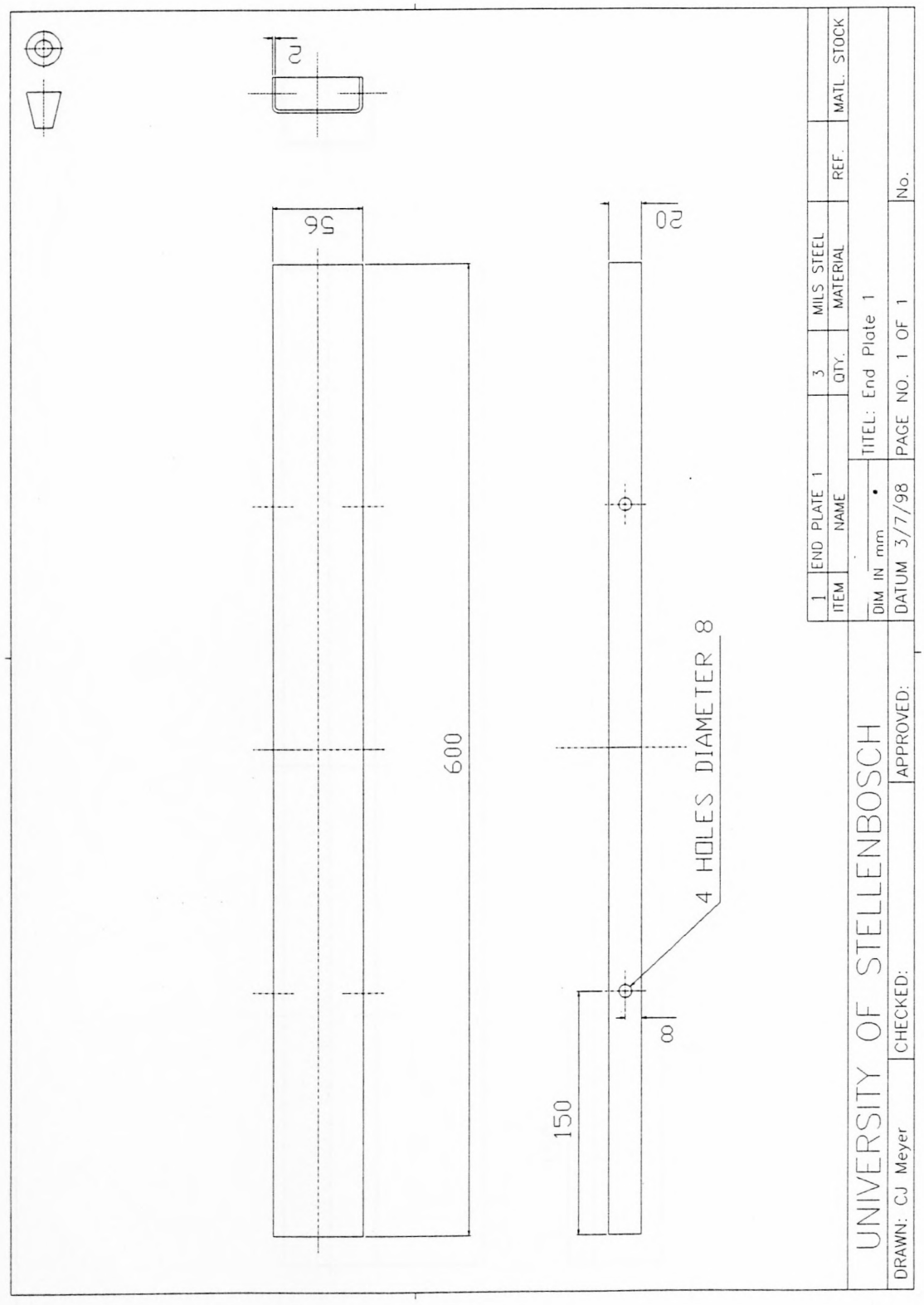

Figure F.3.5 Heat exchanger SM end plate 1.

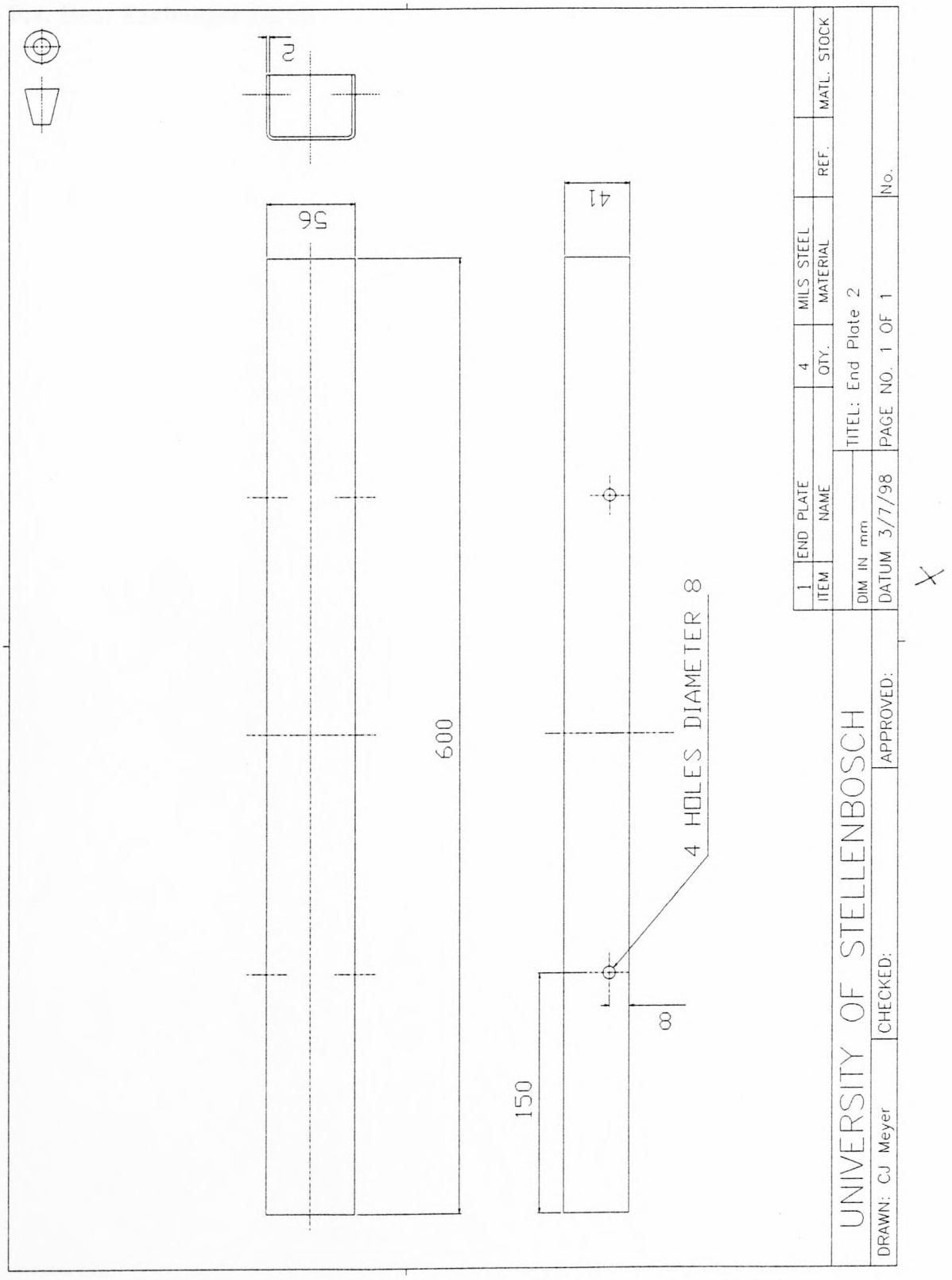

Figure F.3.6 Heat exchanger SM end plate 2.

F.4. Heat Exchanger LUM

Figure F.4.1 Heat exchanger LUM finned tubes

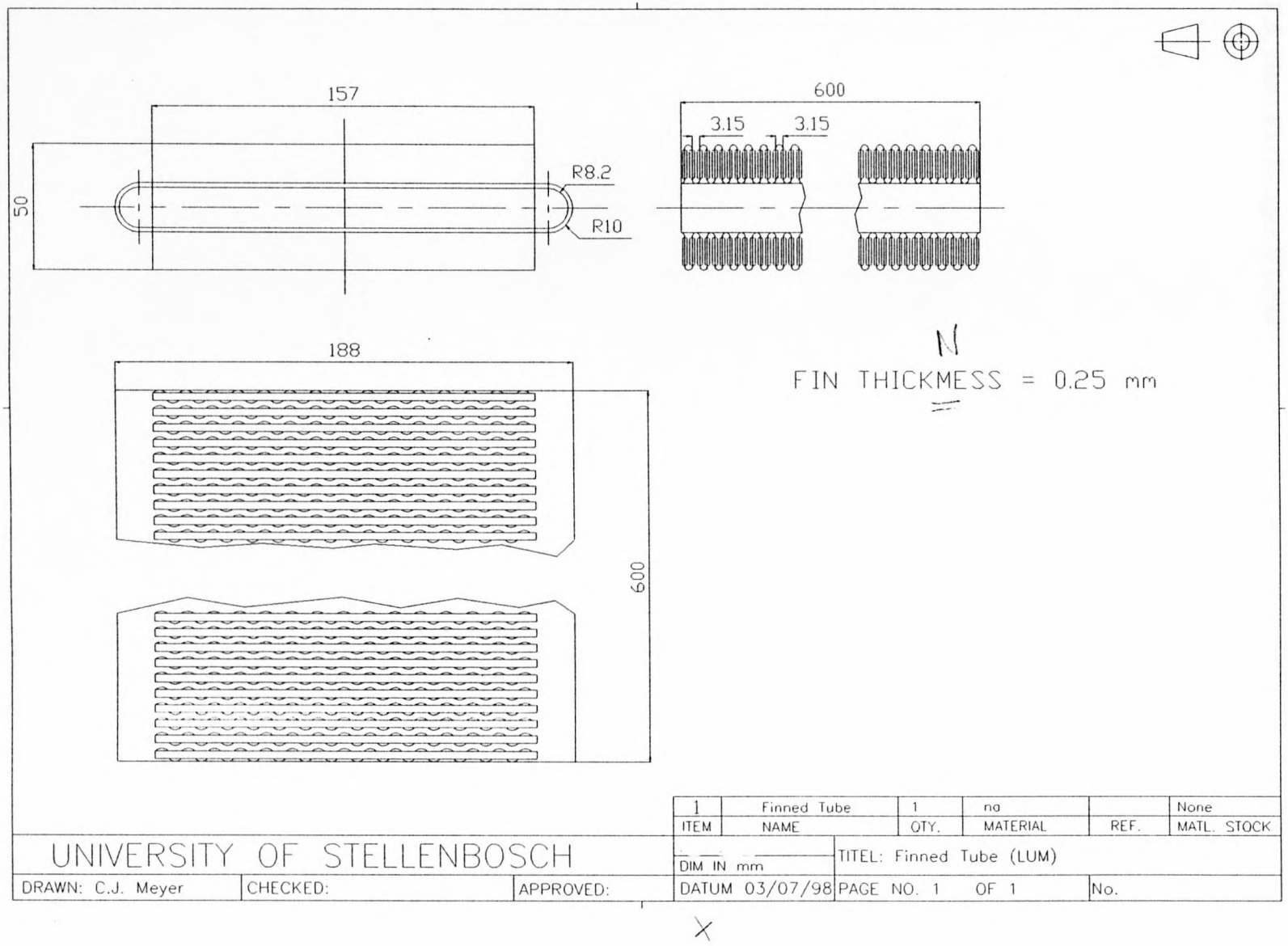

Figure F.4.1 Heat exchanger LUM finned tubes.

F.5. Heat Exchanger HUNG

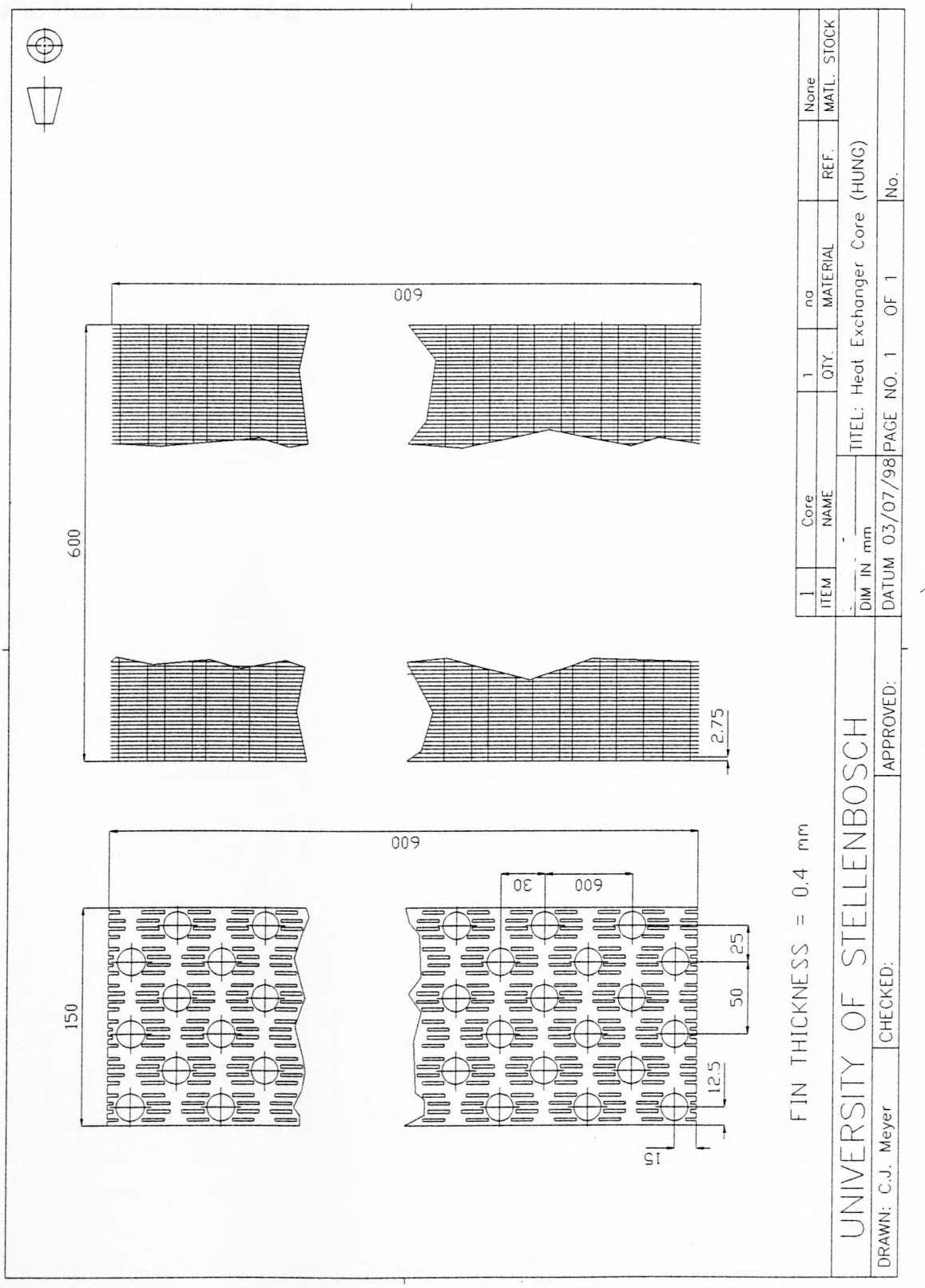

Figure F.5.1 Heat exchanger HUNG core.

F.6. Heat Exchanger RAD

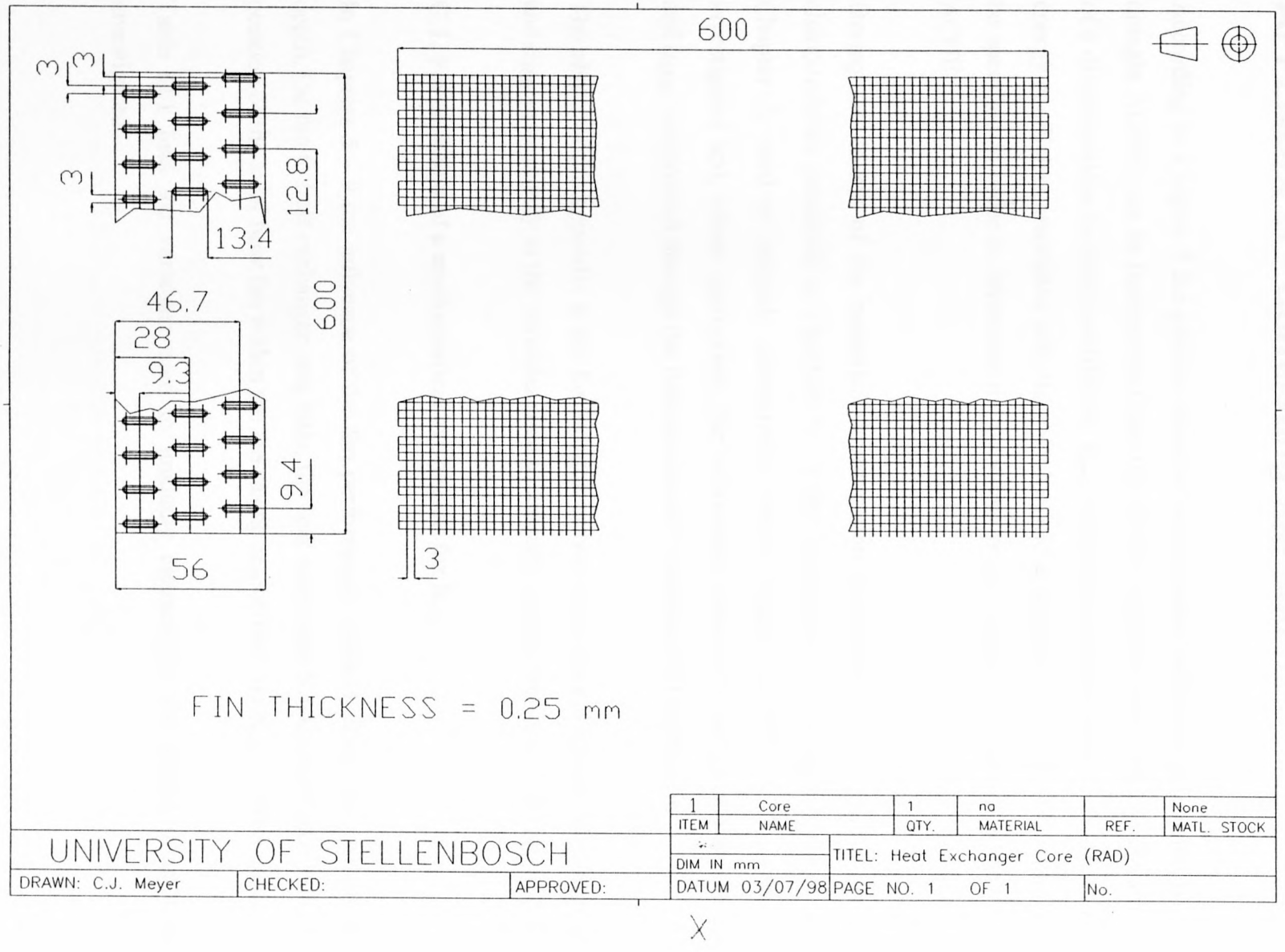

Figure F.6.1 Heat exchanger RAD core.

APPENDIX G - Correlating K_{rec} and α_{eHE}

According to Chapter 2 the plenum chamber aerodynamic behaviour associated with forced draught ACHEs can be incorporated into the ACHE design process through the introduction of a dimensionless recovery coefficient, K_{rec}. Equation (2.26) however shows that the kinetic energy coefficient associated with the velocity field at the heat exchanger exit, α_{eHE} need also be specified in order to determine the operating point volume flow rate of a forced draught ACHE.

During the coarse of the numerical investigation of forced draught ACHE performance characteristics presented in Chapters 5 - 9 the influence of the various variables listed in Chapter 5, used to uniquely characterise forced draught ACHEs, on K_{rec} and α_{eHE} is investigated and, where appropriate, the relationship between a particular variable and K_{rec} and α_{eHE} is expressed through the introduction of a mathematical expression.

The object of this appendix is the formulation of two mathematical expression that relate K_{rec} and α_{eHE} respectively to the variables used to uniquely characterise forced draught ACHEs.

G.1. Formulation of a mathematical expression for K_{rec}

In Chapters 5 - 9 the influence of the fan performance characteristics, the plenum chamber depth, the fan to heat exchanger area ratio, the heat exchanger bundle resistance value and the position of the axial flow fan within the fan casing respectively on K_{rec} is investigated.

Table G.1 lists the variables used to uniquely characterise the forced draught ACHEs investigated.

Table G.1. Variables used to uniquely characterise the forced draught ACHEs investigated.

ACHE characteristics	Variables
Axial flow fan	V, γ_{root}
Plenum chamber height	H_P/d_{FC}
Fan casing to heat exchanger area ratio	A_{FC}/A_{HE}
Heat exchanger bundle Resistance	K_{HE}
Position of axial flow fan in fan casing	L_{te}/d_{FC}

The mathematical expression used to express K_{rec} as a function of the variables listed in table G.1, has the following form

$$K_{rec} = C_1 \cdot f_1(V, \gamma_{root}) \cdot f_2(H_P/d_{FC}) \cdot f_3(A_{FC}/A_{HE}) \cdot f_4(K_{HE}) \cdot f_5(L_{te}/d_{FC}) \qquad (G.1)$$

where C_1 is a constant and f_1 - f_5 are functions that represent the influence on K_{rec} of the variables listed in parenthesis of the respective functions.

G.1.1. The influence of axial flow fan performance on K_{rec}

In figure 5.8 of Chapter 5 K_{rec} is plotted as a function of the operating point volume flow rate, V, and the fan blade root stagger angle, γ_{root}. Due to the complex nature of the relationship between K_{rec} and V and γ_{root} no attempt was made in Chapter 5 to determine the form of $f_1(V, \gamma_{root})$.

The data displayed in figure 5.8 suggest that for a particular γ_{root}-value the relationship between K_{rec} and V takes on the form of a second order polynomial with V the dependent variable so that

$$f_1 = a(\gamma_{root}) \cdot (V - b(\gamma_{root}))^2 + c(\gamma_{root}) \qquad (G.2)$$

where a, b and c are functions of γ_{root}.

Figures G.1 - G.5 display plots of K_{rec} vs. V as well as the second order polynomial fitted through the data points for the respective γ_{root}-values.

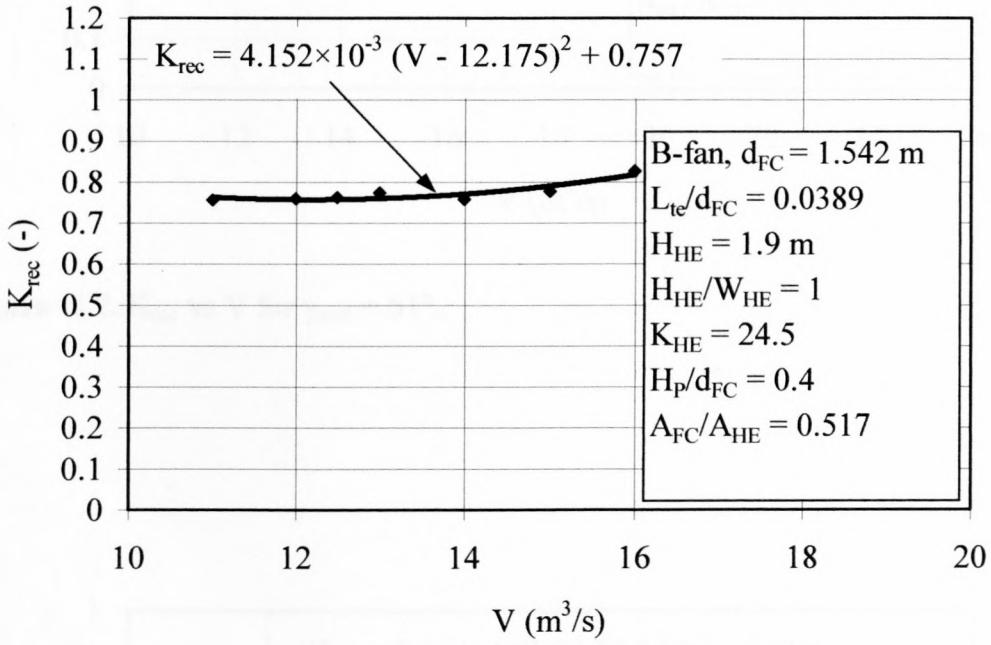

Figure G.1. K_{rec} vs V for γ_{root} = 63.5°.

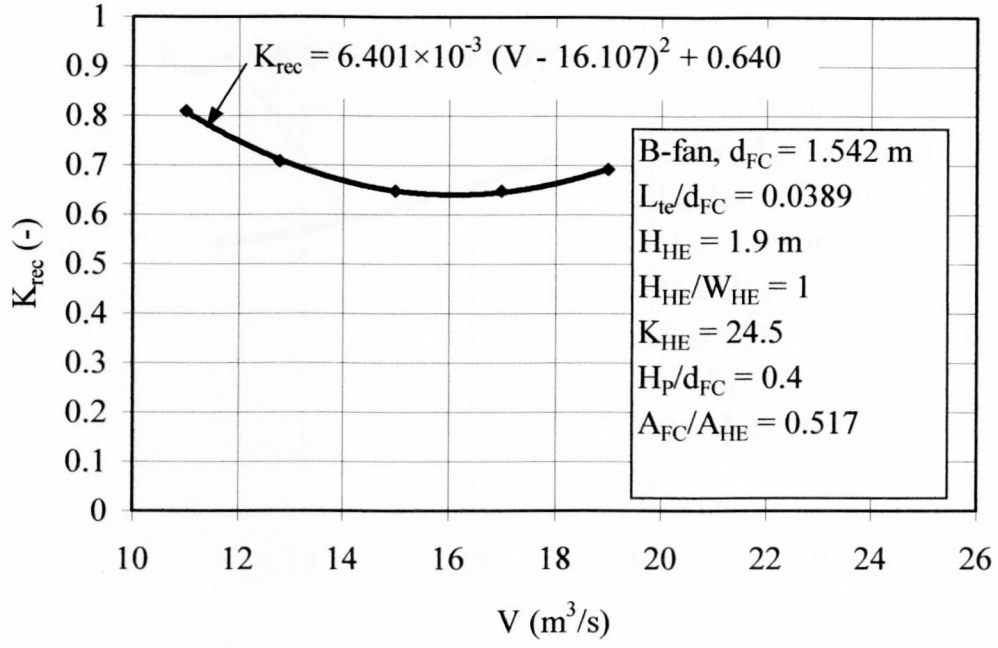

Figure G.2. K_{rec} vs V for $\gamma_{root} = 61°$.

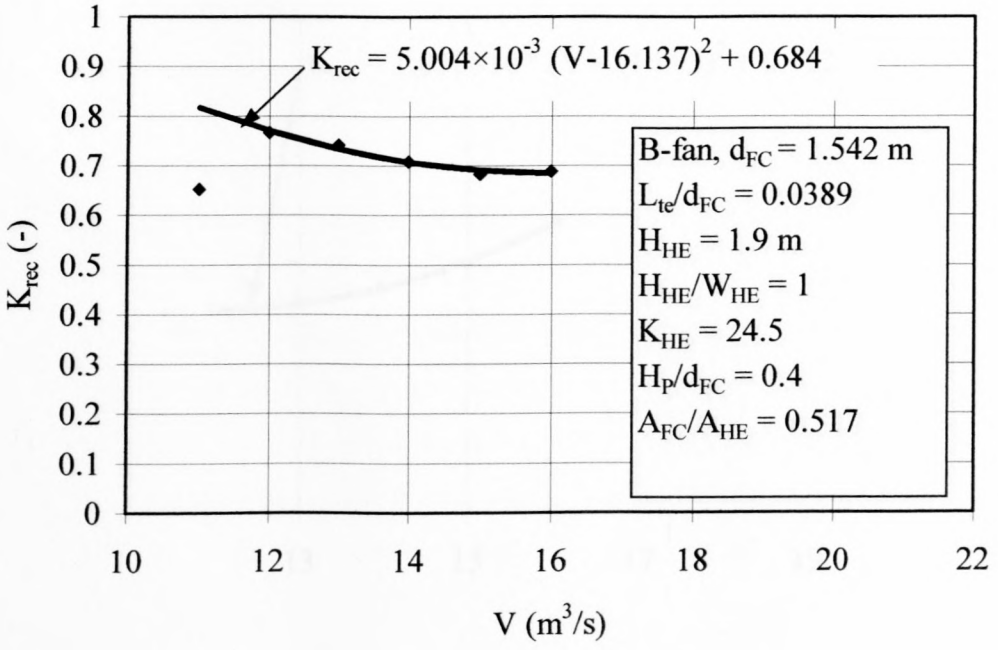

Figure G.3. K_{rec} vs V for $\gamma_{root} = 60°$.

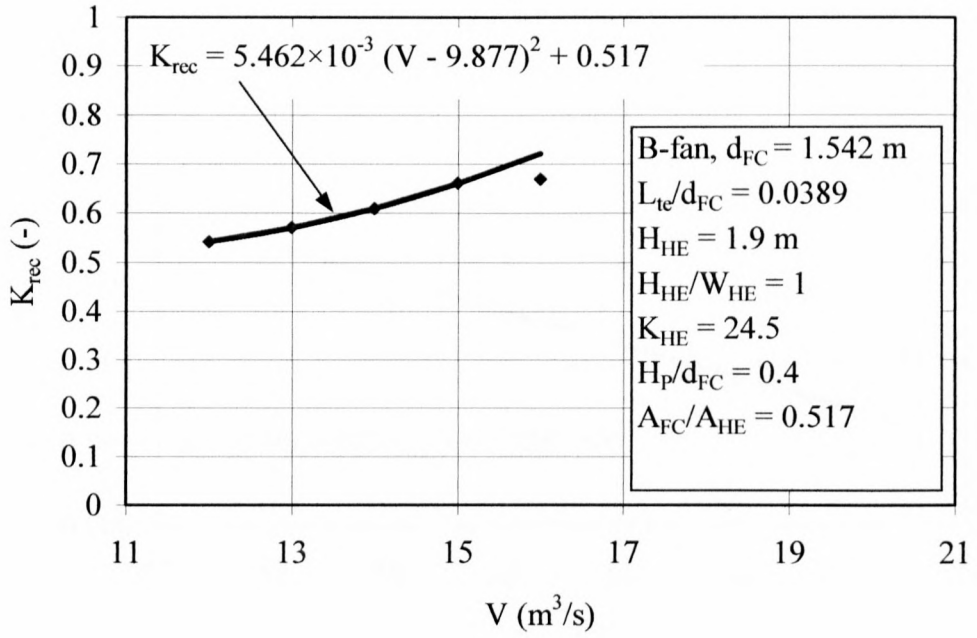

Figure G.4. K_{rec} vs V for $\gamma_{root} = 59°$.

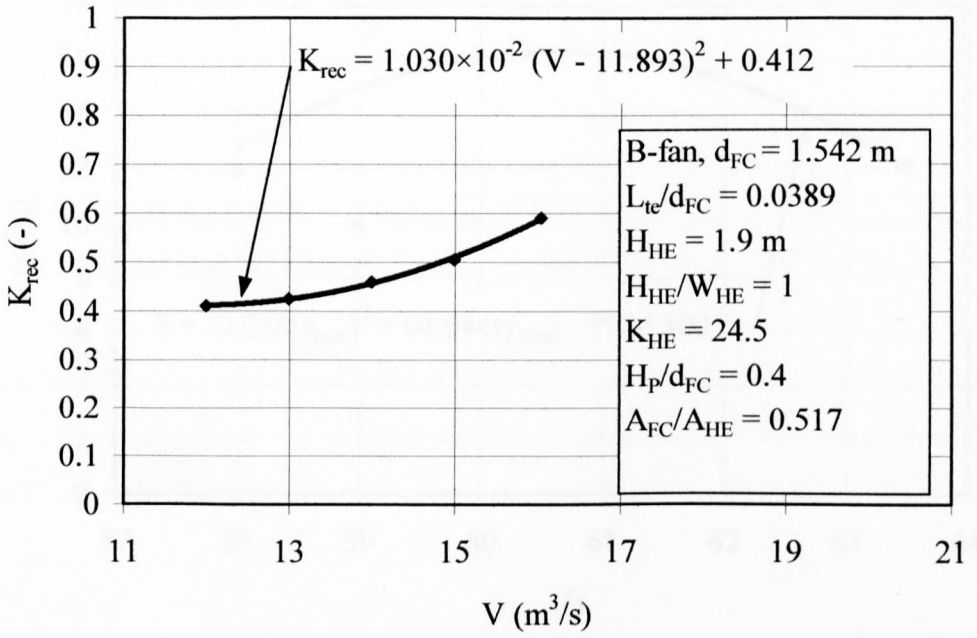

Figure G.5. K_{rec} vs V for $\gamma_{root} = 58°$.

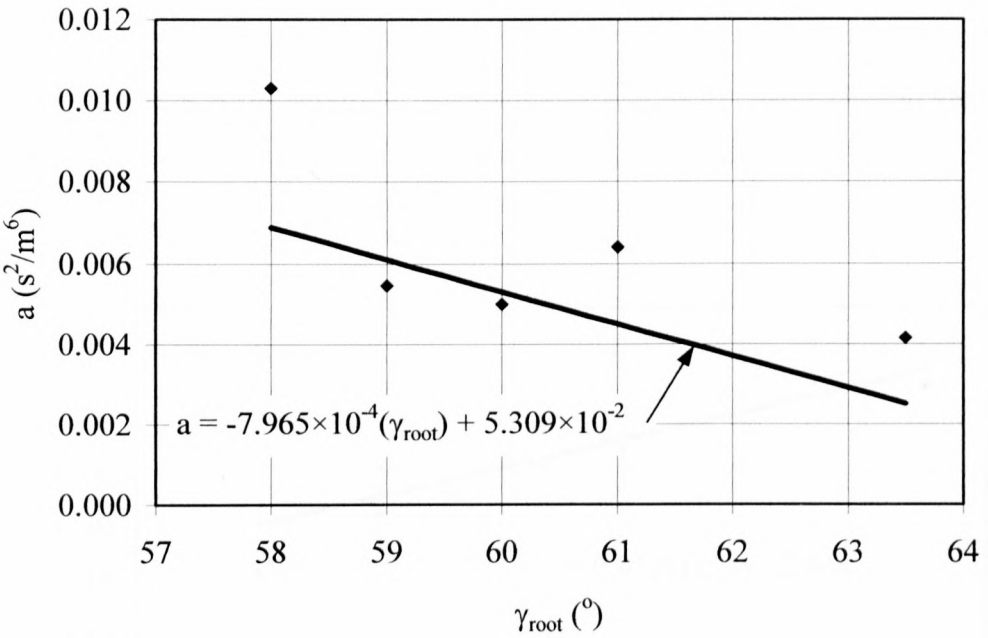

Figure G.6. a vs. γ_{root} for the range of forced draught ACHEs investigated.

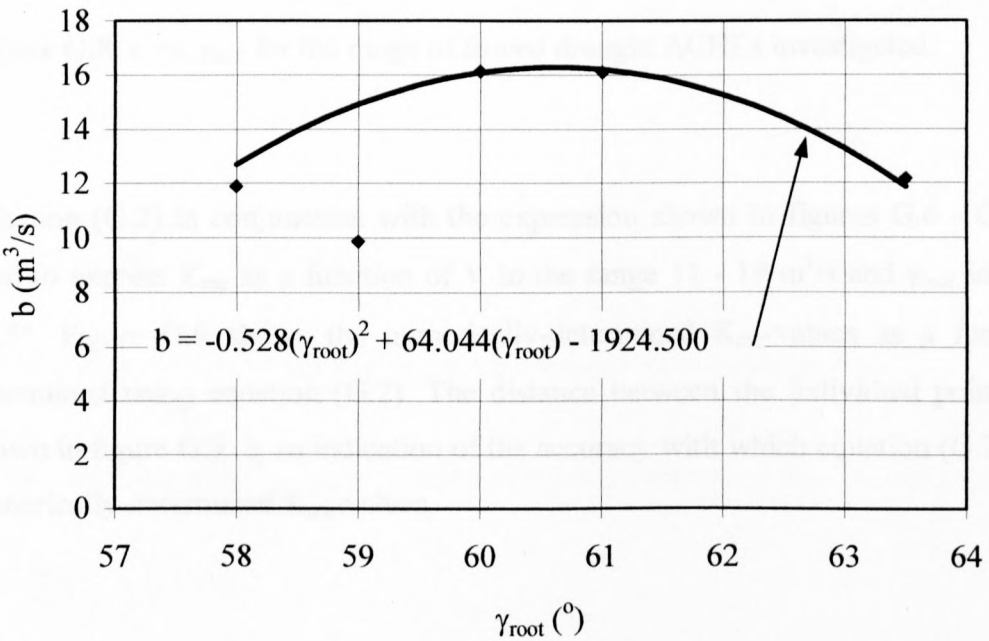

Figure G.7. b vs. γ_{root} for the range of forced draught ACHEs investigated.

From the expressions displayed in figures G.1 - G.5 it is possible to determine the value of functions a, b and c for the respective γ_{root} - values. Figures G.6 - G.8 show the value of a, b and c respectively at the different γ_{root}-values as well as the mathematical expressions used to express the relationship between a, b and c and γ_{root}.

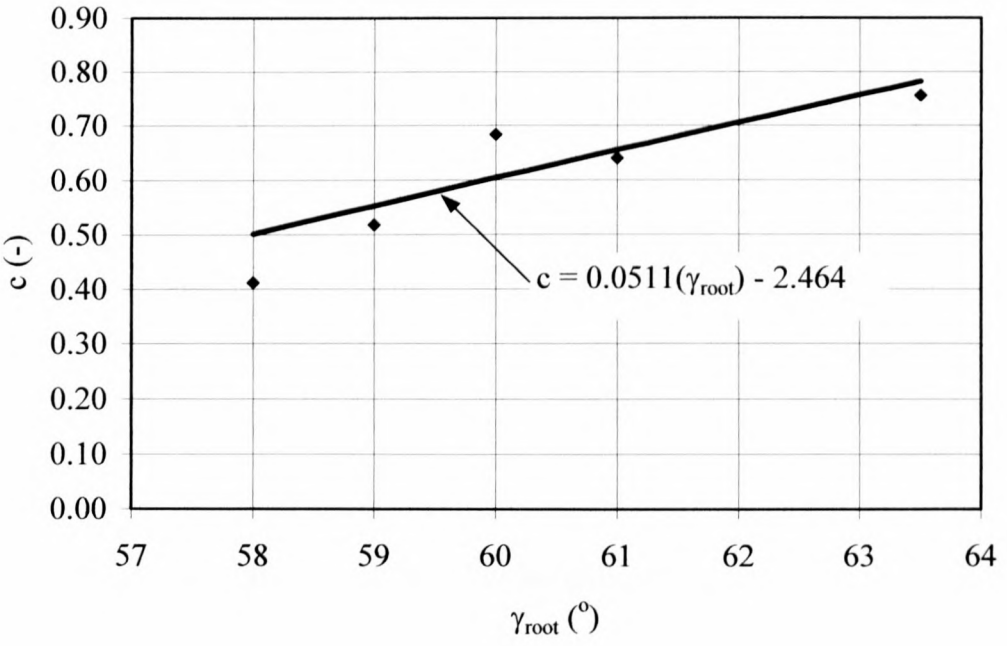

Figure G.8. c vs. γ_{root} for the range of forced draught ACHEs investigated.

Equation (G.2) in conjunction with the expression shown in figures G.6 - G.8 can now be used to express K_{rec} as a function of V in the range 11 - 19 m^3/s and γ_{root} in the range 58 - 63.5°. Figure G.9 shows the numerically-determined K_{rec}-values as a function of those determined using equation (G.2). The distance between the individual points and the line shown in figure G.9 is an indication of the accuracy with which equation (G.2) correlates the numerically-determined K_{rec}-values.

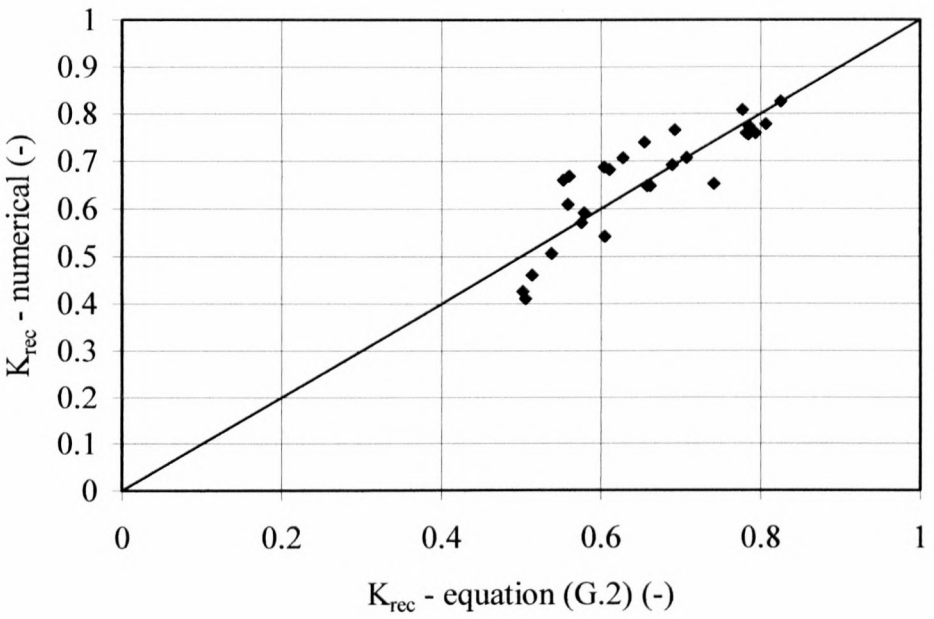

Figure G.9. The numerically-determined K_{rec}-values vs. those obtained using equation (G.2).

G.1.2. The influence of plenum chamber height on K_{rec}

According to Chapter 6, K_{rec} can be expressed as a function of H_P/d_{FC} as follows

$$f_2 = d - e\left(H_P/d_{FC}\right)^f \qquad \text{(G.3)}$$

where d = 1.05, e = 0.086 and f = -1.411

G.1.3. The influence of the fan to heat exchanger area ratio on K_{rec}

According to Chapter 7, K_{rec} can be expressed as a function of A_{FC}/A_{HE} as follows

$$f_3 = g(A_{FC}/A_{HE}) + h \qquad \text{(G.4)}$$

where g = 2.028 and h = -0.429

G.1.4. The influence of the heat exchanger bundle flow resistance on K_{rec}

According to Chapter 8, K_{rec} can be expressed as a function K_{HE} as follows

$$f_4 = i(K_{HE}) + j \qquad (G.5)$$

where i = 0.0025 and j = 0.581

G.1.5. The influence of the position of the axial flow fan on K_{rec}

According to Chapter 9 K_{rec} remains unchanged for a change in L_{te}/d_{FC} and it follows that

$$f_5 = 1 \qquad (G.6)$$

G.1.6. The final expression for K_{rec}

Substitution of equations (G.2) - (G.6) into equation (G.1) yields the following expression for K_{rec}

$$K_{rec} = C_1\left[a(V-b)^2 - c\right]\cdot\left[d - e(H_P/d_{FC})^f\right]\cdot\left[g(A_{FC}/A_{HE}) + h\right]\cdot\left[i(K_{HE}) + j\right] \qquad (G.7)$$

where C_1 = 3.372, a, b and c are expressed by the equations shown in figures G.6 - G.8 respectively, d = 1.05, e = 0.086, f = -1.411, g = 2.028, h = -0.429, i = 0.0025 and j = 0.581.

Equation (G. 7) is valid for the following variable-value ranges:

$11\ m^3/s \le V \le 19\ m^3/s$

$58° \le \gamma_{root} \le 63.5°$

$0.15 \le H_P/d_{FC} \le 0.5$

$0.4 \le A_{FC}/A_{HE} \le 0.6$

$7.5 \le K_{HE} \le 25.6$

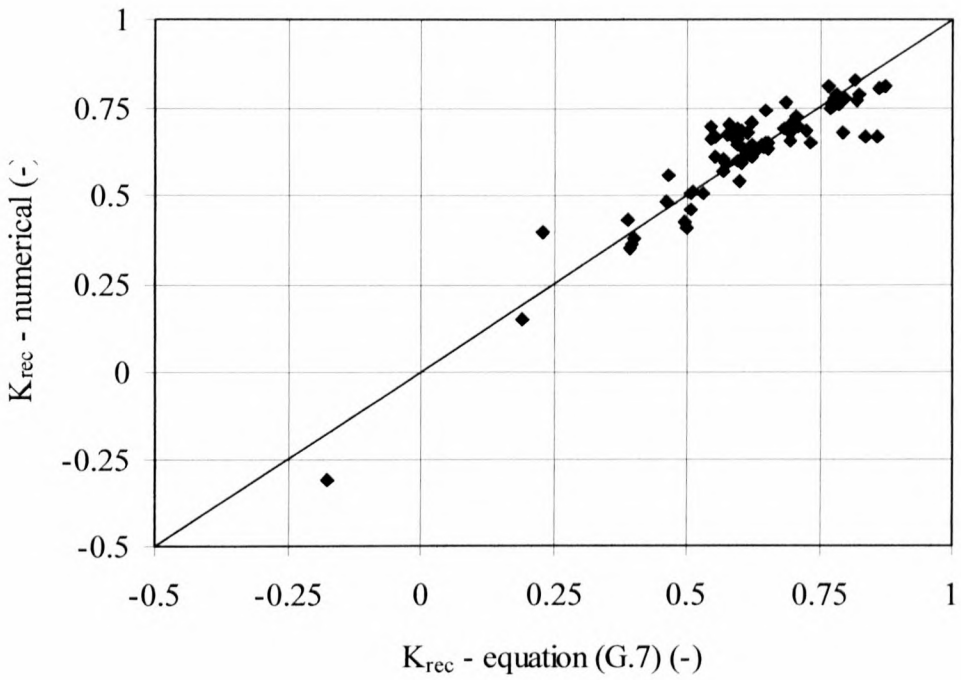

Figure G.10. The numerically-determined K_{rec}-values vs. the K_{rec}-values determined utilising equation (G.7).

Figure G.10 displays a plot of the numerically-determined K_{rec}-values vs. the K_{rec}-values determined utilising equation (G.7).

As mentioned earlier, the distance between the individual points and the line shown in figure G.9 is an indication of the accuracy with which equation (G.7) correlates the numerically-determined K_{rec}-values.

G.2. Formulation of a mathematical expression for α_{eHE}

In Chapters 5 - 9 the influence of the fan performance characteristics, the plenum chamber depth, the fan to heat exchanger area ratio, the heat exchanger bundle resistance value and the position of the axial flow fan within the fan casing respectively on the kinetic energy coefficient at the heat exchanger bundle outlet, α_{eHE} are investigated.

The mathematical expression used to express α_{eHE} as a function of the variables listed in table G.1 has the following form

$$\alpha_{eHE} = C_1 \cdot f_1(V, \gamma_{root}) \cdot f_2(H_P/d_{FC}) \cdot f_3(A_{FC}/A_{HE}) \cdot f_4(K_{HE}) \cdot f_5(L_{te}/d_{FC}) \qquad (G.8)$$

where C_1 is a constant and f_1 - f_5 are functions that represent the influence on α_{eHE} of the variables listed in parenthesis of the respective functions.

G.2.1. The influence of axial flow fan performance on α_{eHE}

In Chapter 5 it was shown that, provided that all variable values listed in table G.1 remain constant save the ACHE operating point volume flow rate, V and fan blade root stagger angle, γ_{root} the α_{eHE}-value can be expressed as a linear function of the kinetic energy coefficient at the fan exit as follows

$$\alpha_{eHE} = a(\alpha_{eF}) + b \qquad (G.9)$$

where a = 0.0518 and b = 0.9229

Standard fan test codes and in particular BS 848 [80BS1] do not make any provision for determining the α_{eF}-value of an axial flow fan. However, it is possible to determine α_{eF} from the results of the numerical investigation of the performance characteristics of the B-fan displayed in Appendix E through the use of the following expression based on equation (2.4)

$$\alpha_{eF} = \sum_{i=1}^{N} \left(v_{zi} \cdot \left(v_{xi}^2 + v_{yi}^2 + v_{zi}^2\right) \cdot A_i\right) / \left(V^3/A_{FC}^2\right) \qquad (G.10)$$

where v_{xi}, v_{yi}, and v_{zi} are the Cartesian components of the velocity vector associated with the i-th cell out of N cells at the fan exit.

Figure G.11 displays the α_{eF}-values of the B-fan as a function of the volume flow rate for the range of γ_{root}-values considered.

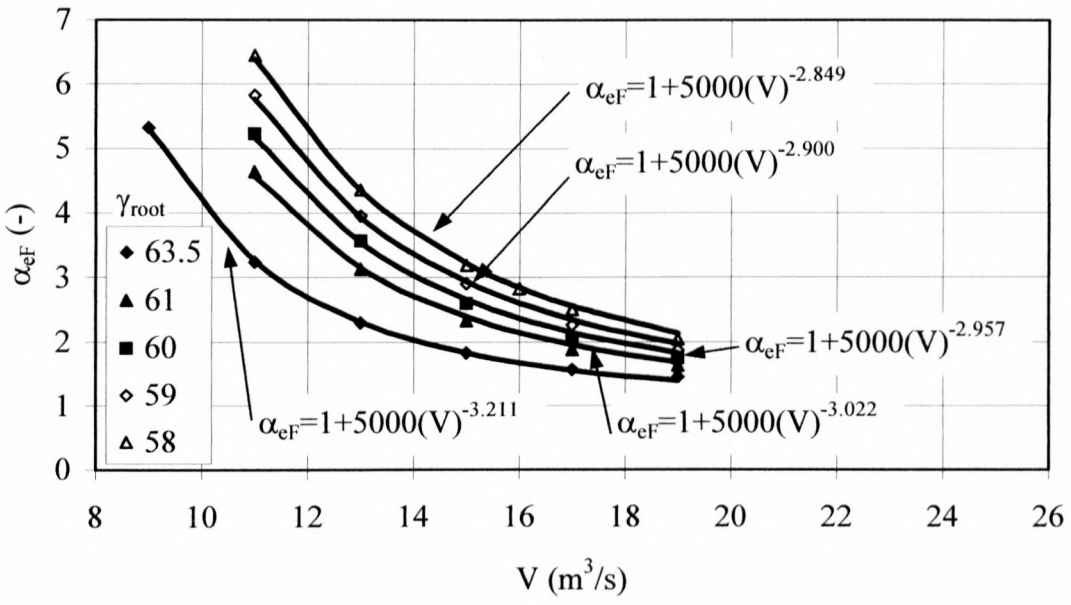

Figure G.11. α_{eF} vs. V for the range of γ_{root}-values investigated.

Figure G.11 indicates that α_{eF} can be expressed as a function of V by the following expression

$$\alpha_{eF} = 1 + 5000V^{c} \qquad \text{(G.11)}$$

where c is a function of the blade root stagger angle, γ_{root}.

Figure G.12 displays c of equation (G.11) as a function of γ_{root}.

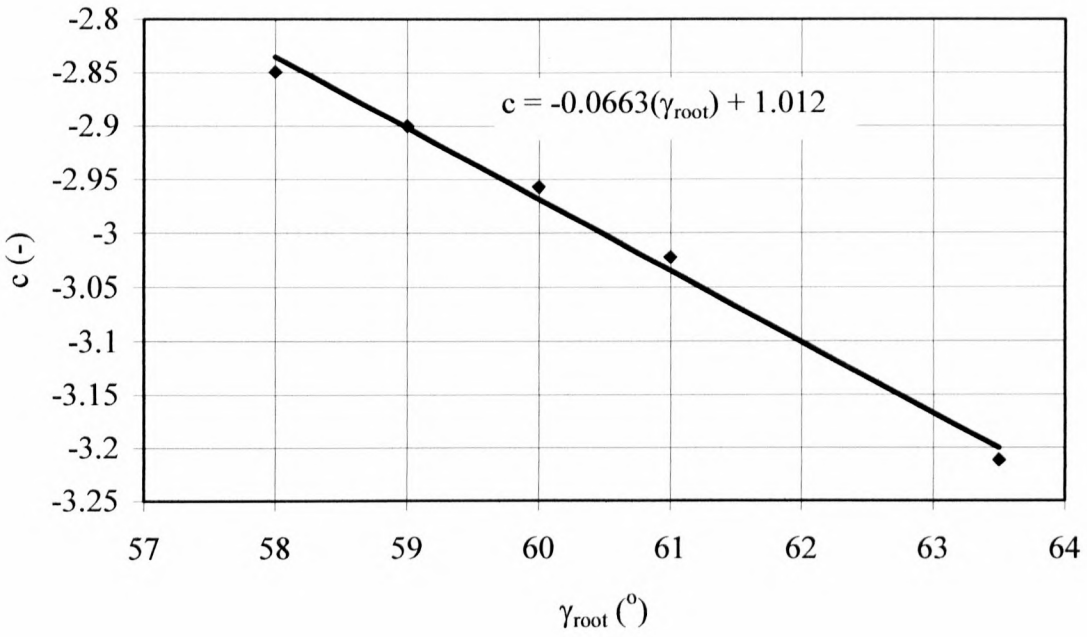

Figure G.12. c vs. γ_{root} for the range of forced draught ACHEs investigated.

Figure G.12 shows that the c-value of equation (G.11) can be presented as a linear function of γ_{root}.

Substitution of equation (G.11) into (G.9) yields the following expression for f_1 in equation (G.8)

$$f_1 = a\left(1 + 5000V^c\right) + b \qquad \text{(G.12)}$$

where

c is given by the linear expression shown in figure G.12, a = 0.0518 and b = 0.9229.

G.2.2. The influence of plenum chamber height on α_{eHE}

According to Chapter 6, α_{eHE} can be expressed as a function of H_P/d_{FC} so that

$$f_2 = 1 + d\left(H_P/d_{FC}\right)^e \qquad \text{(G.13)}$$

where d = 0.032 and e = -0.555.

G.2.3. The influence of the fan to heat exchanger area ratio on α_{eHE}

According to Chapter 7, α_{eHE} can be expressed as a function of A_{FC}/A_{HE} so that

$$f_3 = 1 + f(A_{FC}/A_{HE})^g \qquad \text{(G.14)}$$

where f = 0.00675 and g = 2.535

G.2.4. The influence of the heat exchanger bundle flow resistance on α_{eHE}

According to Chapter 8, α_{eHE} can be expressed as a function K_{HE} so that

$$f_4 = 1 + h(K_{HE})^i \qquad \text{(G.15)}$$

where h = 6.296 and i = -1.612

G.2.5. The influence of the position of the axial flow fan on α_{eHE}

According to Chapter 9, α_{eHE} remains unchanged for a change in L_{te}/d_{FC} and it follows that

$$f_5 = 1 \qquad \text{(G.16)}$$

G.2.6. The final expression for α_{eHE}

Substitution of equations (G.12) - (G.16) into equation (G.8) yields the following expression for K_{rec}

$$\alpha_{eHE} = C_1\left[a\left(1+5000(V)^c\right)+b\right]\cdot\left[1+d\left(H_P/d_{FC}\right)^e\right]\cdot\left[1+f\left(A_{FC}/A_{HE}\right)^g\right]\cdot\left[1+h\left(K_{HE}\right)^i\right] \quad \text{(G.17)}$$

where C_1 = 0.889, a = 0.0518, b = 0.9229, c is a function of γ_{root} and given by the equation shown in figure G.12, d = 0.032, e = -0.555, f = 0.00675, g = -2.535, h = 6.296 and i = -1.612.

Equation (G.17) is valid for the following variable-value ranges:

$11\ m^3/s \le V \le 19\ m^3/s$

$58° \le \gamma_{root} \le 63.5°$

$0.15 \le H_P/d_{FC} \le 0.5$

$0.4 \le A_{FC}/A_{HE} \le 0.6$

$3.5 \le K_{HE} \le 25.6$

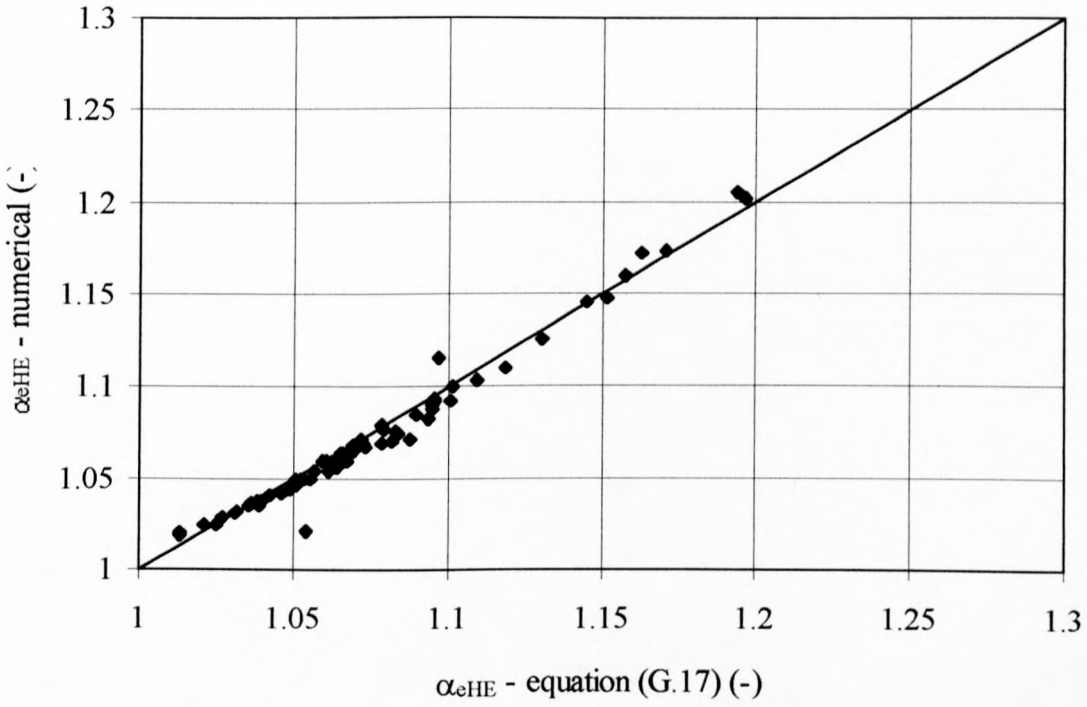

Figure G.13. The numerically-determined α_{eHE}-values vs. the α_{eHE}-values determined utilising equation (G.17).

Figure G.13 displays a plot of the numerically-determined α_{eHE}-values vs. the α_{eHE}-values determined utilising equation (G.17).

As mentioned earlier, the distance between the individual points and the line shown in figure G.12 is an indication of the accuracy with which equation (G.17) correlates the numerically-determined α_{eHE}-values. Figure G.13 shows that the majority of the data points are accurately correlated by equation (G.17). K_{HE}-values are restricted to the range 13.5 - 25.6 as α_{eHE}-values outside of this K_{HE}-value range are not well correlated by equation (G.17) and is more representative of K_{HE}-values used in industrial forced draught ACHEs.

APPENDIX H – Computational grid detail

This appendix displays the computational grids used during the course of the numerical investigation in greater detail. The computational grids used for forced and induced draught ACHEs were very similar and as a result only the computational grid for an induced draught ACHE is displayed in this appendix.

H.1. Fan inlet bell mouth

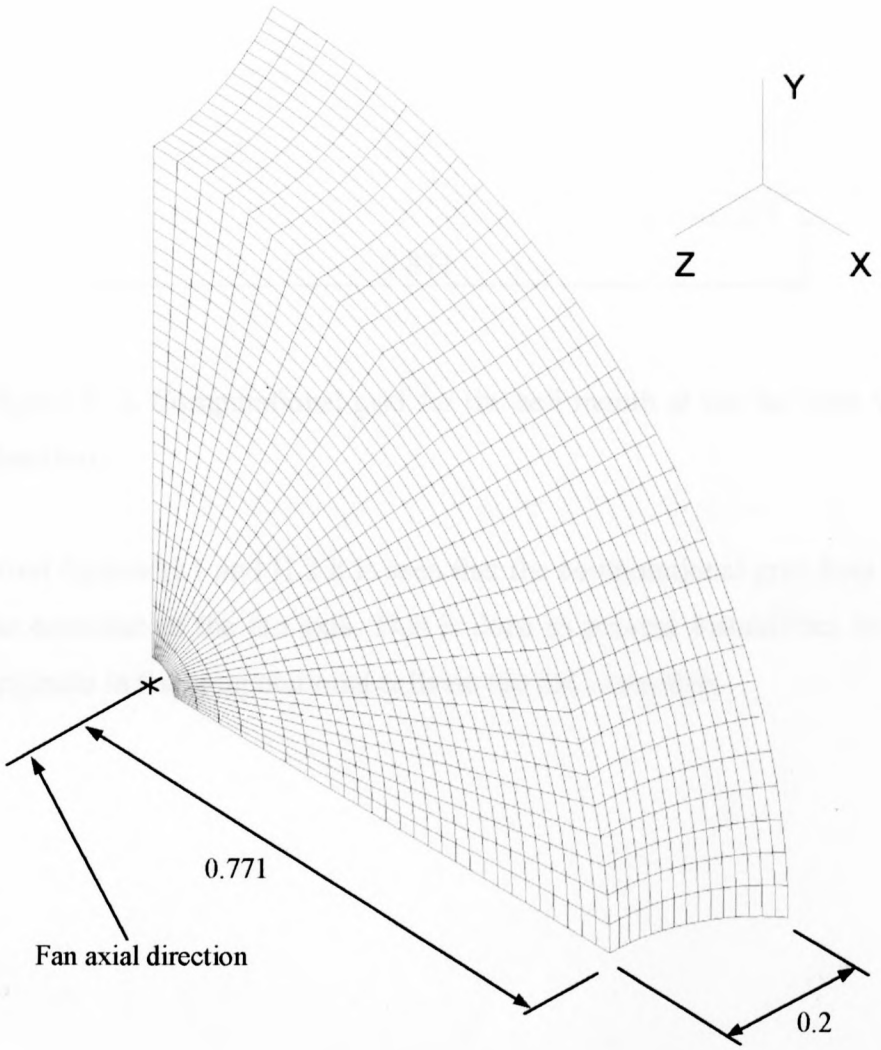

Figure H.1. Computational grid for the bell mouth at the fan inlet.

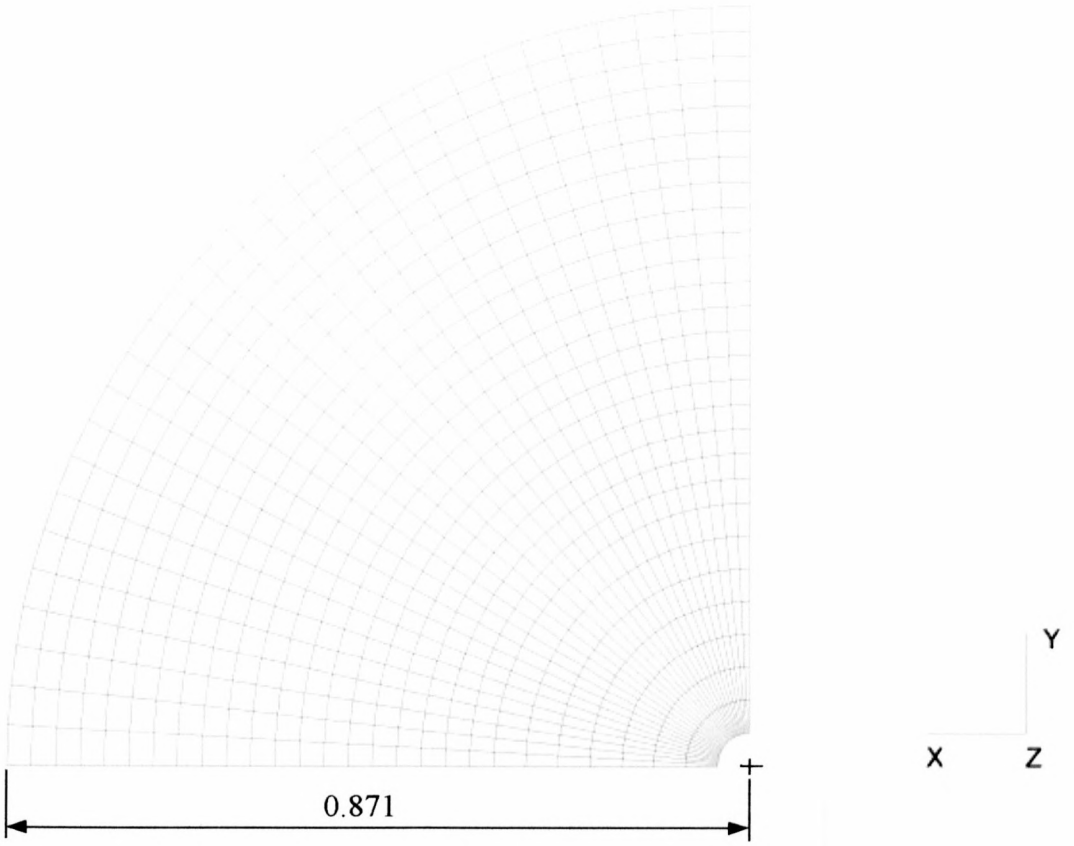

Figure H.2. Computational grid for the bell mouth at the fan inlet viewed in the negative z-direction.

From figures H.1 and H.2 it is seen that the computational grid does not extend completely to the centeline of the fan axis. This is done to prevent instabilities in the solution process that originate in the computational cells on the fan centreline.

H.2. Plenum chamber and heat exchanger

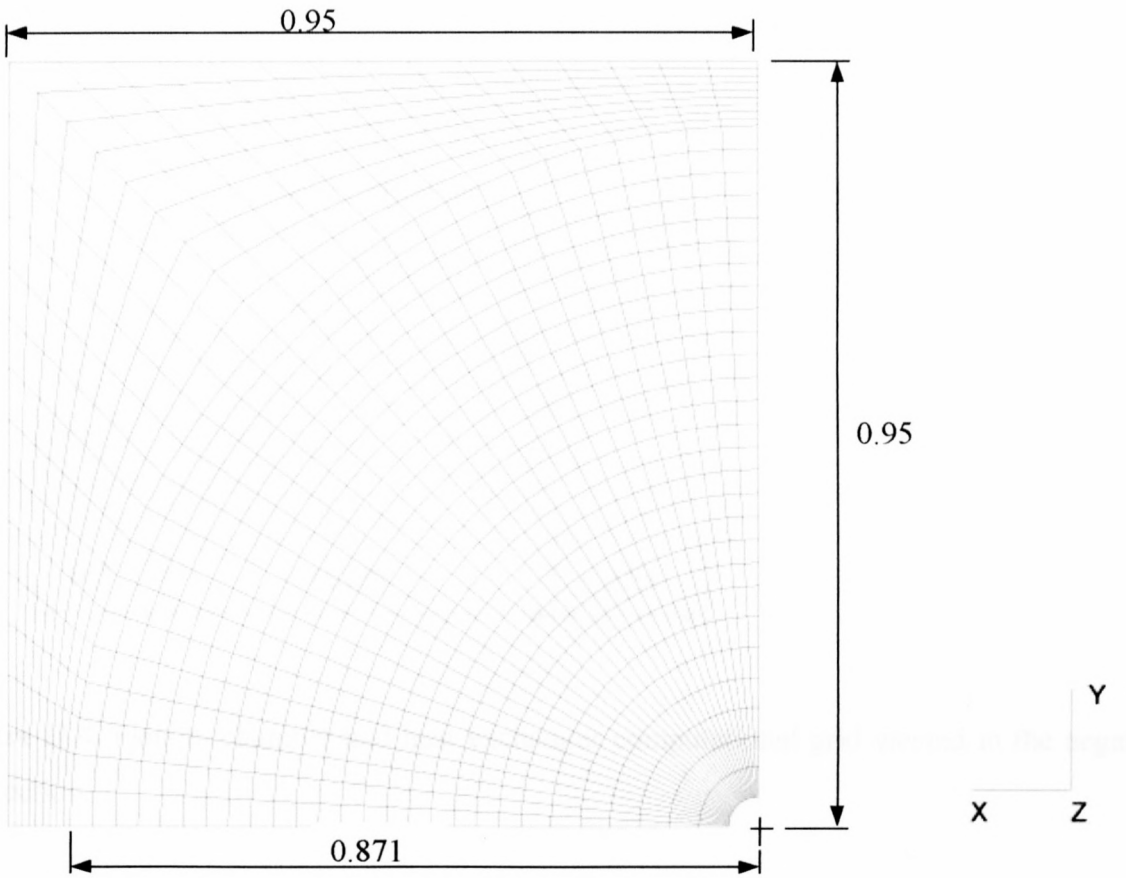

Figure H.3. A cross-sectional view in the xy-plane of the computational grid used for the plenum chamber.

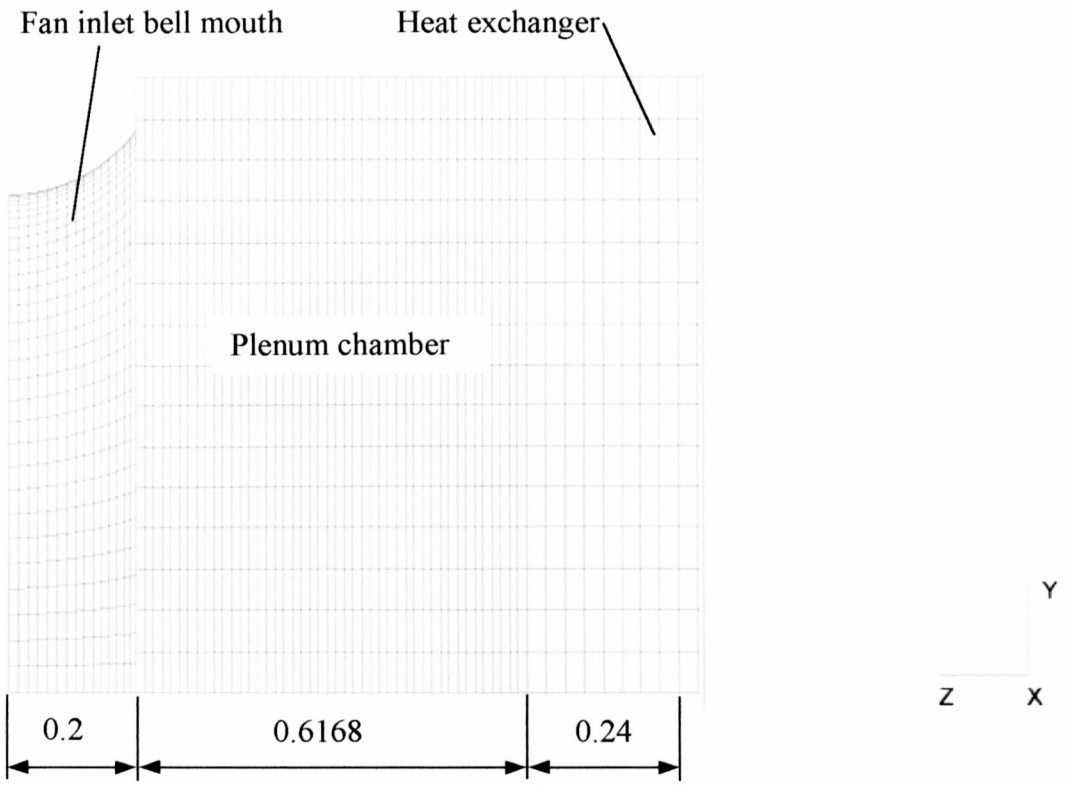

Figure H.4. Plenum chamber and heat exchanger computational grid viewed in the negative x-direction.

H.3. Actuator disc

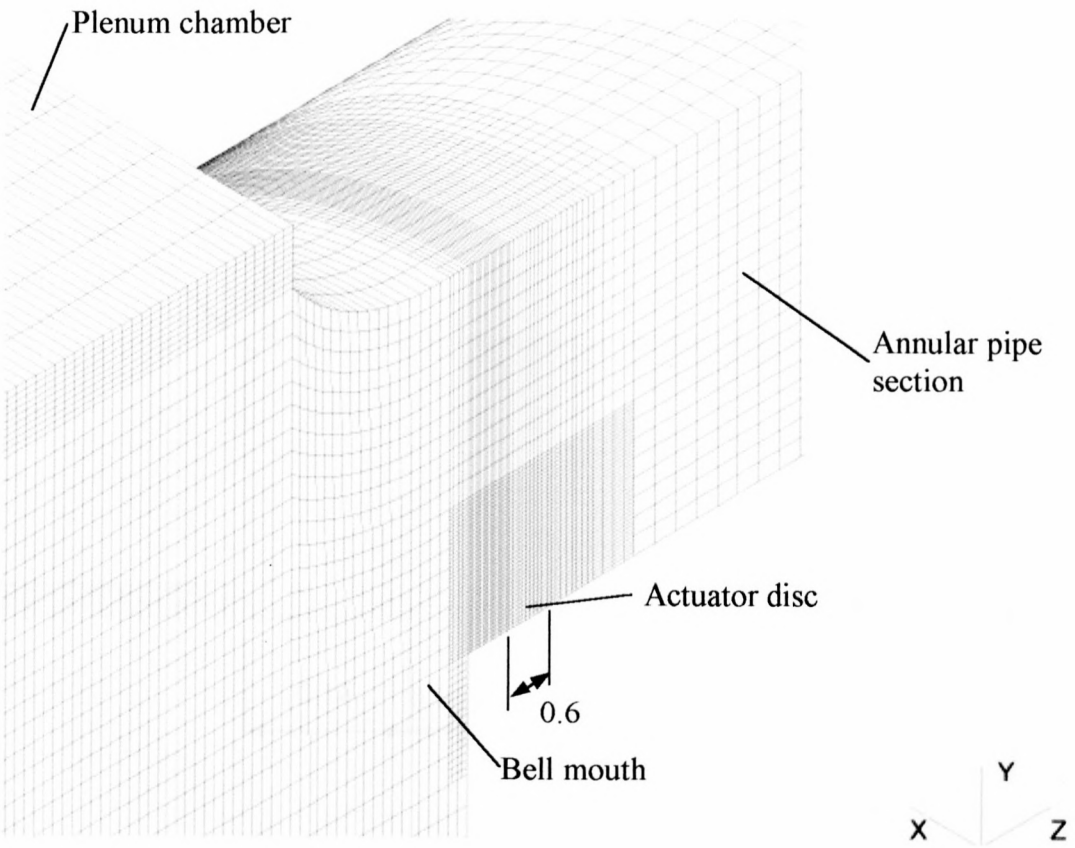

Figure H.5. Location of the actuator disc computational cells.

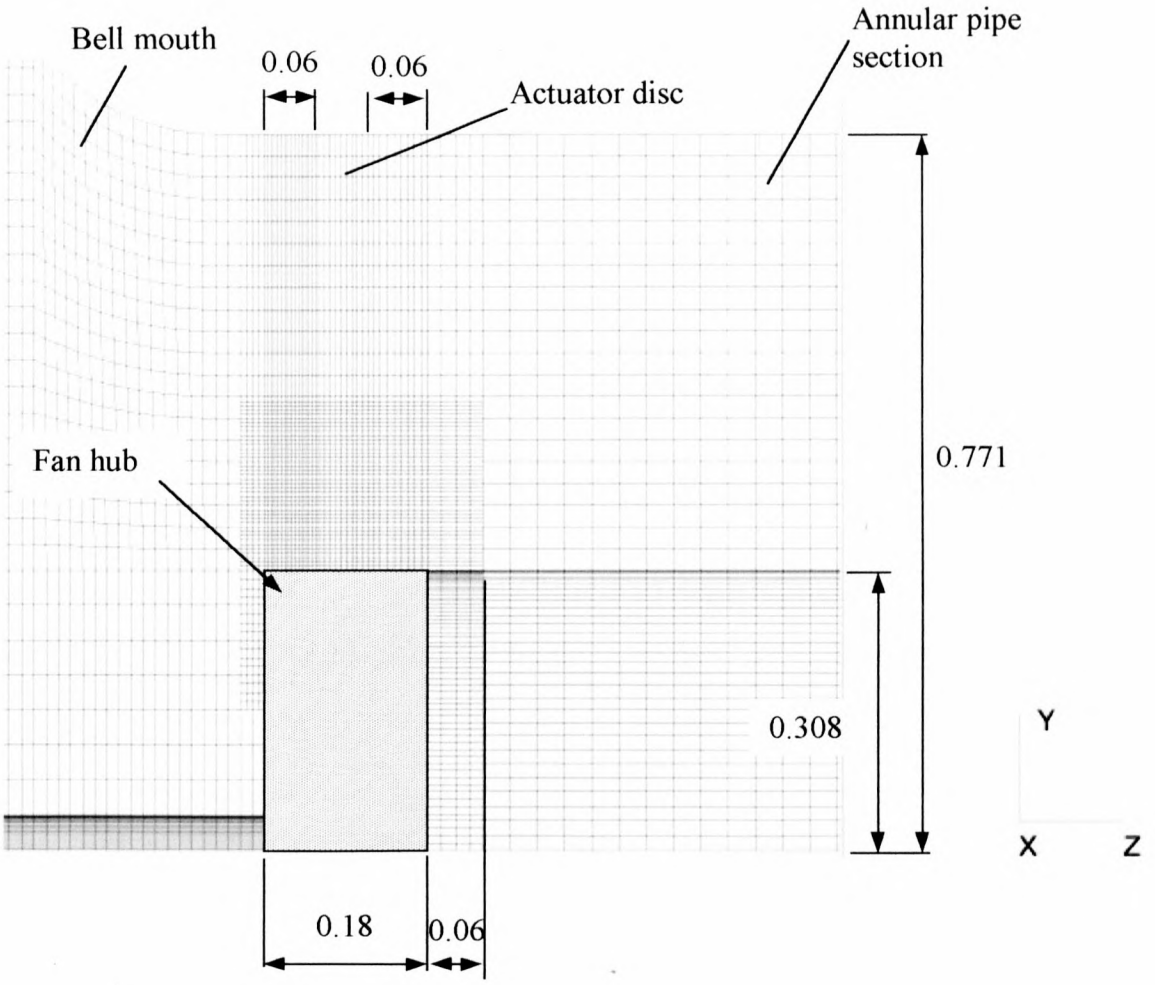

Figure H.6. Actuator disc computational cells viewed in the negative x-direction.

In figure H.6 it is possible to observe regions in the computational grid where grid refinement was applied to ensure a stable solution process. The region directly up-stream of the actuator disc cells is associated with a dramatic increase in the tangential velocity component as the flow approaches the actuator disc cells. Flow separation occurs around the front part of the fan hub necessitating grid refinement in this region. The actuator disc region (note that the actuator disc has a thickness of 0.06 m in the z-direction) is a source of large variable value gradients due to the effect of the actuator disc forces on the fluid.

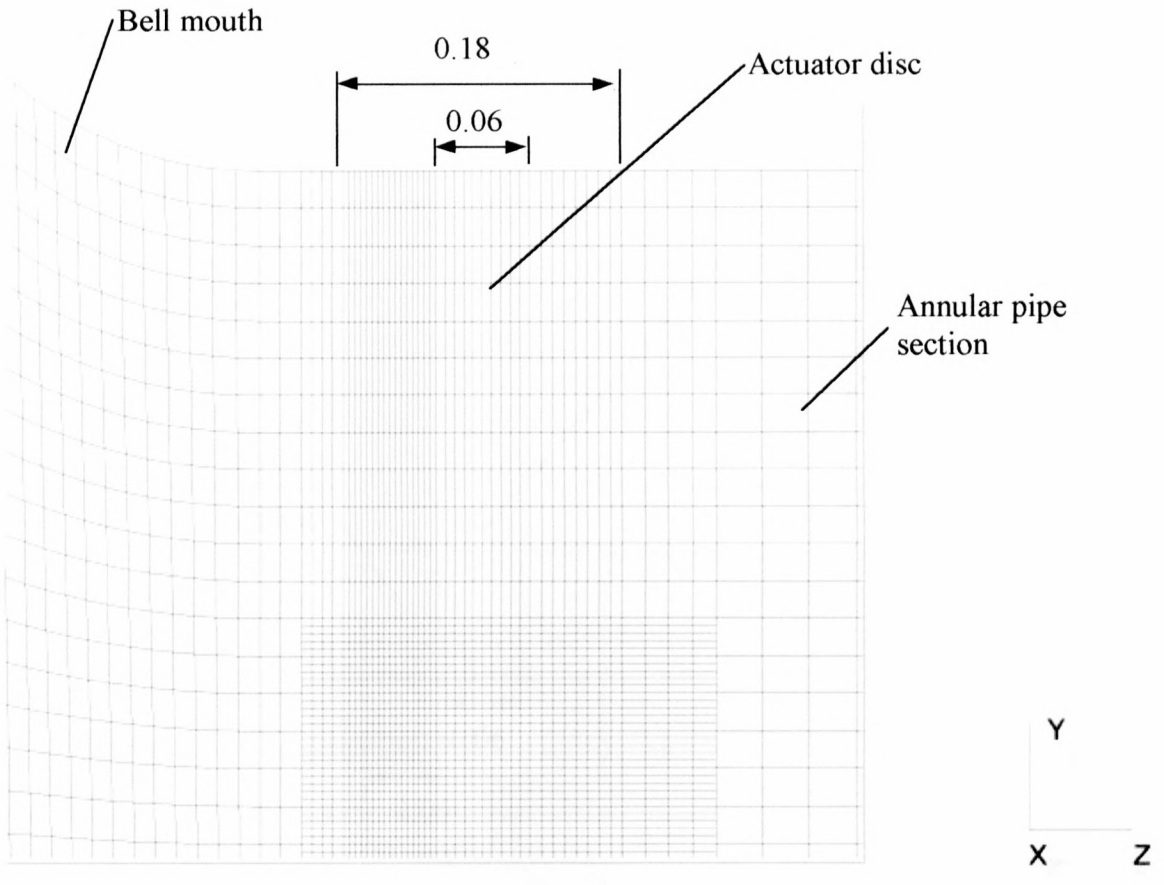

Figure H.7. Detailed view 1 of actuator disc computational cells viewed in the negative x-direction.

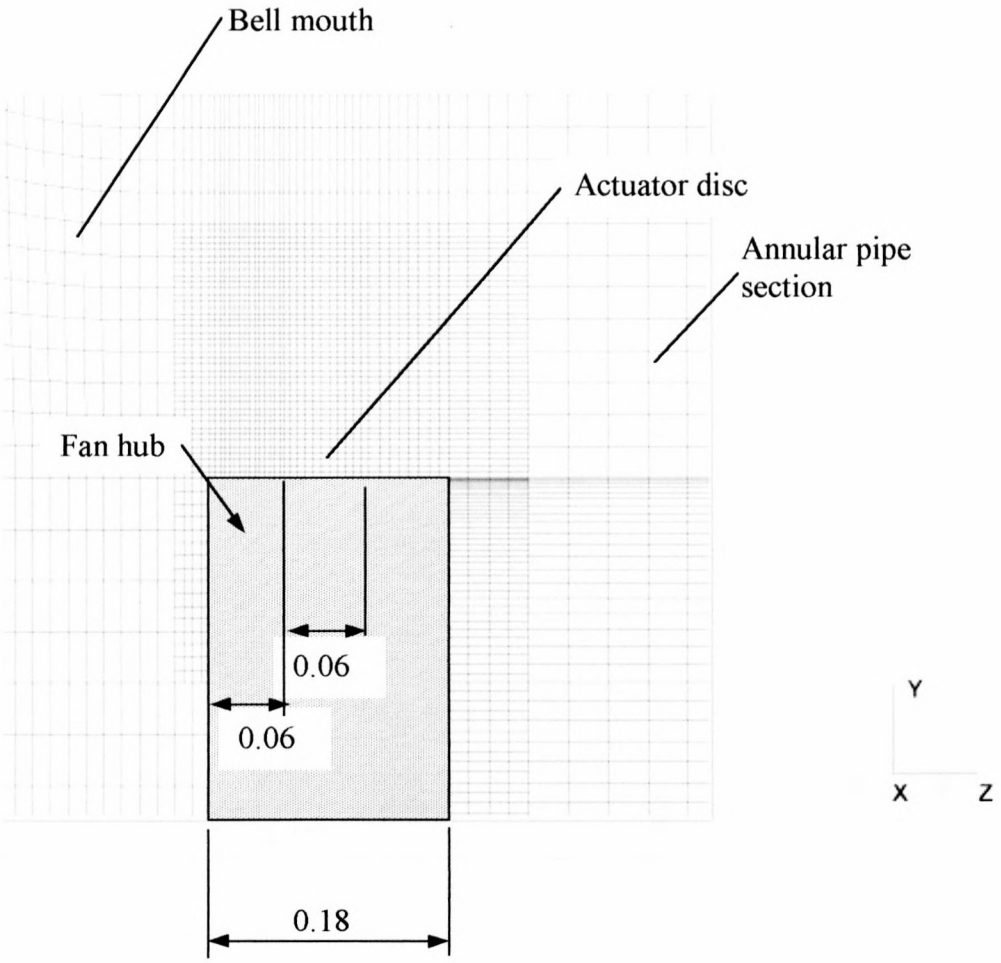

Figure H.8. Detailed view 2 of actuator disc computational cells viewed in the negative x-direction.

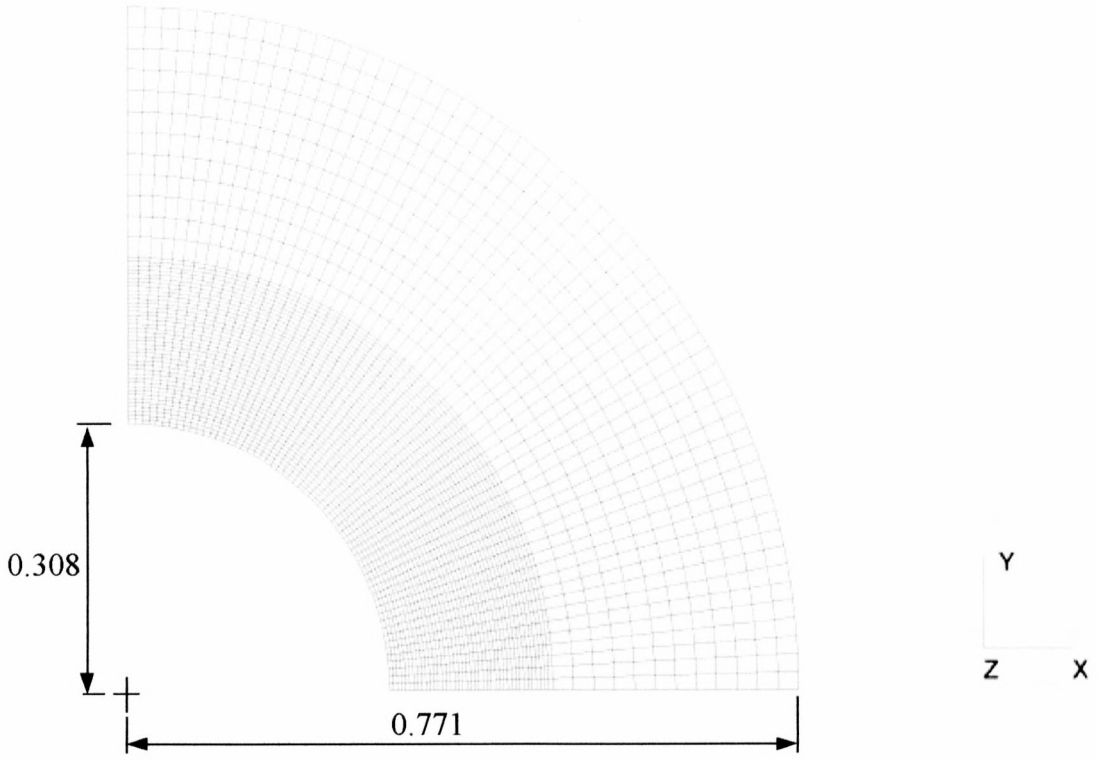

Figure H.9. Cross-sectional view of actuator disc computational cells viewed in the negative z-direction.

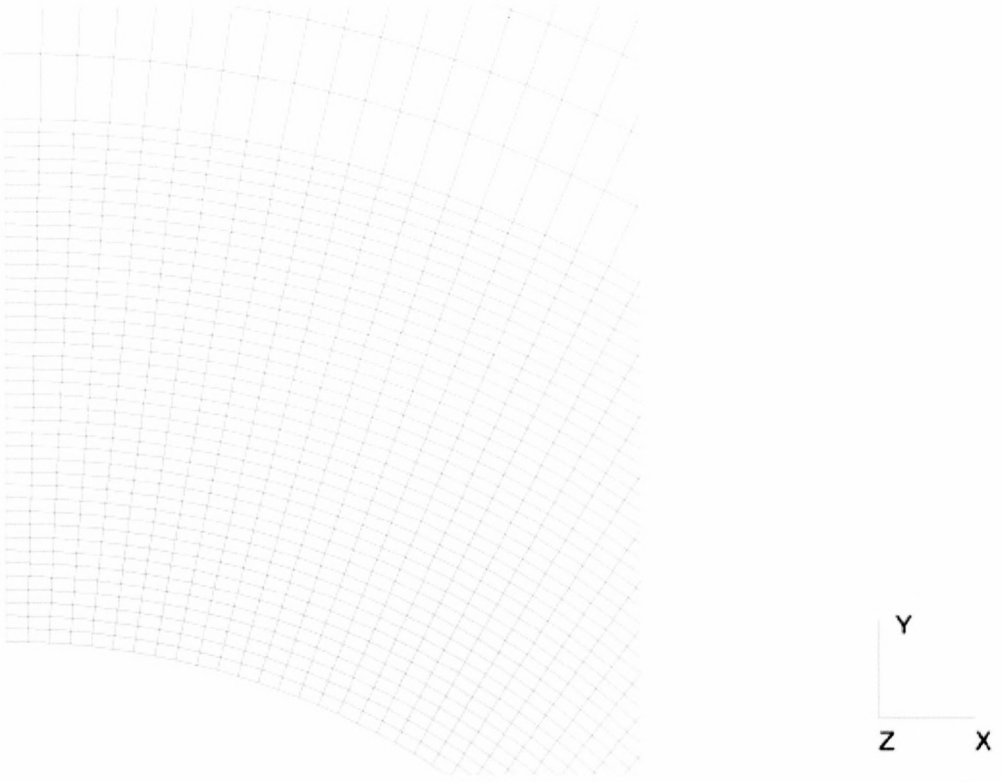

Figure H.10. Detail of cross-sectional view of actuator disc computational cells viewed in the negative z-direction.


meyer_numerical_2000